



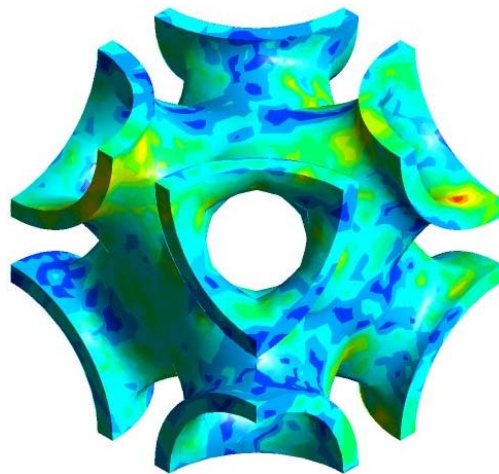
**Universidade de
Aveiro
2013**

Departamento de Engenharia Mecânica

**HENRIQUE
DE
AMORIM
ALMEIDA**

**PROJECTO INTELIGENTE DE SCAFFOLDS OBTIDOS POR
PROTOTIPAGEM RÁPIDA**

**SMART DESIGN OF SCAFFOLDS OBTAINED BY BIOFABRICATION
FOR TISSUE ENGINEERING APPLICATIONS**





**HENRIQUE
DE
AMORIM
ALMEIDA**

**PROJECTO INTELIGENTE DE SCAFFOLDS OBTIDOS POR
PROTOTIPAGEM RÁPIDA**

**SMART DESIGN OF SCAFFOLDS OBTAINED BY BIOFABRICATION
FOR TISSUE ENGINEERING APPLICATIONS**

dissertação apresentada à Universidade de Aveiro para cumprimento dos requisitos necessários à obtenção do grau de Doutor em Engenharia Mecânica, realizada sob a orientação científica do Dr. Paulo Jorge da Silva Bártolo, Professor Coordenador do Centro para o Desenvolvimento Rápido e Sustentado de Produto do Instituto Politécnico de Leiria e co-orientação científica do Dr. José António de Oliveira Simões, Professor Associado com Agregação do Departamento de Engenharia Mecânica da Universidade de Aveiro

This research is supported by the Portuguese Foundation of Science and Technology through a PhD Grant (SFRH/BD/37604/2007) and through a Strategic Project UI 4044 (Pest-OE/EME/UI4044/2011).

This research is also supported through a Marie Curie Research Project designated “International Research Exchange for Biomedical Devices Design and Prototyping” “IREBID”.

Dedico esta dissertação à minha esposa e à filha pelo incansável apoio e compreensão durante o decorrer desta jornada árdua no qual tive igualmente de abdicar muito tempo familiar para atingir a esta meta na minha vida.

o júri

presidente

Doutor Valeri Skliarov
Professor Catedrático, Universidade de Aveiro, Espanha

Doutor Joaquim de Cuirana
Professor Catedrático, Universidade de Girona, Espanha

Doutor Jorge Vicente Lopes da Silva
Investigador, Centro de Tecnologia da Informação Renato Archer, Brasil

Doutor José António de Oliveira Simões
Professor Associado com Agregação, Universidade de Aveiro
Co-orientador

Doutor Paulo Jorge da Silva Bártolo
Professor Coordenador, Instituto Politécnico de Leiria
Orientador

Doutor António Manuel de Amaral Monteiro Ramos
Professor Auxiliar Convidado, Universidade de Aveiro

agradecimentos

Ao Professor Doutor Paulo Jorge da Silva Bártolo, meu orientador científico e grande amigo, agradeço a preciosa e sempre paciente orientação e profundo envolvimento quer em termos de exigência, rigor, minuciosidade e ambição, a disponibilidade prestada, motivação, amizade e o contributo crítico e científico durante o desenvolvimento desta dissertação. A sua amizade e apoio foi uma constante no decorrer desta longa e árdua jornada. Estes factores foram determinantes para a realização deste trabalho, um exemplo a seguir de dedicação e trabalho.

Ao Professor Doutor José António de Oliveira Simões, meu co-orientador científico, agradeço a colaboração e incentivo, durante o desenvolvimento desta dissertação.

Aos investigadores Joana Ferreira, Marco Domingos e Professor Doutor Paulo Jorge da Silva Bártolo pela cedência dos dados experimentais dos ensaios de compressão das matrizes de suporte, por forma a validar a metodologia implementada nesta dissertação, em termos de comportamento mecânico.

A todos os amigos, em especial à Helena Bártolo, do Centro para o Desenvolvimento Rápido e Sustentado de Produto do Instituto Politécnico de Leiria, agradeço todo o apoio, contributo e incentivo prestado durante o desenvolvimento desta dissertação.

A toda a minha família, em especial à minha irmã Ermelinda, e os meus estimados amigos por todo apoio e motivação que foram uma constante durante o decorrer desta jornada.

À minha mulher Graciete pela confiança, motivação e apoio que foram uma constante durante o decorrer do meu doutoramento, encorajando e acreditando sempre no meu valor e dando-me força para continuar quando as circunstâncias incitavam ao desalento, o que me permitiu ultrapassar todos os obstáculos que me surgiram. Agradeço igualmente a sua compreensão pela minha ausência para permitir realizar o trabalho. Apoio esse, que foi determinante para a realização e sucesso deste trabalho.

E à minha filha Raquel pela compreensão da minha ausência para poder realizar a investigação que decorreu nesta dissertação.

A todos, o meu mais sincero agradecimento.

palavras-chave

Engenharia de Tecidos, Scaffolds, Biofabricação, Simulação Numérica, Comportamento Mecânico, Comportamento Vascular, Optimização Topológica.

resumo

A engenharia de tecidos é um domínio tecnológico emergente em rápido desenvolvimento que se destina a produzir substitutos viáveis para a restauração, manutenção ou melhoria da função dos tecidos ou órgãos humanos. Uma das estratégias mais predominantes em engenharia de tecidos envolve crescimento celular sobre matrizes de suporte (scaffolds), biocompatíveis e biodegradáveis. Estas matrizes devem possuir não só elevadas propriedades mecânicas e vasculares, mas também uma elevada porosidade. Devido à incompatibilidade destes dois parâmetros, é necessário desenvolver estratégias de simulação de forma a obter estruturas optimizadas. A previsão real das propriedades mecânicas, vasculares e topológicas das matrizes de suporte, produzidas por técnicas de biofabricação, é muito importante para as diversas aplicações em engenharia de tecidos.

A presente dissertação apresenta o estado da arte da engenharia de tecidos, bem como as técnicas de biofabricação envolvidas na produção de matrizes de suporte. Para o design optimizado de matrizes de suporte foi adoptada uma metodologia de design baseada tanto em métodos de elementos finitos para o cálculo do comportamento mecânico, vascular e as optimizações topológicas, como em métodos analíticos para a validação das simulações estruturais utilizando dados experimentais. Considerando que as matrizes de suporte são estruturas elementares do tipo LEGO, dois tipos de famílias foram consideradas, superfícies não periódicas e as superfícies triplas periódicas que descrevem superfícies naturais. Os objectivos principais desta dissertação são: i) avaliar as técnicas existentes de engenharia de tecidos; ii) avaliar as técnicas existentes de biofabricação para a produção de matrizes de suporte; iii) avaliar o desempenho e comportamento das matrizes de suporte; iv) implementar uma metodologia de design de matrizes de suporte em variáveis tais como a porosidade, geometria e comportamento mecânico e vascular por forma a auxiliar o processo de design; e por fim, v) validar experimentalmente a metodologia adoptada.

keywords

Tissue Engineering, Scaffolds, Biofabrication, Numerical Simulation, Mechanical Behaviour, vascular Behaviour, Topological Optimization.

abstract

The design of optimized scaffolds for tissue engineering is a key topic of research, as the complex macro- and micro- architectures required for a scaffold depends not only on the mechanical properties, but also on the physical and molecular queues of the surrounding tissue within the defect site. Thus, the prediction of optimal features for tissue engineering scaffolds is very important for its mechanical, vascular or topological properties.

The relationship between high scaffold porosity and high mechanical properties is contradictory, as it becomes even more complex due to the scaffold degradation process. A scaffold design strategy was developed, based on the finite element method, to optimise the scaffold design regarding the mechanical and vascular properties as a function of porosity. Scaffolds can be considered as a LEGO structure formed by an association of small elementary units or blocks. In this research work, two types of family elementary scaffold units were considered: non-triple periodic minimal surfaces and triple periodic minimal surfaces that describe natural existing surfaces. The main objectives of this research work are: i) The evaluation of the Tissue Engineering methodology and its different strategies; ii) The evaluation of the existing biofabrication technologies used to produce tissue engineering scaffolds; iii) The evaluation of the scaffold's requirements involved in the scaffold's design; iv) The development of an integrated design strategy based on material, porosity, geometry, mechanical and vascular properties, in order to aid the scaffold design process; and v) The experimental validation of the adopted design strategy.

Index

Index.....	i
Figure Index.....	iii
Table Index.....	xi
Chapter 1 – Introduction.....	1
1. Introduction.....	1
1.1. Tissue Engineering.....	1
1.1.1. Cells.....	7
1.1.2. Scaffolds.....	8
1.2. Research Aims.....	15
1.3. Thesis Structure.....	16
1.4. Research Funding and Publications.....	18
Chapter 2 – Biofabrication.....	23
2. Biofabrication.....	23
2.1. Introduction.....	23
2.2. Conventional Fabrication Techniques.....	23
2.3. Additive Biomanufacturing.....	27
2.3.1. Additive Processes.....	33
(a) Stereolithographic Processes.....	34
(b) Powder-bed fusion / Laser Sintering processes.....	41
(c) Extrusion-based Processes.....	44
(d) Inkjet / Three-dimensional printing processes.....	52
(e) Advantages and Disadvantages of Additive Manufacturing.....	57
Chapter 3 – Scaffold Design.....	59
3. Scaffold Design.....	59
3.1. Computational Design in Tissue Engineering.....	59
3.2. Computational Scaffold Modelling.....	62
3.3. Computer Aided Design of Scaffolds (CADS).....	65
3.4. Geometric Scaffold Modelling.....	67
3.4.1. Non-Triple Periodic Minimal Surfaces.....	67
3.4.2. Triple Periodic Minimal Surfaces.....	73
(a) Schwartz surfaces scaffold elements.....	75
(b) Schoen surfaces scaffold elements.....	76
Chapter 4 – Structural Analysis of Scaffolds for Tissue Engineering.....	79
4. Structural Analysis.....	79
4.1. Mechanical Behaviour of Scaffolds for Tissue Engineering.....	79

4.2.	Constitutive Equations for Structural Analysis	81
4.2.1.	Linear Elastic Behaviour	84
4.2.2.	Crushable Foam Behaviour	86
4.2.3.	Summary	94
4.3.	Mechanical Simulations	95
4.4.	Structural Results and Discussion	101
4.4.1.	Linear Elastic Simulations	101
(a)	Non-Triple Periodic Minimal Surfaces	101
(b)	Triple Periodic Minimal Surfaces	105
(c)	Summary	119
4.4.2.	Crushable Foam Simulations	120
(a)	Summary	133
Chapter 5 – Vascular Analysis of Scaffolds for Tissue Engineering		135
5.	Vascular Analysis	135
5.1.	Vascular Behaviour of Scaffolds in Tissue Engineering	135
5.2.	Blood Characteristics	138
5.3.	Constitutive Equation of Blood Flow	140
5.4.	Scaffold Vascularisation	143
5.5.	Vascular Simulation	145
5.6.	Vascular Results and Discussion	147
(a)	Non-Triple Periodic Minimal Surfaces	147
(b)	Triple Periodic Minimal Surfaces	154
(c)	Summary	162
Chapter 6 – Topological Optimisation of Scaffolds for Tissue Engineering		163
6.	Topological Optimisation	163
6.1.	Design Optimisation of Scaffolds in Tissue Engineering	163
6.2.	Topological Optimisation	165
(a)	Finite Element Discretisation for the Optimisation Problem	168
(b)	Topological Optimisation Algorithm	169
6.3.	Topological Results and Discussion	170
(a)	Topological optimisation of an initial solid block	170
(b)	Bio-surface constrained optimisation of a solid block element	184
Chapter 7 – Conclusions and Future Works		195
7.	Conclusions	195
7.1.	Concluding Remarks	195
7.2.	Future Works	200
References		203

Figure Index

Figure 1.1 – Illustration of Prometheus punishment by Christian Schussele (1824-1879).....	1
Figure 1.2 – Tissue Regeneration Process System involving several steps and advanced technologies (http://ims.postech.ac.kr).....	2
Figure 1.3 – Multidisciplinary nature of the tissue engineering field.	3
Figure 1.4 – Key strategies for engineering personalized bone grafts (Bhumiratana and Vunjak-sectionNovakovic, 2012).	4
Figure 1.5 – Tissue engineering process involving the cell seeding on scaffolds, <i>in vitro</i> culturing and patient implantation, adapted from Bártolo <i>et al</i> (2012) and Liu and Czernuszka (2006).....	6
Figure 1.6 – Mesenchymal stem cells differentiation process in response to cues from the cellular environment (Nikovits and Stockdale, 2007).....	8
Figure 1.7 – SEM images of PCL scaffolds a) before and b) after 25 days of the degradation process (Ferreira, 2011).....	11
Figure 1.8 – Schematic representation of the mechanical contribution of a scaffold as it degrades over time, and the mechanical contribution of the new host tissue as it forms in the presence of appropriate mechanical loading (adapted from Badylak <i>et al</i> (2009)).	13
Figure 1.9 – Flowchart of the topics and objectives that are addressed in the thesis.	16
Figure 2.1 – A schematic of the key components in the electrospinning technique.	25
Figure 2.2 – Electrospinning system developed at the CDRSP (Dias, 2010).....	25
Figure 2.3 – SEM Results of PCL dissolved in acetic acid and added triethylamine (Dias <i>et al</i> , 2012).	25
Figure 2.4 – Cell growth and proliferation of the outer layer of the scaffold, inducing the M&M effect.	26
Figure 2.5 – Steps of biomanufacturing in tissue engineering.	27
Figure 2.6 – Strategy to produce a medical implant or a scaffold.....	28
Figure 2.7 – The structure of an ASCII STL file format.	29
Figure 2.8 – a) Orientation of a triangular facet in a STL file. b) Violation of the vertex-to-vertex rule. c) A correct triangulation (Alves and Bártolo, 2006).....	29
Figure 2.9 – Max-min angle criterion. a) Smaller minimum interior angle. b) Larger minimum interior angle (Alves <i>et al</i> , 2012; Alves and Bártolo, 2008; Chen <i>et al</i> , 1999).....	31
Figure 2.10 – Definition of a layer through the intersection between the 3D STL model and a slicing plane (Alves and Bártolo, 2006).	32
Figure 2.11 – Classification of additive technologies.	33
Figure 2.12 – Stereolithography system.	34
Figure 2.13 – Mask-based writing system and polyHEMA constructs produced at the Polytechnic Institute of Leiria.	35

Figure 2.14 – Multimaterial microstereo-thermal-lithography system (Bártolo, 2011).	36
Figure 2.15 – The principle of multiphoton polymerisation.	37
Figure 2.16 – Sintered HA scaffolds produced by a lost-mould technique (Chu <i>et al</i> , 2001).	38
Figure 2.17 – Process for formation of hydrogel microstructures containing living cells (Liu and Bhatia, 2002).	39
Figure 2.18 – PDLLA scaffolds with a gyroid architecture built by stereolithography. Scale bars represent 500 μm (Melchels <i>et al</i> , 2009).....	40
Figure 2.19 – Selective laser sintering process.	41
Figure 2.20 – SEM micrograph of sintered layer’s surface with irradiated at 1200 mm/s of scanning speed and different laser power: (a) 3.6W. (b) 7.2W (Hao <i>et al</i> , 2005).	42
Figure 2.21 – a) SEM image of PLLA/CHAp nanocomposite microspheres. B) PLLA/CHAp nanocomposite scaffolds (Zhou <i>et al</i> , 2008).	43
Figure 2.22 – Fused Deposition Modelling process.	44
Figure 2.23 – a) The 3D Fiber Deposition system. b) SEM sections of 3D deposited scaffolds with varying deposition geometries (Woodfield <i>et al</i> , 2004).	45
Figure 2.24 – Precision Extruding Deposition System developed by Wei Sun at Drexel University.	46
Figure 2.25 – a) Schematic illustration of the LDM system. b) Example of a porous PLLA/TCP composite scaffold produced by LDM process (Yan <i>et al</i> , 2003a; 2003b).	47
Figure 2.26 – a) Bioextruder System b) Multi-material extrusion system; c) Single-material extrusion (Almeida <i>et al</i> , 2010; Mateus <i>et al</i> , 2008).....	47
Figure 2.27 – Dual-Bioextruder system.....	48
Figure 2.28 – Biocell Printing System.	48
Figure 2.29 – a) The 3D-Bioplotter system. b) Process building of the first layer (Carvalho <i>et al</i> , 2005).	49
Figure 2.30 – a) Hydroxyapatite scaffold. b) PLGA scaffold (Carvalho <i>et al</i> , 2005).	49
Figure 2.31 – SEM micrographs of a scaffold before (a) and after (b) leaching out the core material (Moroni <i>et al</i> , 2006).	50
Figure 2.32 – SEM (a) and optical microscope (b) micrographs showing chondrocytes and ECM formation inside and outside the hollow fibers (Moroni <i>et al</i> , 2006). P = pore; F = fiber; C = chondrocytes.	50
Figure 2.33 – Illustration of the robocasting fabrication process (Miranda <i>et al</i> , 2006).	51
Figure 2.34 – 3D Printing process.....	52
Figure 2.35 – SEM micrographs of endothelial cells attached to alginate structure (Boland <i>et al</i> , 2007). A) Wall with nanosize pores.B) An endothelial cell attach inside an alginate structure. C) Filopodia and lamellapodia interacting with the alginate material. D) Interactions between fibrous secretions and alginate.	55
Figure 2.36 – Cell-jet printing with cell-gel mixture printed structures (Yan <i>et al</i> , 2003b).....	56
Figure 2.37 – Scaffold fabrication through the alginate-based rapid prototyping process.....	56

Figure 2.38 – Gelation of Alginate in a CaCl ₂ solution.....	56
Figure 3.1 – Computer Aided Tissue Engineering.....	60
Figure 3.2 – Modelling Structure of scaffolds for tissue engineering applications.....	64
Figure 3.3 – Modelling Structure of scaffolds for tissue engineering applications.....	64
Figure 3.4 – Structure of CADs.....	66
Figure 3.5 – The <i>n faces pore</i> blocks family classified according to the number of faces per pore. a) 4 face (4F) pore unit, b) 8F unit, c) 12F unit and d) circular (CF) unit.....	67
Figure 3.6 – The <i>m pores per face</i> blocks family classified according to the number of pores per face. Only 4 of the 10 geometries with circular pores are represented and all with 50 % porosity. a) 1 pore (1P) unit, b) 16P unit, c) 49P unit and d) 100P unit.....	68
Figure 3.7 – Representation of the main design parameters.....	68
Figure 3.8 – Poly(ϵ -caprolactone) scaffold with a 0/90° lay-down pattern.....	69
Figure 3.9 – Compression Stress-Strain curves for the five samples with a pore size of 450 μ m... 70	70
Figure 3.10 – Compression Stress-Strain curves for the five samples with a pore size of 550 μ m. 71	71
Figure 3.11 – Compression Stress-Strain curves for the five samples with a pore size of 650 μ m. 71	71
Figure 3.12 – Average compression stress-strain results with the linear elastic curve for each por size.....	72
Figure 3.13 – Schwartz TPMS primitive.....	75
Figure 3.14 – P-minimal surfaces obtained through thickness variation with constant surface radius.....	76
Figure 3.15 – P-minimal surfaces obtained through radius variation with constant surface thickness.....	76
Figure 3.16 – Schoen TPMS primitive.....	76
Figure 3.17 – P-minimal surfaces obtained through thickness variation with constant surface radius.....	77
Figure 3.18 – P-minimal surfaces obtained through radius variation with constant surface thickness.....	77
Figure 3.19 – CAD models illustrating thickness gradient within the scaffold structures for the a) Schwartz and b) Schoen geometries.....	78
Figure 3.20 – Physical models of a) Schwartz and b) Schoen geometries produced through extrusion-based additive manufacturing.....	78
Figure 4.1 – Examples of cellular solids in nature: (a) balsa wood (b) cork (c) inner core of plant stem in (g) (d) trabecular bone (e) iris leaf (f) skull (g) plant stem (h) porcupine quill. (Gibson, 2005; Gibson and Ashby, 1997; Gibson <i>et al</i> , 1995).....	82
Figure 4.2 – Schematic uniaxial stress–strain curve for elastic–plastic foam in compression (Gibson, 2005; Gibson and Ashby, 1997).....	83
Figure 4.3 – Stress-strain curves for cancellous bone at three different relative densities: 0.3, 0.4, and 0.5 (Meyers <i>et al</i> , 2008; Gibson and Ashby, 1997).....	83
Figure 4.4 – Yield stress versus volumetric strain curve for the crushable foam.....	88

Figure 4.5 – Typical yield surface and flow potential for the crushable foam model. 91

Figure 4.6 – Yield surfaces and flow potential for the volumetric hardening model..... 93

Figure 4.7 – Numerical strategy to evaluate the mechanical behaviour of scaffolds..... 95

Figure 4.8 – Mesh elements and loading and boundary conditions for the periodic surface scaffolds for the structural tensile simulations a) Schwartz and b) Schoen geometry (green – boundary constraints, purple – loading solicitations). 96

Figure 4.9 – Mesh elements and loading and boundary conditions for the filament based scaffolds for the structural compression simulations (green – boundary constraints, purple – loading solicitations)..... 97

Figure 4.10 – Loads and constraints for the numerical analysis a) Tensile Solicitation and b) Shear Solicitation. 98

Figure 4.11 – The variation of the material modulus of Poly(caprolactone) material, according to the scaffold porosity for all scaffold units a) elastic modulus and b) shear modulus. 101

Figure 4.12 – The variation of the material modulus of scaffold units as function of the number of pores per face with CF and 4F pores a) elastic modulus and b) shear modulus..... 102

Figure 4.13 – The variation of the material modulus of scaffold units with 4F pores as function of the number of pores per face and level of porosity a) elastic modulus and b) shear modulus..... 103

Figure 4.14 – The variation of the material modulus of scaffold units with CF pores as function of the number of pores per face and level of porosity a) elastic modulus and b) shear modulus..... 104

Figure 4.15 – Schwartz surface: variation of the scaffold porosity with the surface thickness. 105

Figure 4.16 – Schwartz surface: variation of the elastic modulus with the surface thickness. 106

Figure 4.17 – Schwartz surface: variation of the elastic modulus with porosity..... 106

Figure 4.18 – Schwartz surface: variation of the scaffold porosity with the surface radius. 107

Figure 4.19 – Schwartz surface: variation of the elastic modulus with the surface radius..... 108

Figure 4.20 – Schwartz surface: variation of the elastic modulus with the porosity..... 109

Figure 4.21 – Schoen surface: variation of the scaffold porosity with the surface thickness..... 110

Figure 4.22 – Schoen surface: variation of the elastic modulus with the surface thickness. 110

Figure 4.23 – Schoen surface: variation of the elastic modulus with the porosity. 111

Figure 4.24 – Schoen surface: variation of the scaffold porosity with the surface radius..... 111

Figure 4.25 – Schoen surface: variation of the elastic modulus with the surface radius. 112

Figure 4.26 – Schoen surface: variation of the elastic modulus with the porosity. 112

Figure 4.27 – Variation of the Tensile Stress with the node’s X coordinate position. 113

Figure 4.28 – Schwartz surface: variation of the scaffold’s tensile stress with the surface thickness. 115

Figure 4.29 – Schwartz surface: variation of the scaffold’s tensile stress with the surface radius. 116

Figure 4.30 – Schoen surface: variation of the scaffold’s tensile stress with the surface thickness. 117

Figure 4.31 – Schoen surface: variation of the scaffold’s tensile stress with the surface radius... 118

Figure 4.32 – Rigid body for compressive solicitation upon the scaffold. 121

Figure 4.33 – Numerical compressive stress-strain curves for the three different pore sizes. 122

Figure 4.34 – Comparison between the numerical stress-strain curve and the sigmoid fitted curve for the scaffold with a pore size of 450 μm 123

Figure 4.35 – Comparison between the numerical stress-strain curve and the sigmoid fitted curve for the scaffold with a pore size of 550 μm 123

Figure 4.36 – Comparison between the numerical stress-strain curve and the sigmoid fitted curve for the scaffold with a pore size of 650 μm 124

Figure 4.37 – Comparison between the numerical stress-strain curve and the sigmoid curve fitting for the scaffold with a pore size of 450 μm 124

Figure 4.38 – Comparison between the average stress-strain curve and the sigmoid curve fitting for the scaffold with a pore size of 550 μm 125

Figure 4.39 – Comparison between the average stress-strain curve and the sigmoid curve fitting for the scaffold with a pore size of 650 μm 125

Figure 4.40 – Strain variation regarding increments of 20% of compression for the scaffold with a pore size of 450 μm 127

Figure 4.41 – Stress variation regarding increments of 20% of compression for the scaffold with a pore size of 450 μm 128

Figure 4.42 – Strain variation regarding increments of 20% of compression for the scaffold with a pore size of 550 μm 129

Figure 4.43 – Stress variation regarding increments of 20% of compression for the scaffold with a pore size of 550 μm 130

Figure 4.44 – Strain variation regarding increments of 20% of compression for the scaffold with a pore size of 650 μm 131

Figure 4.45 – Stress variation regarding increments of 20% of compression for the scaffold with a pore size of 650 μm 132

Figure 5.1 – Roadmap for the biofabrication of organs fully vascularised (Mironov *et al*, 2009). ... 137

Figure 5.2 – Illustration of Newtonian and Non-newtonian fluid behaviour. 141

Figure 5.3 – Illustration of single red blood cells and an aggregate of red blood cells, rouleaux phenomenon. 141

Figure 5.4 – Illustration of a scaffold hosted within a biofluid environment and the resulting volumes a) scaffold with biofluid b) scaffold and c) biofluid geometry. 145

Figure 5.5 – The family of scaffolds representing the volume related with the flow of biofluids inside the human body, which is classified according to the number of faces per pore. a) 4f unit, b) 8f unit, c) 12f unit and d) cf unit. 145

Figure 5.6 – Biofluid flow within the scaffold illustrating the chamber’s inlet and outlet. 146

Figure 5.7 – Regular geometric scaffolds: variation of the Shear Strain Rate with the pore’s dimensions. 147

Figure 5.8 – Regular geometric scaffolds: variation of the Wall Shear Stress with the pore’s dimensions. 148

Figure 5.9 – Regular geometric scaffolds: variation of the Shear Strain Rate with the pore’s dimensions.	149
Figure 5.10 – Regular geometric scaffolds: variation of the Wall Shear Stress with the pore’s dimensions.	150
Figure 5.11 – Filament orientated 0/90° scaffolds: variation of the Shear Strain Rate with the variation of the pore size.	152
Figure 5.12 – Filament orientated 0/90° scaffold: variation of the Wall Shear Stress with the variation of the pore size.	153
Figure 5.13 – Schoen surface: variation of the Shear Strain Rate with the variation of the thickness.	154
Figure 5.14 – Schoen surface: variation of the Shear Strain Rate with the variation of the radius.	155
Figure 5.15 – Schwartz surface: variation of the Wall Shear Stress with the variation of the thickness.	156
Figure 5.16 – Schoen surface: variation of the Wall Shear Stress with the variation of the thickness.	156
Figure 5.17 – Schoen surface: variation of the Shear Strain Rate with the variation of the radius.	158
Figure 5.18 – Schoen surface: variation of the Shear Strain Rate with the variation of the thickness radius.	159
Figure 5.19 – Schwartz surface: variation of the Wall Shear Stress with the variation of the thickness.	160
Figure 5.20 – Schoen surface: variation of the Wall Shear Stress with the variation of the thickness.	161
Figure 6.1 – Types of engineering optimisations: a) original part b) part after size optimisation c) part after shape optimisation and d) part after topological optimisation.	164
Figure 6.2 – A general topological optimisation process.	166
Figure 6.3 – Illustration of a topological optimisation.	167
Figure 6.4 – Illustration of the Meshed model of the scaffold.	171
Figure 6.5 – Simulation scenarios considered for topological optimisation.	173
Figure 6.6 – Illustration of topologically optimised scaffold models from Scenario 2 with a porosity of a) 80 % b) 90 %.	178
Figure 6.7 – Illustration of topologically optimised scaffold models from Scenario 3 with a porosity of a) 80 % b) 90 %.	178
Figure 6.8 – Illustration of topologically optimised scaffold models from Scenario 8 with a porosity of a) 50 % b) 60% c) 70 % d) 80 % e) 90 %.	179
Figure 6.9 – Illustration of topologically optimised scaffold models from Scenario 9 with a porosity of a) 60 % b) 70% c) 80 % d) 90 %.	180

Figure 6.10 – Illustration of topologically optimised scaffold models from Scenario 12 with a porosity of a) 60 % b) 70% c) 80 % d) 90 % 181

Figure 6.11 – Illustration of topologically optimised scaffold models from Scenario 6 with a porosity of a) 30 % b) 40% c) 50 % d) 60 % e) 70 % f) 80 % g) 90 % 182

Figure 6.12 – a) μ CT STL file and b) STL file after removing the triangular imperfections. 184

Figure 6.13 – Definition of the datum planes on the STL model limiting the scaffold’s boundary. 185

Figure 6.14 – Illustration of the curves obtained from the intersection between the datum planes and the STL model. 185

Figure 6.15 – Illustration of the a) Loading and constraint surfaces and b) free non-solicited surfaces. 185

Figure 6.16 – Illustration of the scaffold block element considered for the topological simulations. Red – regions subjected to either loading or constraint conditions; Green – regions free of either loading or constraint conditions. 186

Figure 6.17 – Illustration of the Meshed model of the scaffold. 186

Figure 6.18 – Illustration the variation of the solicitations according to each direction, maintaining the other two directions constrained: a) DX - Displacement in the XX direction b) DY - Displacement in the YY direction c) DZ - Displacement in the ZZ direction. 188

Figure 6.19 – Illustration the variation of the constraints according to each direction, maintaining the other two directions under displacement: a) CX - Constraint in the XX direction b) CY - Constraint in the YY direction c) CZ - Constraint in the ZZ direction. 189

Figure 6.20 – Illustration the topological optimisation results according to each displacement direction: a) DX - Displacement in the XX direction b) DY - Displacement in the YY direction c) DZ - Displacement in the ZZ direction. 191

Figure 6.21 – Illustration the topological optimisation results according to each constraint direction: a) CX - Constraint in the XX direction b) CY - Constraint in the YY direction c) CZ - Constraint in the ZZ direction. 192

Table Index

Table 1.1 – Main areas of Tissue engineering, adapted from: Kuppan <i>et al</i> (2012) and Jeong <i>et al</i> (2007) and Tabata (2001).	4
Table 1.2 – Relevant growth factors for tissue engineering applications, adapted from Tessmar and Gopferich (2007), Boontheekul and Mooney (2003) and Rose and Oreffo (2002).....	5
Table 1.3 – Relationship between scaffold characteristics and the corresponding biological effect (Mahajan, 2005).	9
Table 1.4 – Ideal scaffold pore sizes for different cell types.	12
Table 2.1 – Scaffold porosity values (Leong <i>et al</i> , 2008).....	57
Table 2.2 – Characteristics of rapid prototyping scaffolds.	58
Table 2.3 – List of achieved mechanical properties (Leong <i>et al</i> , 2008).	58
Table 3.1 – Geometric parameters for the design of the scaffolds.	69
Table 3.2 – Mechanical compressive properties of the extruded structures for different pore sizes.	72
Table 4.1 – Material compressive properties.	120
Table 5.1 – Shear Stress values for cell cultures within bioreactors.....	144

Chapter 1 – Introduction

1.1. Tissue Engineering

Since the early years of mankind's existence, the regeneration of tissues and organs has been an issue of dreams, as well as relevant domain for ancient Greek Mythology (Dougherty, 2006). According to the Mythology, Prometheus, a Greek Titan, disobeyed a direct order from the God Zeus, and for that reason Prometheus was chained to a rock in the Caucasus Mountains where his torture should take place. Every day, a great eagle would come to Prometheus and eat his liver, leaving only at nightfall when the liver would begin to grow back once more (Figure 1.1). At daybreak, the eagle would return to the chained Prometheus and again attack his body, eating his liver. The daily ritual would repeat itself into eternity, or until Zeus decided to relieve Prometheus from his punishment. This myth clearly identifies that even in ancient Greece, man wanted to restore tissues and organs, which was also reflected on the understanding they had on the ability of specific tissues to regenerate.



Figure 1.1 – Illustration of Prometheus punishment by Christian Schussele (1824-1879).

Today, its incidence in modern medicine is growing with the ageing of the population and higher expectations for a better quality of life, together with the increasing number of required implants and organ shortage. The loss or failure of an organ or tissue is a frequent, devastating, and costly problem in health care. Currently, this problem is treated either by transplanting organs from one individual to another or performing surgical reconstructions, transferring tissue from one location in the human body into the diseased site. The need for substitutes to replace or repair tissues or organs due to disease, trauma, or congenital problems is overwhelming. Tissue engineering (Figure 1.2) emerged to overcome these limitations by creating cell-based substitutes of native tissues (Risbud, 2001; Langer and Vacanti, 1993).

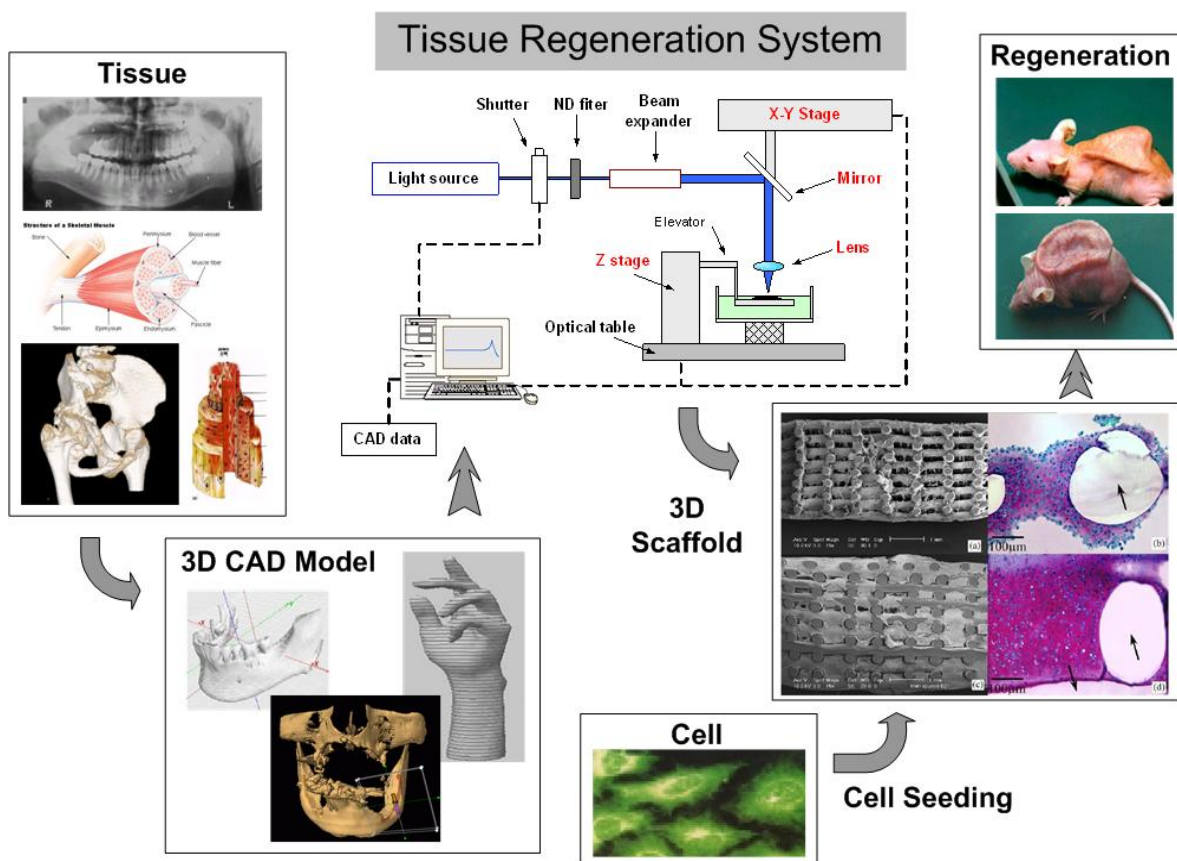


Figure 1.2 – Tissue Regeneration Process System involving several steps and advanced technologies (<http://ims.postech.ac.kr>).

Tissue engineering is a multidisciplinary field focusing on the use of cells and engineered materials (Figure 1.3), combining the principles of biology, engineering and medicine to create biological substitutes for lost or defective native tissues (Eshraghi and Das, 2010; Bártolo *et al*, 2009a; 2009b; 2008; Gibson, 2005; Tan *et al*, 2005; Vozzi *et al*, 2003; Risbud, 2001). According to Skalak and Fox (1988), tissue engineering can be described as “the application of the principles and methods of engineering and life sciences toward the fundamental understanding of structure-function relationships in normal and pathological mammalian tissues and the development of biological substitutes to restore, maintain, or improve tissue and organ functions” (Bártolo *et al*, 2008). This new research domain emerged as a rapidly expanding approach to address the organ shortage problem and comprises tissue regeneration, organ substitution and gene therapy (Table 1.1). Diseases, such as Parkinson, Alzheimer, osteoporosis, spine injuries or cancer, might in the near future be treated with methods aiming at regenerating diseased or damaged tissues. An historical overview of this field can be found in a report published by the National Science Foundation (2003) of the United States of America (USA). Recently, de Bartolo *et al* (2012) presented a vision of the future of this medical domain in 2030.

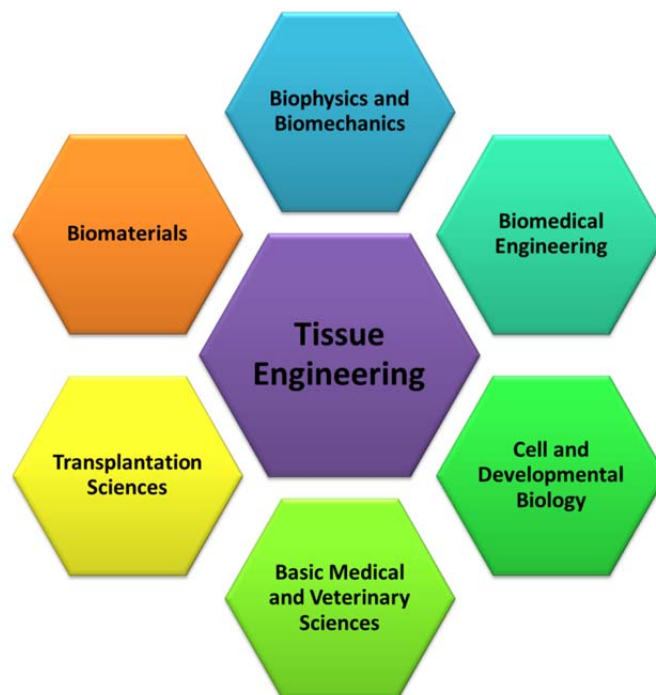


Figure 1.3 – Multidisciplinary nature of the tissue engineering field.

Table 1.1 – Main areas of Tissue engineering, adapted from: Kuppan *et al* (2012) and Jeong *et al* (2007) and Tabata (2001).

	Purpose	Techniques/methodology
Tissue regeneration	<i>In vitro</i> production of tissue constructs	Cell scaffolding, bioreactor, microgravity
	<i>In vivo</i> natural healing process	Cell scaffolding, controlled release, physical barrier
	Ischemia therapy	Angiogenesis
Organ substitution	Immunoisolation	Biological barrier
	Nutrition and oxygen supply	Angiogenesis
	Temporary assistance for organ function	Extracorporeal system
Gene Therapy	Inhibiting induction of a specific gene, or by editing undesirable genomic mutations.	Intracellular transfer of nucleic acid drugs to modulate cellular functions and responses by expressing exogenous proteins

Three general strategies, illustrated in Figure 1.4, were adopted by several authors, such as: Bhumiratana and Vunjak-Novakovic (2012), Norrotte *et al* (2009), Bártolo *et al* (2008), Matsumoto and Mooney (2006), Mistry and Mikos, (2005), Fuchs *et al* (2001), Langer (1997) and Langer and Vacanti (1993) for the creation of new tissues:

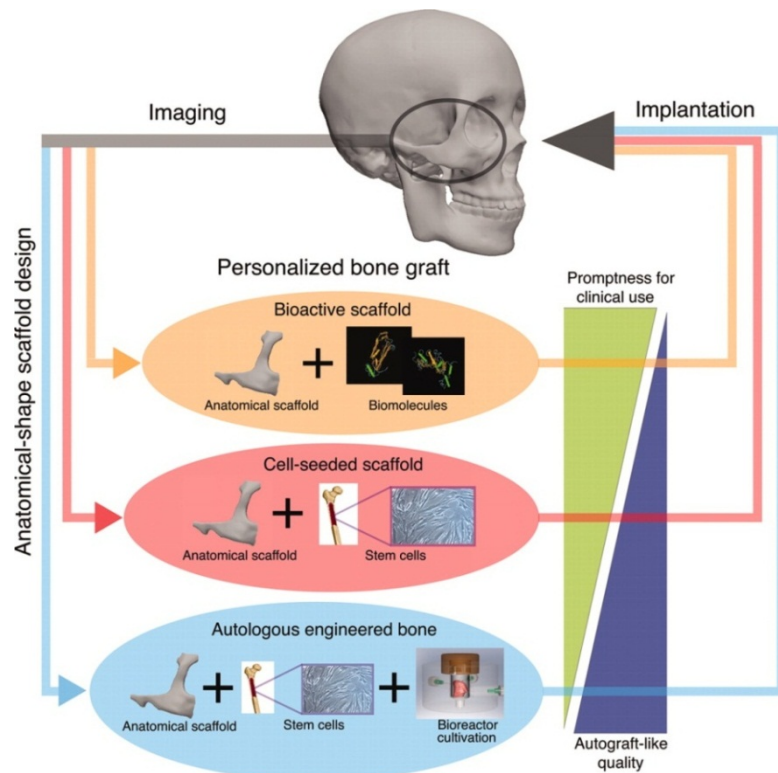


Figure 1.4 – Key strategies for engineering personalized bone grafts (Bhumiratana and Vunjak-sectionNovakovic, 2012).

1. **Cell-based strategies**, involves the direct *in vivo* implantation of isolated cells or cell substitutes and it is based on cells synthesizing their own extracellular matrix (ECM). This approach avoids surgery complications allowing replacing only the damaged cells required for a specific function. The main limitations include immunological rejection and failure of the encapsulated cells.
2. **Growth-factor-based strategies**, based on the use of growth factors and controlled-released systems. Growth factors are proteins secreted by several cell types functioning as signalling molecules, promoting cell adhesion, proliferation, migration and differentiation (Tessmar and Gopferich, 2007; Boonthekul and Mooney, 2003; Rose and Oreffo, 2002). The success of this strategy depends on the growth factors and controlled released systems. Relevant growth factors for bone regeneration and wound healing applications are indicated in Table 1.2.

Table 1.2 – Relevant growth factors for tissue engineering applications, adapted from Tessmar and Gopferich (2007), Boonthekul and Mooney (2003) and Rose and Oreffo (2002).

Bone Regeneration	
Growth Factor	Relevant activities
Transforming growth factor- β (TGF- β)	Proliferation and differentiation of bone
Bone morphogenetic protein (BMP)	Differentiation of bone forming cells
Insulin-like growth factor (IGF)	Stimulates proliferation of osteoblasts and the synthesis of bone matrix
Fibroblast growth factor (FGF)	Proliferation of osteoblasts
Platelet-derived growth factor (PDGF)	Proliferation of osteoblasts
Wound Healing	
Growth Factor	Relevant activities
Platelet-derived growth factor (PDGF)	Active in all stages of healing process
Epidermal growth factor (EGF)	Mitogenic for keratinocytes
Transforming growth factor- β (TGF- β)	Promotes keratinocyte migration, ECM synthesis and remodeling, and differentiation of epithelial cells
Fibroblast growth factor (FGF)	General stimulant for wound healin

3. **Scaffold-based methods**, based on the use of a temporary scaffold, provide a substrate for the implanted cells and a physical support for tissue formation in an organized way. In this approach, transplanted cells adhere

to the scaffold, proliferate, secrete their own ECM and stimulate new tissue formation. This strategy involves either a closed or an open system. In a closed system, cells are isolated from the body by a permeable membrane that allows exchange of nutrients and wastes, and protects cells from the immune response of the body. An open system begins with the *in vitro* culture of cells, which are then seeded onto a scaffold. The cell-matrix construct is then implanted into the body.

The cell-seeded temporary scaffold approach is the most widely used strategy for tissue engineering (Fuchs *et al*, 2001). In this approach, living cells are obtained from a tissue harvest, from either the patient (auto-graft) or a different person (allograft), and cultured *in vitro* on a three-dimensional biodegradable scaffold to obtain a tissue construct suitable for transplantation (Liu and Czernuszka, 2006). Scaffolds provide an initial biochemical substrate so that the novel tissue can grow until cells produce their own ECM. Therefore, scaffolds not only define the 3D space for the formation of new tissues, but also serve as temporary skeletons to accommodate and stimulate new tissue growth with appropriate functions (Bártolo *et al*, 2012). This cell-seeded temporary scaffold approach is illustrated in Figure 1.5.

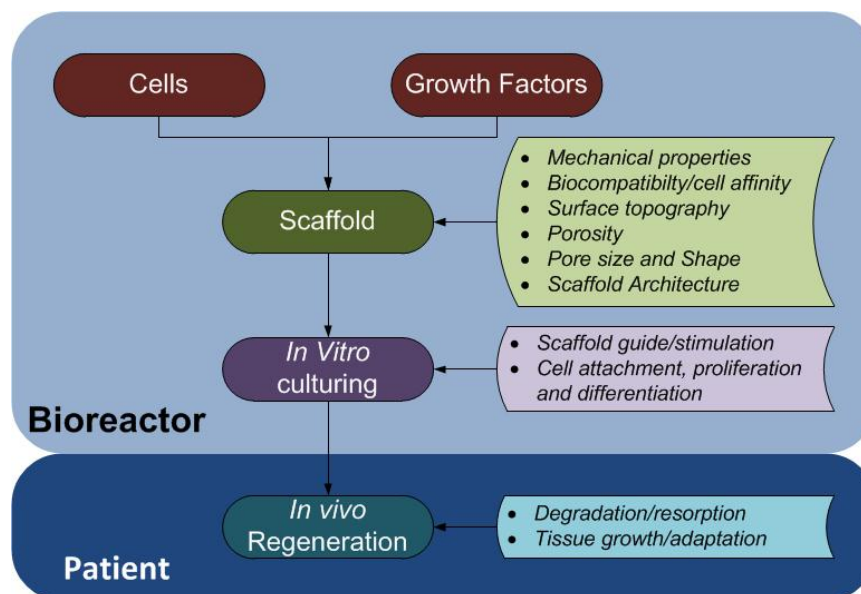


Figure 1.5 – Tissue engineering process involving the cell seeding on scaffolds, *in vitro* culturing and patient implantation, adapted from Bártolo *et al* (2012) and Liu and Czernuszka (2006).

1.1.1. Cells

Therapeutic strategies in tissue engineering involve:

- cellular implantation where cells, derived from an endogenous source in the patient or a donor, are either injected into the damaged tissue or combined *in vitro* with a degradable scaffold, and then implanted;
- tissue regeneration where a scaffold is implanted directly into the damaged tissue, stimulates the cells to promote local tissue repair.

Cells used in tissue engineering may be allogeneic, xenogeneic, syngeneic or autologous (Fuchs *et al*, 2001). They should be non-immunogenic, highly proliferate, easy to harvest, with a high capacity to differentiate into a variety of cell types of specialised functions (Fuchs *et al*, 2001; Marler *et al*, 1998). Skeletal muscle satellite cells, cardiomyocytes, endothelial cells, fibroblasts, osteoblasts and chondrocytes were used in many tissue engineering applications. An ideal cell source for tissue engineering should have the capacity to proliferate and then differentiate *in vitro*, in a manner that can be reproducibly controlled.

The growth and differentiation of many cell types is regulated by four major sources of external signalling (Santos *et al*, 2012), as shown in Figure 1.6:

1. Soluble growth and differentiation factors;
2. Nature and organization of insoluble and soluble ECM constituents;
3. Intercellular interactions;
4. Environmental stress induced by fluid flow and/or mechanical stimuli, as well other physical cues (oxygen, tension, pH effects).

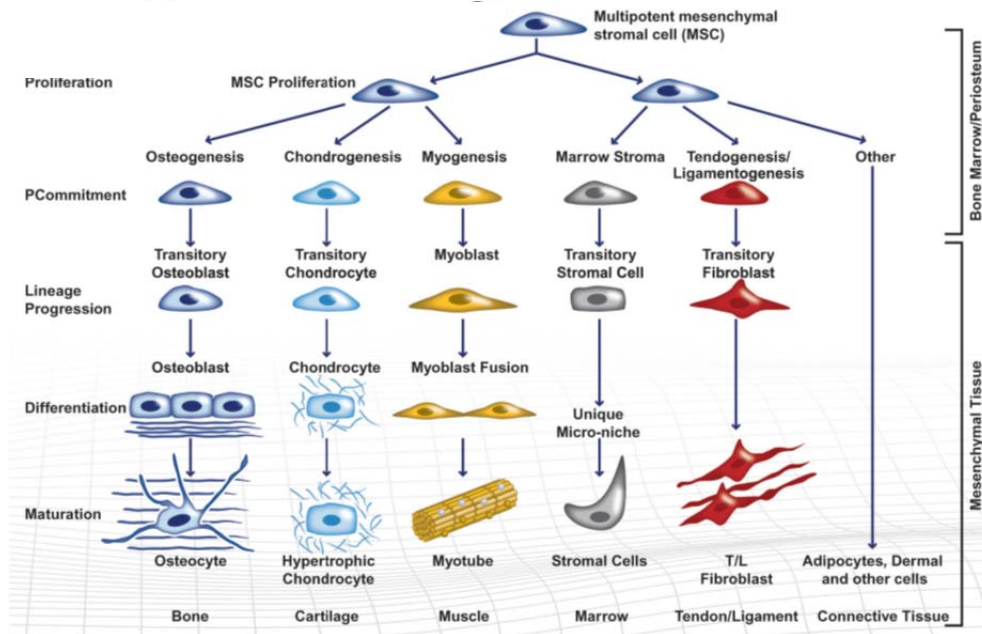


Figure 1.6 – Mesenchymal stem cells differentiation process in response to cues from the cellular environment (Nikovits and Stockdale, 2007).

1.1.2. Scaffolds

According to Feder-Mengus *et al* (2008), scaffolds are a porous 3D cell culture substrates, which provides a temporary template for cell organization into tissue structures, both *in vitro* and *in vivo*, as they serve some of the following purposes (Billiet *et al*, 2012; Truscetto *et al*, 2012; Guillotin and Guillemot, 2011; Bártolo *et al*, 2009a; 2009b; 2008; Tan and Teoh, 2007; Liu and Czernuszka, 2006; Kreke *et al*, 2005; Gomes and Reis, 2004; Gross and Rodriguez-Lorenzo, 2004; Leong *et al*, 2003; Kreeger and Shea, 2002; Hutmacher, 2001; Kim and Mooney, 2001; Langer and Vacanti, 1993):

- Serve as an adhesion substrate for cells, allowing cell attachment, proliferation and differentiation;
- Deliver and retain cells and growth factors;
- Enable diffusion of cell nutrients and oxygen;
- Provide temporary mechanical and biological environment to the newly grown tissue enabling tissue regeneration in an organised way.

An ideal scaffold must satisfy some biological and physical requirements as indicated in Table 1.3 (Bártolo *et al*, 2012; Billiet *et al*, 2012; Reverchon and Cardea, 2012; Vasanthan *et al*, 2012; Bártolo *et al*, 2009a; 2009b; 2008; Sanz-Herrera *et al*, 2009; Leong *et al*, 2008). Such properties affect not only cell survival, signalling, growth, propagation and reorganization, influencing also cell shape modelling and gene expressions (Chen *et al*, 1997; Mooney *et al*, 1992).

Table 1.3 – Relationship between scaffold characteristics and the corresponding biological effect (Mahajan, 2005).

Scaffold characteristics	Biological effect
Biocompatibility	Cell viability and tissue response
Biodegradability	Aids tissue remodelling
Porosity	Cell migration inside the scaffold - Vascularisation
Chemical properties of the material	Aids in cell attachment and signalling in cell environment Allows release of bioactive substances
Mechanical properties	Affects cell growth and proliferation response In-vivo load bearing capacity

a) Biological requirements

- Biocompatibility is related to the acceptance of an implant by both the surrounding tissues and the whole body. The implant should be compatible with these tissues in terms of mechanical, chemical, surface and pharmacological properties (Ramakrishna *et al*, 2001; Angelova and Hunkeler, 1999). Biocompatibility is also related to the ability of the implant material to perform an appropriate host response in a specific application (Ramakrishna *et al*, 2001; Angelova and Hunkeler, 1999). In tissue engineering, materials should interact positively with the cells, allowing cell attachment, proliferation, differentiation and host environment, without eliciting adverse host tissue responses (Kim *et al*, 2003b).
- Controlled Degradation Rate – the degradation rate of the scaffold must be adjustable in order to match the rate of tissue regeneration.

- **Biodegradability** – Scaffolds must degrade into non-toxic products with a controlled degradation rate matching the regeneration rate of the native tissue. The *in vivo* degradation process of polymeric scaffolds is influenced by different and often conflicting variables, such as those related to the material's structure (i.e., chemical composition, molecular weight and molecular weight distribution, crystallinity, morphology, etc.), its macroscopic features (i.e., implant shape or size, porous shape, size and interconnectivity, etc.) and the environmental conditions (i.e., temperature, pH of the medium, presence of enzymes or cells and tissues). The chemical degradation of polymers can mainly proceed either via degradation by biological agents (enzymes), or hydrolytic degradation (hydrolysis) mediated by water, or a combination of both effects (Figure 1.7) (Ferreira, 2011). Other degradation processes are attributed to other agents, such as super oxides, phagocytic attack or even mechanical stress.

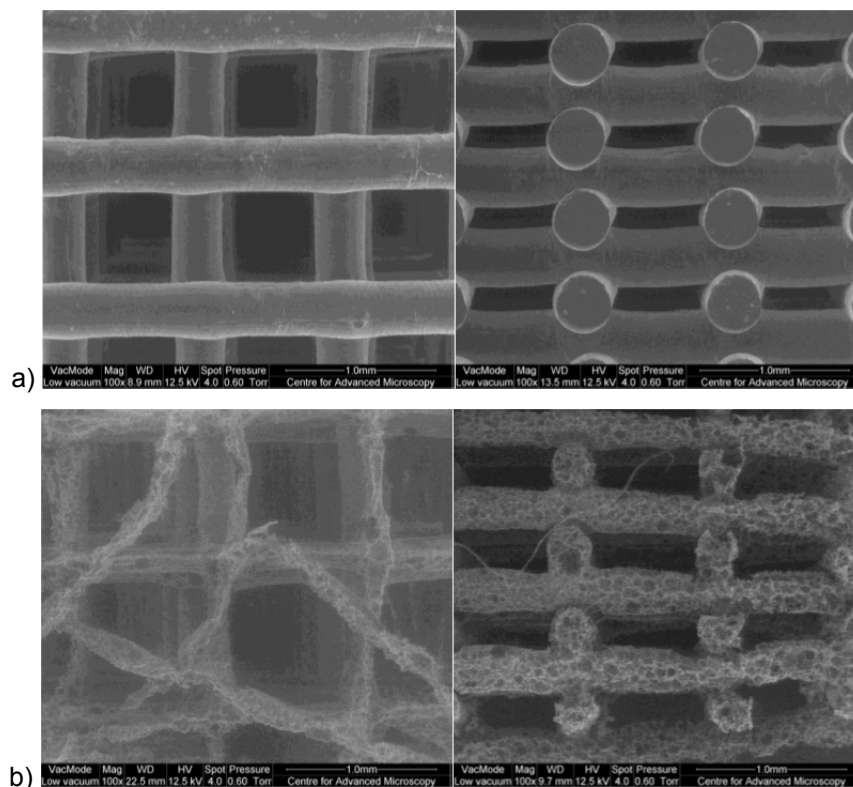


Figure 1.7 – SEM images of PCL scaffolds a) before and b) after 25 days of the degradation process (Ferreira, 2011).

- Bioactive – Scaffolds should be bioactive, promoting and guiding cell proliferation, differentiation and tissue growth. This bioactivity can be achieved by adding growth factors and functionalizing the scaffold with proteins or adhesion-specific peptide sequences, which often resembles the ECM providing appropriate biomolecular signals to the cells (Wei *et al*, 2007; Nathan and Sporn, 1991).
- Appropriate porosity, pore size and pore shape – Generally, a high level of porosity is required (> 90%) because it increases the surface area, enabling high cell seeding efficiency, migration and proliferation and neovascularisation (Sun *et al*, 2007; Chong and Chang, 2006; Beckstead *et al*, 2005; Karageorgiou and Kaplan, 2005; Miot *et al*, 2005; Woodfield *et al*, 2005; Martin *et al*, 2004; Sun *et al*, 2004a; 2004b; Taguchi *et al*, 2004; Salem *et al*, 2002; Sherwood *et al*, 2002; Freyman *et al*, 2001; Zeltinger *et al*, 2001; Kuboki *et al*, 1998; Nehrer *et al*, 1997; LeGeros and LeGeros, 1995; Whang *et al*, 1995). Pore size plays also an important role in terms of cell adhesion/migration, vascularisation and new tissue ingrowth (Bártolo *et al*, 2009a; 2009b; Jones *et al*, 2009; Lee *et al*, 2008; Leong *et al*, 2008; Bártolo *et al*, 2008; Rouwkema *et al*, 2008; O'Brien *et al*, 2005; Hollister *et al*, 2002). Macro-pores (i.e. >50 μm) are of an appropriate scale to influence tissue function, while micro-pores (i.e. <50 μm) influence cell function (e.g. cell attachment), as mammalian cells typically have 10-20 μm in size. Smaller pores enhance cell adhesion and differentiation *in vitro*, while bigger pores promote higher cell adhesion, viability and vascularisation *in vivo*. If the pores are too large, cells will fail to migrate and form networks throughout the scaffold. When the pores are too small, its occlusion by cells will prevent cellular penetration and matrix elaboration within the scaffolds (Rout *et al*, 1988). Pore interconnectivity (a 100% interconnected network of internal channels is required) is also a critical

parameter in terms of cell viability and tissue regeneration. The degree of pore interconnectivity directly affects the diffusion of physiological nutrients and gases, as well the removal of metabolic waste and by-products from cells that penetrated into the scaffold (Mikos *et al*, 1993; Vacanti *et al*, 1988). Table 1.4 presents the ideal scaffold pore sizes for different cell types.

Table 1.4 – Ideal scaffold pore sizes for different cell types.

Cell Types	Cell Size [μm]	Ideal Pore Diameter [μm]
Hepatocytes	20-40 (Galameau <i>et al</i> , 2007)	20 (Yang <i>et al</i> , 2001)
Fibroblast	20-50 (Salem <i>et al</i> , 2002)	90-360 (Wang <i>et al</i> , 2005)
Bone	20-30 (Oota <i>et al</i> , 2006)	100-350 (Yang <i>et al</i> , 2001)

b) Mechanical and physical requirements

- Mechanical Strength – Scaffolds are required to withstand both *in vitro* manipulation and stresses in the host tissue environment (Bignon *et al*, 2003; Leong *et al*, 2003; Prendergast and Meulen, 2001; Temenoff and Mikos, 2000; Brekke, 1996). *In vitro*, engineered culture tissue constructs should maintain their mechanical properties to preserve the required space for cell growth and matrix formation. For *in vivo* applications, it is important that scaffolds mimic as closely as possible the mechanical properties of the native tissue in order to provide a temporary mechanical support for tissue regeneration, providing structural stability to the injured site. Initially, the scaffold must withstand all stresses and loads in the host tissue environment, before gradually transferring them to the regenerated tissue (Figure 1.8).

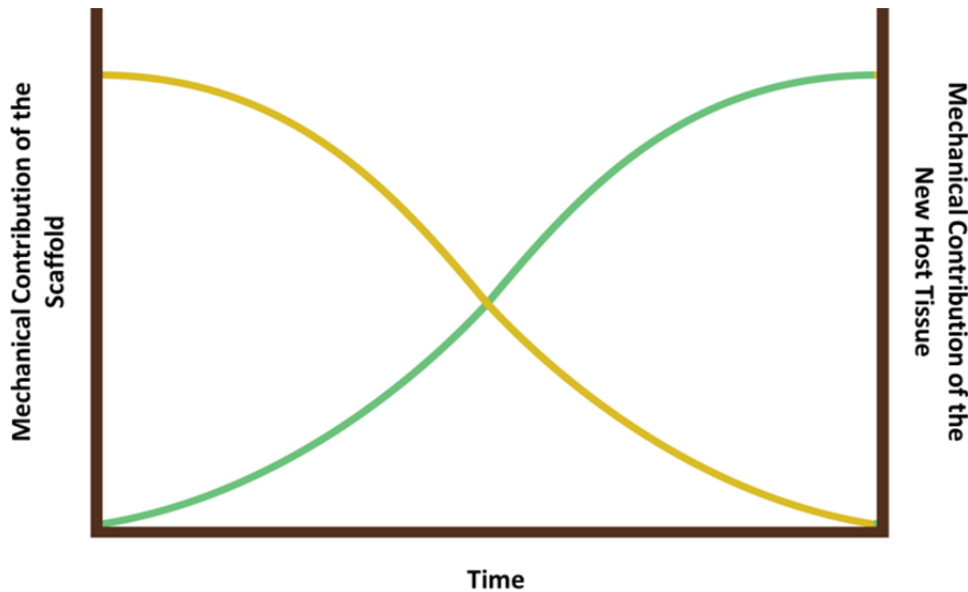


Figure 1.8 – Schematic representation of the mechanical contribution of a scaffold as it degrades over time, and the mechanical contribution of the new host tissue as it forms in the presence of appropriate mechanical loading (adapted from Badylak *et al* (2009)).

- Adequate surface finish – Cell attachment, the initial step in cell-biomaterial surface interaction, is closely related to the surface properties of biomaterials (Saltzman, 1997), such as morphology, hydrophilicity, surface energy and charge (Yang *et al*, 2002). The surface should be conducive to cell growth, promoting cellular adhesion, migration and differentiation, so that the resultant tissue is comparable to the surrounding native tissue with respect to structure and functionality (Morsi *et al*, 2008). An adequate surface enables a good biomechanical coupling between the scaffold and the new and host tissue (Mustafa *et al*, 2005; Cheng and Teoh, 2004; Zhao *et al*, 2003; Singhvi *et al*, 1994). The morphology and the physiochemistry of the scaffold's surface, a material dependent property, are important factors that influence cell attachment, migration and intracellular signalling *in vitro* and cell recruitment, as well healing and bonding with the cellular host tissue in the tissue-scaffold interface *in vivo* (McClary *et al*, 2000; Healy *et al*, 1992).

Since most biodegradable materials have a hydrophobic polymer surface, chemical activation of the polymer substrate becomes critical in

the polymer-bioactive molecule (such as proteins or cells) interaction (Safinia *et al*, 2005). New efforts have been reported to encourage cell attachment focusing on mimicking the surface chemistry of autogenous ECM (Hynes, 1992). Several methods were developed to modify polymer surfaces for improving their wetting characteristics, including mechanical, wet chemical and atmospheric treatments, as well low-pressure plasma and corona discharge (Chen-Yang *et al*, 2000; Gupta *et al*, 2000; Mutel *et al*, 2000). Plasma treatment techniques enable the introduction of desired functionalities and grafting of polymer chains onto the surface, thereby improving the adhesive properties, printability, and permeability of polymer surfaces (Yildirim *et al*, 2008; Berry *et al*, 2004; Grace and Gerenser, 2003; Greene *et al*, 2003; Tahara *et al*, 2003; Webb *et al*, 1998; Shelton *et al*, 1988). Such surface treatments remove surface contaminants, roughen the polymer surface, and increase surface reactivity by altering the surface energy and charge of the material (Safinia *et al*, 2005). The modified surfaces that undergo surface restructuring with time, a disadvantage of polymer surface treatments (Yang *et al*, 2002), due to the mobility of the polymer chain in the amorphous regions (Kim *et al*, 2003a; Murakami *et al*, 1998), driven by the thermodynamic need to lower the overall interfacial energy of the system (Koberstein *et al*, 1998).

- Easily manufactured and sterilised – Implants should be rapidly produced with high accuracy and repeatability and easily sterilized by exposure to high temperatures, UV light, γ -radiation, plasma, ethylene oxide (ETO) gas, or by immersion in a sterilisation agent, remaining unaffected by either of these processes (Allan *et al*, 2001; Fischbach *et al*, 2001). The sterilisation process must not alter the material's chemical composition, which can affect its bioactivity, biocompatibility or degradation properties.

1.2. Research Aims

The design of optimised scaffolds for tissue engineering is a key topic of research, as the complex macro- and micro- architectures required for a scaffold depends on the mechanical properties, physical and molecular queues of the surrounding tissue within the defect site. Thus, the prediction of the optimal properties for tissue engineering scaffolds is very important, for mechanical, vascular or topological properties.

The relationship between high scaffold porosity and high mechanical properties is contradictory as it becomes even more complex due to the degradation process of the scaffolds. A scaffold design strategy based on the finite element method was developed in order to optimise the scaffold design, regarding mechanical and vascular properties as a function of porosity. Scaffolds are considered as a LEGO structure formed by an association of small elementary units or blocks. In this research work, two types of family elementary scaffold units were considered: non-triple periodic minimal surfaces and triple periodic minimal surfaces that describe natural existing surfaces. The main objectives of this research work are:

- The evaluation of the Tissue Engineering methodology and its different strategies;
- The evaluation of the existing biofabrication technologies used to produce tissue engineering scaffolds;
- The evaluation of the scaffold's requirements involved in the scaffold's design;
- The development of an integrated design strategy based on material, porosity, geometry, mechanical and vascular properties, in order to aid the scaffold design process;
- The experimental validation of the adopted design strategy.

1.3. Thesis Structure

This thesis is structured into 7 chapters as illustrated in Figure 1.9.

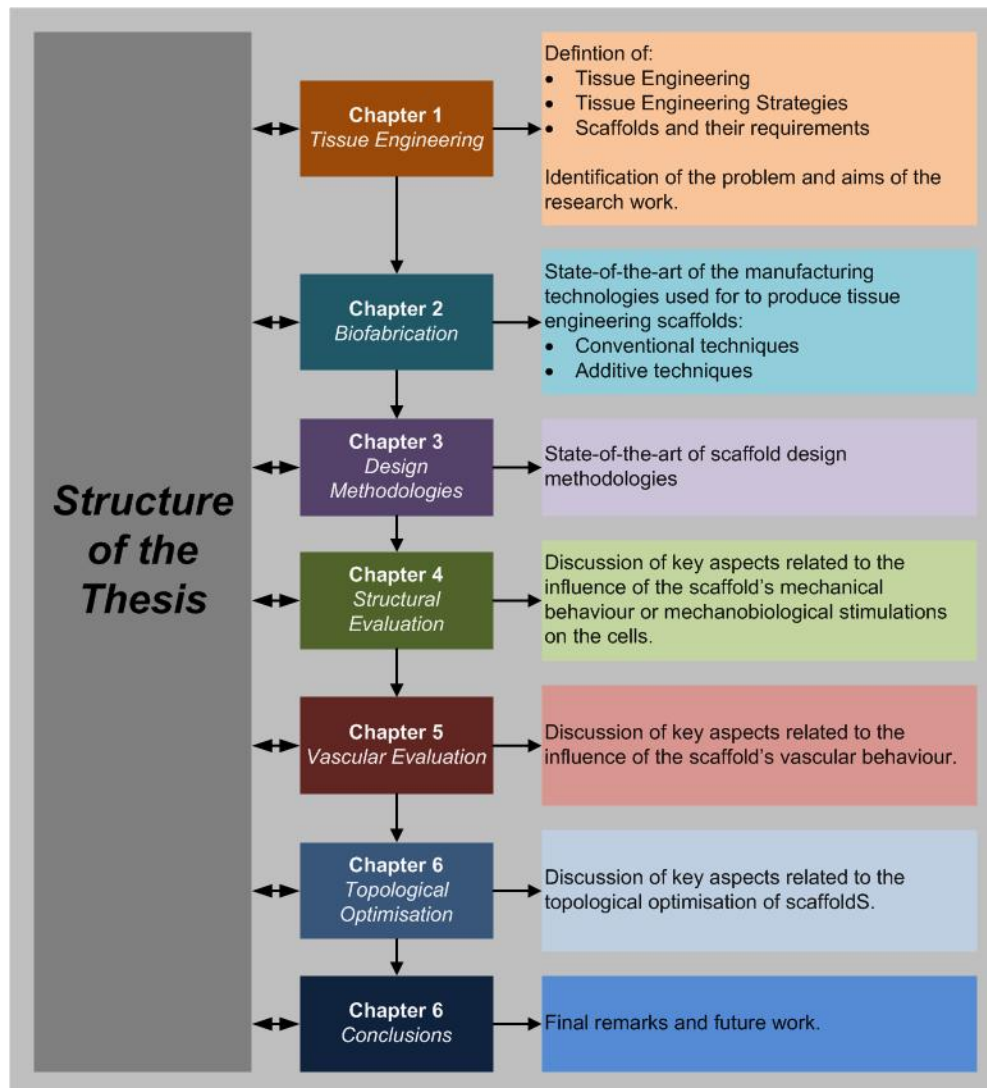


Figure 1.9 – Flowchart of the topics and objectives that are addressed in the thesis.

The first chapter presents a detailed overview of the tissue engineering field, as well the tissue engineering scaffolds. An in depth description of scaffolds, regarding its purpose, functionality, biological and physical requirements and characteristics, is also presented.

The second chapter comprises a detailed description of advanced scaffold fabrication technologies, namely biomanufacturing. Both conventional and additive manufacturing technologies are described, highlighting additive manufacturing. The processing procedures from CAD data to physical models are also explained. Biomanufacturing technologies are grouped into four categories: Stereolithographic Processes, Laser Sintering, Extrusion-based and Three-dimensional printing. Each category is also defined presenting the most relevant research activities and their results.

The third chapter describes the state-of-the-art in computational design and modelling methodologies of scaffolds for tissue engineering applications, as scaffolds can be designed and modelled based on μ CT data or surface/solid CAD modelling. Several scaffold unit families are presented, namely Non-Triple Periodic Minimal Surface and Triple Periodic Minimal Surface geometric models, as well the mathematical formulations for the design of Triple Periodic Minimal Surfaces.

The next three chapters correspond to the numerical simulation, evaluation and prediction of the scaffold's behaviour under structural and vascular loading, and its topological optimisation. Each chapter presents a detailed state-of-the-art description of the influence of the scaffold's behaviour on the cells with the corresponding finite element formulations involved in the simulations. The numerical analysis set-up for each simulation is described and the results are then presented and discussed for each of the scaffold unit families. Each scaffold's numerical behaviour is evaluated as a function of a design parameter, such as pore size, thickness, radius, etc. Each chapter corresponds to a scaffold simulation topic: Chapter Four to its structural simulation, Chapter Five to its vascular simulation, and Chapter Six to its topological optimisation.

The aim of this chapter is to provide an overall summary of the thesis. It starts with a summary and conclusions that can be drawn from the research work carried out. Possible future directions for research following on this thesis are also presented.

1.4. Research Funding and Publications

This research work was supported by the Portuguese Foundation of Science and Technology through a PhD grant (SFRH/BD/37604/2007). The research work undertaken in this thesis was also supported by the following research projects:

1. **Internacional Research Exchange for Biomedical Devices Design and Prototyping** “IREBID”, funded by the People Marie Curie Actions, International Research Staff Exchange Scheme.
2. **Development of Scaffolds with Controlled Microstructure for Bone Tissue Engineering** (PTDC/EME-PME/104498/2008), funded by the Portuguese Foundation for Science and Technology.
3. **Software development for arthroplasty preparation** (PTDC/SAU-BEB/103408/2008), funded by the Portuguese Foundation for Science and Technology.
4. **Strategic Project UI 4044** (Pest-OE/EME/UI4044/2011), funded by the Portuguese Foundation for Science and Technology.
5. **ToolingEdge**, funded by the Portuguese Agency for Innovation.
6. **Rede IberoAmericana de Biofabricação: Materiais, Processos e Simulação**, funded by the CYTED – Ciencia Y Tecnologia Para El Desarrollo.
7. **Numerical simulation and optimisation through genetic algorithms for stereolithographic biofabrication of tissue engineering scaffolds**, funded by the GRICES/SECyT.
8. **Computational Modelling of Bone Structure – Application to Bone Tissue Engineering** (PTDC/EME-PME/71436/2006), funded by the Portuguese Foundation for Science and Technology.
9. **Biofabrication in Tissue Engineering for the year 2020**, funded by the British Council and the Portuguese Foundation for Science and Technology.

10. **Optimisation and Rapid Fabrication of Engineering Scaffolds for Bone Ingrowth** (POCI/SAU-BMA/60287/2004), funded by the Portuguese Foundation for Science and Technology.
11. **BIOMAS – Biomanufacturing and Engineering Scaffolds**, funded by the Portuguese Agency for Innovation.

The following publications and patents also emerged from the research work carried out:

Book chapters:

1. H.A. Almeida & P.J. Bártolo, **Scaffold Design Methodologies in Tissue Engineering**, *Biofabrication for Tissue Science and engineering*, W. Sun & G. Forgacs, Elsevier (accepted).
2. H.A. Almeida & P.J. Bártolo, **Computacional Technologies in Tissue Engineering**, *Tissue Engineering: Computer Modeling, Biofabrication and Cell Behavior*, P. Fernandes & P.J. Bártolo, Springer (accepted).
3. H.A. Almeida & P.J. Bártolo (2012), **Structural and Vascular Analysis of Tissue Engineering Scaffolds: Part 1 – Numerical Fluid Analysis**, *Computer-Aided Tissue Engineering*, M. Liebschner & D. Kim, Springer, Chapter 12: 183-207.
4. H.A. Almeida & P.J. Bártolo (2012), **Structural and Vascular Analysis of Tissue Engineering Scaffolds: Part 2 – Topology Optimization**, *Computer-Aided Tissue Engineering*, M. Liebschner & D. Kim, Springer, Chapter 13: 209-236.
5. H.A. Almeida & P.J. Bártolo (2010), **Simulação Computacional**, *Processos de Biofabricação, Rede IberoAmericana de Biofabricação: Materiais, Processes e Simulação*, 3(9).
6. K. Voloshyna, P.J. Bártolo, H.A. Almeida & J.V.L. Silva (2010), **Processos de Impressão**, *Processos de Biofabricação, Rede IberoAmericana de Biofabricação: Materiais, Processes e Simulação*, 3(6).

7. A. Pedrosa, P.J. Bártolo, H.A. Almeida & J.V.L. Silva (2010), **Processos de extrusão**, *Processos de Biofabricação, Rede IberoAmericana de Biofabricação: Materiais, Processes e Simulação*, 3(5).
8. J. Dias, P.J. Bártolo, H.A. Almeida & J.V.L. Silva (2010), **Processos de Sinterização**, *Processos de Biofabricação, Rede IberoAmericana de Biofabricação: Materiais, Processes e Simulação*, 3(4).
9. P.J. Bártolo, H.A. Almeida, C.S. Moura, F.L. Ferreira & J.V.L. Silva (2010), **Processos Estereolitográficos**, *Processos de Biofabricação, Rede IberoAmericana de Biofabricação: Materiais, Processes e Simulação*, 3(3).
10. C.S. Moura, P.J. Bártolo & H.A. Almeida (2010), **Scaffolds para Engenharia de Tecidos**, *Processos de Biofabricação, Rede IberoAmericana de Biofabricação: Materiais, Processes e Simulação*, 3(1).
11. P.J. Bártolo, H.A. Almeida, R. Rezende, T. Laoui & B. Bidanda (2008), **Advanced Processes to Fabricate Scaffolds for Tissue Engineering**, *Virtual Prototyping & Bio-Manufacturing in Medical Applications*, B. Bidanda & P.J. Bártolo (Eds.), Springer, Chapter 8:151-174.

Articles in international journals edited with review:

1. H.A. Almeida & P.J. Bártolo, **Design of Tissue Engineering Scaffolds based on Hyperbolic Surfaces: Mechanical Evaluation**, *Medical Engineering and Physics* (accepted).
2. H.A. Almeida & P.J. Bártolo (2012), **Structural Shear Stress Evaluation of Hyperbolic Scaffolds for Tissue Engineering Applications**, *Tissue Engineering and Regenerative Medicine*, 3rd Termis World Congress 2012, 6(S1):233.
3. S.R. Almeida, H.A. Almeida & P.J. Bártolo (2012), **Vascular simulation of polymer degrading scaffolds for tissue engineering applications**, *Journal of Biomechanics*, Proceedings of the 18th Congress of the European Society of Biomechanics, 45(S1):S664.
4. H.A. Almeida & P.J. Bártolo (2012), **Cell mechanobiology design of scaffolds based on hyperbolic surfaces**, *Journal of Biomechanics*,

- Proceedings of the 18th Congress of the European Society of Biomechanics, 45(S1):S663.
5. H.A. Almeida & P.J. Bártolo (2010), **Virtual Topological Optimization of Scaffolds for Rapid Prototyping**, *Medical Engineering and Physics*, 32(7):775-782.
 6. P.J. Bártolo, C.K. Chua, H.A. Almeida, S.M. Chou & A.S.C Lim (2009), **Biomanufacturing for Tissue Engineering: Present and Future Trends**, *Virtual and Physical Prototyping*, 4(4):203-216.
 7. H.A. Almeida & P.J. Bártolo (2009), **Structural Evaluation of Multi-material Scaffolds for Tissue Engineering**, *Tissue Engineering & Regenerative Medicine*, Official Journal of the Korean Tissue Engineering & Regenerative Medicine Society, 6(12): S117.
 8. H.A. Almeida, P.J. Bártolo & T. Laoui (2009), **Rapid Prototyping & Manufacturing for Tissue Engineering Scaffolds**, *Computer Applications in Technology*, 36(1):1-9.

Patents:

1. **Bioreactor Multifuncional para a Engenharia de Tecidos**, D.M. Freitas, A.P. Tojeira, R.F. Pereira, P.J. Bártolo, N.M. Alves, A.L. Mendes, C.A. Capela & H.A. Almeida, Portuguese National Patent N° 105176 (submitted).
2. **Prototipagem Rápida por Bio-Extrusão**, H.A. Almeida, P.J. Bártolo, C.M. Mota, A.J. Mateus, N. Ferreira, M. Domingos & N.M. Alves, Portuguese National Patent N° 104247, 04/02/2010.

Chapter 2 – Biofabrication

2.1. Introduction

Fabrication techniques to produce 3D scaffolds can be divided into two broad categories: conventional techniques and additive technologies (Bártolo *et al*, 2012; Gualandi, 2011; Bártolo *et al*, 2009a; 2009b; 2008; Hutmacher *et al*, 2008).

2.2. Conventional Fabrication Techniques

According to Reignier and Huneault (2006), Ho *et al* (2004), Gomes and Reis (2004), Ma (2004), Leong *et al* (2003) and Yang *et al* (2001), there are several conventional methods to fabricate scaffolds, as follows:

- *Solvent casting/salt leaching* involves mixing solid impurities, such as sieved sodium chloride particles, into a polymer solvent solution, as well casting its dispersion to produce a membrane containing polymer and salt particles. The salt particles are then leached out with water to yield a porous membrane. According to the abovementioned authors, porosity and pore size are dependent on salt weight fraction and particle size, pore diameters of 100-500 μm and porosities of 87-91 % were obtained.
- *Phase separation* involves dissolving a polymer in a suitable solvent, placing it in a mould, and then cooling the mould rapidly until the solvent is frozen. The solvent is removed by freeze-drying, leaving behind the polymer, a foam with pore sizes of 1-20 μm in diameter.
- *Foaming* is carried out by either dissolving a gas, usually Carbon Dioxide (CO_2), at elevated pressure or incorporating a chemical blowing agent that yields gaseous decomposition products. This process generally leads to porous structures not fully interconnected, and produces a skin-core structure.

- *Gas saturation* uses high pressure CO₂ to produce macroporous sponges at room temperature. Polymeric sponges with large pores (~100 μm) and porosities up to 93% were produced.
- *Electrospinning* is a process for generating fine fibres by applying an electric field to either droplets of a polymer solution or melt, passing through a tip of a fine orifice (Mitchell *et al*, 2011; Mitchell and Davis; 2011; Greiner and Wendorff, 2007), as shown in Figure 2.1. As a consequence of the Coulombic electric forces arising from the application of the high voltage, this small droplet will be charged and its shape distorted into a cone-like geometry (Taylor, 1964). Dependent on the strength of the applied electric field together with the solution or melt viscosity, surface tension and dielectric properties of the solution, the integrity of the droplet will break down and a fine fibre of polymer will be produced and deposited on the collector electrode. During the flight, the fibre will be subjected to instabilities which extend the fibre and lead to a considerable reduction in its diameter (Sin *et al*, 2001; Reneker *et al*, 2000). An important feature of this technique is the production of fibres with diameters ranging from 10 nm (or even smaller) to a few microns, dimensions not generally available using other techniques, except at the higher end by melt blowing (Ellison *et al*. 2007).

Dias (2010) used an electrospinning system, developed at the Centre for Rapid and Sustainable Product (Figure 2.2), to obtain tissue meshes composed of nanoscale fibres for cartilage applications. Polycaprolactone fibres were produced under the following processing conditions: applied voltage of 12 kV; feed rate between 0.72 and 3.17 ml/h; needle diameter of 0.6 mm, and distance between tip and collector of 10 cm. Three different solvents were also used during this experimental work (acetic acid, triethylamine and a mixture of both). Results show that a more homogenous mesh is obtained by adding triethylamine to the solvent solution. It can also be observed that a non uniform dependence of the mesh quality is obtained with an increase in the flow rate. Figure 2.3 illustrates SEM results of PCL fibre meshes with different flow rates and solvent concentrations.

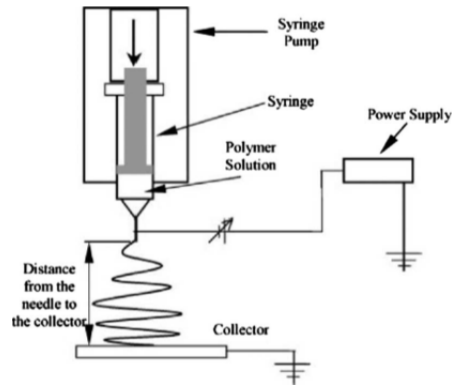


Figure 2.1 – A schematic of the key components in the electrospinning technique.

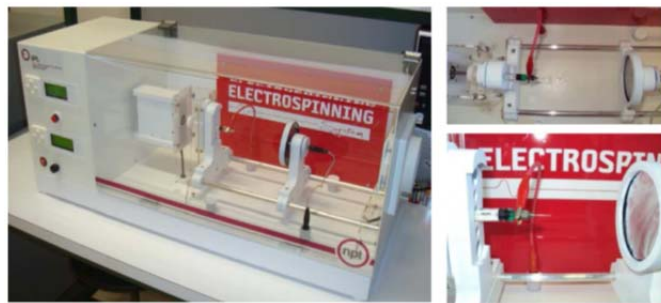


Figure 2.2 – Electrospinning system developed at the CDRSP (Dias, 2010).

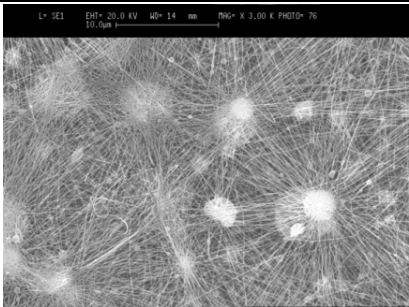
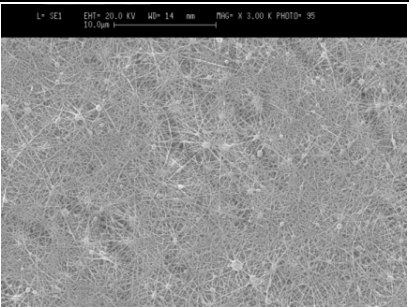
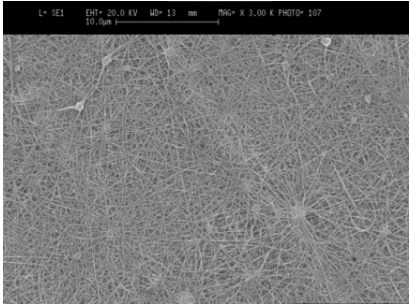
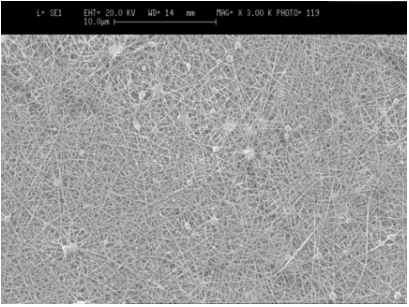
PCL + Acetic acid + TEA	Flow Rate	
	0.72 ml/h	3.17 ml/h
Concentration 9 wt%		
	Average Diameter = 0.058 μm	Average Diameter = 0.047 μm
Concentration 11 wt%		
	Average Diameter = 0.050 μm	Average Diameter = 0.047 μm

Figure 2.3 – SEM Results of PCL dissolved in acetic acid and added triethylamine (Dias *et al*, 2012).

These techniques present several limitations as they usually do not enable to properly control pore size, pore geometry and spatial distribution of pores, on top of almost not allowing to construct internal channels within the scaffold (Yeong *et al*, 2004). Although the shape and size of the pores can vary by changing process parameters, the resulting scaffold organisation of pores is random. This can lead to pore pathways that are only partially connected following contorted routes, which could inhibit the supply of nutrients and the ingrowth of tissue within the scaffold. These techniques are labour-intensive processes with long fabrication times, usually involving the use of toxic organic solvents, which are severe limitations. Using these conventional techniques, it is not possible to produce scaffolds enabling the formation of thick 3D tissues, as the cells proliferate only at the surface of the produced matrices (Figure 2.4). Conventional techniques are limited in terms of reproducibility and repeatability, due to the lack of pore interconnectivity that promotes the so-called M&M effect (cells die due to the lack of nutrients' supply and vascularisation). Therefore, additive biofabrication processes are considered as viable alternatives to fabricate scaffolds for tissue engineering as they offer better control and the ability to actively design the porosity and interconnectivity of scaffolds.

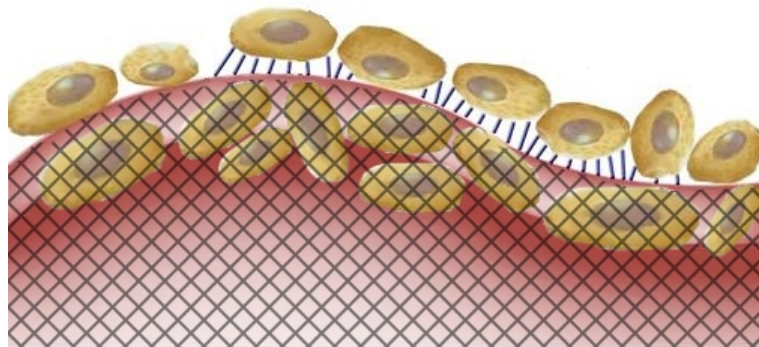


Figure 2.4 – Cell growth and proliferation of the outer layer of the scaffold, inducing the M&M effect.

2.3. Additive Biomanufacturing

In 2005, Biomanufacturing was defined as “the use of additive technologies, biodegradable and biocompatible materials, cells, growth factors, etc., to produce biological structures for tissue engineering applications”, during a Biomanufacturing Workshop hosted by Tsinghua University at China. More recently, during the Spring 2008 Meeting sponsored by the National Science Foundation (USA), biomanufacturing was defined as “the design, fabrication, assembly and measurement of bio-elements into structures, devices, and systems, and their interfacing and integration into / with larger scale structures *in vivo* or *in vitro* environment such that heterogeneity, scalability and sustainability are possible”.

A general overview of the necessary steps to produce scaffolds for tissue engineering through biomanufacturing technologies is illustrated in Figure 2.5 (Bártolo *et al*, 2012; Bártolo, 2006; Bártolo *et al*, 2003). The first step is the generation of the corresponding computer solid model through one of the currently available medical imaging techniques, such as computer tomography, magnetic resonance imaging, etc. These imaging methods produce continuous volumetric data (voxel-based data), providing the input data for the digital model generation (Bártolo, 2006). The model is then tessellated as an STL file (Figure 2.6). The STL model is then mathematically sliced into thin layers (sliced model). The data is then sent to a biomanufacturing device to produce the biocompatible and biodegradable constructs containing or not cells and growth factors.

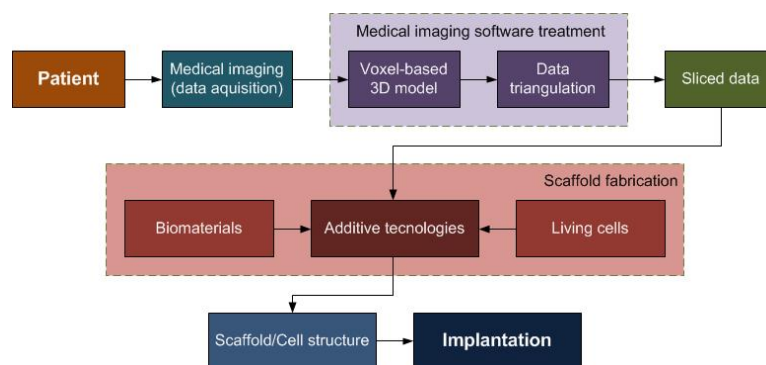


Figure 2.5 – Steps of biomanufacturing in tissue engineering.

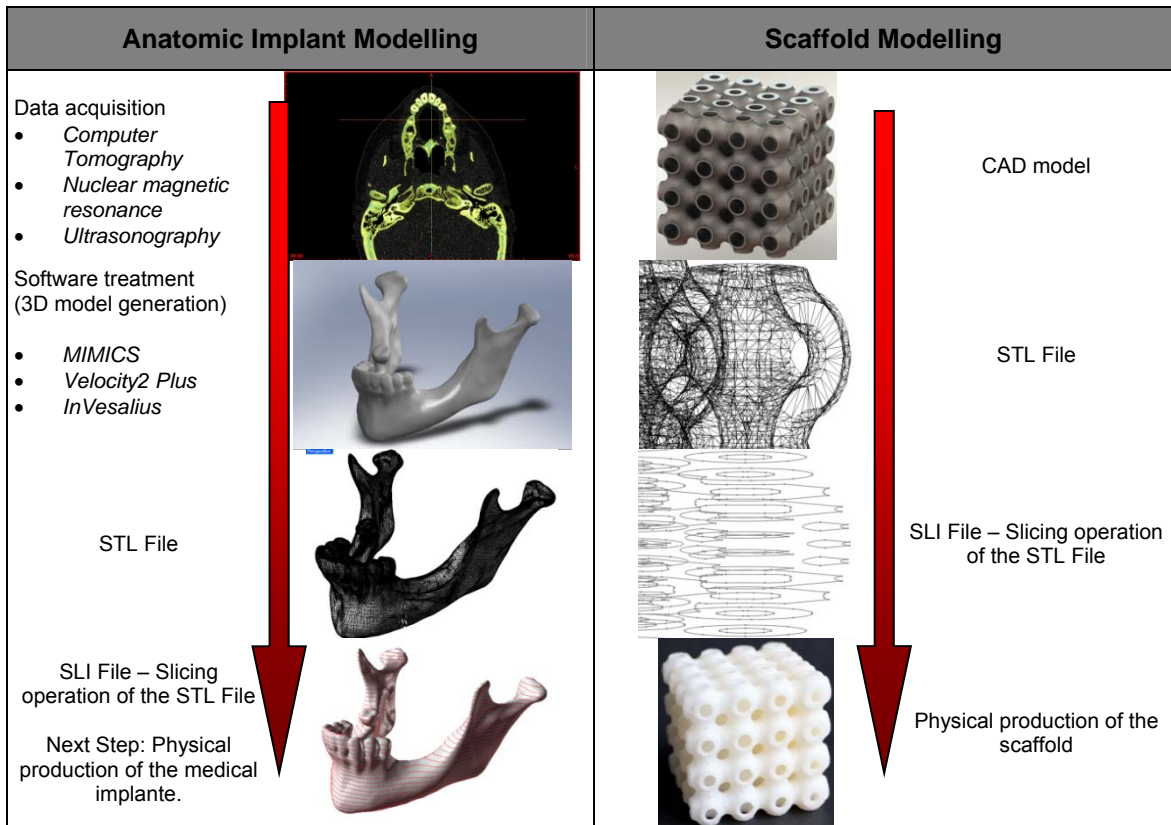


Figure 2.6 – Strategy to produce a medical implant or a scaffold.

The STL file format is the standard format for the data input of all types of additive manufacturing systems. In this format, 3D models are represented by a number of three sided planar facets (triangles), each facet defining part of the external surface of the object.

There are two types of STL file formats, the ASCII (American Standard Code for Information Interchange) and Binary file formats. The information contained in each type of STL file is functionally identical. For each facet, the three vertices and the unit normal vector are specified. The format of the data expression is the only difference of these two types of file. The structure of an ASCII STL file (Figure 2.7) starts with the word **solid** followed by the name of the file, and ends with the word **endsolid** (Chua *et al*, 2003; Szilvási-Nagy and Mátyási, 2003). The coordinates of the vertices are ordered according to the right hand screw rule, an anti-clockwise direction, such as the normal of the facet directed away from the model (Alves and Bártolo, 2006).

solid <i>name</i>	The STL filename
facet normal $n_i n_j n_k$	The unit normal vector of facet
outer loop	
vertex $V_{x1} V_{y1} V_{z1}$	Coordinates of vertex 1
vertex $V_{x2} V_{y2} V_{z2}$	Coordinates of vertex 2
vertex $V_{x3} V_{y3} V_{z3}$	Coordinates of vertex 3
endloop	
endfacet	
endsolid <i>name</i>	

Figure 2.7 – The structure of an ASCII STL file format.

The generation of the STL representation follows two important rules shown in Figure 2.8 (Alves and Bártolo, 2006; Chen *et al*, 1999), as follows:

- Facet orientation rule: the facets define the surface of the 3D object. The orientation of the facet involves the definition of the vertices for each triangle in a counter-clockwise order;
- Adjacency rule: each triangular facet must share two vertices with each of its adjacent triangles.

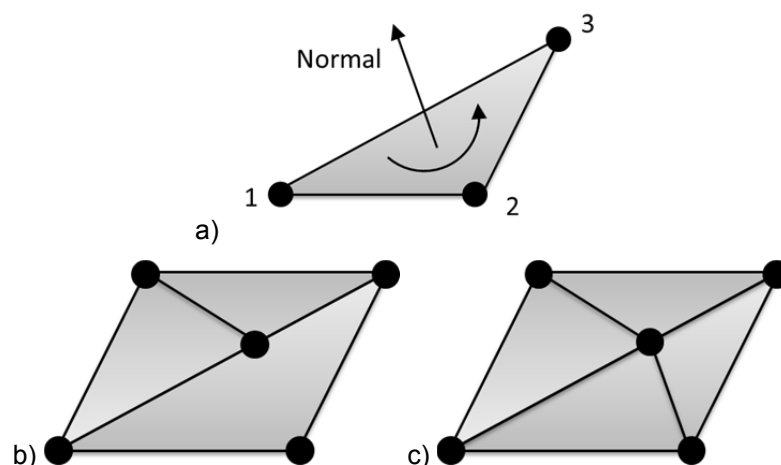


Figure 2.8 – a) Orientation of a triangular facet in a STL file. b) Violation of the vertex-to-vertex rule. c) A correct triangulation (Alves and Bártolo, 2006).

To assure that the adjacency rule is obeyed, it is necessary to verify the following consistency rules (Alves and Bártolo, 2006):

- The number of triangles must be even;
- The number of edges must be a multiple of three;
- The number of triangles must be equal to two thirds of the number of edges.
- The number of vertices is given by:

$$V = 0.5 \times T + 2 \quad (2.1)$$

where V is the number of vertices and T is the number of triangles.

To assure that the set of STL triangles comprises a closed volume, it is necessary to verify the Euler's rule for solids. According to this rule, the definition of a proper solid implies that the following equation is verified (Alves and Bártolo, 2006):

$$T - E + V - H = 2 \times (B - P) \quad (2.2)$$

with E being the number of edges, H the number of face holes, B the number of separate, disjoint bodies and P the number of passages, i.e., holes through the entire body.

Triangles generated by triangulation must be equiangular whenever possible to avoid thin and long triangles. According to Chen *et al* (1999), the Delaunay triangulation satisfies the equiangularity criterion, expressed in terms of the maximum of minimum angles in a triangulation. The *max-min* angle criterion refers to the choice of the diagonal of a quadrilateral, i.e., a pair of triangles maximising the minimum of the six interior angles of the triangles, when the quadrilateral is strictly convex. The minimum interior angle "*bdc*", illustrated in Figure 2.9.a, is smaller than the minimum interior angle "*bac*", represented in Figure 2.9.b, so the second triangulation (Figure 2.9.b) is advantageous. If this strategy is locally applied to all edges of each triangle, the resulting triangulation is globally optimal (Alves *et al*, 2012; Chen *et al*, 1999).

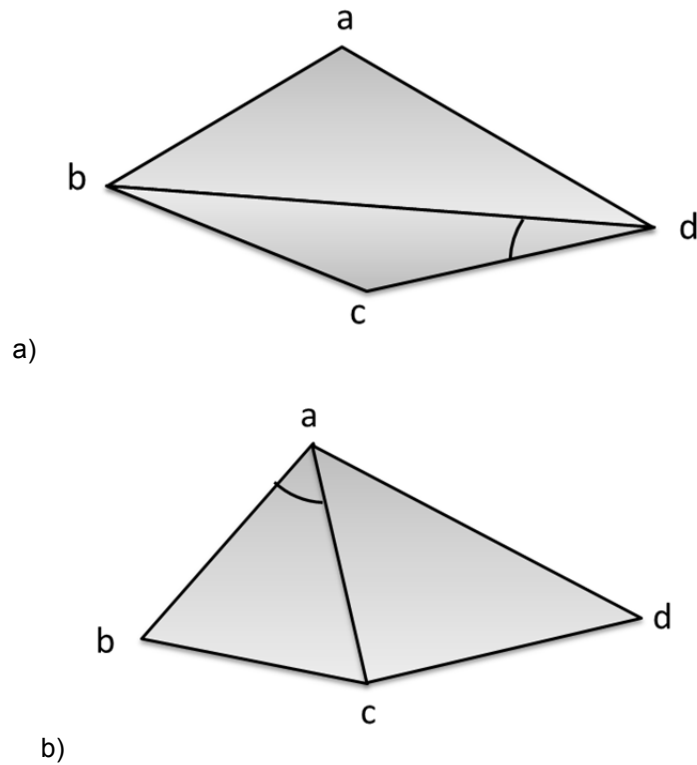


Figure 2.9 – Max-min angle criterion. a) Smaller minimum interior angle. b) Larger minimum interior angle (Alves *et al*, 2012; Alves and Bártolo, 2008; Chen *et al*, 1999).

The disadvantages of the use of a tessellated representation, as a standard in additive manufacturing, are the following ones (Sunil and Pande, 2008):

- It is a first-order approximation of the original CAD model;
- It is a list of triangles with no topological information;
- High degree of redundancy: each triangle is individually recorded and shared coordinates are duplicated in the file;
- The user needs to input acceptable cordal tolerance, which is the distance between the plane of a triangle and its approximating surface. Increasing the number of triangles smoothens the surface, but leads to larger data files.

Many CAD systems generate incorrect STL files when the CAD models are very complex. Possible errors are non-manifold facets, gaps, incorrect normals, overlapping facets, etc (Sunil and Pande, 2008).

Once finished, the STL file must be sliced. Slicing refers to intersecting a CAD model with a plane, in order to determine two dimensional contours (Figure 2.10). The slicing can be uniform, where the layer thickness is kept constant or adaptive, the layer thickness changes based on the surface geometry of the CAD model (Kulkarni *et al*, 2000).

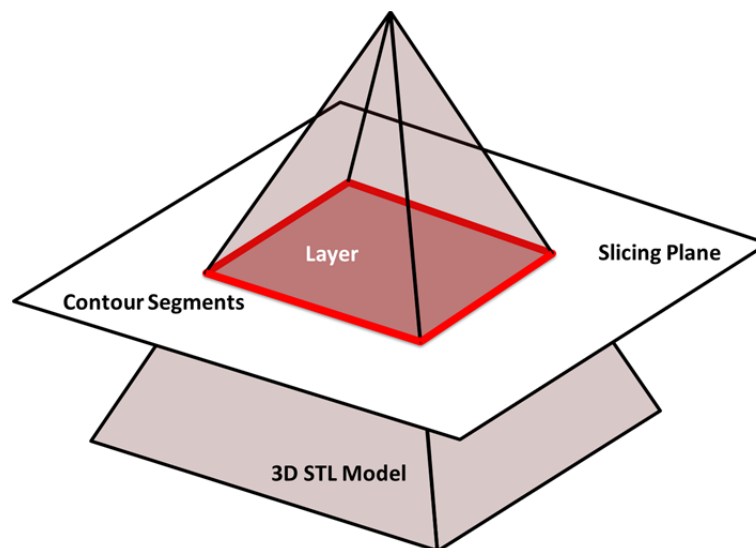


Figure 2.10 – Definition of a layer through the intersection between the 3D STL model and a slicing plane (Alves and Bártolo, 2006).

Adaptive slicing involves slicing with varying layer thickness. In this strategy, surfaces of high curvature are sliced with thinner layer thickness and surfaces of low curvature are sliced with thicker layers. Adaptive slicing yields better surface quality, as the staircase effect decreases and the variations in the cusp height across the layers is minimized. The main advantage of adaptive slicing is that it gives the user explicit control over the surface quality (Kulkarni *et al*, 2000).

2.3.1. Additive Processes

Additive biomanufacturing technologies include different fabrication strategies as indicated in Figure 2.11 (Bártolo *et al*, 2008).

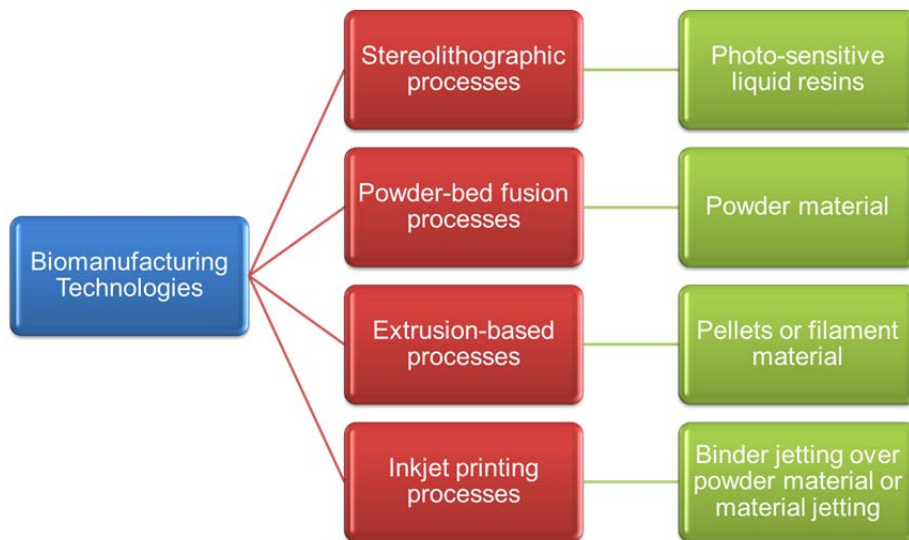


Figure 2.11 – Classification of additive technologies.

The main advantages of additive biomanufacturing technologies are both the capacity to rapidly produce very complex 3D models and the ability to use various raw materials. When combined with clinical imaging data, these fabrication techniques can be used to produce constructs customised to the shape of the defect or injury. Some processes operate at room temperature, thus allowing for cell encapsulation and biomolecule incorporation without significantly affecting its viability. In the field of tissue engineering, additive biomanufacturing technologies are used to produce scaffolds with customised external shape and predefined internal morphology, allowing good control of pore distribution and size (Bártolo *et al*, 2012; Bártolo *et al*, 2008; Leong *et al*, 2008; Hutmacher *et al*, 2007; Bártolo, 2006; Yeong *et al*, 2006; 2005; Hutmacher *et al*, 2004; Tsang and Bhatia, 2004; Leong *et al*, 2003).

(a) *Stereolithographic Processes*

Stereolithographic processes produce three-dimensional solid objects in a multi-layer procedure, through the selective photo-initiated cure reaction of a polymer (Bártolo and Mitchell, 2003). These processes usually employ two distinct methods of irradiation. The first method is the mask-based method in which an image is transferred to a liquid polymer by irradiating through a patterned mask. The irradiated part of the liquid polymer is then solidified. In the second method, a direct writing process using a focused UV beam produces polymer structures (Figure 2.12).

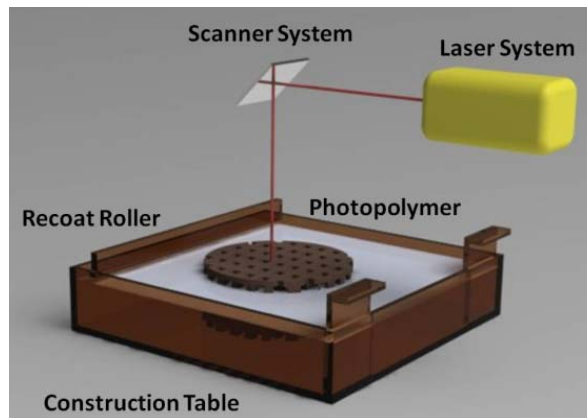


Figure 2.12 – Stereolithography system.

The direct or laser writing approach consists of a vat containing a photosensitive polymer, a moveable platform on which the model is built, a laser to irradiate and cure the polymer, and a dynamic mirror system to direct the laser beam over the polymer surface “writing” each layer. After drawing a layer, the platform dips into the polymer vat, leaving a thin film from which the next layer will be formed.

Mask-based writing systems build models by shining a flood lamp through a mask, which lets light pass through it. These systems generally require the generation of a lot of masks with precise mask alignments. One solution for this problem is the use of a liquid crystal display (LCD), or a digital processing projection system as a flexible mask (Figure 2.13).

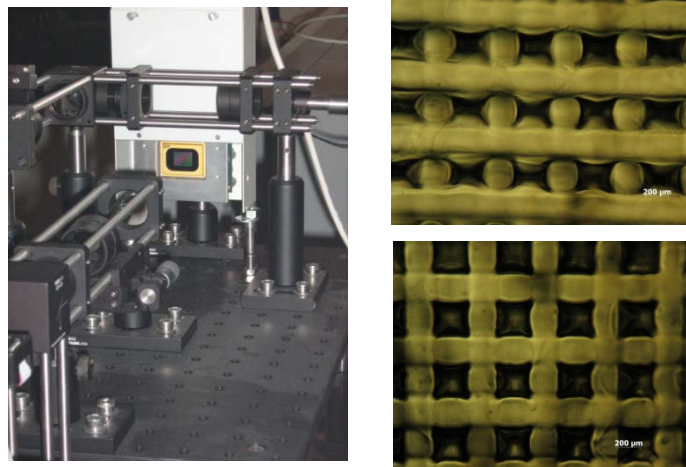


Figure 2.13 – Mask-based writing system and polyHEMA constructs produced at the Polytechnic Institute of Leiria.

Microstereolithography is a relatively recent development, similar to conventional stereolithography. However, to get a better resolution, the beam needs to be more precisely focused, in order to reduce the spot size to a few micrometres of diameter. Several strategies were proposed (Bertsch *et al*, 2003): constrained surface techniques, free surface techniques, and integral processes. Integral microstereolithography represents the most recent advancement in this field, enabling the solidification of each layer in one irradiation step by projecting the corresponding image onto the surface of the photo-polymerisable resin, through either a liquid crystal display or a digital micro mirror device. MicroTEC (Germany) is one of the few companies producing commercial applications of microstereolithography. This technology, known as Rapid Micro Product Development (RMPD), uses an excimer laser as a light source that works on a vector-by-vector basis.

Currently, a Multimaterial Microstereo-thermal-lithography system is being developed at the Centre for Rapid and Sustainable Product Development at the Polytechnic Institute of Leiria. This novel process combines both Ultra-Violet and Infrared radiation for a single separate or combined radiation of both light sources, allowing to process single or multiple materials available in the rotating platform. Figure 2.14 illustrates the system being developed.

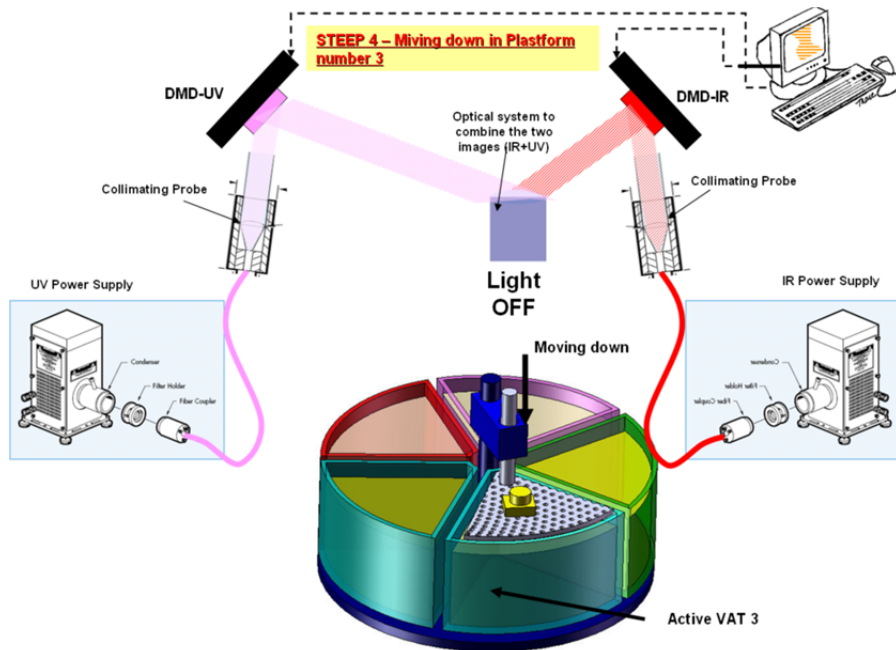


Figure 2.14 – Multimaterial microstereo-thermal-lithography system (Bártolo, 2011).

All of the abovementioned stereolithographic approaches are based on a single-photon initiated polymerisation procedure. Two-photon-initiated polymerisation curing processes represent a useful stereolithographic alternative strategy to produce micro/nanoscale structures by using femtosecond infrared laser without photo-masks (Lemerancier *et al*, 2005; Tormen *et al*, 2004; Kowata and Sun, 2003). In this process, the molecule simultaneously absorbs two photons instead of one, being excited to higher singlet states. The use of two-photon-initiated polymerisation allows a submicron 3D resolution, on top of enabling both a 3D fabrication at greater depth and an ultra-fast fabrication.

The photopolymerisation of biomaterials via multiphoton excitation can also provide an efficient method of scaffold microfabrication. In this process, the beam of an ultra-fast infrared laser is tightly focused into the volume of a photosensitive material (Figure 2.15). The polymerisation process can be initiated by non-linear absorption within the focal volume. A multiphoton excitation was applied to fabricate scaffolds of a wide range of polymers and bulk protein formulations, such as collagen, laminin, fibronectin, bovine serum albumin, alkaline phosphatase, etc.

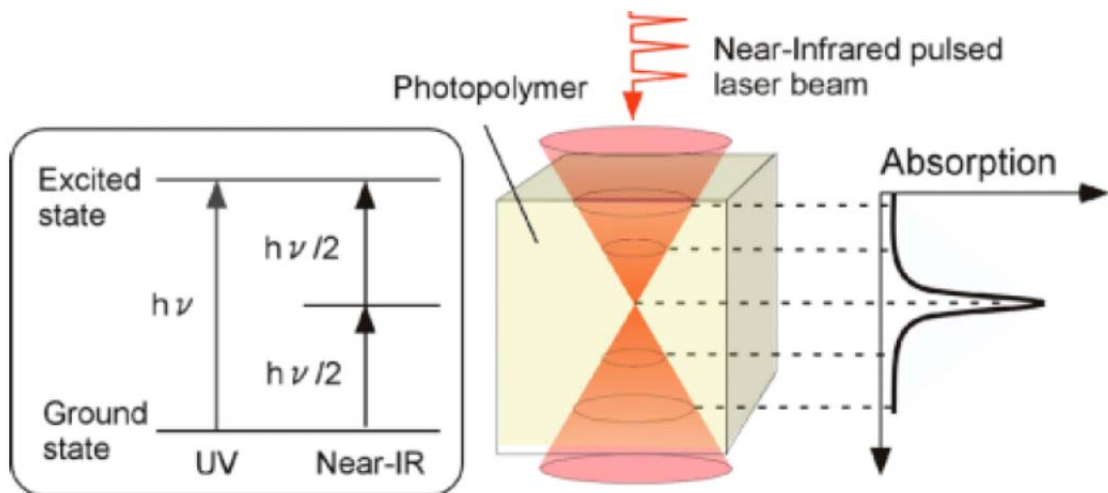


Figure 2.15 – The principle of multiphoton polymerisation.

Several groups developed stereolithographic processes for tissue engineering. Levy *et al* (1997) used a direct irradiation stereolithographic process to produce hydroxyapatite (HA) ceramic scaffolds for orbital floor prosthesis. A suspension of fine HA powder into a UV-photocurable resin was formulated and used as building material. The photo-cured resin acts as a binder to hold the HA particles together. The resin is then burnt out and the HA powder assembly sintered for consolidation. A similar approach was used by Griffith and Halloran (1996) to produce ceramic scaffolds using suspensions of alumina, silicon nitride and silica particles with a photo-curable resin. The binder was removed by pyrolysis and the ceramic structures sintered.

Bryant and Anseth (2001) used a photopolymerisation process to encapsulate chondrocytes in poly(ethylene oxide) (PEO) hydrogels structures, with thicknesses varying from 2 to 8 mm. The hydrogel structures were photo-cured at low light intensity ($\sim 10 \text{ mW/cm}^2$) during 10 minutes. The chondrocytes encapsulated, in the hydrogel structures and cultured *in vitro* during 6 weeks, remained viable and produced cartilaginous tissue. Results suggest that an increase in the hydrogel thickness from 2 to 8 mm do not change cell viability and uniformity.

Stereolithography is also commonly used to produce a negative replica filled typically with ceramic slurries and burnt away during sintering. Chu *et al* (2001) developed a lost-mould technique to produce implants with designed channels and connection patterns (Figure 2.16). Stereolithography was used to create epoxy moulds, designed from negative image of implants. A highly loaded HA-acrylate suspension was cast into the mould. The mould and the acrylic binder were removed by pyrolysis, and the HA green scaffold submitted to a sintering process. The finest channel size achieved was about 366 μm , and the range of implant porosity between 26% and 52%.

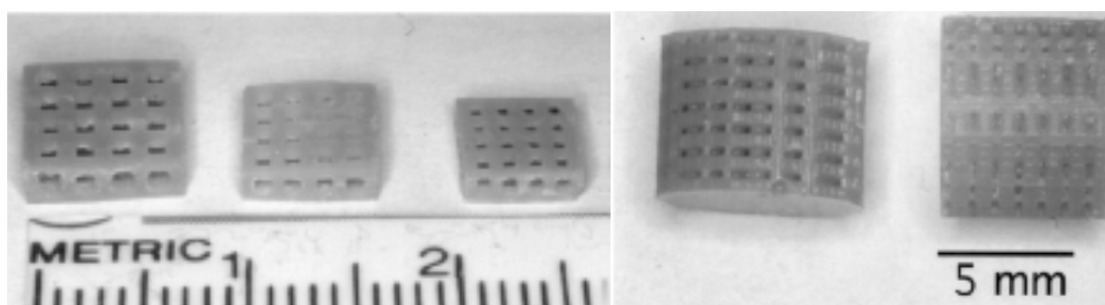


Figure 2.16 – Sintered HA scaffolds produced by a lost-mould technique (Chu *et al*, 2001).

A direct fabrication of biopolymeric scaffolds was also reported by Cooke *et al* (2002). They used a biodegradable resin mixture of diethyl fumarate, poly(propylene fumarate) and bisacylphosphine oxide as photoinitiator to produce scaffolds for bone ingrowth.

Similarly, Matsuda and Mizutani (2002) developed a photopolymer containing biodegradable copolymer of trimethylene carbonate and ϵ -caprolactone. UV light was also used to fabricate hydrogel polymer scaffolds. The main limitation was the development of water-soluble components, both functional and photolabile (Fischer *et al*, 2001).

A mask-based writing system can be used to pattern hydrogel structures with high resolution. Liu and Bhatia (2002) reported a method where multiple steps of micropatterned photopolymerisation processes can be coupled to produce 3D cell matrix structures with micro-scale resolution (Figure 2.17).

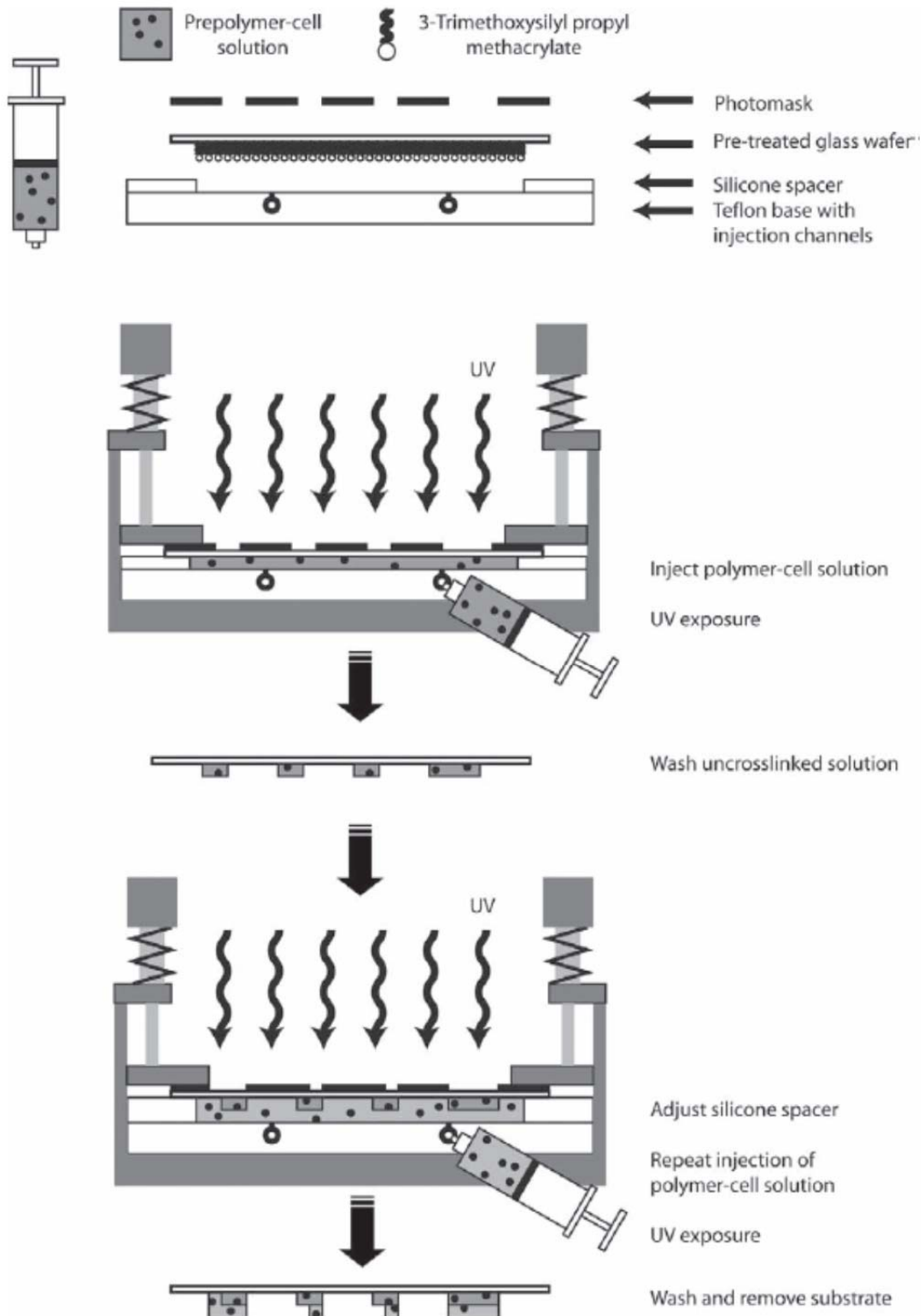


Figure 2.17 – Process for formation of hydrogel microstructures containing living cells (Liu and Bhatia, 2002).

Lan *et al* (2009) produced poly(propylene fumarate) (PPF) scaffolds with highly interconnected porous structure and a porosity of 65%. The scaffolds were coated by applying accelerated biomimetic apatite and arginini-glycine-aspartic acid peptide coating to improve cell behaviour. The coated scaffolds were seeded with MC3T3-E1 pre-osteoblasts, and their biologic properties were evaluated using an MTS assay and histologic staining. Melchels *et al* (2009) used a resin based on poly(D,L-lactide) macromonomers and a non-reactive diluent to produce porous scaffolds with gyroid architecture (Figure 2.18). In this work, it was also possible to observe that the pre-osteoblasts readily adhered and proliferated well on these scaffolds.

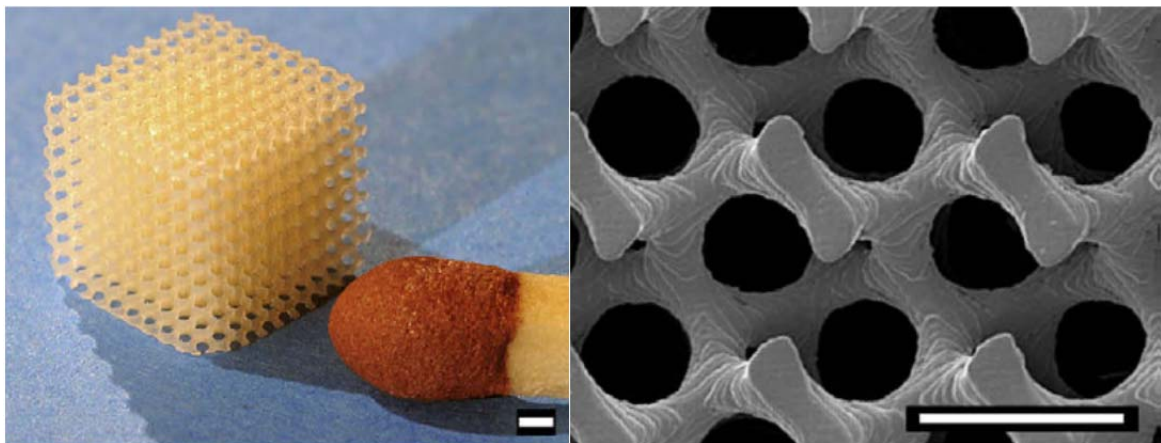


Figure 2.18 – PDLLA scaffolds with a gyroid architecture built by stereolithography. Scale bars represent 500 μm (Melchels *et al*, 2009).

The main advantages of stereolithographic processes include the ability to fast curing at physiological temperatures. Most commonly used photopolymerisable materials for scaffolds include derivatives of polyethylene glycol (PEG) acrylate, PEG methacrylate, polyvinyl alcohol (PVA) and modified polysaccharides (Hutmacher *et al*, 2004). However, the number of materials with the appropriate characteristics, in terms of biodegradability, biocompatibility and mechanical properties, is still limited.

(b) Powder-bed fusion / Laser Sintering processes

Selective laser sintering (SLS) uses a laser emitting infrared radiation, to selectively heat powder material just beyond its melting point (Figure 2.19). The laser traces the shape of each cross-section of the model to be built, sintering powder in a thin layer. It also supplies energy that not only fuses neighbouring powder particles, but also bonds each new layer to those previously sintered. For polymeric powders, the sintering process takes place in a sealed heated chamber at a temperature near the melting point filled with nitrogen or argon. After each layer is solidified, the piston over the model retracts to a new position and a new layer of powder is supplied using a mechanical roller. The powder that remains unaffected by the laser acts as a natural support for the model, and remains in place until the model is complete. An important limitation of SLS is the dependence between the pores of the scaffold, the particle size of the powder material and the compaction pressure.

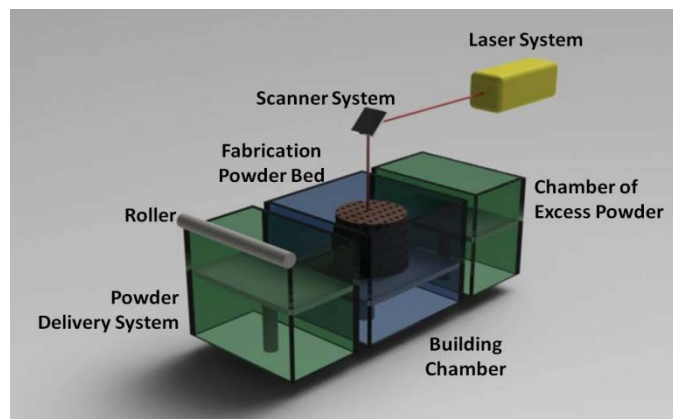


Figure 2.19 – Selective laser sintering process.

Materials most commonly used in tissue engineering scaffolds by laser sintering are biocompatible polymers, such as polycaprolactone (PCL) and poly lactic acid (PLA) and biocompatible ceramics. PCL is a bioresorbable polymer used for bone and cartilage repair. It is more stable at ambient conditions than PCL, less expensive and readily available (Williams *et al*, 2005).

Williams *et al* (2005) explored the potential of SLS to produce PCL scaffolds for the replacement of skeletal tissues. The scaffolds were seeded with bone morphogenetic protein-7 (BMP-7) transduced fibroblasts. *In vivo* results show that these scaffolds enhance tissue in-growth, on top of possessing mechanical properties within the lower range of trabecular bone. Compressive modulus (52 to 67 MPa) and yield strength (2.0 to 3.2 MPa) were in the lower range of human trabecular bone properties.

Lee and Barlow (1996) coated calcium phosphate powder with polymer, by spray drying slurry of particulate and emulsion binder. The coated powder was then sintered to fabricate calcium phosphate bone implants. Afterwards, these structures were infiltrated with calcium phosphate solution or phosphoric acid-based inorganic cement in order to increase cell behaviour.

Hao *et al* (2005) investigated the use of SLS to fabricate HA mixed high density polyethylene (HDPE) scaffolds. Different scanning speeds and laser power values were considered. HA and HDPE powders with 40 % HA by volume ratio were mixed using a high speed blender. Different process parameters resulted in different sintered morphologies (Figure 2.20). Results show that for low power or high scanning speed the layers were in general not sintered or very fragile.

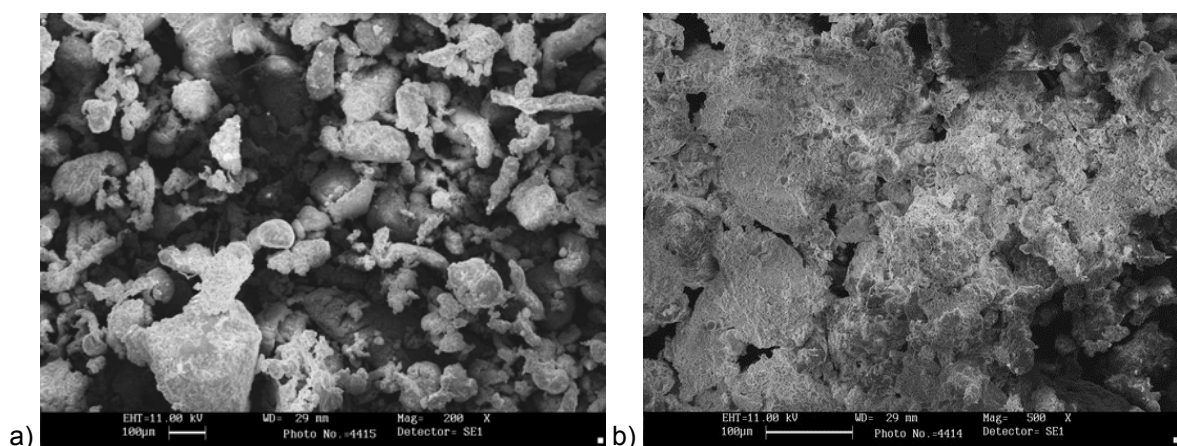


Figure 2.20 – SEM micrograph of sintered layer's surface with irradiated at 1200 mm/s of scanning speed and different laser power: (a) 3.6W. (b) 7.2W (Hao *et al*, 2005).

Zhou *et al* (2008) studied the use of bio-nano-composite microspheres, consisting of carbonated hydroxyapatite (CHAp) nanospheres within a PLLA matrix to produce scaffolds (Figure 2.21). PLLA microspheres and PLLA/CHAp nanocomposites microspheres were prepared by emulsion techniques. The resultant microspheres had a size of 5-30 μm , suitable for the SLS process. The use of PLLA/CHAp nanocomposite microspheres seems to offer a solution to the problem of removing the excessive powder from the pores after fabrication.

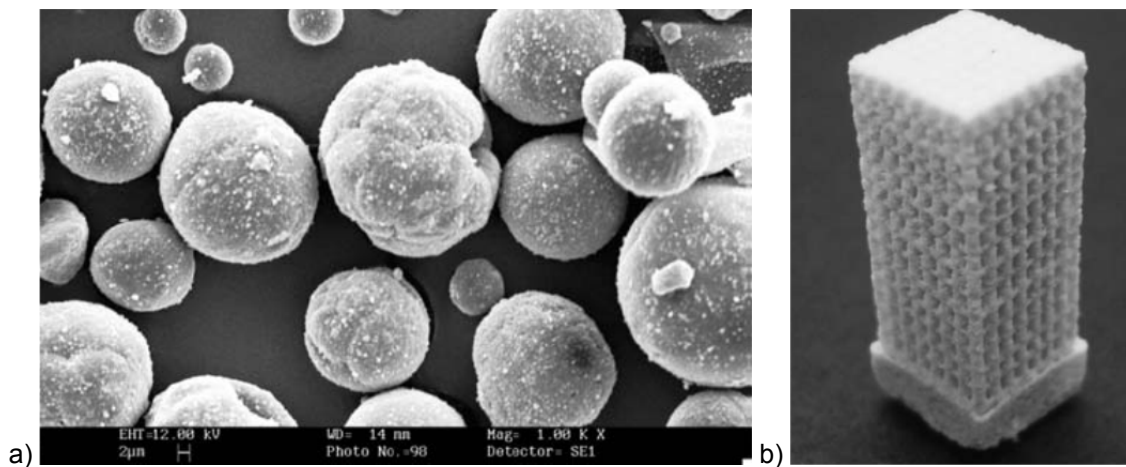


Figure 2.21 – a) SEM image of PLLA/CHAp nanocomposite microspheres. B) PLLA/CHAp nanocomposite scaffolds (Zhou *et al*, 2008).

Popov *et al* (2004) proposed the concept of Surface Selective Laser Sintering (SSLS) technique enabling to extend the range of polymers that can be used for scaffold fabrication. Unlike conventional selective laser sintering, where polymer has a strong absorption at the laser wavelength, the SSLS process is based on melting the particle. This particle is transparent for laser radiation, due to the laser beam absorption by a small amount (<0.1 wt%) of biocompatible carbon black homogeneously distributed along the polymer surface. This process allows preventing significant overheating of the particles internal domains that can lead to property change and degradation.

(c) *Extrusion-based Processes*

The extrusion-based process, commercially known as Fused Deposition Modelling (FDM), was developed by Scott Crump (1989). It works on an additive principle by laying down material during the construction process in a layer-by-layer fashion. A plastic filament unwound from a coil or plastic granules within a chamber, supplies the material to an extrusion nozzle that extrudes small struts of thermoplastic material to form the part being produced. The extrusion nozzle is heated to melt the material. It can be moved in the horizontal direction as the construction platform moves vertically. Both the extrusion nozzle and platform is controlled by a computer to form the three-dimensional object (Figure 2.22). The material leaves the extruder in a liquid form and hardens immediately. The previously formed layer, which is the substrate for the next layer, must be maintained at a temperature just below the solidification point of the thermoplastic material, to assure good interlayer adhesion.

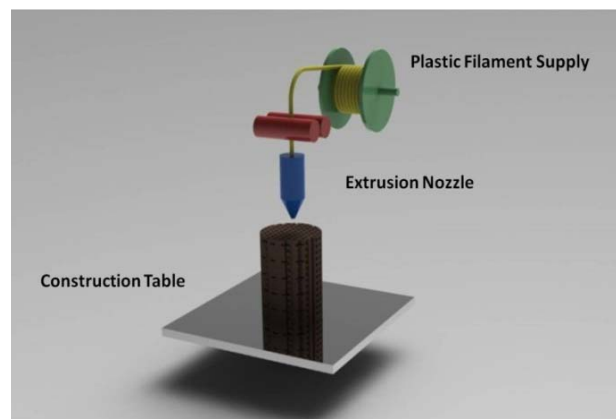


Figure 2.22 – Fused Deposition Modelling process.

Extrusion-based processes have been used to successfully produce scaffolds in PCL, PP-TCP, PCL-HA, PCL-TCP with resolution of 250 μm . Some of the major limitations of FDM are both the use of filament-based materials and the high heat effect on raw material. In order to solve some limitations of the FDM process, such as the requirement of precursor filaments or high processing temperatures, some alternative processes were developed.

Woodfield *et al* (2004) used a FDM-like technique, called 3D Fibre Deposition, to produce poly(ethylene glycol)-terephthalate-poly(butylene terephthalate) (PEGT/PBT) scaffolds for engineering of articular cartilage (Figure 2.23). By varying the co-polymer composition, porosity and pore geometry, scaffolds were produced with a range of mechanical properties close to articular cartilage. The scaffolds seeded with bovine chondrocytes supported a homogeneous cell distribution and subsequent cartilage-like tissue formation.

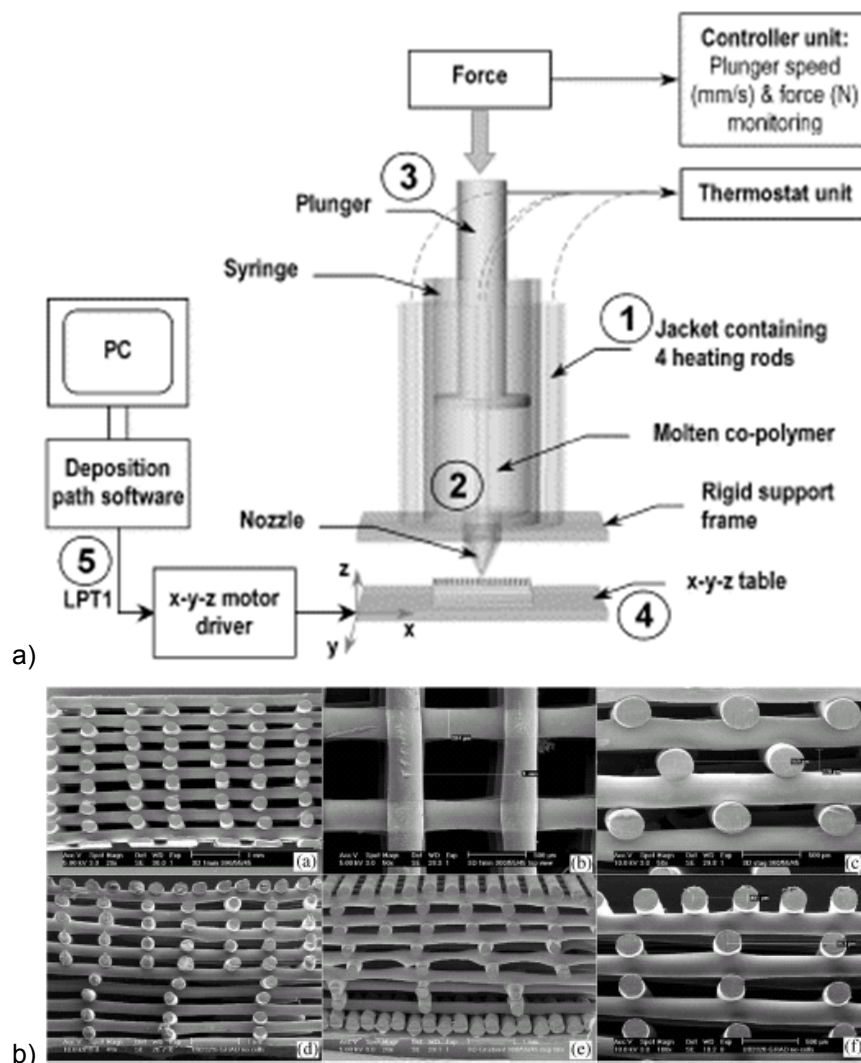


Figure 2.23 – a) The 3D Fiber Deposition system. b) SEM sections of 3D deposited scaffolds with varying deposition geometries (Woodfield *et al*, 2004).

Drexel University researchers (Wang *et al*, 2004) developed a variation of FDM called *Precision Extruding Deposition* (PED), for the fabrication of bone tissue scaffolds (Figure 2.24). In this process, material in pellet or granule form is fed into a chamber where it is liquefied. Pressure from a rotating screw forces the material down a chamber and out through a nozzle tip. This process was used by Wang *et al* (2004) to directly fabricate PCL scaffolds, with controlled pore size of 250 μm and designed structural orientations ($0^\circ/90^\circ$, $0^\circ/120^\circ$ or combined $0^\circ/120^\circ$ and $0^\circ/90^\circ$ patterns). Proliferation studies were performed using cardiomyoblasts, fibroblasts and smooth muscle cells.

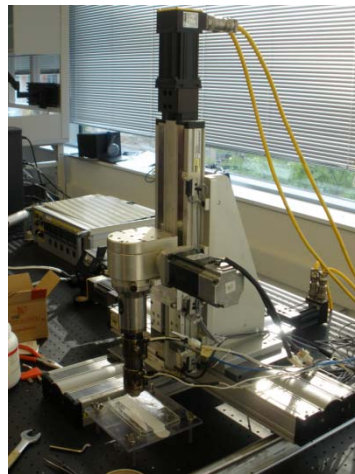


Figure 2.24 – Precision Extruding Deposition System developed by Wei Sun at Drexel University.

In order to eliminate the elevated temperatures required by the extrusion-based processes, Xiong *et al* (2005) at Tsinghua University, developed a process called *Low-temperature Deposition Manufacturing* (LDM) to produce scaffolds at a low temperature environment under 0°C . The LDM system comprises a multi-nozzle extrusion process and a thermally induced phase separation process (Figure 2.25). The LDM process was used to produce poly(L-lactide) (PLLA) and TCP composite scaffolds with BMP growth factor. The scaffolds were implanted into rabbit radius and canine radius with large-segmental defects. After 12 weeks, it was possible to observe that the rabbit radius defect was successfully repaired and the regenerated bone had properties similar to the healthy bone. For the canine radius, similar results were observed after 24 weeks (Yan *et al*, 2003a; 2003b).

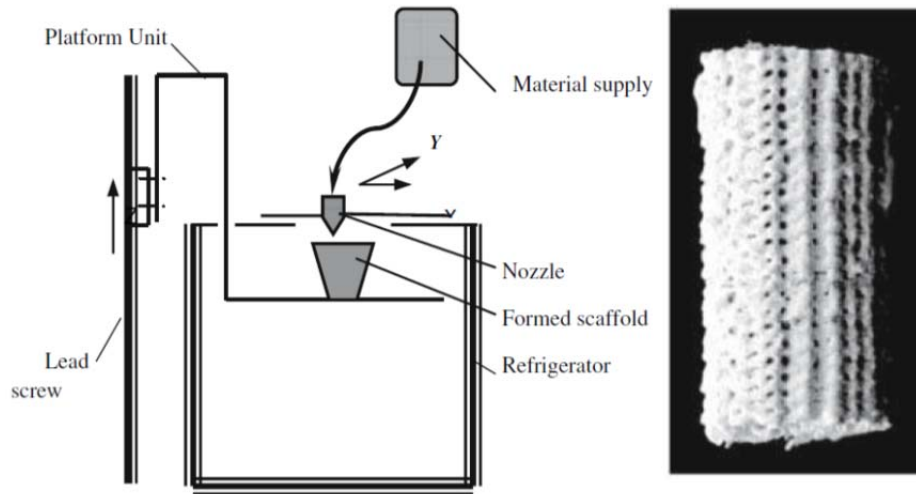


Figure 2.25 – a) Schematic illustration of the LDM system. b) Example of a porous PLLA/TCP composite scaffold produced by LDM process (Yan *et al*, 2003a; 2003b).

The Centre for Rapid and Sustainable Product Development, Polytechnic Institute of Leiria, developed a variation of FDM called BioExtruder (Figure 2.26.a) (Almeida *et al*, 2010; Mateus *et al*, 2008). It is a highly reproducible and low cost system enabling the controlled definition of pores into the scaffold, to modulate mechanical strength and molecular diffusion, as well the fabrication of multi-material scaffolds. It comprises two different deposition systems: one rotational system for multi-material deposition acted by a pneumatic mechanism, and another one for a single material deposition that uses a screw to assist the deposition process (Figures 2.26.b and 2.26.c). A new version of this system, the Dual-Bioextruder, comprises a double head extrusion system to process multiple materials (Figure 2.27).

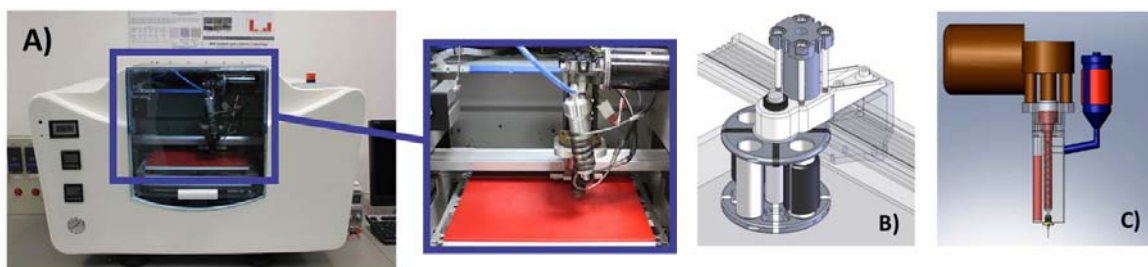


Figure 2.26 – a) Bioextruder System b) Multi-material extrusion system; c) Single-material extrusion (Almeida *et al*, 2010; Mateus *et al*, 2008).

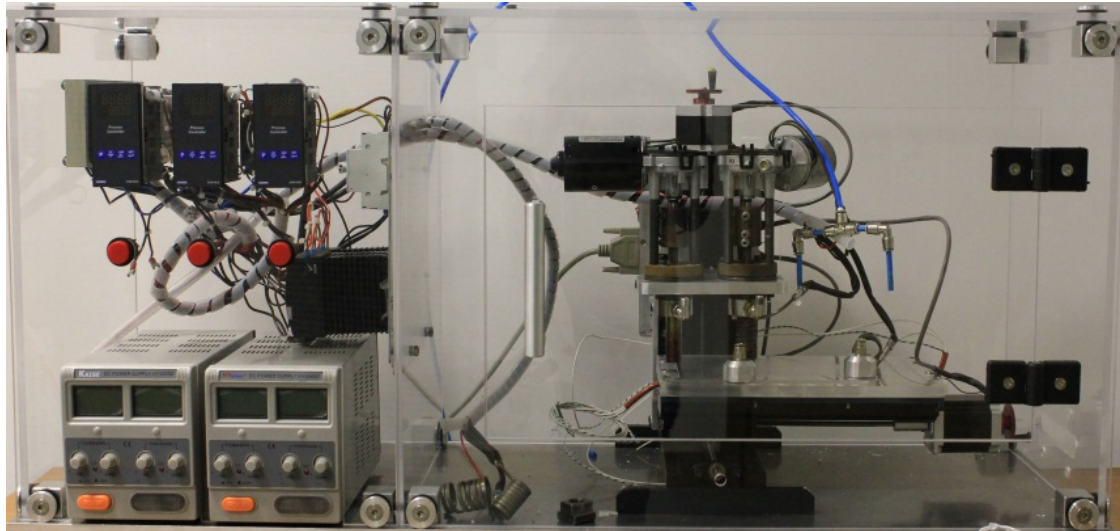


Figure 2.27 – Dual-Bioextruder system.

Recently, the Centre for Rapid and Sustainable Product Development at the Polytechnic Institute of Leiria developed another version of the Bioextruder system called BioCell Printing (Figure 2.28). The novel system is composed by four separate sections. The first section contemplates the multiple head extrusion system where scaffolds are produced. Scaffolds are then sterilised either chemically or physically in the second section before the cell seeding in the third section. Finally, the cell seeded scaffolds are then cultured *in vitro* under dynamic conditions inside the bioreactor located in the last section.

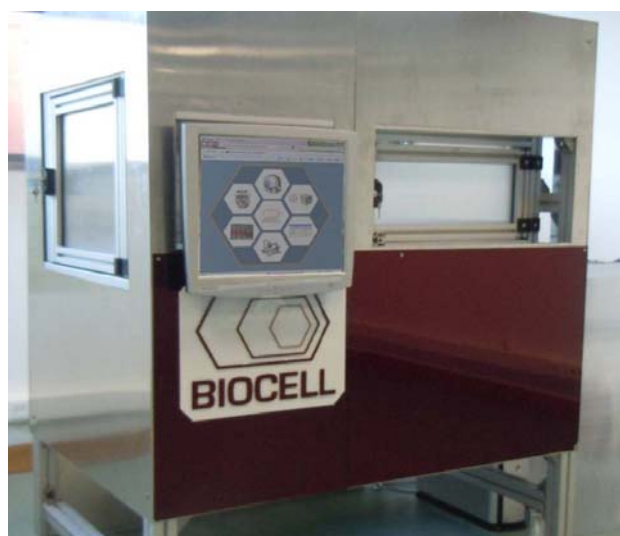


Figure 2.28 – Biocell Printing System.

Bioplotting (Figure 2.29), a technique developed by the Freiburg Materials Research Centre and Envisiontec, Germany, uses a pressure-controlled dispenser to deposit material into a reactive liquid medium of comparable density. This balance of media densities, which allows scaffolds to be created without the need of support structures, is a key characteristic of this process. Buoyancy can be provided to the plotted material, making strands of material remaining in the correct position instead of sinking, due to gravitational effects. Figure 2.30 illustrates some examples of scaffold structures made by the 3D-Bioplotter system. Materials, such as melts of poly(lactides), poly(lactide-co-glycolide), poly(hydroxybutyrate-co-valeriate), poly(caprolactone), poly(butylene terephthalate-block-oligoethylene oxide), solutions of agar and gelatine, collagen and reactive biosystems involving fibrin formation and polyelectrolyte complexation were used by Pfister *et al* (2004).

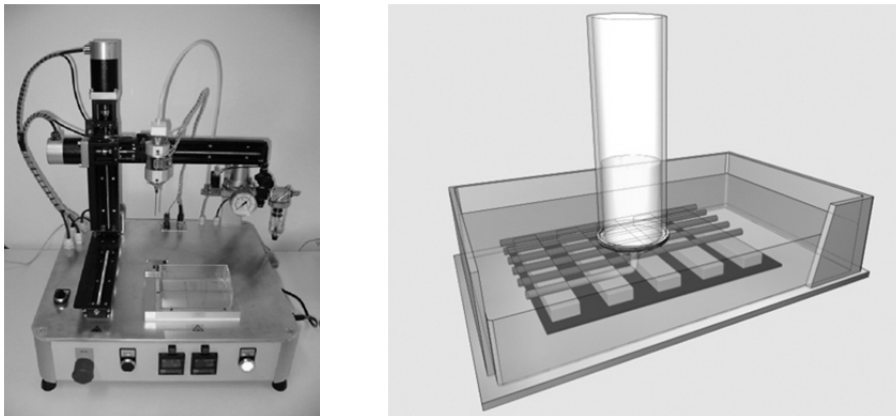


Figure 2.29 – a) The 3D-Bioplotter system. b) Process building of the first layer (Carvalho *et al*, 2005).

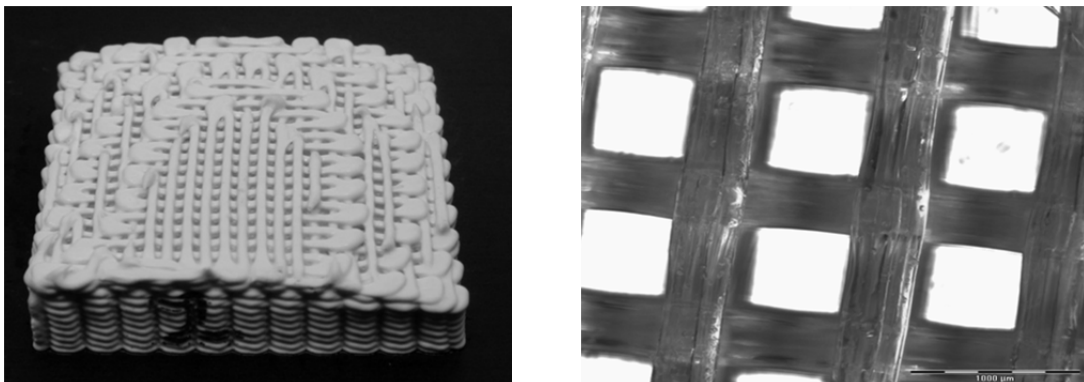


Figure 2.30 – a) Hydroxyapatite scaffold. b) PLGA scaffold (Carvalho *et al*, 2005).

Moroni *et al* (2006) reported a novel strategy to create hollow fibres with controlled shell thickness and lumen diameter, organizing them into 3D scaffolds. Hollow fibres (Figure 2.31), are made by extrusion of a blend of poly(butylmethacrylate-methylmethacrylate) (P(BMA/MMA)) and poly(ethylene oxideterephthalate)-co-poly(butylene terephthalate) (PEOT/PBT), using the Bioplotter system. The polymer with lower viscosity tends to shift towards the walls during the flow along the nozzle of the extruder, due to viscosity differences. The consequent separation of the polymers produces a stratification effect. Hollow fibres are produced by removing the core polymer through selective dissolution. It was also observed that bovine primary articular chondrocytes grow and form ECM, not only in the scaffold macropores but also inside the hollow cavities (Figure 2.32). The use of these hollow matrices for selective drug release is under investigation.

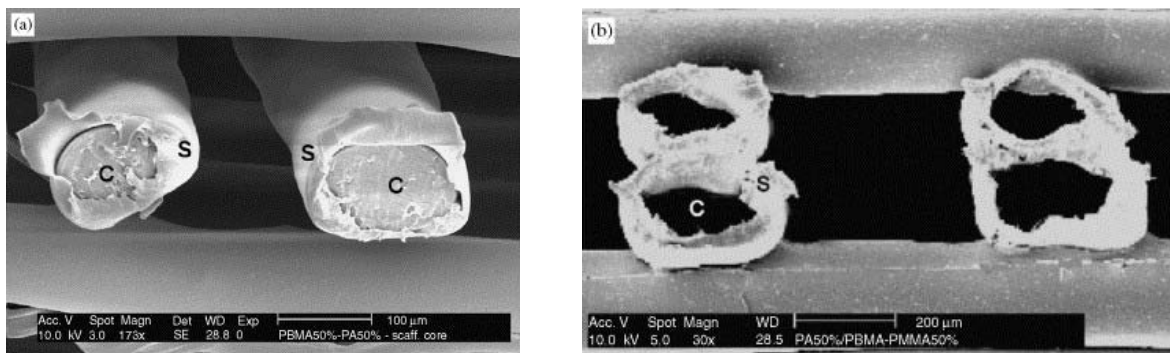


Figure 2.31 – SEM micrographs of a scaffold before (a) and after (b) leaching out the core material (Moroni *et al*, 2006).

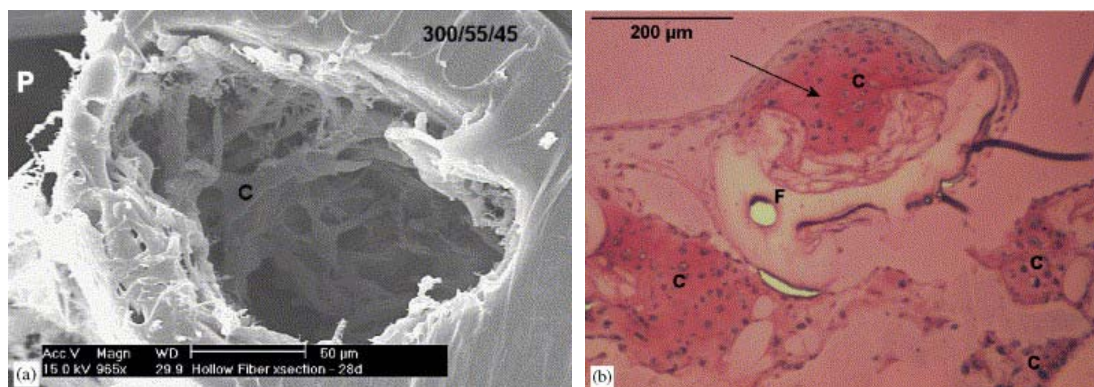


Figure 2.32 – SEM (a) and optical microscope (b) micrographs showing chondrocytes and ECM formation inside and outside the hollow fibers (Moroni *et al*, 2006). P = pore; F = fiber; C = chondrocytes.

An alternative process is the *Pressure Assisted Microsyringe* (PAM) that involves the deposition of polymer dissolved in solvent through a syringe (Vozzi *et al*, 2003). The thickness of the polymer stream can be varied by changing the syringe pressure, solution viscosity, syringe tip diameter and motor speed. A resolution as low as 10 μm was achieved on a 2D structure.

Robocasting (Figure 2.33), also known as direct-write assembly, consists of a robotic deposition of highly concentrated colloidal suspensions capable of fully supporting their own weight during assembly, due to their viscoelastic properties (Miranda *et al*, 2006). This technique was used to fabricate β -tricalcium phosphate (β -TCP) scaffolds (Saiz *et al*, 2007; Miranda *et al*, 2006).

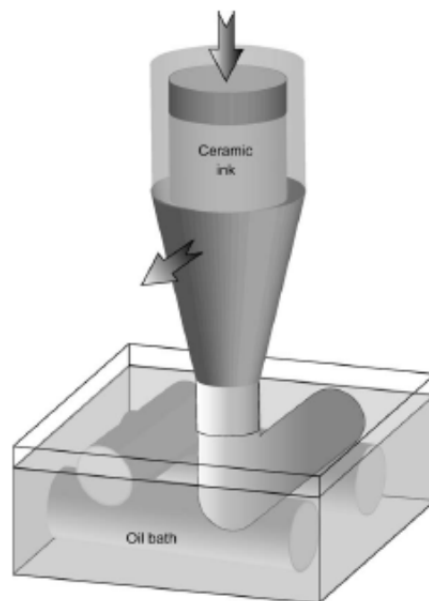


Figure 2.33 – Illustration of the robocasting fabrication process (Miranda *et al*, 2006).

Ang *et al* (2002) developed a rapid prototyping robotic dispersing (RPBOD) system using the same principle of the 3D bio-plotting system to produce chitosan-HA scaffolds. Solutions of chitosan-HA were extruded into a sodium hydroxide and ethanol medium to induce the precipitation of chitosan. The scaffolds were then hydrated, frozen and freeze-dried.

(d) Inkjet / Three-dimensional printing processes

Three-dimensional printing (3DP) was developed at the Massachusetts Institute of Technology (USA) by Sachs *et al* (1989). The process deposits a stream of micro-particles of a binder material over the surface of a powder bed, joining particles together where the object is to be formed (Figure 2.34). A piston lowers the powder bed, so that a new layer of powder can be spread over the surface of the previous layer and then selectively joined to it. *Therics Incorporated* applied the 3DP process to tissue engineering and developed the *TheriForm* process to fabricate drug delivery devices and scaffolds. Scaffolds can be tailored by varying the printing speed, the flow rate and drop position of the liquid water-based binder. 3DP operates at room temperature, allowing the use of a wide range of biomaterials.

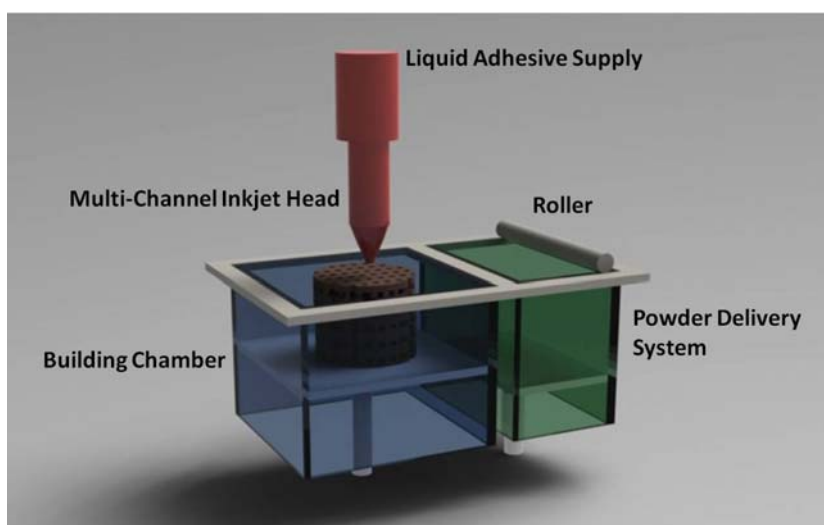


Figure 2.34 – 3D Printing process.

Kim *et al* (1998) employed 3DP with particulate leaching to create porous scaffolds, using polylactide-coglycolide (PLGA) powder mixed with salt particles and a suitable organic solvent. The salt particles were leached using distilled water. Cylindrical scaffolds measuring 8 mm (diameter) by 7 mm (height) with pore sizes of 45-150 μm and 60% porosity, were fabricated. Hepatocytes were successfully attached to the scaffolds.

The influence of pore size and porosity on cell adhesion and proliferation were investigated by Zeltinger *et al* (2001). Disc shaped poly(L-lactic acid) (L-PLA) scaffolds measuring 10 mm (diameter) by 2 mm (height) were produced through both 3DP and salt and leaching methods. The scaffolds were produced with two different porosities (75% and 90%) and four different pore size distributions (<38, 38-63, 63-106 and 106-150 μm), and tested with cell culture using canine dermal fibroblasts, vascular smooth muscle cells and microvascular epithelial cells.

Lam *et al* (2002) developed a blend of starch-based powder containing corn-starch (50%), dextran (30%) and gelatine (20%), bounded by printing distilled water. Cylindrical scaffolds were produced, measuring 12.5 mm (diameter) by 12.5 mm (height), and infiltrated with different amounts of a copolymer solution consisting of 75% L-PLA and 25% polycaprolactone in dichloromethane to improve their mechanical properties.

Leukers *et al* (2005) produced HA scaffolds with complex internal structures and high resolution. MC3T3-E1 cells were seeded on the scaffolds, and cultivated under static and dynamic setups. Dynamic cultivation was performed in perfusion containers with a flow rate of 18 $\mu\text{l}/\text{min}$. A histological evaluation was carried out to characterise the cell ingrowth process. It was observed that the dynamic cultivation method lead to a stronger population compared to the static cultivation method. Static cell culture led to multiple cell layers located on the surface of HA granules. Dynamic cells culture tends to grow in between the cavities of the granules. It was also found that cells proliferated deep into the structure, forming close contact to HA granules.

Sachlos *et al* (2003) used an indirect approach to produce collagen scaffolds with complex internal morphologies and macroscopic shapes by using a 3DP sacrificial mould. A dispersion of collagen was cast into the mould and frozen. The mould was then dissolved with ethanol, and the collagen scaffold was dried with liquid carbon dioxide. Further research by Taboas *et al* (2003), Limpanuphap and Derby

(2002) and Park *et al* (1998), also exploited the capabilities of 3DP for tissue engineering.

Ink-jet printing systems were used to print both aqueous solutions onto supports and cell within a scaffold (Saunders *et al*, 2004; Pardo *et al*, 2003). During the droplet formation process, the liquid material experiences shear rates close to 10^4 s^{-1} , and similar strains occurs during the impact (Saunders *et al*, 2004). Therefore, cells in suspension are subjected to large stresses and deformation. Nevertheless, ink-jet printing is a viable method for cell deposition and patterning (Saunders *et al*, 2004). Boland *et al* (2007) explored a cell and organ printing fabrication strategy to print cells and proteins within 3D hydrogel structures. Several examples of printed tissues, such as contractile cardiac hybrids, were developed. Alginate hydrogels were used as support structures. As indicated in Figure 2.35, endothelial cell attachment was observed. Filopodia can be seen at the leading edge of the cell, and lamellapodia at the trailing edge, suggesting cell migration into pores. It was postulated that local variation in the mechanical compliance of alginate structures induces cells to attach to the areas with greatest stiffness or highest stress. Since endothelial cells are also known to grow well on surfaces, it is not surprising to observe cell attachment on the inner surfaces of the alginate pores. Nevertheless, the exact mechanism of cell attachment to alginate structures is still unknown and requires further research.

Similar procedures were used by Mironov *et al* (2003) and Yan *et al* (2003b), that developed the concept of cell printing (Figure 2.36). This process prints gels, single cells and cell aggregates offering a possible solution for organ printing. An analogous process, called Alginate-based Rapid Prototyping, was developed at the Polytechnic Institute of Leiria (Figure 2.37). This process produces alginate solid structures, by extruding a solution of sodium alginate, mixed with a solution of calcium chloride, providing a temporary support for the seeded cells in culture (Bártolo, 2006; Bártolo *et al*, 2004). Alginate is an anionic copolymer composed of homopolymeric regions of 1,4-linked β -D-mannuronic (M blocks) and α -L-guluronic acid (G blocks), interspersed with regions of alternating structure. Gelation occurs

when divalent ions take part in the interchain ionic binding between G-blocks in the polymer chain, giving rise to a three dimensional network (Figure 2.38). Such binding zones between the G-blocks are often referred to as “egg boxes”. These ions act as cross-linkers stabilising alginate chains to form a gel structure, which contains cross-linked chains spread with more freely movable chains that bind and entrap large quantities of water. The gelification process is characterised by a re-organisation of the gel network, accompanied by the expulsion of water. Gels containing M-rich alginate are softer and more fragile, and may also have lower porosity, due to the lower binding strength between the polymer chains and to the higher flexibility of the molecules. The gelification process is highly dependent upon diffusion of gelification ions into the polymer network. Transmittancy, swelling and viscoelasticity of alginate structures are highly affected by the M/G ratio.

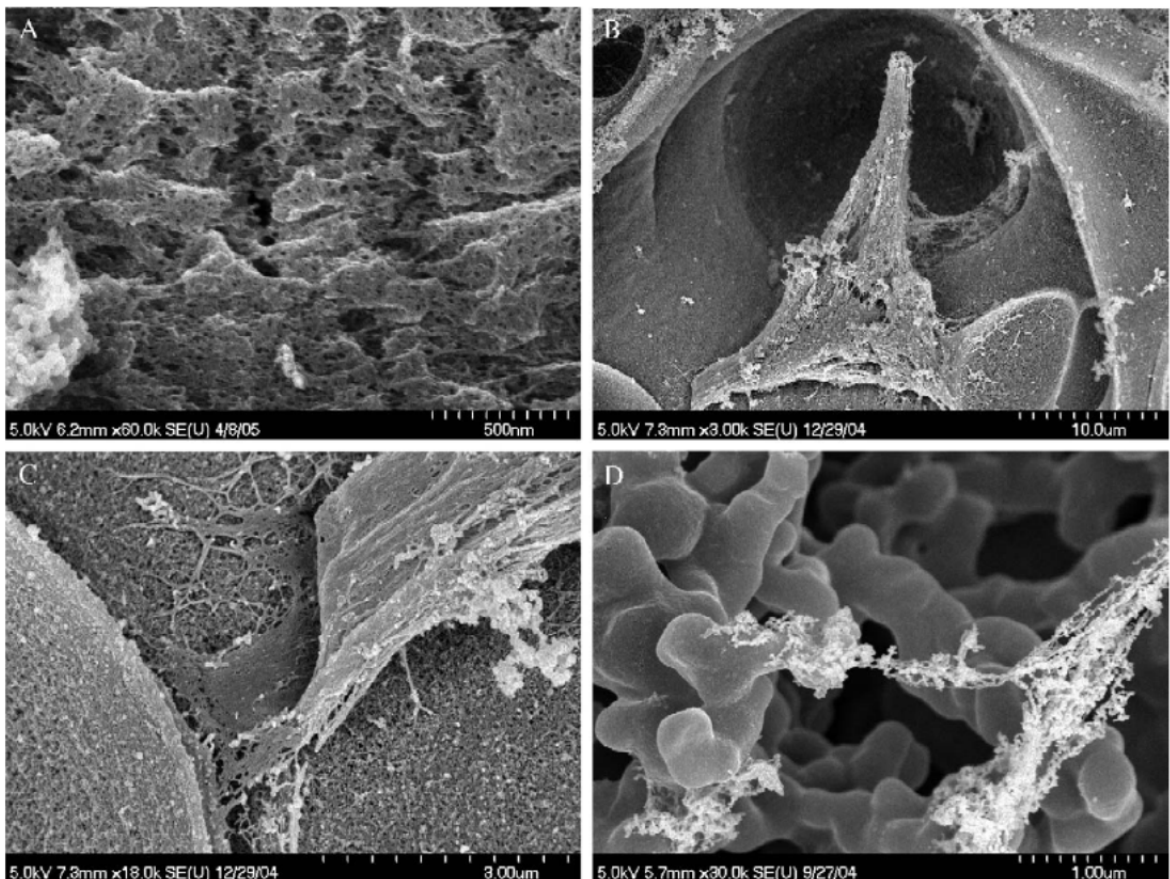


Figure 2.35 – SEM micrographs of endothelial cells attached to alginate structure (Boland *et al*, 2007). A) Wall with nanosize pores. B) An endothelial cell attach inside an alginate structure. C) Filopodia and lamellapodia interacting with the alginate material. D) Interactions between fibrous secretions and alginate.

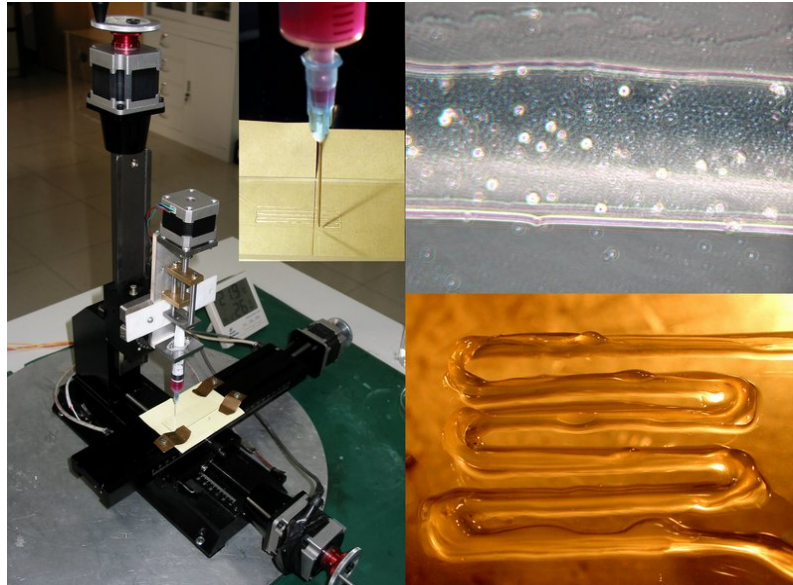


Figure 2.36 – Cell-jet printing with cell-gel mixture printed structures (Yan *et al*, 2003b).

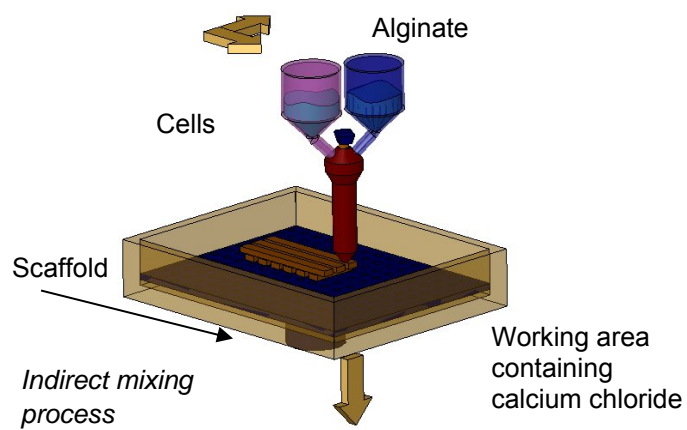


Figure 2.37 – Scaffold fabrication through the alginate-based rapid prototyping process.

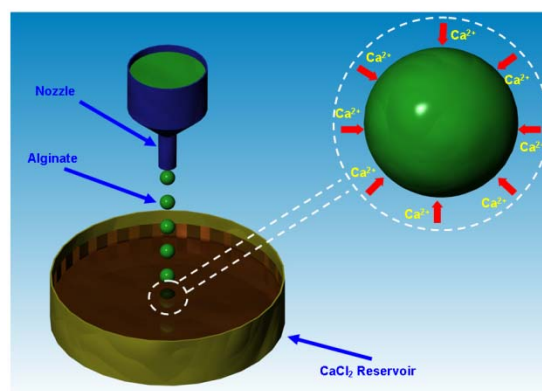


Figure 2.38 – Gelation of Alginate in a CaCl_2 solution.

(e) *Advantages and Disadvantages of Additive Manufacturing*

Additive biomanufacturing has been established as a viable set of processes to produce three-dimensional scaffolds of various materials, including polymers, hydrogels and ceramics. These technologies have a great potential, offering a high degree of freedom for tissue engineering for either the design of scaffolds (pore size, pore geometry, orientation, interconnectivity, etc.) or its fabrication. Scaffold fabrication, using these techniques, allows the possibility of indirectly controlling macroscopic properties, such as the bulk mechanical properties and the permeability for nutrient transport considerations. Several materials can also be used, enabling the production of both soft and hard scaffolds. These characteristics can enhance the fabrication of biomimetic scaffolds, functionally graded scaffolds and scaffolds for complex biomechanical applications. The emergence of these technologies in tissue engineering also increases the need for adaptation of the existing standards. Future developments will possibly lead to establishing additive biomanufacturing as a key tool for tissue reconstruction and regeneration.

Scaffold porosity, pore and filament size achieved by additive biomanufacturing techniques, are listed in Table 2.1. The main advantages and limitations of additive biomanufacturing scaffolds for tissue engineering applications are indicated in Table 2.2. Table 2.3 shows the achieved mechanical properties of some biomanufactured scaffolds.

Table 2.1 – Scaffold porosity values (Leong *et al*, 2008).

Process	Achieved Porosity	Pore Size	Filament Size
3DF	70 % - 87 %	-	-
3DP	40 % - 90 %	45-150 µm	-
FDM	21 % - 77 %	160-700 µm	250-370 µm
SLA	26 % - 90 %	366 µm	-
SLS	37.5 % - 74 %	-	-

Table 2.2 – Characteristics of rapid prototyping scaffolds.

Process	Advantages
SLA	Relatively easy to achieve small feature
SLS	Relatively higher mechanical strength and solvent free
FDM	No material trapped in the scaffold and solvent free
3DP	Low heat effect on raw powder; easy process and low cost
Bio-plotting	Large variety of materials for both soft and hard tissues
Process	Limitations
SLA	Limited by the development of photo-polymerisable, biocompatible and biodegradable materials; currently limited to reactive and mostly toxic resins
SLS	Powder material trapped in small inner holes can be difficult to remove; high temperatures in the chamber
FDM	High heat effect on raw material; limited geometrical complexity
3DP	Materials trapped in small inner holes; low mechanical properties
Bio-plotting	Low geometrical complexity

 Table 2.3 – List of achieved mechanical properties (Leong *et al*, 2008).

Process	Biomaterials	Mechanical Properties
3DF	PEGT-PBT	Dynamic compressive modulus:
		4.33 MPa
3DP	Corn-starch, dextran and gelatine	Compressive modulus:
		0.059-0.102 MPa
	HA (followed by sintering)	Compressive strength: up to 22 MPa
	Poly(urethane)	Young's modulus: 580 MPa
FDM	PCL	Compressive modulus: 4-77 MPa
		Compressive strength: 2.4-20.2 MPa
	Alumina (indirect fabrication)	Compressive strength: 50 MPa
SLS	PCL	Compressive modulus: 52-67 MPa
	PCL – HA	Compressive modulus: 33-102 MPa

Chapter 3 – Scaffold Design

3.1. Computational Design in Tissue Engineering

A temporary three-dimensional scaffold mimicking the physiological functions of the native ECM is vital for maintaining the cells' ability to express their native differentiated phenotypes. An optimal scaffold design will promote cell proliferation and cell-specific matrix production that would eventually take over the supporting role of the degrading scaffold (Leong *et al*, 2008). In addition to comply with the listed biological and physical requirements (see Section 1.1.2), an optimum scaffold must also have functional and anatomical requirements, similar to the functional gradient of the host tissue or organ. The external geometry and size of the scaffold must be the same of the natural tissue, in order to anchor the scaffold onto the defected location (Leong *et al*, 2008; Sun *et al*, 2005).

In the past years, several tools have been developed to support the design of scaffolds for tissue engineering, such as the *Computer-Aided Tissue Engineering (CATE)* developed by Sun *et al* (2004a; 2004b; Sun and Lal; 2002) and the *Computer Aided System for Tissue Scaffolds (CASTS)* developed by Naing *et al* (2008; 2005). These computational tools (Figure 3.1) integrate different routines and systems to support both the design and fabrication of scaffolds. The Centre for Rapid and Sustainable Product Development developed a computational tool called *Expert System for Medical Applications (ESYSMA)* enabling the selection of appropriate materials for medical applications (Moura *et al*, 2010). Figure 3.1 explains how the most relevant advanced engineering systems can be integrated in order to aid the design and fabrication process for tissue engineering scaffolds. These systems integrate several tools and systems ranging from the design to engineering to the biomanufacturing of the structures, to optimize scaffold's performance.

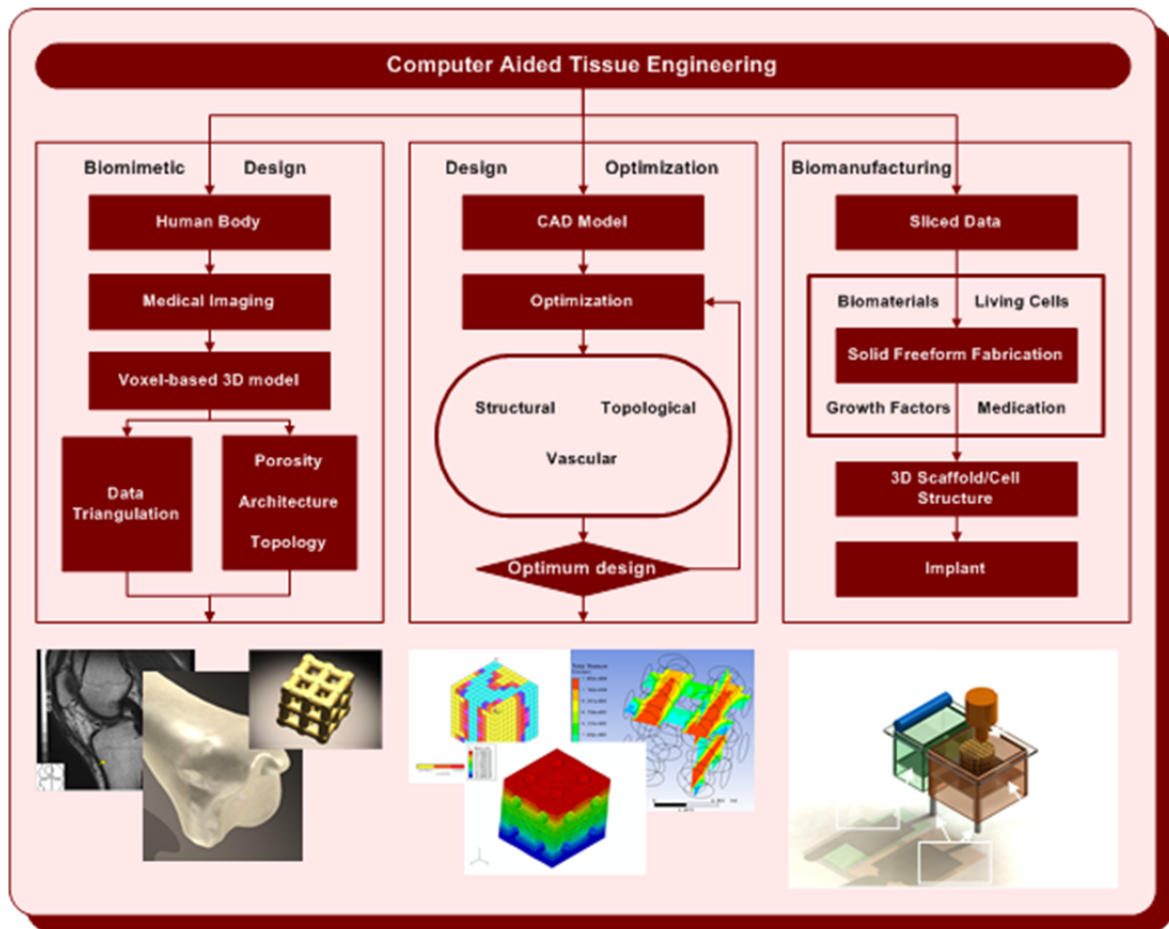


Figure 3.1 – Computer Aided Tissue Engineering.

This *ESYSMA* system (Figure 3.1) is structured into four main levels:

- Level 1: Automatic identification of the appropriated biomaterial for a certain application;
- Level 2: Automatic definition of the most appropriate geometry, porosity and pore topology of scaffolds for a certain application;
- Level 3: Automatic definition of the growth factor to be used in a certain application;
- Level 4: Automatic identification of the manufacturing technology regarding or not the encapsulation of cells.

The material's selection for a specific medical application is performed on the requirements of the desired material's performance based on a hierarchical knowledge structure, combining Case-Based and Ruled-Based Reasoning. To identify the most adequate material, a set of questions and the corresponding answers must be carried out concerning issues such as:

- the biodegradability of the material;
- the permeability to water;
- its absorption ability;
- whether it will be in contact with organic fluids;
- whether it will need to sustain a structural application;
- whether it has to be environmentally responsive to changes of pH and/or temperature, etc.

An extensive database of biomaterials was also developed and integrated into the developed system. This computational system can assist in the selection process of an appropriate biomaterial for a given medical application.

3.2. Computational Scaffold Modelling

The design of optimised scaffolds for tissue engineering is a key topic of research, as the complex macro- and micro- architectures required for a scaffold depends on the mechanical properties, physical and molecular queues of the surrounding tissue, at the defect site. One way to achieve such hierarchical designs is to create a library of unit cells (the scaffold is assumed to be a “Lego” structure), which can be assembled through a specific computational tool (Bucklen *et al*, 2008; Naing *et al*, 2008; Adachi, 2006; Hollister, 2005; Cheah *et al*, 2004).

The modelling of scaffolds for tissue engineering applications can be grouped into four main domains, as illustrated in Figure 3.2:

1. The analytical methods contain empirical relationships between structural parameters and mechanical properties. They only provide an estimate of the global mechanical properties.
2. In the CAD-based modelling method, the porous structure is approximated using a 3D repetition of building blocks (called “unit cells”) of simply geometry. The unit cells can be generated by Boolean operations. Simple CAD software tools may be used in this process.
3. The CT-based modelling uses an image-based approach, where a 3D image of a structure serves as a basis for the mesh generation.

Several existing computational tools that can be used to process medical imaging data and obtain the 3D data of the desired anatomic model, such as Invesalius, Mimics, 3D-Doctor, Anatomics.

Invesalius is a free medical software used to reconstruct structures of the human body. It is based on two-dimensional images, acquired by Computed tomography or Magnetic resonance imaging equipments. The software

generates virtual three-dimensional models correspondent to anatomical parts of the human body. After reconstructing three-dimensionally the DICOM images, the software allows the generation of STL files. These files can then be used for additive fabrication. Invesalius was developed at Renato Archer Technology of Information Centre (CTI), a research institute of the Brazilian Science and Technology Centre.

Mimics is another medical imaging processing software package for 3D design and modelling, developed by Materialise NV, Belgium. Mimics generates and modifies surface 3D models from stacked image data such as Computed Tomography (CT), Confocal Microscopy, Micro CT, and Magnetic Resonance Imaging (MRI) through image segmentation. The 3D files are represented in the STL format. The most common input format is DICOM, but other image formats such as TIFF, JPEG, BMP and Raw are also compatible. The output file formats differ, depending on the subsequent application: common 3D output formats include STL, VRML, PLY and DXF. The 3D files can also be optimized for FEA or CFD, and then exported to Abaqus in INP format, to Ansys in INP, CDB and MSH format, to Nastran in OUT, NAS and BDF format, and to Comsol in MPHTXT format. The files can also be exported in IGES format or as Point Cloud Data for Computer-aided design.

4. The Homogenisation theory is a multi-level approach, where the micro-level model represents the exact micro-architecture of the structure, while the macro-level model is a continuum model of the whole structure.

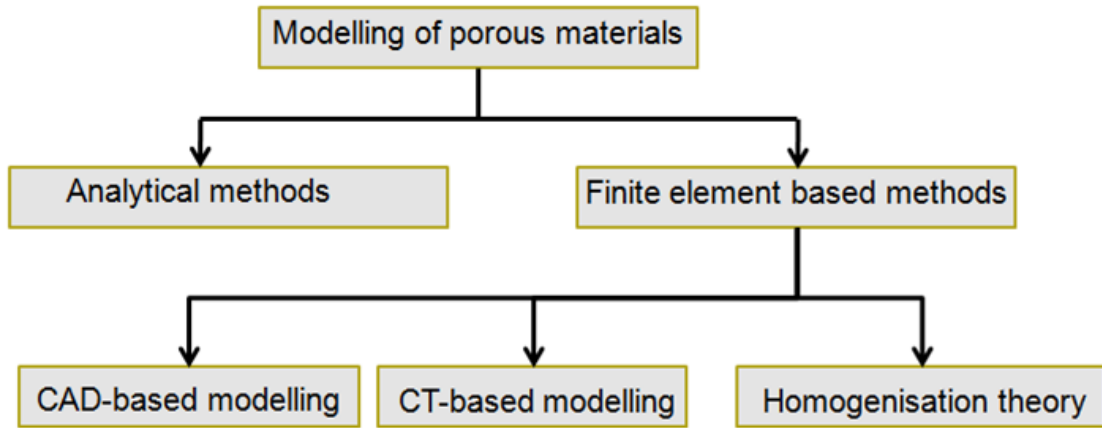


Figure 3.2 – Modelling Structure of scaffolds for tissue engineering applications.

The CT-based modelling and the Homogenisation theory are very complex methods. These two methods need powerful computers in order to undergo the modelling and numerical calculations, due to the high number elements within the polygon meshes. In order to overcome the existing limitations of these methods, a CAD-based modelling strategy was adopted for this research work (Figure 3.3). Thus CAD-based modelling approach uses finite element methods for the numerical simulation of both the mechanical and vascular behaviour and the topological optimisation, as well analytical methods to compare experimental results with numerical data.

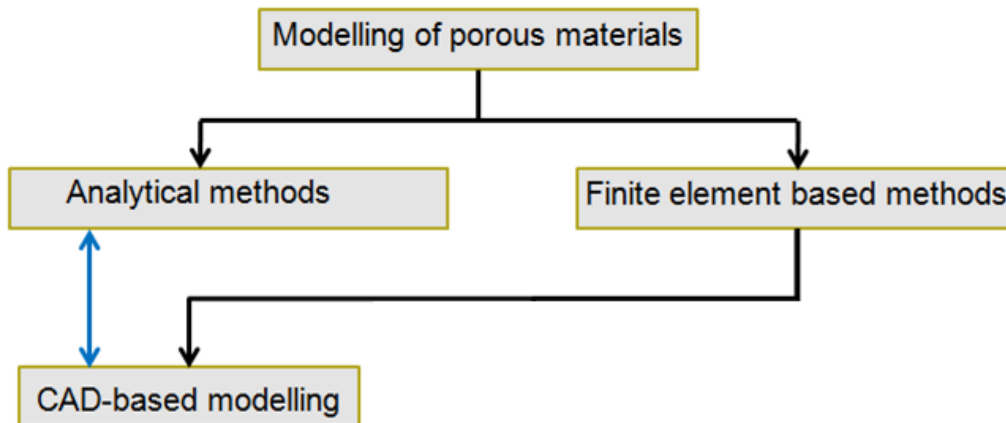


Figure 3.3 – Modelling Structure of scaffolds for tissue engineering applications.

3.3. Computer Aided Design of Scaffolds (CADS)

The prediction of the effective optimal properties of tissue scaffolds is very important for tissue engineering applications, to obtain the mechanical, vascular or topological properties. To implement the proposed strategy, already defined in the previous Section (3.2), a computational tool was developed, named *Computer-Aided Design of Scaffolds (CADS)*, enabling to quantify the structural heterogeneity, and the mechanical and vascular properties of a scaffold with a designed macro and microstructure.

CADS comprises 4 main domains for the modelling, simulation and optimisation of scaffolds:

- The first domain concerns the scaffold modelling, where two types of scaffold units can be defined, namely non-triple and triple periodic minimal surfaces.
- The second domain regards the biomaterial properties for hard or soft tissue applications. In this case, the materials considered can be characterized by the *ESYSMA* material database. After this material selection process, the selected material's properties are introduced in the *CADS* platform for the numerical calculations.
- The third domain is concerned with the material behaviour. Two analytical models are considered, namely linear and non-linear elasticity.
- The fourth domain corresponds to the type of analysis to be performed: mechanical, vascular or topological optimisation.

Figure 3.4 illustrates the four domains and its contents within the *CADS* software.

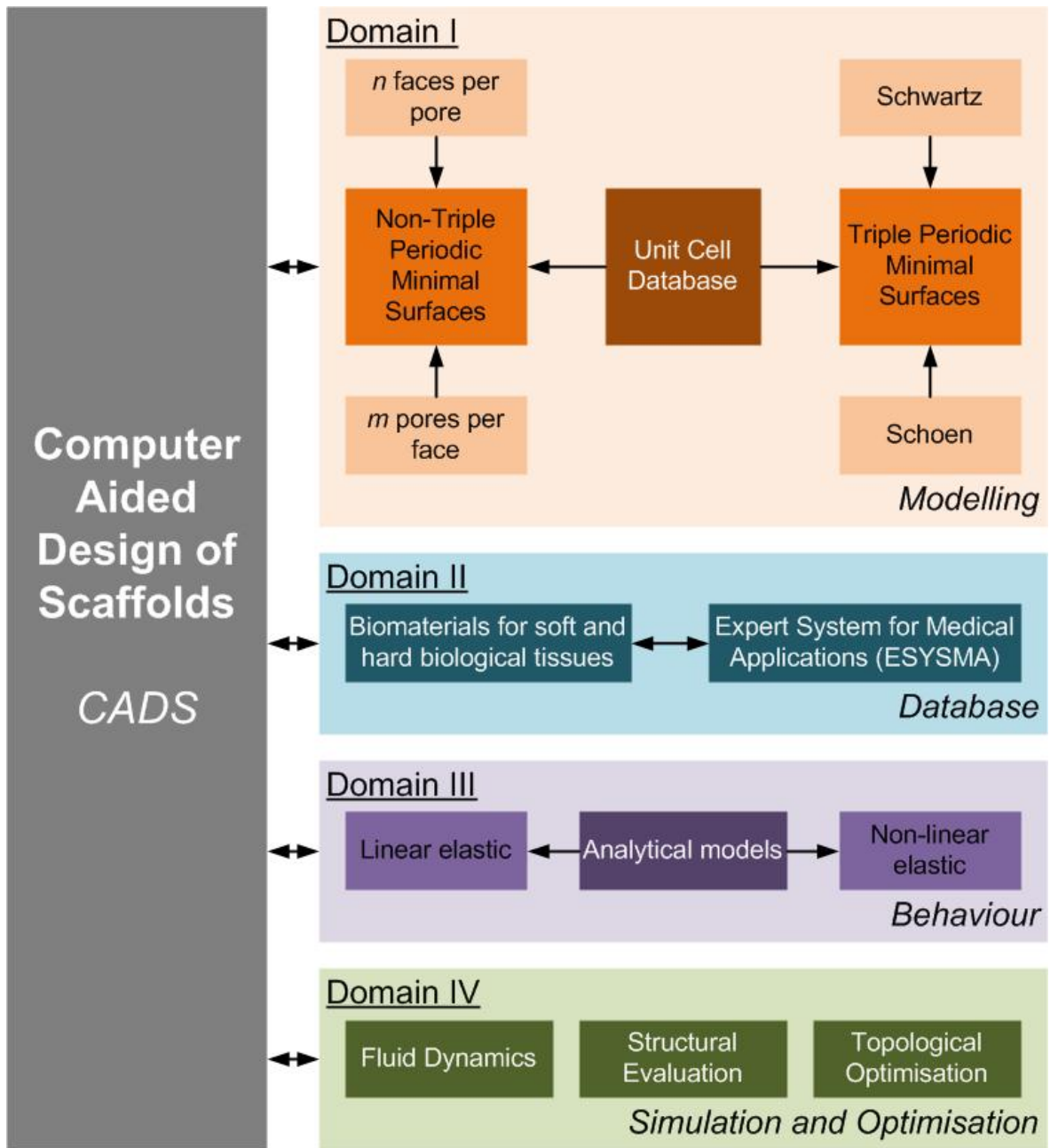


Figure 3.4 – Structure of CADs.

3.4. Geometric Scaffold Modelling

In this research work, scaffolds are considered as a LEGO structure formed by an association of small elementary units or blocks. Two types of elementary scaffold units were considered:

- Non-triple periodic minimal surfaces;
- Triple periodic minimal surfaces.

3.4.1. Non-Triple Periodic Minimal Surfaces

Figure 3.5 illustrates elementary scaffold units of the so-called “*n faces per pore*” block family, while Figure 3.6 represents elementary scaffold units of the so-called “*m pores per face*” block family. The “*n faces per pore*” block family are elements consisting of 4 pores per face, in which the number of faces per pore varies from 4 faces per pore “4F”, to 8 faces “8F”, 12 faces “12F” and infinite faces (circular pores “CF”). The “*m pores per face*” block family are elements consisting of multiple pores per face within each unit, while maintaining a specific scaffold’s porosity.

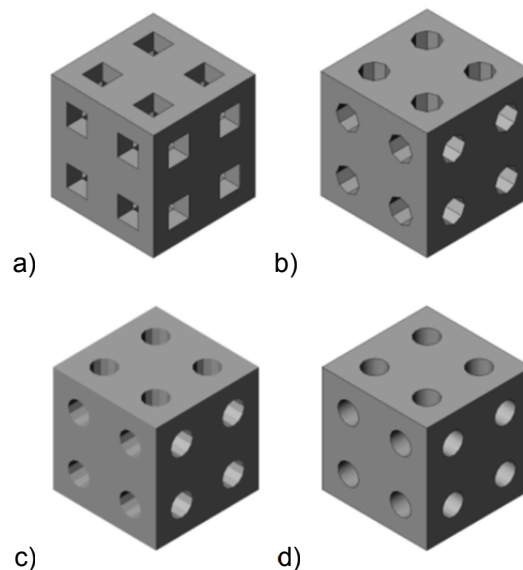


Figure 3.5 – The *n faces pore* blocks family classified according to the number of faces per pore. a) 4 face (4F) pore unit, b) 8F unit, c) 12F unit and d) circular (CF) unit.

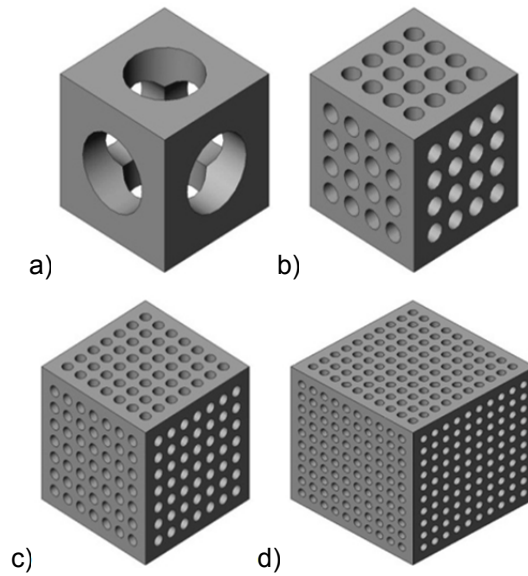


Figure 3.6 – The *m pores per face* blocks family classified according to the number of pores per face. Only 4 of the 10 geometries with circular pores are represented and all with 50 % porosity. a) 1 pore (1P) unit, b) 16P unit, c) 49P unit and d) 100P unit.

Scaffold units with rectangular pores were produced in PCL for the mechanical evaluation. Rectangular prisms measuring 30 x 30 x 8 mm were initially designed with a 0°/90°, using CAD software. Scaffold units were produced using the Bioextruder system (see Section 2.7) with different pore sizes. Figure 3.7 shows the main design parameters considered, while Table 3.1 indicates the values of both design and processing parameters. An example of a PCL unit is illustrated in Figure 3.8.

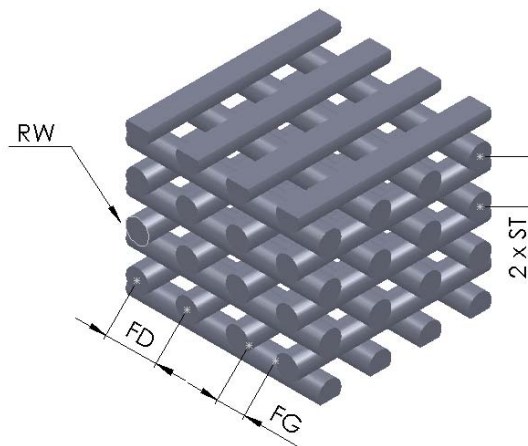


Figure 3.7 – Representation of the main design parameters.

Table 3.1 – Geometric parameters for the design of the scaffolds.

Parameters	Values		
Filament Distance (FD, μm)	650	550	450
Filament Gap (FG, μm)	350	250	150
ST: Slice Thickness (ST, μm)	280		
Filament Width (FW, μm)	300		
Deposition velocity (DV, mm/s)	7		
Screw rotation velocity (SRV, rpm)	84		
Heating temperature (HT, $^{\circ}\text{C}$)	80		

Figure 3.8 – Poly(ϵ -caprolactone) scaffold with a 0/90 $^{\circ}$ lay-down pattern.

Produced scaffolds were submitted to compression tests. The constructs were cut into block-shape specimens characterized by the following dimensions: 5 x 5 x 8 mm (length (l) x width (w) x height (h_0)). All tests were carried out in dry state at a rate of 1 mm/min up to a strain value of 0.5, using an Ingstrom 5566 testing system equipped with a 1 KN load cell. Five compression tests were considered for each group of design parameters.¹

¹ The experimental compressive data was performed by Prof. António Glória from the University of Naples in Italy, through a research project with Joana Ferreira, Marco Domingos and Paulo Bártole from the Centre for Rapid and Sustainable Product Development of the Polytechnic Institute of Leiria.

The “apparent” stress was evaluated as the force F , measured through the load cell divided by the total area of the apparent cross section of the scaffold ($A = l \times w$):

$$\sigma = \frac{F}{A} \quad (3.1)$$

while the strain ε was defined as the ratio between the scaffold height variation Δh (i.e. the vertical displacement equal to the cross head displacement) and the scaffold initial height h_0 :

$$\varepsilon = \frac{\Delta h}{h_0} \quad (3.2)$$

The Figures 3.9, 3.10 and 3.11 illustrate the compressive stress-strain curves obtained. The results show that the 3D scaffold’s mechanical behaviour is similar to the flexible foam behaviour (Gibson, 2005).

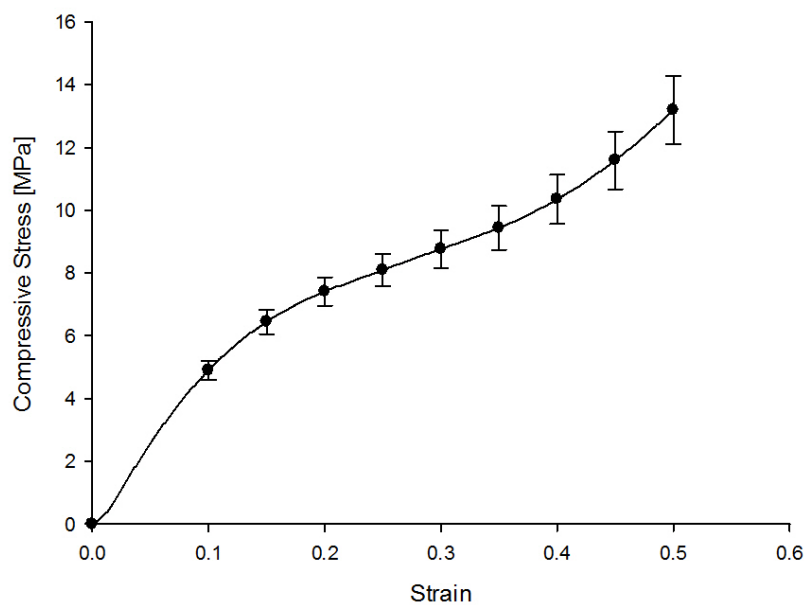


Figure 3.9 – Compression Stress-Strain curves for the five samples with a pore size of 450 μm .

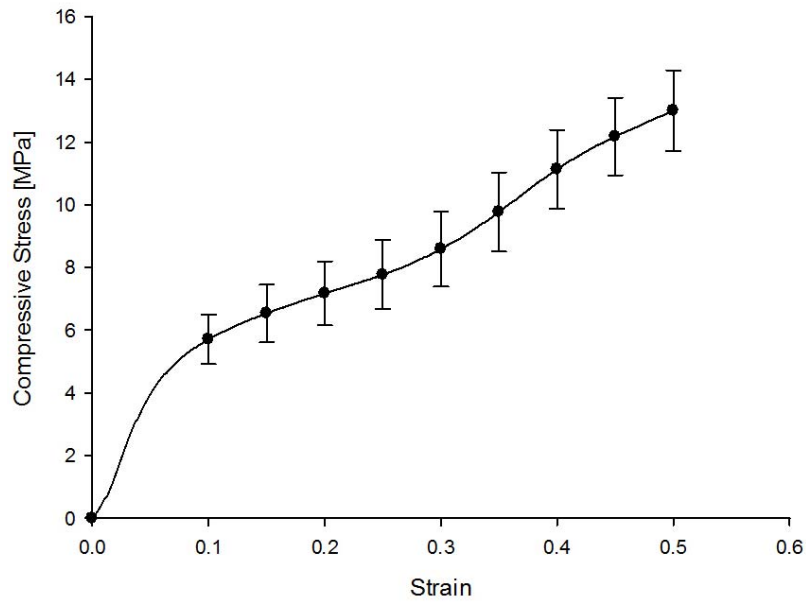


Figure 3.10 – Compression Stress-Strain curves for the five samples with a pore size of 550 μm .

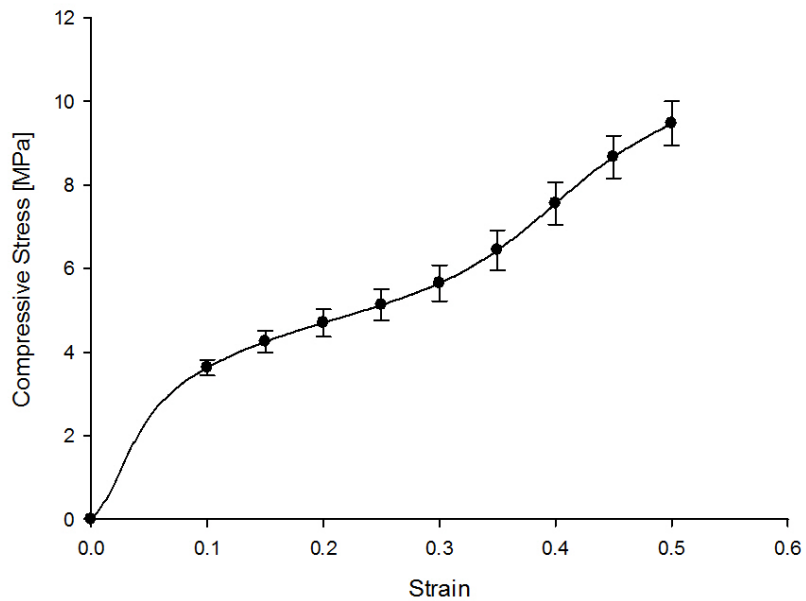


Figure 3.11 – Compression Stress-Strain curves for the five samples with a pore size of 650 μm .

After obtaining the stress-strain curves for each test sample, an average stress-strain curve was calculated for each pore size. Figures 3.9, 3.10 and 3.11 shows average stress-strain curve and its deviation for each pore size. Figure 3.12 shows a comparison of all the average stress-strain behaviours obtained for the scaffolds tested in this research work.

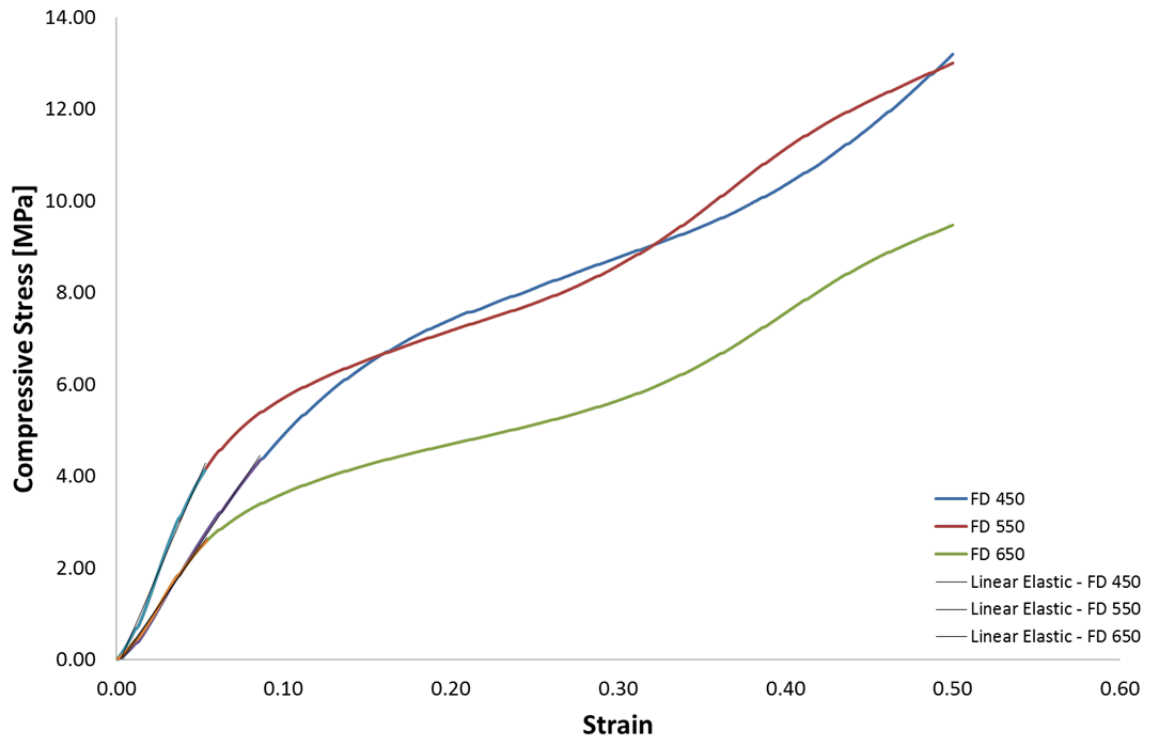


Figure 3.12 – Average compression stress-strain results with the linear elastic curve for each pore size.

Once determined the average stress-strain curves for each pore size, the compressive bulk modulus and the compressive tensile stress were evaluated. The compressive tensile stress corresponds to both the limit value of the scaffold's elastic behaviour and the starting point of the scaffold's plastic behaviour. The Maximum Tensile Stress, which represents the tensile cut-off stress in the numerical simulations, was also determined. The obtained data can be observed in Table 3.2.

Table 3.2 – Mechanical compressive properties of the extruded structures for different pore sizes.

Pore Size [μm]	Bulk Modulus [MPa]	Tensile Stress [MPa]	Maximum Stress [MPa]
450	51.051 ± 3.206	4.358 ± 0.273	13.200 ± 1.079
550	77.385 ± 10.678	4.140 ± 0.571	13.003 ± 1.293
660	47.568 ± 5.507	2.594 ± 0.308	9.473 ± 0.526

3.4.2. Triple Periodic Minimal Surfaces

Minimal periodic surfaces are the most studied hyperbolic surfaces. If a minimal surface has space group symmetry, it is periodic in three independent directions, so it is called Triple Periodic Minimal Surfaces (TPMS) (Qi and Wang, 2009; Jung *et al*, 2007; Wang, 2007; Gandy *et al*, 2001; Wohlgemuth *et al*, 2001).

TPMS are also biomimetic surfaces describing several natural shapes, such as lyotropic liquid crystals, zeolite sodalite crystal structures, diblock polymers, hyperbolic membranes (prolamellar structure of chloroplasts in plants), echinoderm plates (interface between the inorganic crystalline and organic amorphous matter in the skeleton), cubosomes and certain cell membranes (Larsson *et al*, 2003; Hyde, 1996; Andersson, 1983; Scriven, 1976).

A periodic surface can be defined as:

$$\phi(r) = \sum_{k=1}^K A_k \cos[2\pi(h_k \cdot r)/\lambda_k + p_k] = C \quad (3.3)$$

where r is the location vector in Euclidean space, h_k is the k^{th} lattice vector in reciprocal space, A_k is the magnitude factor, λ_k is the wavelength of periods, p_k is the phase shift, and C is a constant. Specific periodic structures and phases can be constructed based on this implicit form (Qi and Wang, 2009; Wang, 2007).

In the case of the TPMS, the Weierstrass formula describes their parametric form in the following way:

$$\begin{cases} x = \operatorname{Re} \int_{\omega_0}^{\omega_1} e^{i\theta} (1 - \omega^2) R(\omega) d\omega \\ x = \operatorname{Im} \int_{\omega_0}^{\omega_1} e^{i\theta} (1 + \omega^2) R(\omega) d\omega \\ x = -\operatorname{Re} \int_{\omega_0}^{\omega_1} e^{i\theta} (2\omega) R(\omega) d\omega \end{cases} \quad (3.4)$$

where ω is a complex variable, θ is the so-called Bonnet angle, and $R(\omega)$ is the function that varies for different surfaces.

From a multi-dimensional control parameter space view, the geometric shape of a periodic surface is specified by a periodic vector, defined by the following equation (Qi and Wang, 2009; Wang, 2007):

$$V = \langle A, H, P, \Lambda \rangle_{K \times 6} \quad (3.5)$$

where:

$$A = [A_k]_{K \times 1}$$

$$H = [h_k]_{K \times 3}$$

$$P = [p_k]_{K \times 1}$$

$$\Lambda = [\lambda_k]_{K \times 1}$$

are row concatenations of magnitudes, reciprocal lattice matrix, phases, and period lengths respectively.

Two types of parametric hyperbolic surfaces are considered:

- Schwartz surfaces;
- Schoen surfaces.

The effect of two relevant design parameters is also investigated:

- Thickness
- Radius

(a) *Schwartz surfaces scaffold elements*

A Schwartz periodic surface (Figure 3.13) is described by the following equation (Qi and Wang, 2009; Wang, 2007):

$$\emptyset(r) = A_p [\cos(2\pi x/\lambda_x) + \cos(2\pi y/\lambda_y) + \cos(2\pi z/\lambda_z)] = 0 \quad (3.6)$$

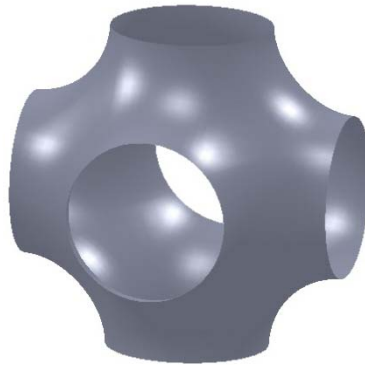


Figure 3.13 – Schwartz TPMS primitive.

The concatenations of the magnitudes vector, reciprocal lattice matrix and phase vector are given by the following equations (Qi and Wang, 2009; Wang, 2007):

$$\begin{aligned} A^T &= [1 \quad 1 \quad 1] \\ H^T &= \begin{bmatrix} 1 & 0 & 0 \\ 0 & 1 & 0 \\ 0 & 0 & 1 \end{bmatrix} \\ P^T &= [0 \quad 0 \quad 0] \end{aligned} \quad (3.7)$$

Figures 3.14 and 3.15 illustrate the effect of both thickness and radius design parameters on the Schwartz scaffold units.

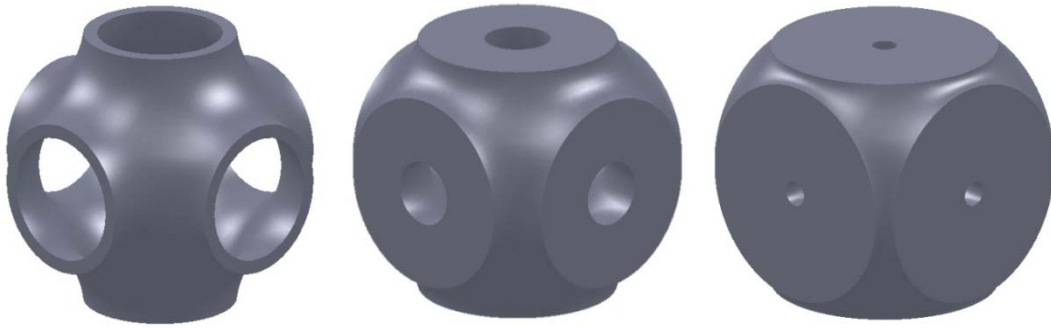


Figure 3.14 – P-minimal surfaces obtained through thickness variation with constant surface radius.



Figure 3.15 – P-minimal surfaces obtained through radius variation with constant surface thickness.

(b) Schoen surfaces scaffold elements

A Schoen periodic surface (Figure 3.16) is given by the following equation (Qi and Wang, 2009; Wang, 2007):

$$\Phi(r) = A_1 \begin{bmatrix} 2\cos(2\pi x/\lambda_x) \cos(2\pi y/\lambda_y) + 2\cos(2\pi y/\lambda_y) \cos(2\pi z/\lambda_z) \\ 2\cos(2\pi z/\lambda_z) \cos(2\pi x/\lambda_x) \\ -\cos(4\pi x/\lambda_x) - \cos(4\pi y/\lambda_y) - \cos(4\pi z/\lambda_z) \end{bmatrix} = 0 \quad (3.8)$$

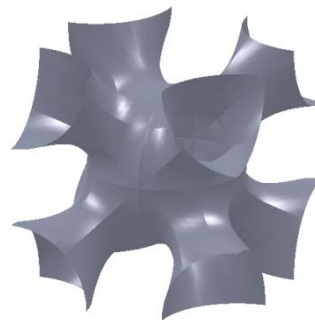


Figure 3.16 – Schoen TPMS primitive.

The concatenations of magnitudes vector, reciprocal lattice matrix and phase vector are given by the following equations (Qi and Wang, 2009; Wang, 2007):

$$\begin{aligned}
 A^T &= [1 \quad 1 \quad 1 \quad 1 \quad 1 \quad 1 \quad -1 \quad -1 \quad -1] \\
 H^T &= \begin{bmatrix} 1 & 1 & 0 & 0 & 1 & 1 & 2 & 0 & 0 \\ -1 & 1 & 1 & 1 & 0 & 0 & 0 & 2 & 0 \\ 0 & 0 & -1 & 1 & -1 & 1 & 0 & 0 & 2 \end{bmatrix} \\
 P^T &= [0 \quad 0 \quad 0 \quad 0 \quad 0 \quad 0 \quad 0 \quad 0 \quad 0]
 \end{aligned}
 \tag{3.9}$$

Figures 3.17 and 3.18 illustrate the effect of both thickness and radius design parameters on the Schoen scaffold units.

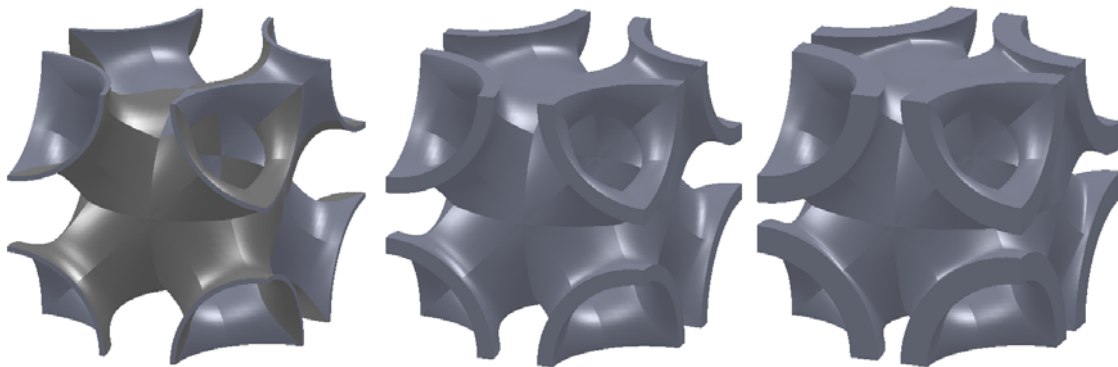


Figure 3.17 – P-minimal surfaces obtained through thickness variation with constant surface radius.

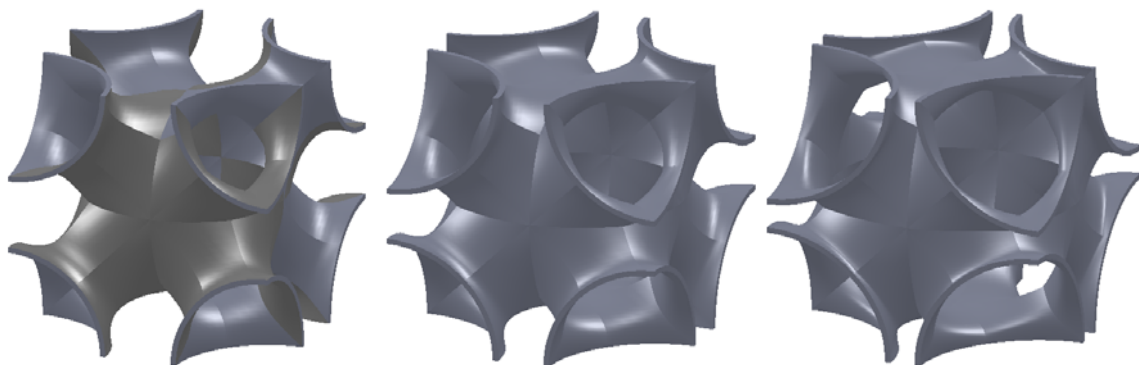


Figure 3.18 – P-minimal surfaces obtained through radius variation with constant surface thickness.

Schwartz and Schoen primitives can be easily manipulated from a computational view, through operations like union, difference, intersection, modulation, convolution, etc. Figure 3.19 illustrates the Boolean operations by the addition of

the basic units into an arbitrary unit with thickness variation, resulting in a scaffold with a thickness gradient. Scaffolds composed of Schwartz and Schoen basic units were produced using an extrusion based system as indicated in Figure 3.20.

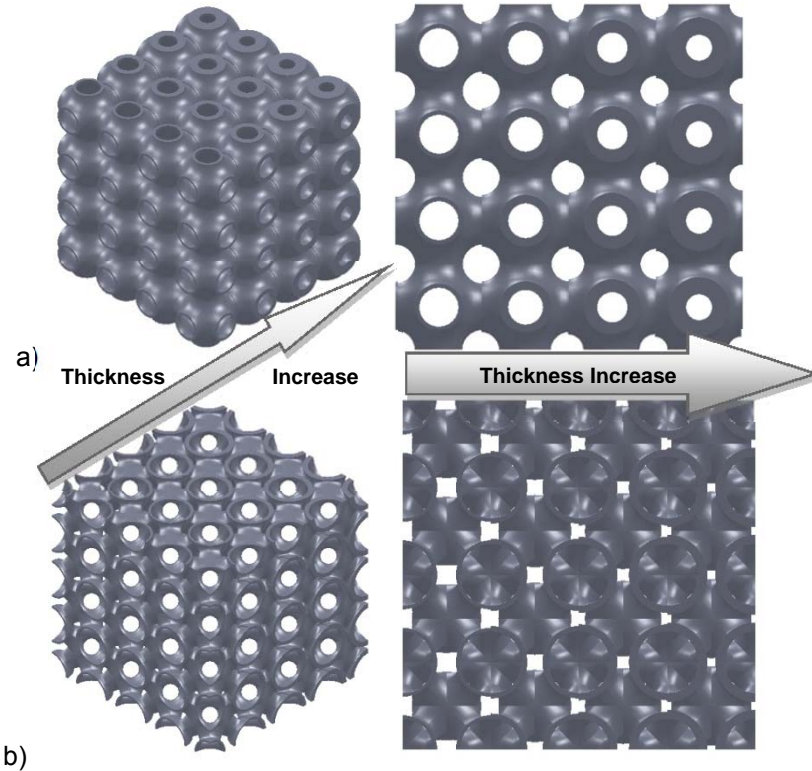


Figure 3.19 – CAD models illustrating thickness gradient within the scaffold structures for the a) Schwartz and b) Schoen geometries.

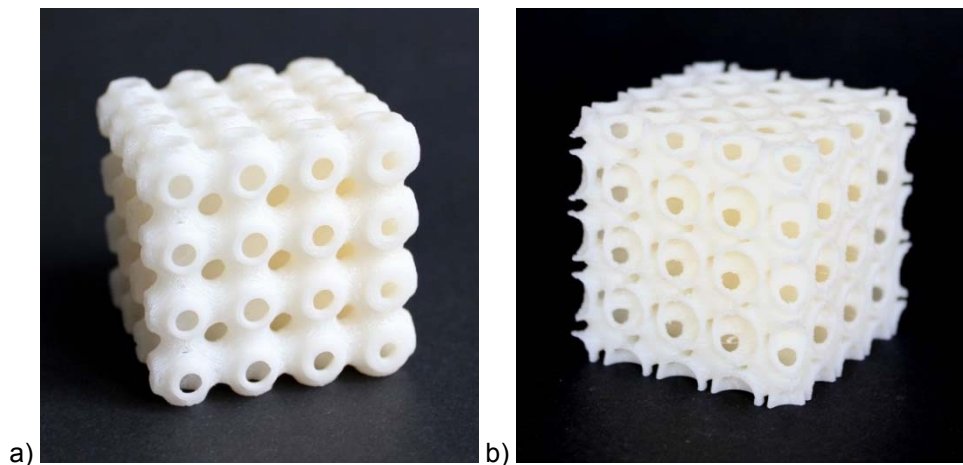


Figure 3.20 – Physical models of a) Schwartz and b) Schoen geometries produced through extrusion-based additive manufacturing.

Chapter 4 – Structural Analysis of Scaffolds for Tissue Engineering

4.1. Mechanical Behaviour of Scaffolds for Tissue Engineering

It is well known that tissues grow and remodel in response to changes in mechanical forces (Wang and Thampatty, 2006), and a typical example is bone, which changes its shape, density, and stiffness when the mechanical loading conditions are altered (Turner and Pavalko, 1998; Mullender *et al*, 2004). Similarly, blood vessels remodel themselves in response to altered blood pressure and shear stress (Owens, 1996; Williams, 1998). On the other hand, the mechanical forces play a fundamental role in the regulation of cell functions, including gene induction, protein synthesis, cell growth, death, and differentiation, which are essential to maintain tissue homeostasis. Abnormal mechanical loading conditions alter cellular function and change the structure and composition of the ECM, eventually leading to tissue or organ pathologies such as osteoporosis, osteoarthritis, tendinopathy, atherosclerosis, and fibrosis in the bone, cartilage, tendon, vessels, heart, lung, and skin (Bag *et al*, 2004; Borer *et al*, 2004; Eckes and Krieg, 2004; Lammerding *et al*, 2004; Ingber, 2003; Riley *et al*, 2002; Ireland *et al*, 2001; Grodzinsky *et al*, 2000; Chicurel *et al*, 1998; Ross, 1986).

The mechanical stimulation induced on the cells, to increase their proliferation and differentiation or its biological process, which is regulated by mechanical signals, is designated as Mechanobiology (Chen *et al*, 2011). This domain has been receiving increasing attention over the recent years (van der Meulen and Huiskes, 2002; Huiskes *et al*, 2000). It is believed that biophysical stimulus play a key role in regulating the tissue growth and remodelling process of bones (Jacobs *et al*, 2010; Kelly and Jacobs, 2010), during the fracture healing process (Kelly and Prendergast, 2005; Carter *et al*, 1988) or the tissue regeneration process in

porous scaffolds (Tsubota *et al*, 2009; Adachi *et al*, 2006). A mechano-regulatory model can be defined as the mechanical strain and fluid flow that modulates cell differentiation, showing considerable potential to capture the growth details of various cell phenotypes under different levels of biophysical stimuli (Prendergast *et al*, 1997). Byrne *et al* (2007) divided this phenomenon into two different levels. The first one at the scaffold level, where the mechanical and fluidic fields were analysed through a poroelasticity model. The second one at the cellular level, where the proliferation and differentiation of MSCs were simulated based on the correlation between the levels of mechano-regulatory stimuli and experimental data. Mechanical loading not only affects the ECM synthesis of native tissues, but also modulates the ECM structure, composition, and mechanical properties of tissue engineering constructs (Wang and Thampatty, 2006).

In this research work, the Byrne *et al* (2007) approach was adopted by considering the mechano-regulatory model at the scaffold level, where the mechanical and vascular behaviour were analysed. Once the scaffold is seeded and cultured, the formation of tissues with desirable properties relies on the scaffold's mechanical properties, both at a macroscopic and microscopic level. Macroscopically, the scaffold must bear loads to provide stability to the tissues as they form and fulfil its volume maintenance function. At the microscopic level, cell growth and differentiation and the ultimate tissue formation are dependent on the mechanical input to the cells. Consequently, the scaffold must be able to both withstand specific loads and transmit them, in an appropriate manner, to the growing and surrounding cells and tissues. The specific mechanical properties of scaffolds that were considered in this research work were the elasticity, compressibility and tensile strength.

4.2. Constitutive Equations for Structural Analysis

Many natural materials are not fully dense, i.e. they possess internal cavities similar to the designed structures considered in this research work. This type of design is intentional, since it reduces the structure's density, and in some cases present optimal performance regarding mechanical solicitations (Meyers *et al*, 2008). An example of a biological cellular material is cancellous bone, which is designed to have a variable density, where regions subjected to higher stresses are denser (Meyers *et al*, 2008). By definition, a cellular solid (Figure 4.1) is made up of an interconnected network of solid struts or plates, which form the edges and faces of cells (Gibson and Ashby, 1997). According to this definition, polymeric and ceramic tissue engineering scaffolds are characterized as cellular structures. The stress–strain curve for a cellular solid in compression is characterized by different behaviours (Figure 4.2): i) a linear elastic one, corresponding to cell edge bending or face stretching; ii) a stress plateau, corresponding to progressive cell collapse by elastic buckling, iii) a plastic yielding or brittle crushing, depending on the nature of the solid from which the material is made; and iv) a densification one, corresponding to the collapse of the cells throughout the material and subsequent loading of the cell edges and faces against one another (Gibson, 2005). Figure 4.3 illustrates the compression stress-strain curve for cancellous bone with three different relative densities (Meyers *et al*, 2008; Gibson and Ashby, 1997).

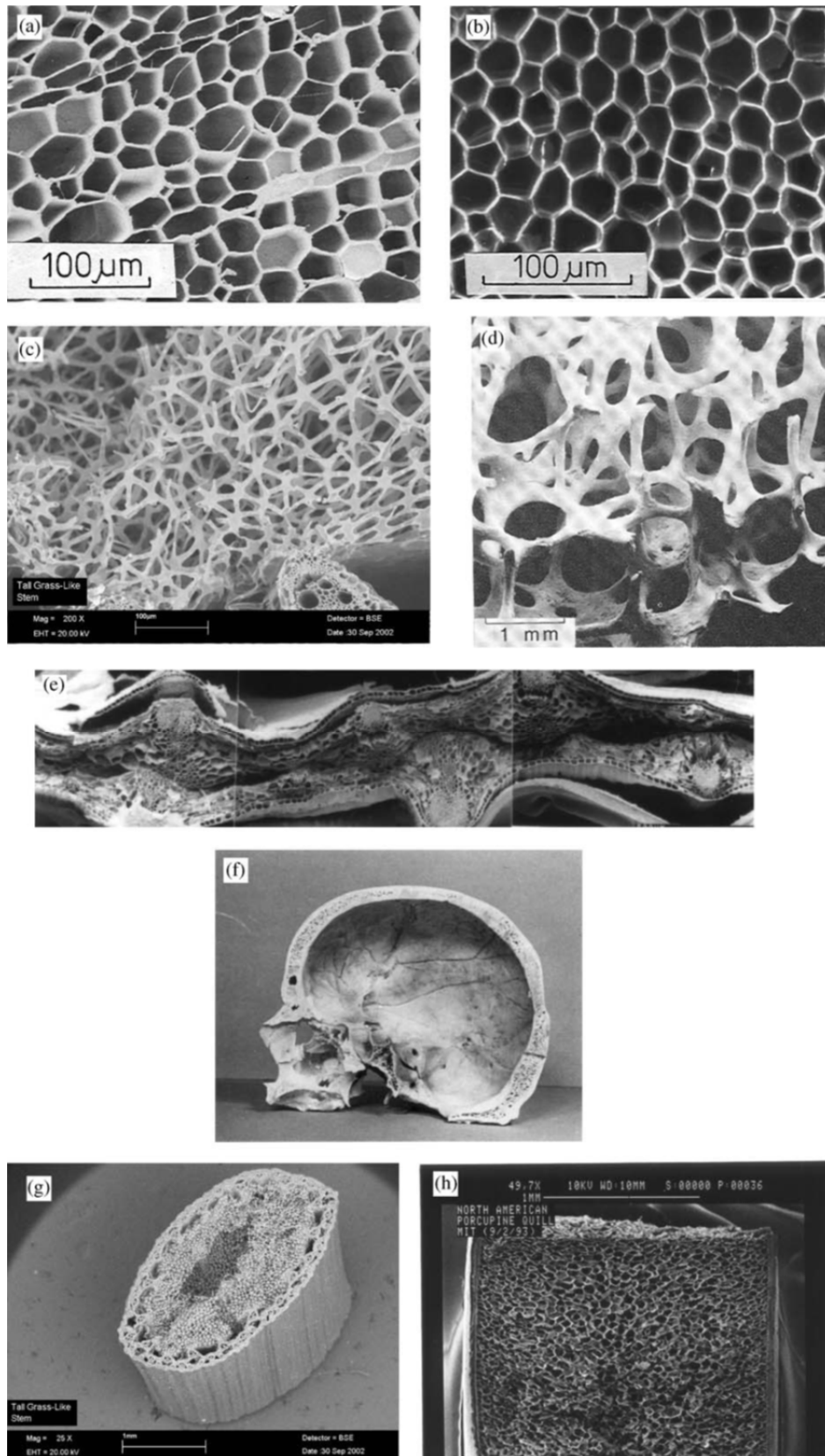


Figure 4.1 – Examples of cellular solids in nature: (a) balsa wood (b) cork (c) inner core of plant stem in (g) (d) trabecular bone (e) iris leaf (f) skull (g) plant stem (h) porcupine quill. (Gibson, 2005; Gibson and Ashby, 1997; Gibson *et al*, 1995).

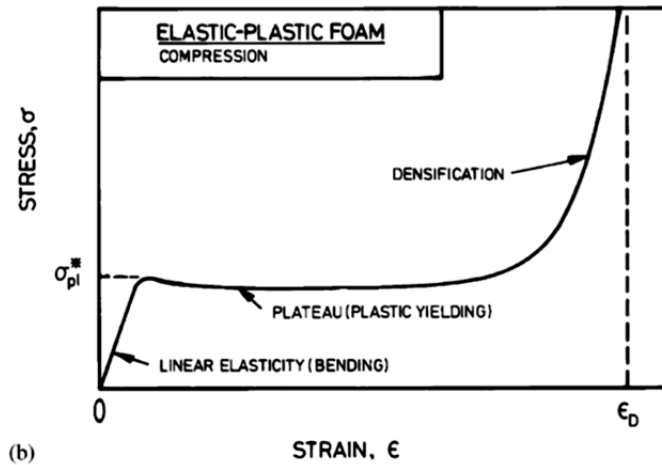


Figure 4.2 – Schematic uniaxial stress–strain curve for elastic–plastic foam in compression (Gibson, 2005; Gibson and Ashby, 1997).

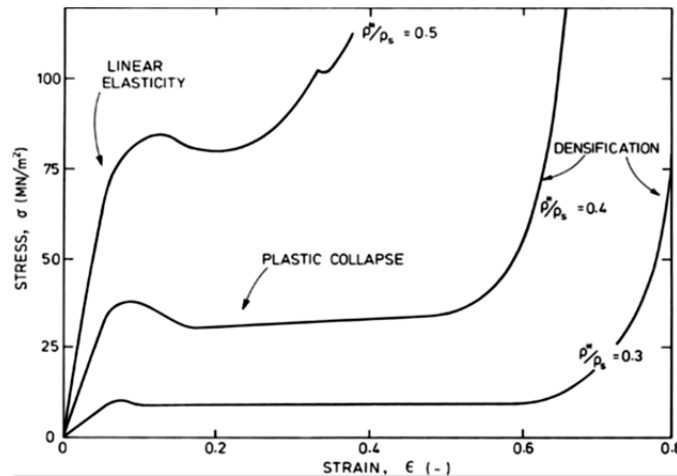


Figure 4.3 – Stress-strain curves for cancellous bone at three different relative densities: 0.3, 0.4, and 0.5 (Meyers *et al*, 2008; Gibson and Ashby, 1997).

To investigate the mechanical behaviour of scaffolds, two different mechanical behaviours were considered:

- Firstly, a linear elastic behaviour to understand the behaviour of each basic scaffold unit;
- A crushable foam behaviour to simulate the complex stress-strain relationship in cellular constructs.

4.2.1. Linear Elastic Behaviour

In this research work, scaffolds are assumed to be homogeneous and isotropic with a linear elastic behaviour. From a mathematical view, a linear elastic material can be described by the following equation (Humphrey and Delange, 2003; Fung, 1990):

$$\sigma_{ij} = C_{ijkl} e_{kl} \quad (4.1)$$

where σ_{ij} is the stress tensor, e_{kl} is the strain tensor, and C_{ijkl} is a tensor of elastic constants or moduli, which are independent of stress or strain.

In the case of isotropic materials, Equation 4.1 can be simplified as follows:

$$\sigma_{ij} = \lambda e_{xx} \delta_{ij} + 2\mu e_{ij} \quad (4.2)$$

with λ and μ , being the Lamé constants.

Similarly, the strain tensor for an isotropic linear elastic material is given by the following equation:

$$e_{ij} = \frac{1+\nu}{E} \sigma_{ij} - \frac{\nu}{E} \sigma_{kk} \delta_{ij} \quad (4.3)$$

In a three dimensional Cartesian space, the compact Equations 4.2 and 4.3 are given by:

$$\begin{aligned} \sigma_{xx} &= \lambda (e_{xx} + e_{yy} + e_{zz}) + 2G e_{xx} & \sigma_{xy} &= 2G e_{xy} \\ \sigma_{yy} &= \lambda (e_{xx} + e_{yy} + e_{zz}) + 2G e_{yy} & \sigma_{yz} &= 2G e_{yz} \\ \sigma_{zz} &= \lambda (e_{xx} + e_{yy} + e_{zz}) + 2G e_{zz} & \sigma_{zx} &= 2G e_{zx} \end{aligned} \quad (4.4)$$

and

$$\begin{aligned}
 e_{xx} &= \frac{1}{E} [\sigma_{xx} - \nu(\sigma_{yy} + \sigma_{zz})] & e_{xy} &= \frac{1+\nu}{E} \sigma_{xy} = \frac{1}{2G} \sigma_{xy} \\
 e_{yy} &= \frac{1}{E} [\sigma_{yy} - \nu(\sigma_{xx} + \sigma_{zz})] & e_{yz} &= \frac{1+\nu}{E} \sigma_{yz} = \frac{1}{2G} \sigma_{yz} \\
 e_{zz} &= \frac{1}{E} [\sigma_{zz} - \nu(\sigma_{xx} + \sigma_{yy})] & e_{zx} &= \frac{1+\nu}{E} \sigma_{zx} = \frac{1}{2G} \sigma_{zx}
 \end{aligned} \tag{4.5}$$

The constants E (Young modulus) and ν (Poisson ratio) are related to λ , and G (shear elastic modulus) is related to μ . These constants can be evaluated by the following equations (Humphrey and Delange, 2003; Fung, 1990):

$$\begin{aligned}
 \lambda &= \frac{2G\nu}{1-2\nu} = \frac{G(E-2G)}{3G-E} = \frac{E\nu}{(1+\nu)(1-2\nu)} \\
 G &= \frac{\lambda(1-2\nu)}{2\nu} = \frac{E}{2(1+\nu)} \\
 \nu &= \frac{\lambda}{2(\lambda+G)} = \frac{\lambda}{(3K-\lambda)} = \frac{E}{2G} - 1 \\
 E &= \frac{G(3\lambda+2G)}{\lambda+G} = \frac{\lambda(1+\nu)(1-2\nu)}{\nu} = 2G(1+\nu)
 \end{aligned} \tag{4.6}$$

Under a compressive load in the z direction, the corresponding strain can be determined by:

$$e_{zz} = \frac{1}{E} \sigma_{zz} \tag{4.7}$$

However, as a consequence of this compressive effect, the lateral sides of the compressed part will bulge out. A compression load induces lateral bulging, while a tensile load induces lateral shrinking. This phenomenon can be evaluated as follows:

$$e_{xx} = -\frac{\nu}{E} \sigma_{zz} \quad e_{yy} = -\frac{\nu}{E} \sigma_{zz} \tag{4.8}$$

If the part is also subjected to stresses σ_{xx} and σ_{yy} , then the influence of σ_{xx} on e_{yy} , e_{zz} and σ_{yy} on both e_{xx} and e_{zz} must be the same as the influence of σ_{zz} on e_{xx} and e_{yy} , *i.e.*,

$$e_{zz} = \frac{1}{E}\sigma_{zz} - \frac{\nu}{E}\sigma_{xx} - \frac{\nu}{E}\sigma_{yy} \quad (4.9)$$

In the case of shear effects, the stresses σ_{ij} and the strains e_{ij} ($i \neq j$) are directly proportional.

4.2.2. Crushable Foam Behaviour

The constitutive model for crushable foams, described in this section, is considered for the analysis of materials typically used in energy absorption structures. The crushable foam plasticity models present the following characteristics:

- can be used to model crushable materials other than foams, such as balsa wood;
- are used to model the enhanced ability of a foam material to deform in compression, due to cell wall buckling processes. It is assumed that the resulting deformation is not instantaneously recoverable, ideally presenting a plastic behaviour for short duration events;
- can be used to model the difference between a foam material's compressive strength and its much smaller tensile bearing capacity, resulting from the cell wall breakage in tension;
- must be used in conjunction with the linear elastic material model;
- can be used when rate-dependent effects are important;
- are intended to simulate material response under essentially monotonic loading.

Two phenomenological constitutive models are presented:

- The volumetric hardening model;
- The isotropic hardening model.

Both models use a yield surface with an elliptical dependence of either the deviatoric stress or the pressure stress in the meridional plane.

The volumetric hardening model was developed based on the different response foam structures usually experience in compression and tension. In compression the ability of the material to deform volumetrically is enhanced by cell wall buckling processes, as described by Gibson *et al* (1982), Gibson and Ashby (1982) and Maiti *et al* (1984). It is assumed that the resulting deformation is not instantaneously recoverable, ideally presenting a plastic behaviour for short duration events. On the other hand, in tension, cell walls break readily, as a result the tensile load bearing capacity of crushable foams may be considerably smaller than its compressive load bearing capacity. Under monotonic loading, the volumetric hardening model assumes perfectly plastic behaviour for pure shear and negative hydrostatic pressure stress states, while hardening takes place for positive hydrostatic pressure stress states.

The isotropic hardening model was originally developed for metallic foams by Deshpande and Fleck (2000). It assumes symmetric behaviour in tension and compression, and the evolution of the yield surface is governed by an equivalent plastic strain, contributes for both the volumetric plastic strain and the deviatoric plastic strain.

This isotropic foam model crushes one-dimensionally with a Poisson's ratio that is essentially zero. The stress–strain behaviour is depicted in Figure 4.4, showing an example of unloading from point “a” to the tension cut-off stress at “b”, then unloading to point “c”, and finally reloading to point “d”. At point “d” the reloading will continue along the loading curve. It is important to use nonzero values for the tension cut-off, to prevent the disintegration of the material under small tensile loads. For high values of tension cut-off, the behaviour of the material will be similar in tension and compression.

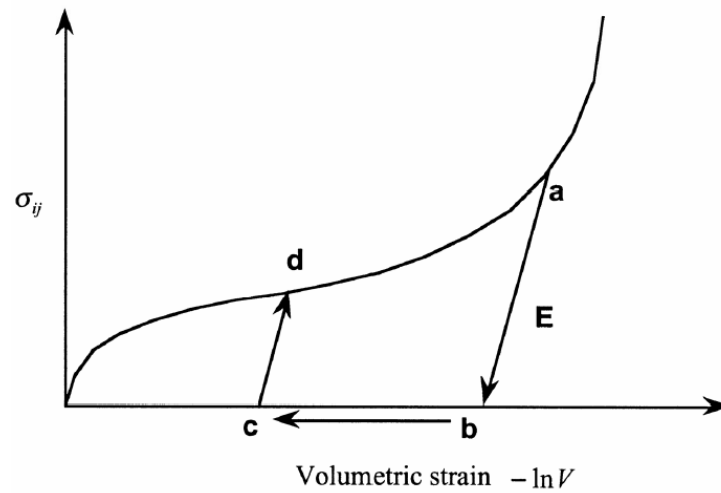


Figure 4.4 – Yield stress versus volumetric strain curve for the crushable foam.

For the implementation of this model, it is assumed that the Young's modulus is constant and the stress elastic behaviour updated along time, as follows:

$$\sigma_{ij}^{trial} = \sigma_{ij}^n + E \dot{\epsilon}_{ij}^{n+1/2} \Delta t^{n+1/2} \quad (4.10)$$

The magnitudes of the principal values, $\sigma_i^{trial}, i = 1,3$ are then checked, to evaluate the yield stress, σ_y , is exceeded, and if so they are scaled back to the yield surface, as follows:

$$if \quad \sigma_y < |\sigma_i^{trial}| \quad then \quad \sigma_i^{n+1} = \sigma_y \frac{\sigma_i^{trial}}{|\sigma_i^{trial}|} \quad (4.11)$$

After the scale of the principal values, the stress tensor is transformed back into the global system. The yield stress is a function of the natural logarithm of the relative volume, V , i.e., the volumetric strain, as illustrated in Figure 4.4.

The mechanical behaviour of crushable foams is known to be sensitive to the rate of straining. This effect can be introduced by either a piecewise linear law or the overstress power law model.

The strain rate decomposition

The volume change is decomposed as in the following way:

$$J = J^{el} \cdot J^{pl} \quad (4.12)$$

where J is the ratio of current volume to original volume, J^{el} is the elastic (recoverable) part of the ratio of current to original foam volume, and J^{pl} is the plastic (non-recoverable) part of the ratio of current to original foam volume.

Volumetric strains are defined as:

$$\begin{aligned} \varepsilon_{vol} &= \ln J \\ \varepsilon_{vol}^{el} &= \ln J^{el} \\ \varepsilon_{vol}^{pl} &= \ln J^{pl} \end{aligned} \quad (4.13)$$

Equations 4.12 and 4.13 result in the usual additive strain rate decomposition for volumetric strains according to the following equations:

$$\dot{\varepsilon}_{vol} = \dot{\varepsilon}_{vol}^{el} + \dot{\varepsilon}_{vol}^{pl} \quad (4.14)$$

The model also assumes that the deviatoric strain rate decompose additively, so that the total strain rate decomposes as follows:

$$\dot{\varepsilon} = \dot{\varepsilon}^{el} + \dot{\varepsilon}^{pl} \quad (4.15)$$

Elastic behaviour

Only the linear elastic behaviour can be modelled as follows:

$$\sigma = D^{el} : \varepsilon^{el} \quad (4.16)$$

where D^{el} represents the fourth-order elasticity tensor and σ and ε^{el} are the second-order stress and elastic strain tensors, respectively.

Plastic behaviour

The yield surface and the flow potential for the crushable foam models are defined in terms of the pressure stress, according to the following equation:

$$p = -\frac{1}{3} \text{trace } \sigma = -\frac{1}{3} \sigma : I \quad (4.17)$$

and the Von-Mises stress calculated by the following equation:

$$q = \sqrt{\frac{3}{2} S : S} \quad (4.18)$$

The yield surface is defined as follows:

$$F = \sqrt{q^2 + \alpha^2 (p - p_0)^2} - B = 0 \quad (4.19)$$

and the flow potential is defined by the following equation:

$$G = \sqrt{q^2 + \beta^2 p^2} \quad (4.20)$$

where F and G can each be represented as an ellipse in the $p - q$ stress plane, with α and β representing the shape of the yield ellipse and the ellipse for the flow potential, respectively; p_0 is the centre of the yield ellipse, and B is the length of the (vertical) q -axis of the yield ellipse. The flow potential is an ellipse centred in the origin. The yield surface and the flow potential are depicted in Figure 4.5.

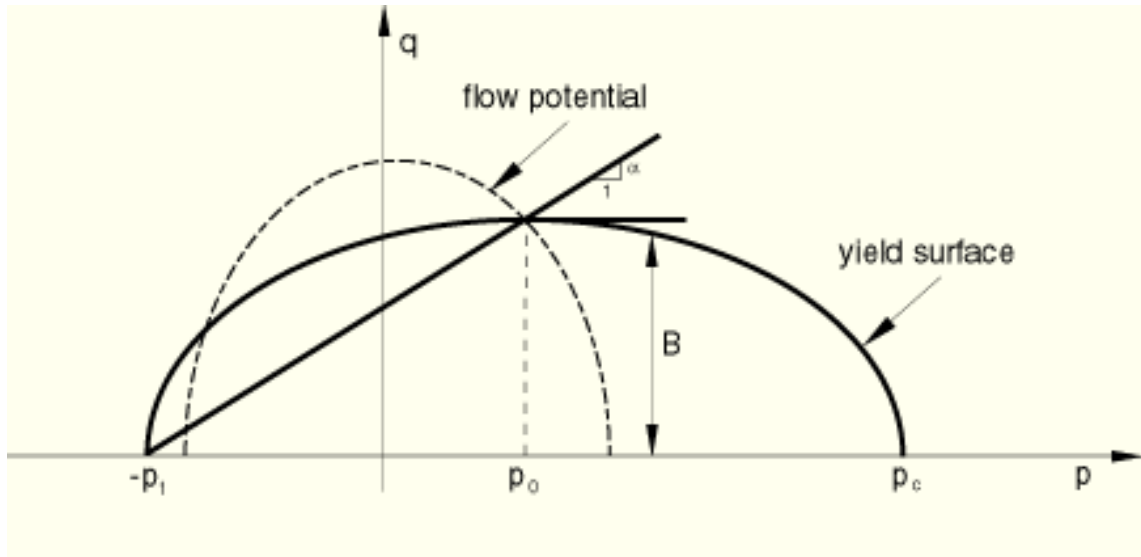


Figure 4.5 – Typical yield surface and flow potential for the crushable foam model.

The parameters p_0 and B of the yield ellipse (Equation 4.19) are related to both the yield strength in hydrostatic compression, p_c , and to the yield strength in hydrostatic tension, p_t , represented by the following equations:

$$p_0 = \frac{p_c - p_t}{2} \quad (4.21)$$

and

$$B = \alpha A = \alpha \frac{p_c + p_t}{2} \quad (4.22)$$

where p_c and p_t are positive quantities, and A is the length of the (horizontal) p -axis of the yield ellipse.

The shape factor, α , remains as a constant during any plastic deformation process. The evolution of the yield ellipse is controlled by a plastic strain measure, $\bar{\varepsilon}$, which is the volumetric compacting plastic strain, $-\varepsilon_{vol}^{pl}$, for the volumetric hardening model, and the equivalent plastic strain, $\bar{\varepsilon}^{pl}$ (to be defined later), for the isotropic hardening model.

Crushable foam model with volumetric hardening

The volumetric hardening model assumes that the hydrostatic tension strength, p_t , remains constant throughout any plastic deformation process. By contrast, the hydrostatic compression strength progresses as a result of compaction (increase in density) or dilation (reduction in density) of the material, as follows:

$$p_c = p_c(\bar{\varepsilon}) \quad (4.23)$$

where

$$\bar{\varepsilon} \equiv -\varepsilon_{vol}^{pl} = -trace\varepsilon^{pl} \quad (4.24)$$

Yield surface

The yield surface for the crushable foam model, depicted in Figure 4.6, is defined by the following equation:

$$F = \sqrt{q^2 + \alpha^2(p - p_0)^2} - B = 0 \quad (4.25)$$

where the parameter α represents the shape of the yield ellipse in the $p - q$ stress plane, which can be calculated from the initial yield strength in uniaxial compression, σ_c^0 , taken as a positive value; the initial yield strength in hydrostatic compression, p_c^0 ; and the yield strength in hydrostatic tension, p_t ; as follows:

$$\alpha = \frac{3k}{\sqrt{(3k_t + k)(3 - k)}} \quad (4.26)$$

with

$$k = \frac{\sigma_c^0}{p_c^0} \quad (4.27)$$

and

$$k_t = \frac{p_t}{p_c^0} \quad (4.28)$$

where the yield stress ratios, $k(\theta, f_i)$ and $k_t(\theta, f_i)$, provided by the user, can be a function of temperature and other field variables. For a valid yield surface, the choice of yield stress ratios must be such that $0 < k < 3$ and $k_t \geq 0$. The yield surface is the Mises circle in the deviatoric stress plane.

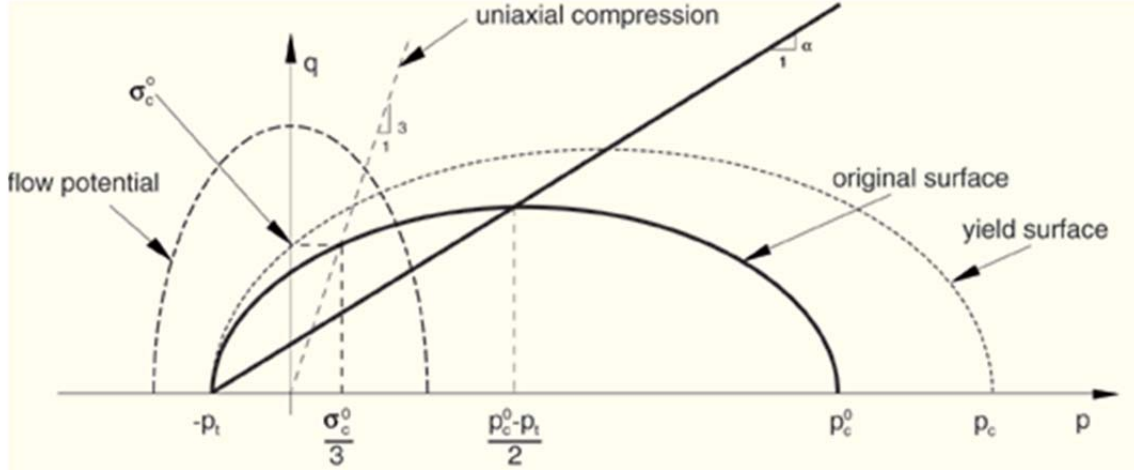


Figure 4.6 – Yield surfaces and flow potential for the volumetric hardening model.

Flow potential

The plastic strain rate for the volumetric hardening model is assumed to be as follows:

$$\dot{\varepsilon}^{pl} = \dot{\bar{\varepsilon}}^{pl} \frac{\partial G}{\partial \sigma} \quad (4.29)$$

where $\dot{\bar{\varepsilon}}^{pl}$ is the equivalent plastic strain rate defined by the following equation:

$$\dot{\bar{\varepsilon}}^{pl} = \frac{\sigma: \dot{\varepsilon}^{pl}}{G} \quad (4.30)$$

and G is the flow potential, given by the following equation:

$$G = \sqrt{q^2 + \frac{9}{2}p^2} \quad (4.31)$$

The flow potential is a particular case of Equation 4.20 with $\beta = 3/\sqrt{2} \approx 2.12$. A geometrical representation of the flow potential in the $p - q$ stress plane is shown in Figure 4.6.

Hardening

The yield surface intersects the p -axis at $-p_t$ and p_c . It is assumed that p_t remains fixed throughout any plastic deformation process. By contrast, the compressive strength, p_c , evolves as a result of compaction (increase in density) or dilation (reduction in density) of the material. The evolution of the yield surface can be expressed through the evolution of the yield surface size on the hydrostatic stress axis, $p_c + p_t$, as a function of the value of volumetric compacting plastic strain, $-\varepsilon_{vol}^{pl}$. With p_t constant, this relation can be obtained from a user-provided uniaxial compression test data as follows:

$$p_c(\varepsilon_{vol}^{pl}) = \frac{\sigma_c(\varepsilon_{axial}^{pl}) \left[\sigma_c(\varepsilon_{axial}^{pt}) \left(\frac{1}{\alpha^2} + \frac{1}{9} \right) + \frac{p_t}{3} \right]}{p_t + \frac{\sigma_c(\varepsilon_{axial}^{pl})}{3}} \quad (4.32)$$

along with the fact that $\varepsilon_{axial}^{pl} = \varepsilon_{vol}^{pl}$ in uniaxial compression (due to zero plastic Poisson's ratio). Thus, the user provides input to the hardening law by specifying only the value of the yield stress in uniaxial compression as a function of the absolute value of the axial plastic strain.

4.2.3. Summary

In this research work, two constitutive models were considered:

- A linear elastic behaviour model for small deformations within the scaffold's elastic domain;
- A crushable foam behaviour model, where a linear elastic model was also considered for the deformation within the elastic domain, combined with the volumetric hardening model for the high deformations within the plastic domain. The volumetric hardening model is the most adequate model, as the cellular structures considered in this work are polymer based.

4.3. Mechanical Simulations

The main goal for simulating the scaffold mechanical behaviour is to evaluate the porosity dependence on both elastic and shear modulus. For the mechanical simulations, two types of loads were used. A tensile solicitation was applied to both triple periodic and non-triple periodic surfaces. In order to validate the proposed approach, a compression solicitation was also applied to non-triple periodic surfaces and the obtained results compared with experimental data. The mathematical formulation described in this section was implemented in Abaqus (*Abaqus v6.10 from Simulia*). Figure 4.7 illustrates the implemented simulation algorithm.

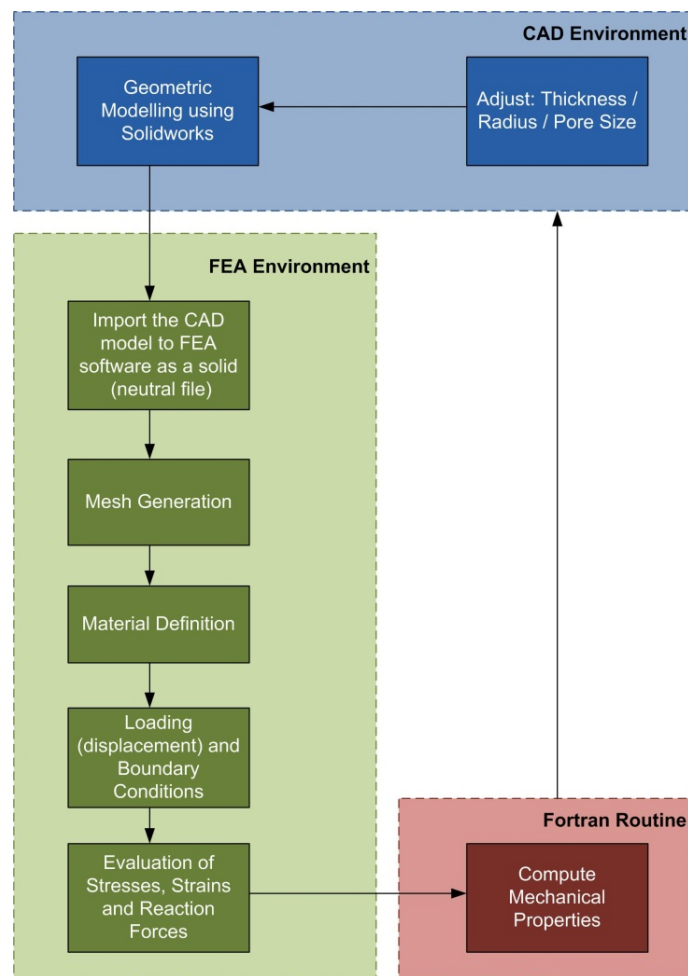


Figure 4.7 – Numerical strategy to evaluate the mechanical behaviour of scaffolds.

Figure 4.8 illustrates two triple periodic surface scaffold elements under tensile solicitation, and Figure 4.9 illustrates a non-triple periodic surface scaffold subjected to a compression solicitation. Both Figures also illustrate the considered loading and boundary conditions.

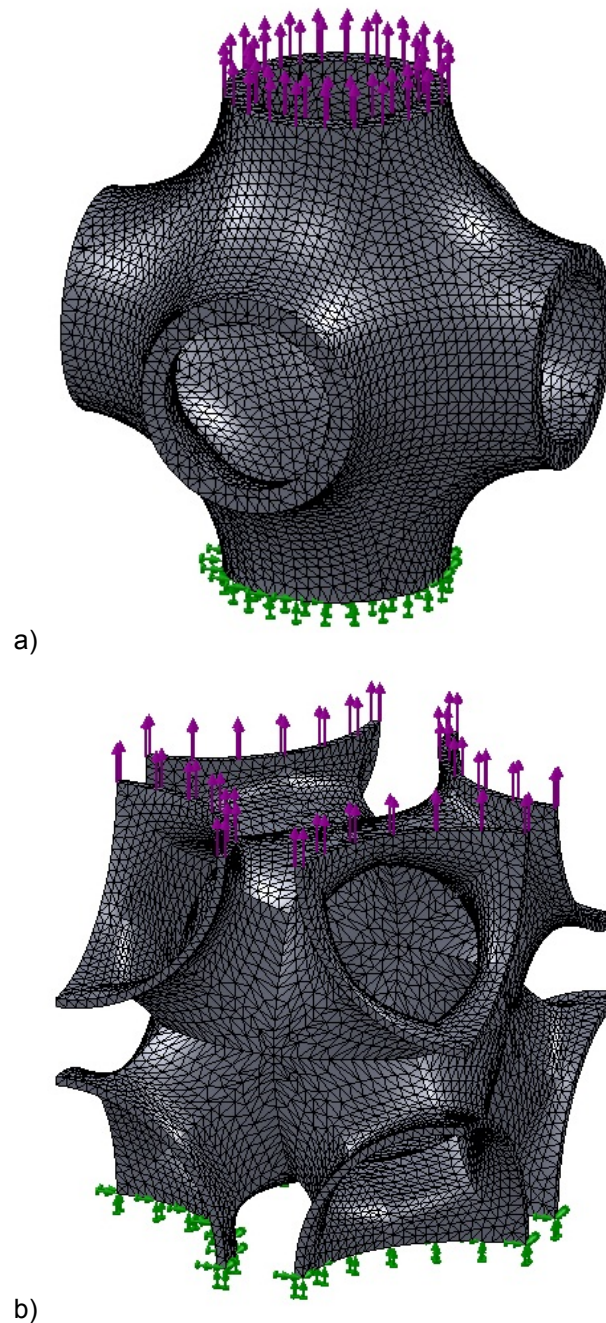


Figure 4.8 – Mesh elements and loading and boundary conditions for the periodic surface scaffolds for the structural tensile simulations a) Schwartz and b) Schoen geometry (green – boundary constraints, purple – loading solicitations).

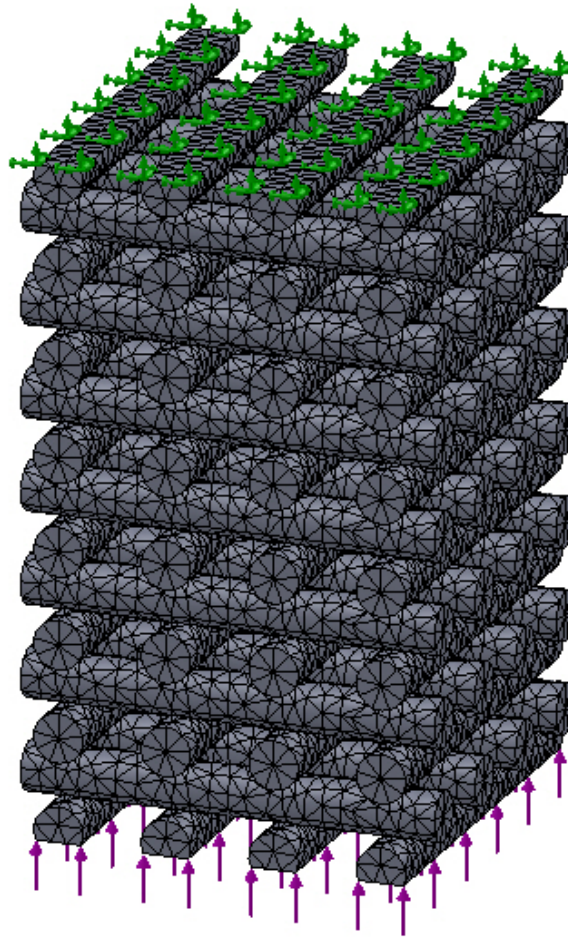


Figure 4.9 – Mesh elements and loading and boundary conditions for the filament based scaffolds for the structural compression simulations (green – boundary constraints, purple – loading solicitations).

For the numerical computation of the elastic modulus, a uniform displacement in a single direction is considered (the X direction), which is equivalent to the strain on the same direction (ϵ_x), imposed to a face of the block (Face A) (Figure 4.10). The opposite face (Face B) of the scaffold unit is constrained and unable to have any displacement (Figure 4.10.a). The average reaction force produced on Face B is used to determine the elastic modulus, due to the imposed displacement. For the numerical evaluation of the shear modulus, a uniform displacement is applied on the top of a surface, being the opposite face also unable to have any displacement (Figure 4.10.b). Each unit is considered isotropic.

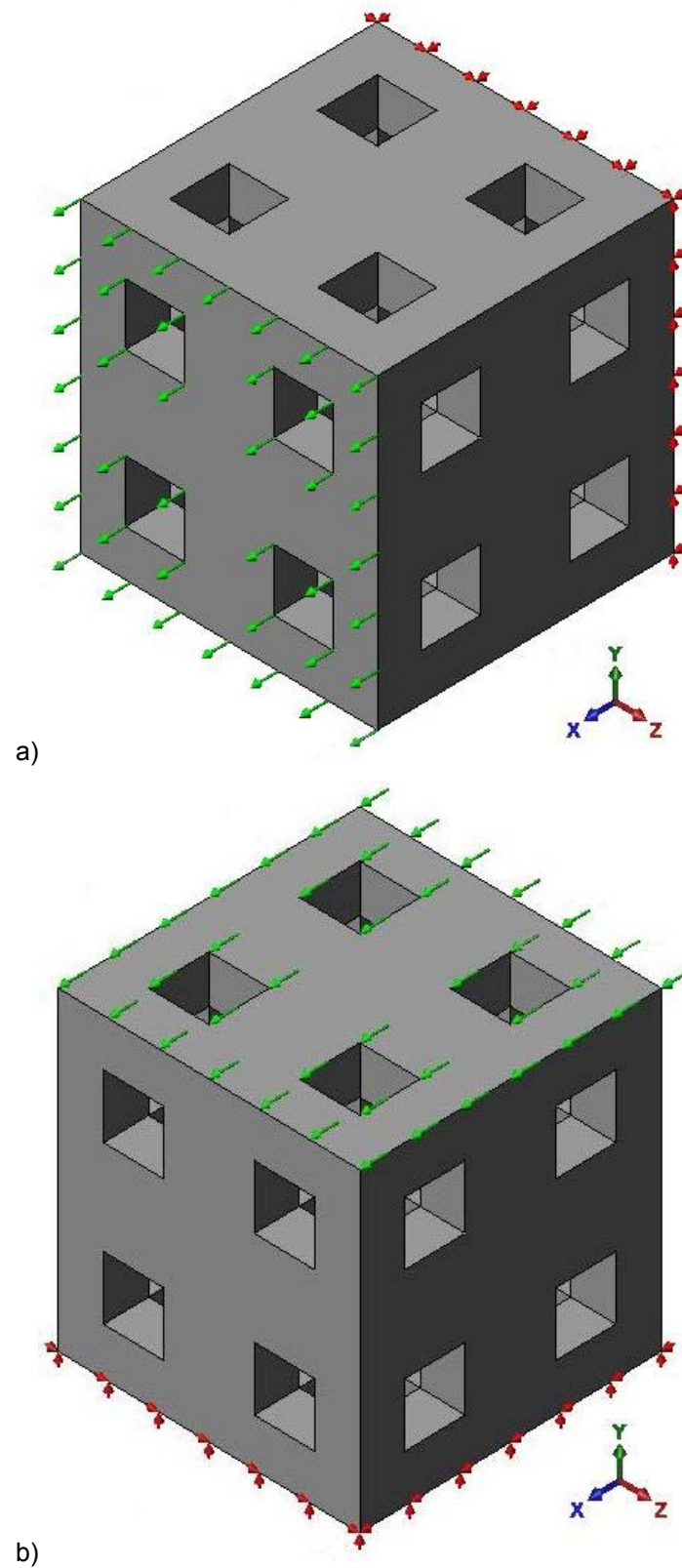


Figure 4.10 – Loads and constraints for the numerical analysis a) Tensile Solicitation and b) Shear Solicitation.

The elastic modulus is calculated according to the following equation:

$$E = \frac{\sigma}{\varepsilon} \quad (4.33)$$

where

σ - Normal Stress

ε - Elastic Strain

and the tensile and strain are calculated according to the following equations:

$$\sigma = \frac{R}{A} \quad (4.34)$$

$$\varepsilon = \frac{Ux}{L} = \frac{Pd \times L}{L} = Pd \quad (4.35)$$

where

R – Reaction Force

A – Surface Area

Ux – Displacement

L – Face length

Pd – Displacement percentage of 0.1 %

Replacing Equations 4.34 and 4.35 in Equation 4.33:

$$E = \frac{\frac{R}{A}}{Pd} = \frac{R}{Pd \times A} \quad (4.36)$$

Rewriting the previous equation only for a specific displacement in the XX direction:

$$E_{xx} = \frac{\frac{R}{A}}{Pd} = \frac{R_x}{Pd \times A_{Fc}} \quad (4.37)$$

where the value of the total reaction force, R_x , is calculated according to the following equation:

$$Rx = \int_{Fc} Nx dA \quad (4.38)$$

where

Nx – Node number

The shear modulus is calculated according to the following equation:

$$G_{xy} = \frac{\sigma_{xy}}{\gamma_{xy}} \quad (4.39)$$

where

σ_{xy} - Shear Stress

γ_{xy} - Angular Strain

and the shear and strain are calculated according to:

$$\sigma_{xy} = \frac{Rx}{Ay} \quad (4.40)$$

$$\gamma_{xy} = \frac{Ux}{Ly} = \frac{Pd \times Ly}{Ly} = Pd \quad (4.41)$$

where

R – Reaction Force

A – Surface Area

Ux – Displacement

L – Face length

Pd – Displacement percentage

Rewriting the previous equation only for a specific displacement in the XX direction, the following equation can be obtained:

$$G_{xy} = \frac{\frac{Rx}{Ay}}{Pd} = \frac{Rx}{Pd \times Ay} \quad (4.42)$$

4.4. Structural Results and Discussion

4.4.1. Linear Elastic Simulations

(a) *Non-Triple Periodic Minimal Surfaces*

The effect of the pore architecture, illustrated by Figures 4.11.a and 4.11.b, show the decrease of both the elastic and shear modulus for PCL with the increase of porosity. For tensile loads, the findings show that a “4F” unit is the unit with the worst performance (below 50% porosity), being the best scaffold unit for higher percentages of porosity, as below 50% porosity the circular pore scaffolds are the units with better material modulus. For shear solicitations, results show that the “4F” unit is the unit with the worst performance, being the “CP” scaffolds the unit with better performance.

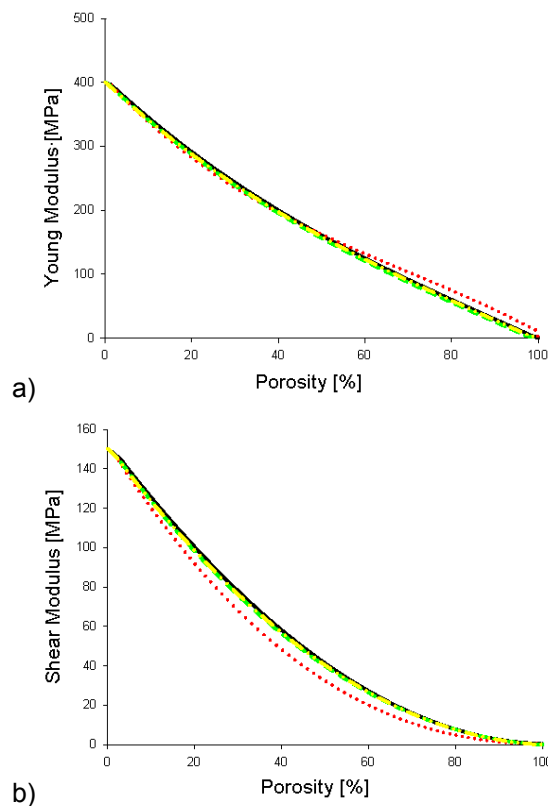


Figure 4.11 – The variation of the material modulus of Poly(caprolactone) material, according to the scaffold porosity for all scaffold units a) elastic modulus and b) shear modulus.

Another aspect of critical importance is the effect of the number of pores per face on the mechanical behaviour of the scaffold. It is possible to observe that the scaffold's modulus increases with the number of pores per face, for each unit, as illustrated in Figures 4.12, 4.13 and 4.14

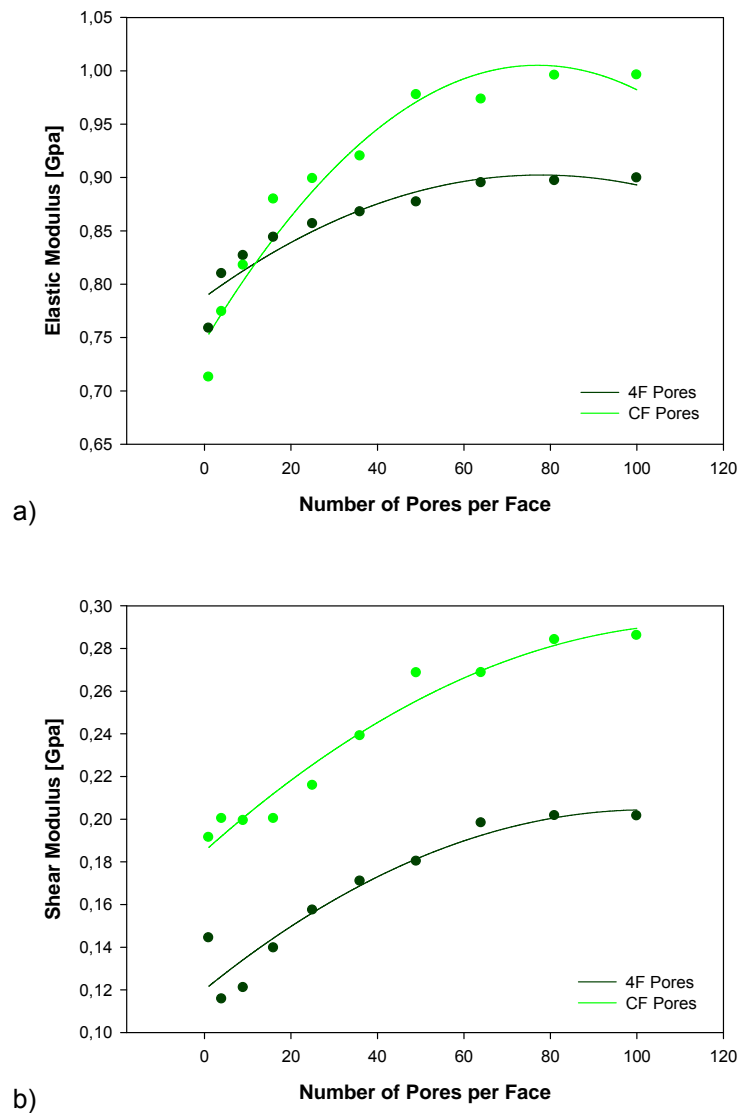


Figure 4.12 – The variation of the material modulus of scaffold units as function of the number of pores per face with CF and 4F pores a) elastic modulus and b) shear modulus.

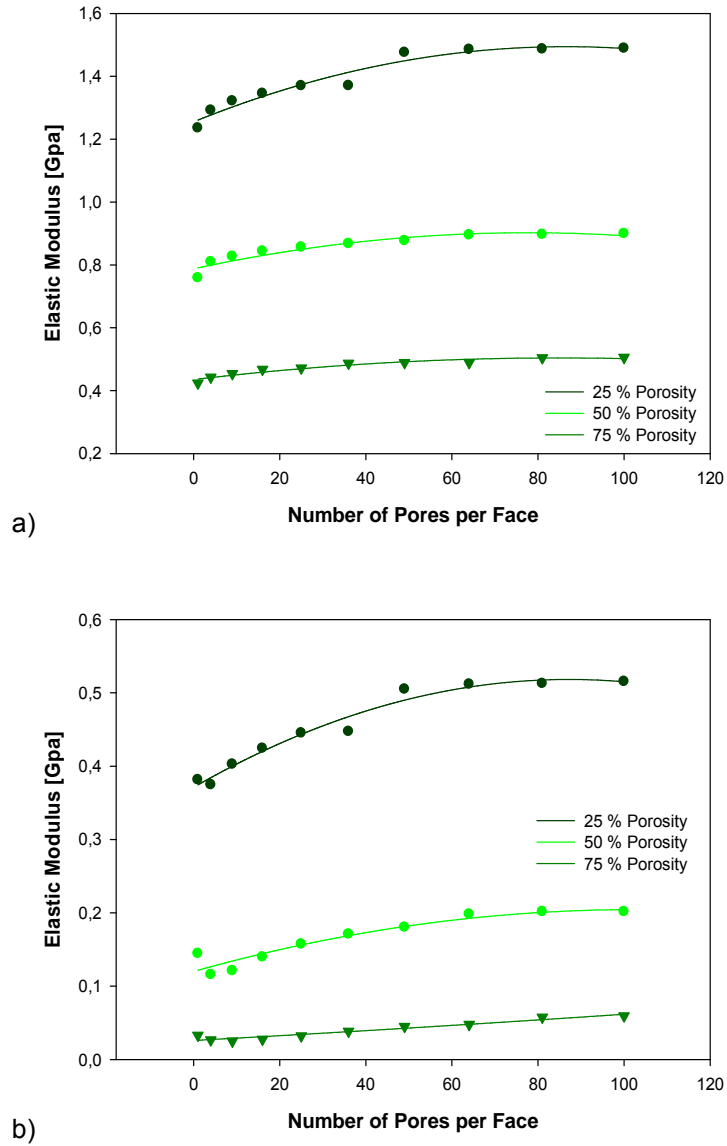


Figure 4.13 – The variation of the material modulus of scaffold units with 4F pores as function of the number of pores per face and level of porosity a) elastic modulus and b) shear modulus.

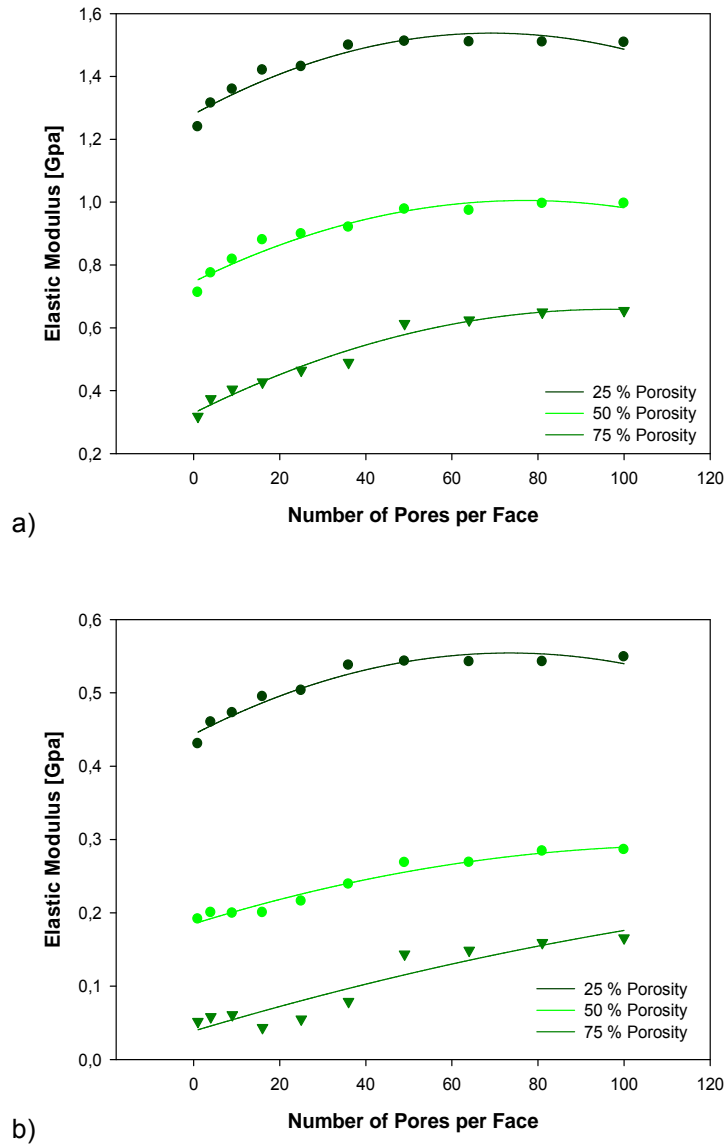


Figure 4.14 – The variation of the material modulus of scaffold units with CF pores as function of the number of pores per face and level of porosity a) elastic modulus and b) shear modulus.

(b) *Triple Periodic Minimal Surfaces*

The variation of scaffold porosity and elastic modulus, as a function of the surface thickness for Schwartz surfaces, are presented in Figures 4.15 and 4.16. Results show that the porosity decreases by an increase on the surface thickness, while the elastic modulus increases. Figure 4.17 shows a linear dependence between the scaffold porosity and the elastic modulus.

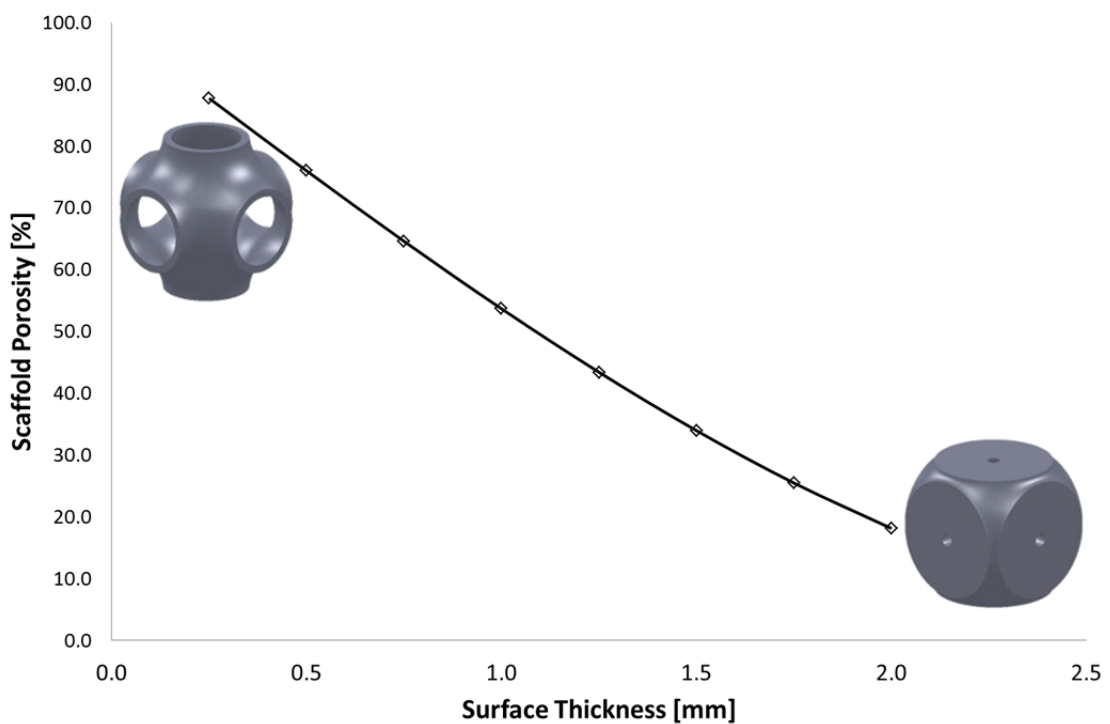


Figure 4.15 – Schwartz surface: variation of the scaffold porosity with the surface thickness.

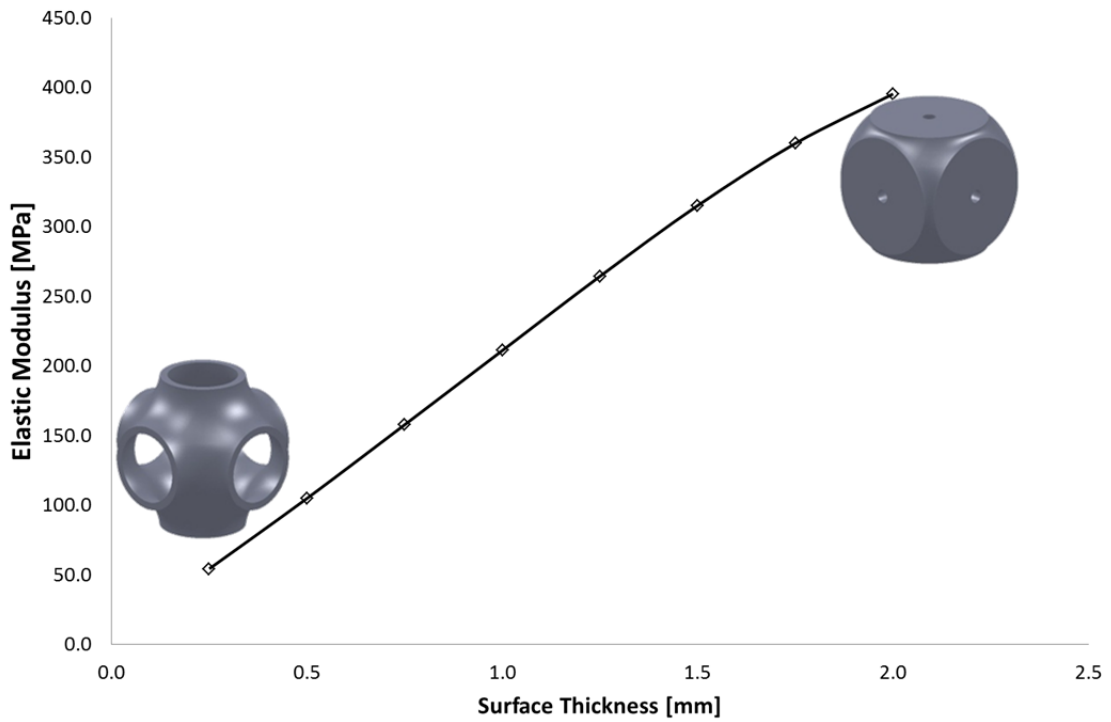


Figure 4.16 – Schwartz surface: variation of the elastic modulus with the surface thickness.

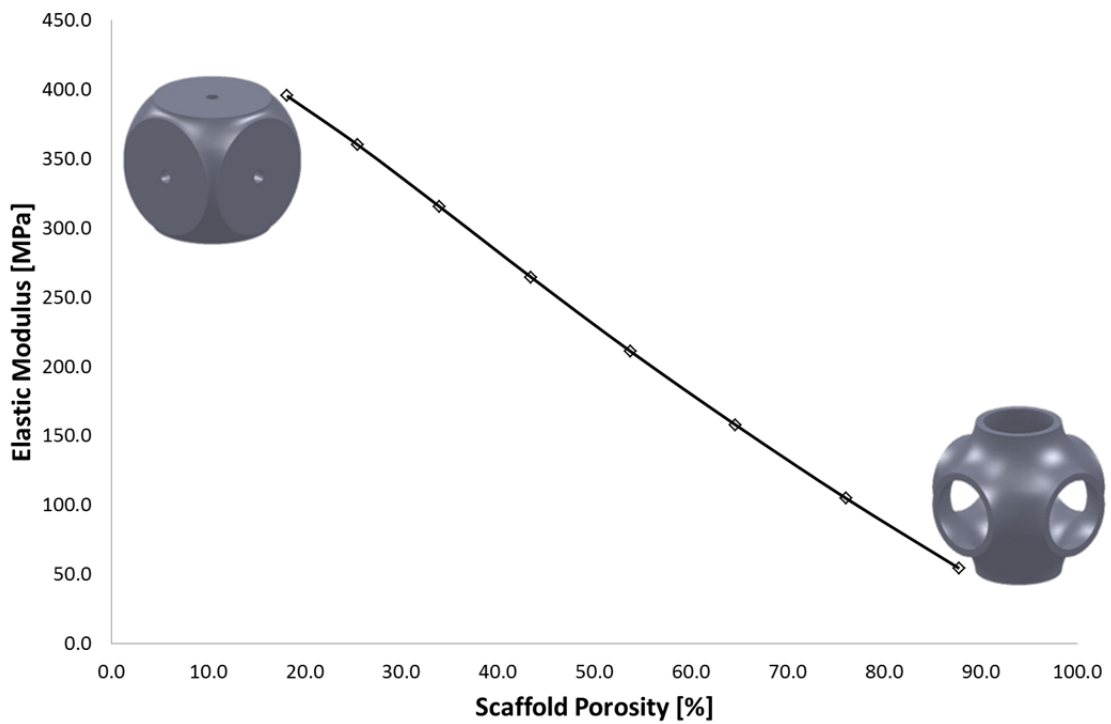


Figure 4.17 – Schwartz surface: variation of the elastic modulus with porosity.

Figures 4.18 and 4.19 present the effect of changing the surface radius for Schwartz surfaces, on both porosity and elastic modulus. It is possible to observe that the porosity decreases by increasing the surface radius till a threshold value, from which it starts to increase. The elastic modulus decreases by increasing the surface radius.

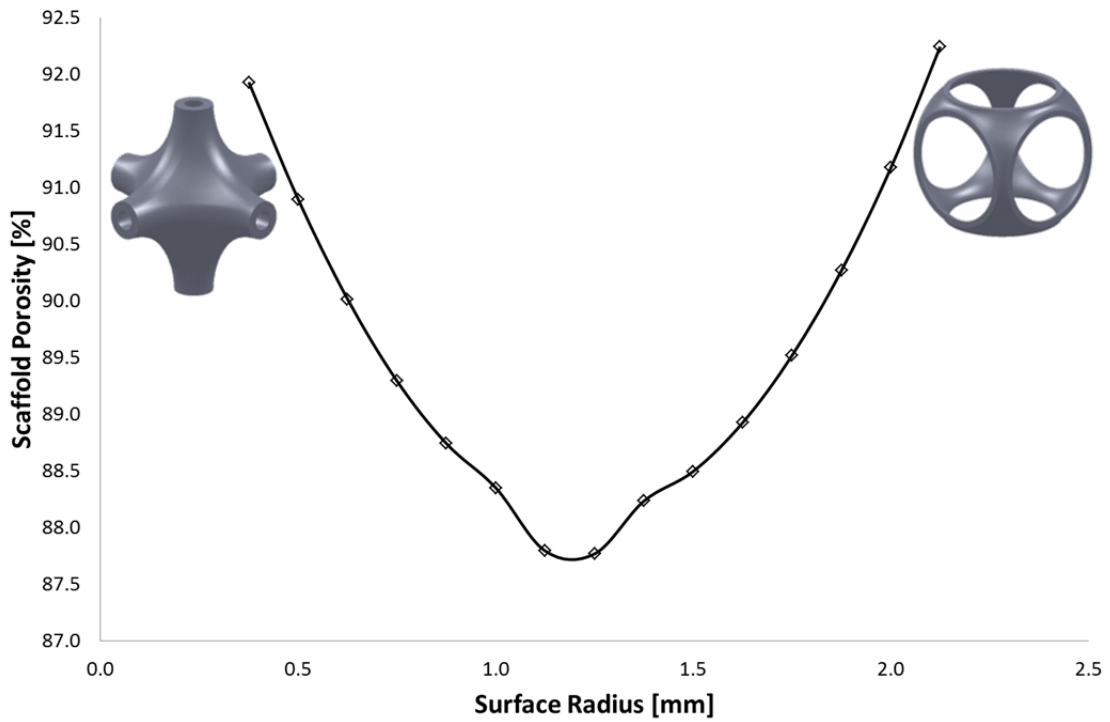


Figure 4.18 – Schwartz surface: variation of the scaffold porosity with the surface radius.

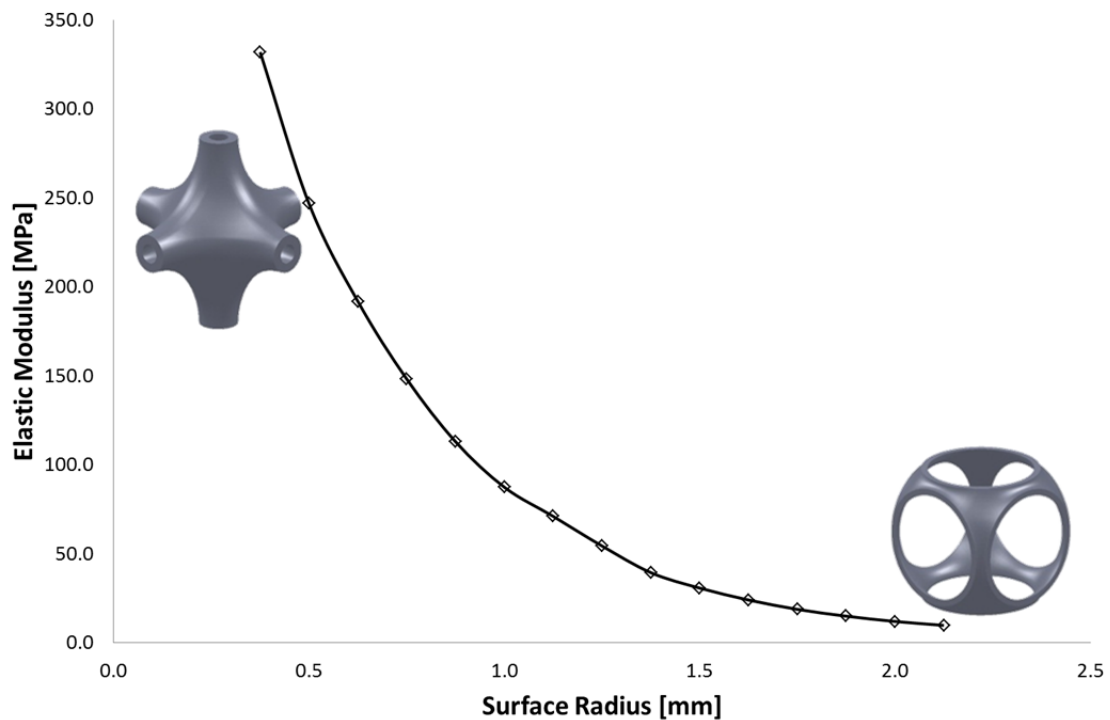


Figure 4.19 – Schwartz surface: variation of the elastic modulus with the surface radius.

The relationship between porosity and surface radius has a hyperbolic behaviour. A similar behaviour was observed regarding the relationship between elastic modulus and porosity (Figure 4.20), so we can decrease or increase the elastic modulus of the scaffold while maintaining high porosity values, which can offer great flexibility regarding scaffold design. High porosity is critical for vascularization and tissue ingrowth.

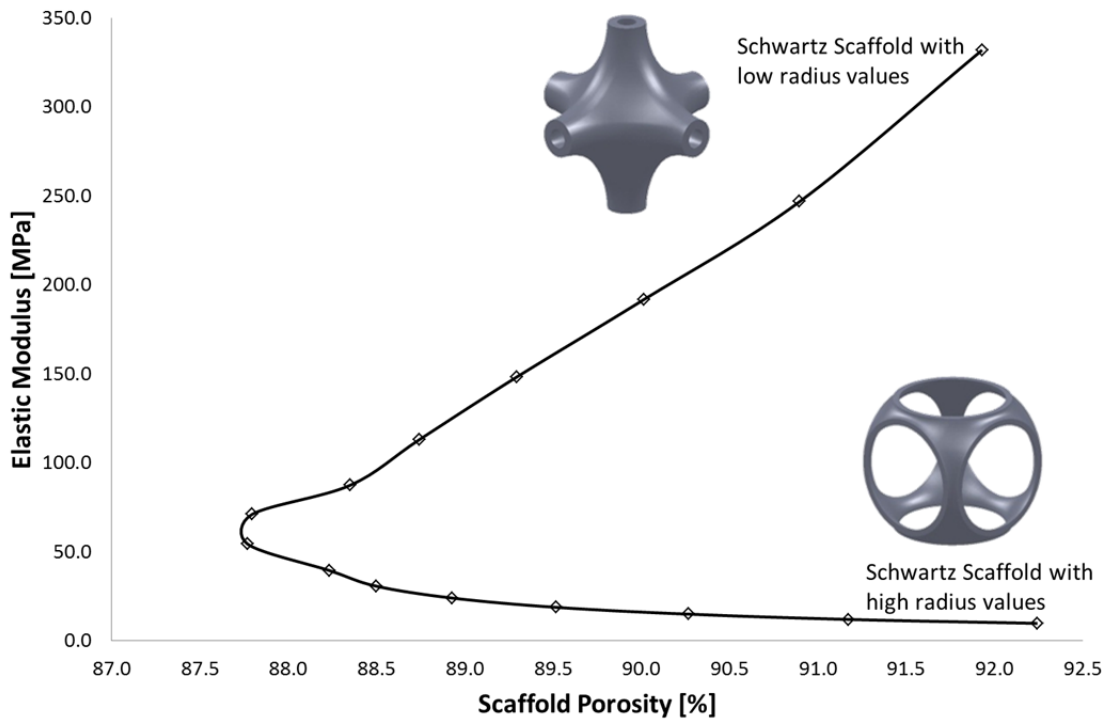


Figure 4.20 – Schwartz surface: variation of the elastic modulus with the porosity.

Figures 4.21 to 4.26 present the effect of thickness and surface radius variation for Schoen geometries. The porosity decreases by increasing surface thickness, as observed in Figure 4.21. Figures 4.22 and 4.23 shows that the elastic modulus increases with thickness and decreases with porosity. The effect of changing the surface radius (Figure 4.24), shows that the porosity increases by increasing the surface radius. In the case of Schoen surfaces, the elastic modulus decreases by increasing either the surface radius (Figure 4.25) or the porosity (Figure 4.26).

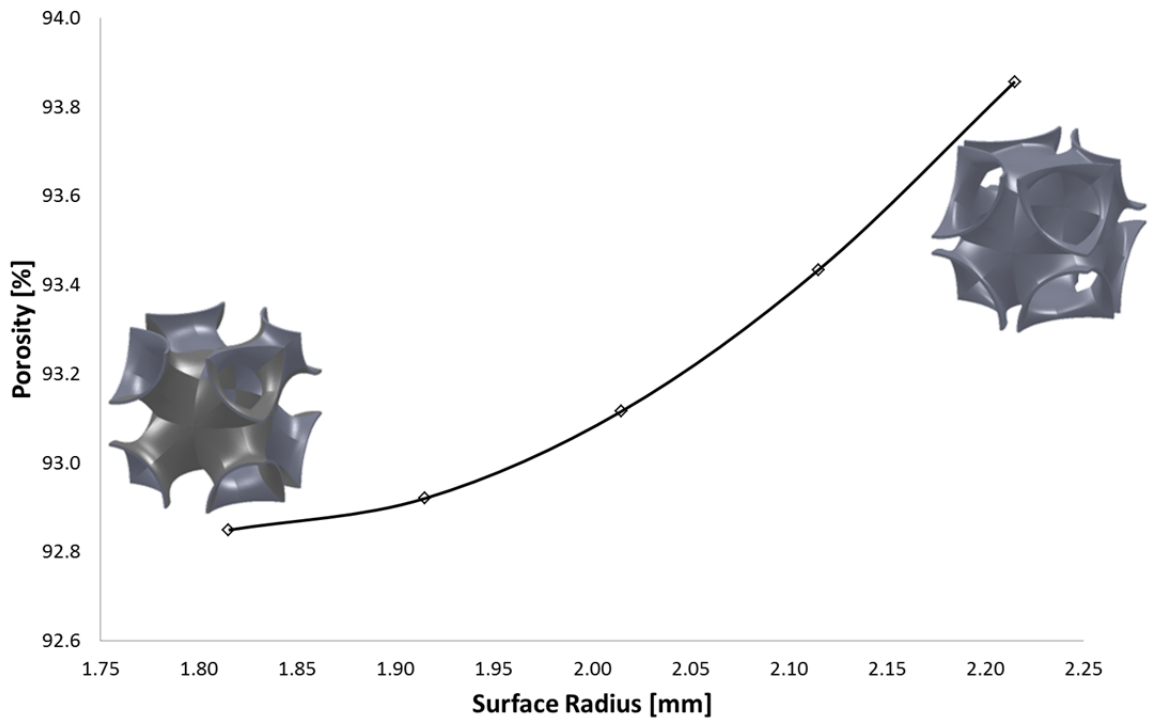


Figure 4.21 – Schoen surface: variation of the scaffold porosity with the surface thickness.

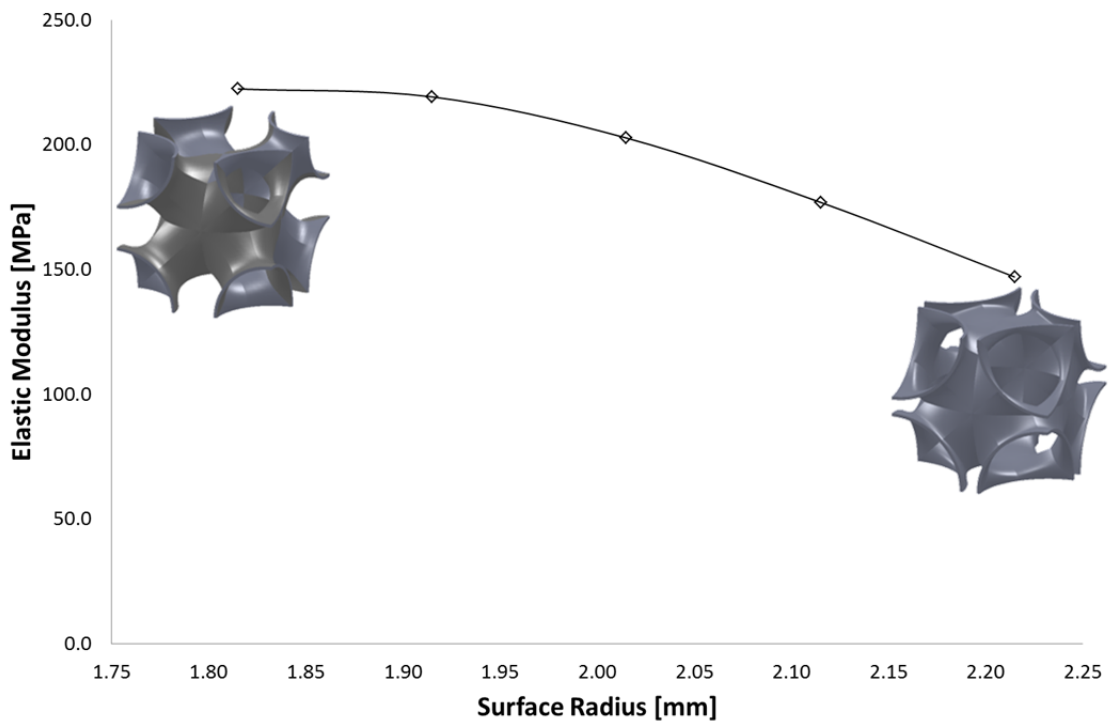


Figure 4.22 – Schoen surface: variation of the elastic modulus with the surface thickness.

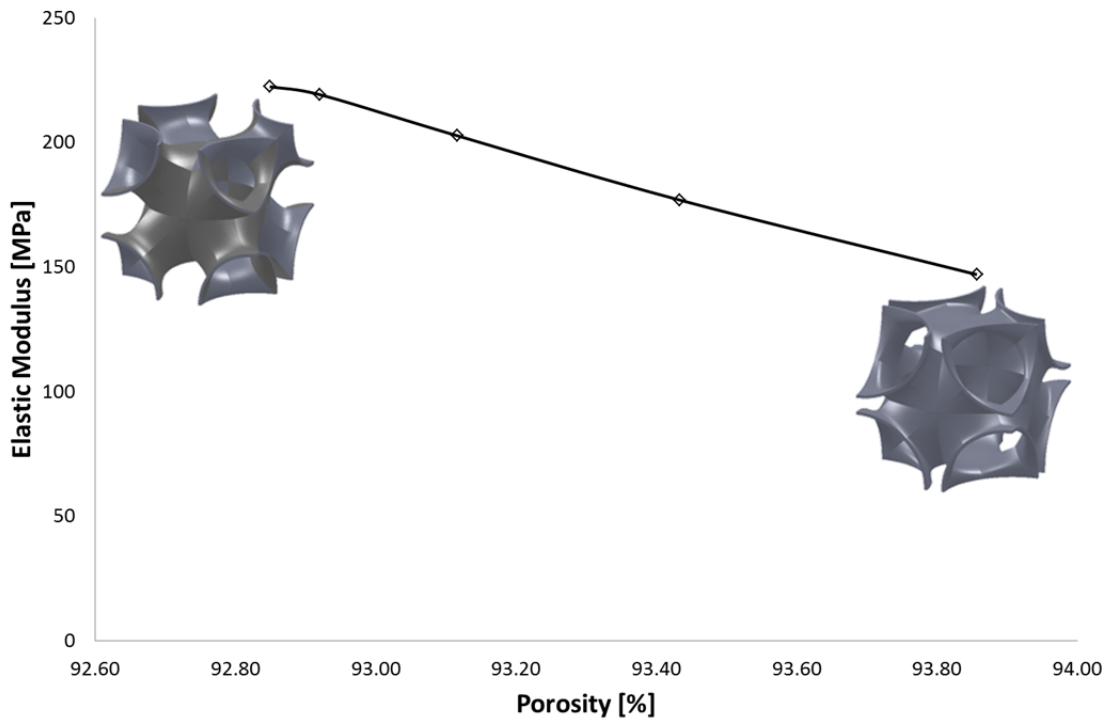


Figure 4.23 – Schoen surface: variation of the elastic modulus with the porosity.

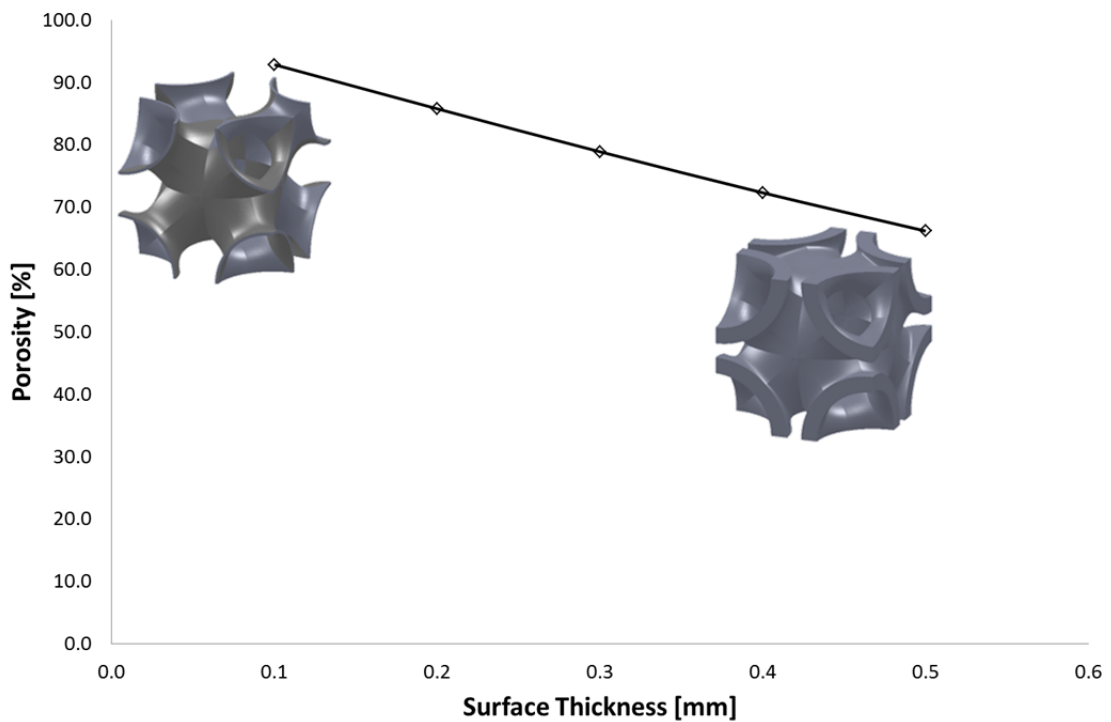


Figure 4.24 – Schoen surface: variation of the scaffold porosity with the surface radius.

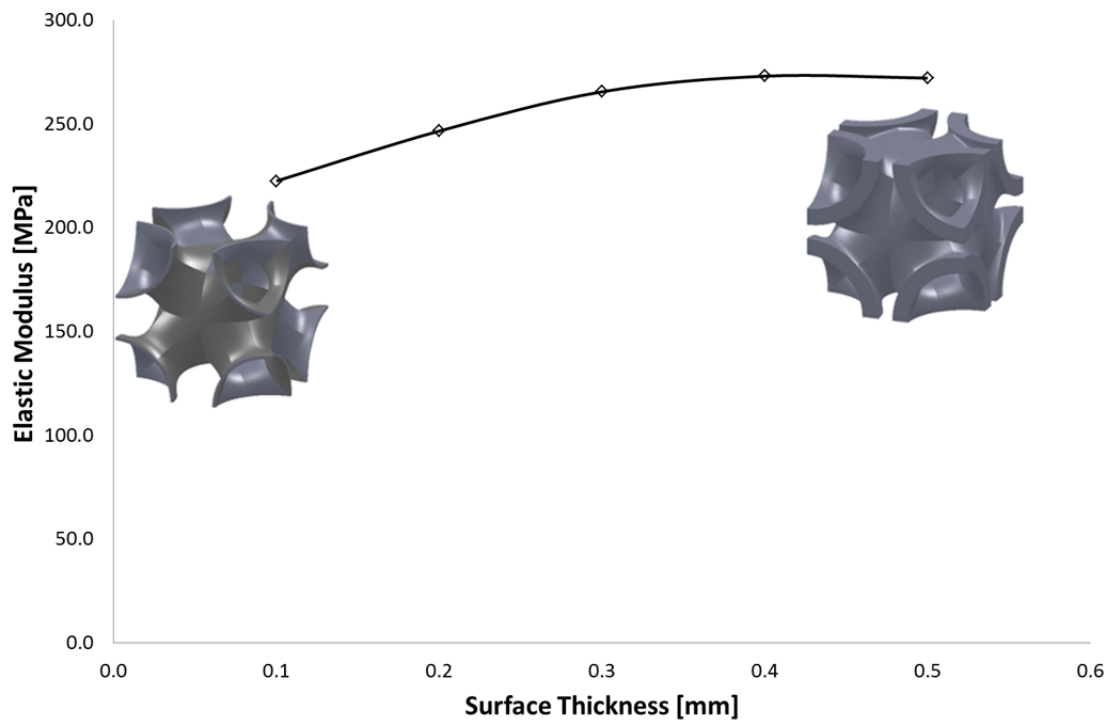


Figure 4.25 – Schoen surface: variation of the elastic modulus with the surface radius.

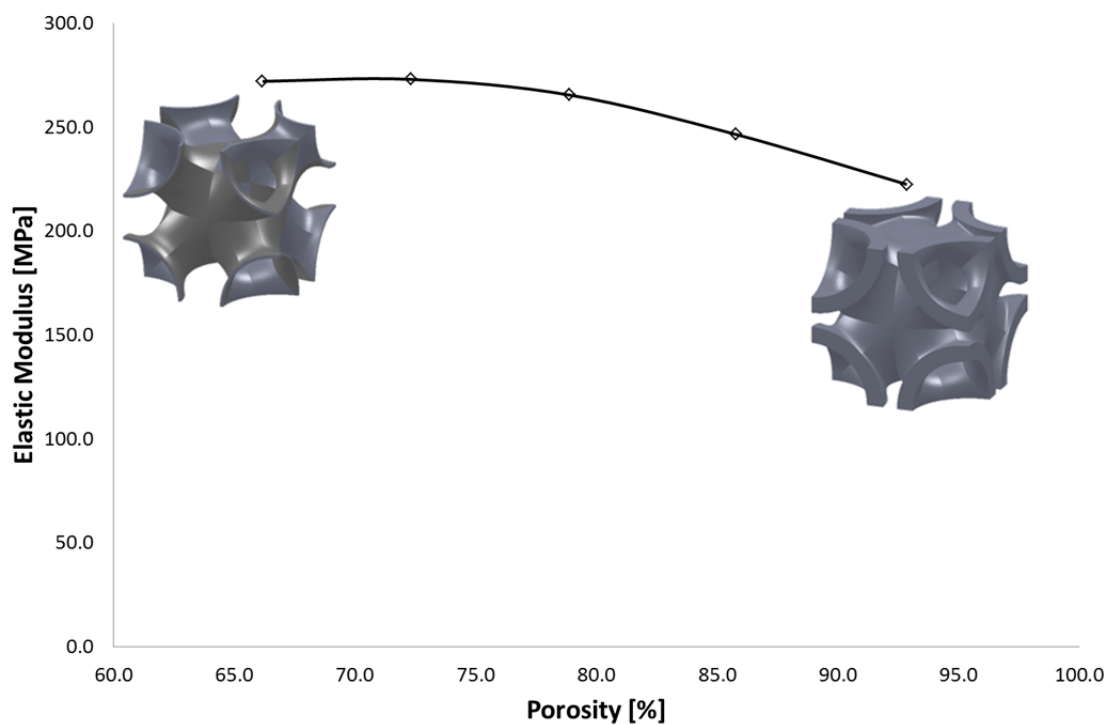


Figure 4.26 – Schoen surface: variation of the elastic modulus with the porosity.

Figures 4.15 to 4.26 illustrate the scaffold basic unit mechanical behaviour on a macro-scale level, regarding porosity and geometric parameters like radius and thickness, for both Schwartz and Schoen surfaces. Figure 4.27 illustrates the Von Mises tensile stresses and the normal σ_{xx} stress variation, according to the node's geometric "X" position in the scaffold basic unit. Figure 4.27 shows that both tensile stresses are similar, which means that the other tensile or shear stresses are less significant. It is also possible to observe that the geometric transition, from the corner channel to the central sphere, is characterized by a decrease on the average tensile stresses, i.e., if cells are seeded on this particular scaffold and then placed in a perfusion bioreactor, in the presence of a mechanical stimuli, they will tend to differentiate and proliferate in the corner channels, and the central sphere correspond to both the largest surface area of the scaffold and the high mechanical stimuli/surface ratio.

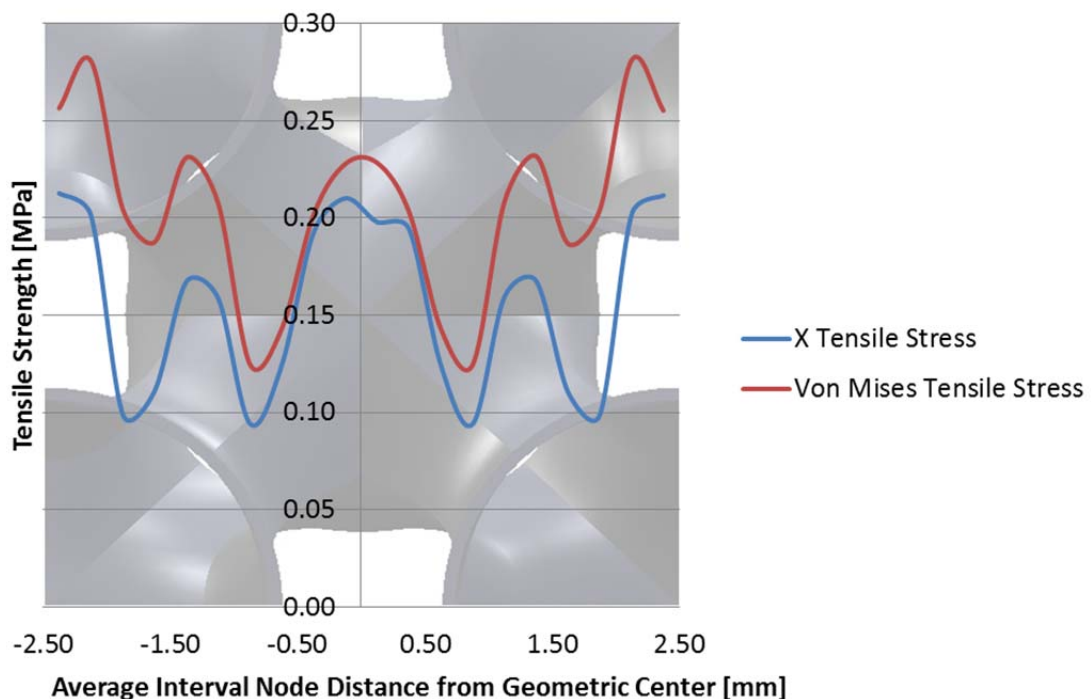


Figure 4.27 – Variation of the Tensile Stress with the node's X coordinate position.

Figures 4.28 to 4.31 illustrate the tensile stress variation of the scaffold on a micro-scale level, considering the variation of both the thickness (Figure 4.28 for the Schwartz geometry, and Figure 4.30 for the Schoen one) and the radius (Figure 4.29 for the Schwartz geometry and Figure 4.31 for the Schoen one).

Figure 4.28 shows that, by increasing the thickness in the Schwartz geometries, the tensile stresses tend to assume the higher values at the two lateral faces, resulting in an uneven tensile stress distribution. The scaffold presents a more homogenous tensile distribution for lower thickness values. Regarding the radius variation, illustrated in Figure 4.29, there is no significant tensile stress variation with the radius increase.

A similar behaviour is observed for the Schoen's thickness variation. As illustrated in Figure 4.30, the Schoen geometries present a more homogenous tensile stress for lower thickness values. Regarding the radius variation (Figure 4.31), results show that, as the radius increases, a more differentiated tensile stress distribution is observed, namely in the central sphere of the Schoen geometry. In this case, Schoen geometries with lower radius values present a more optimum mechanical distribution for cell differentiation and proliferation.

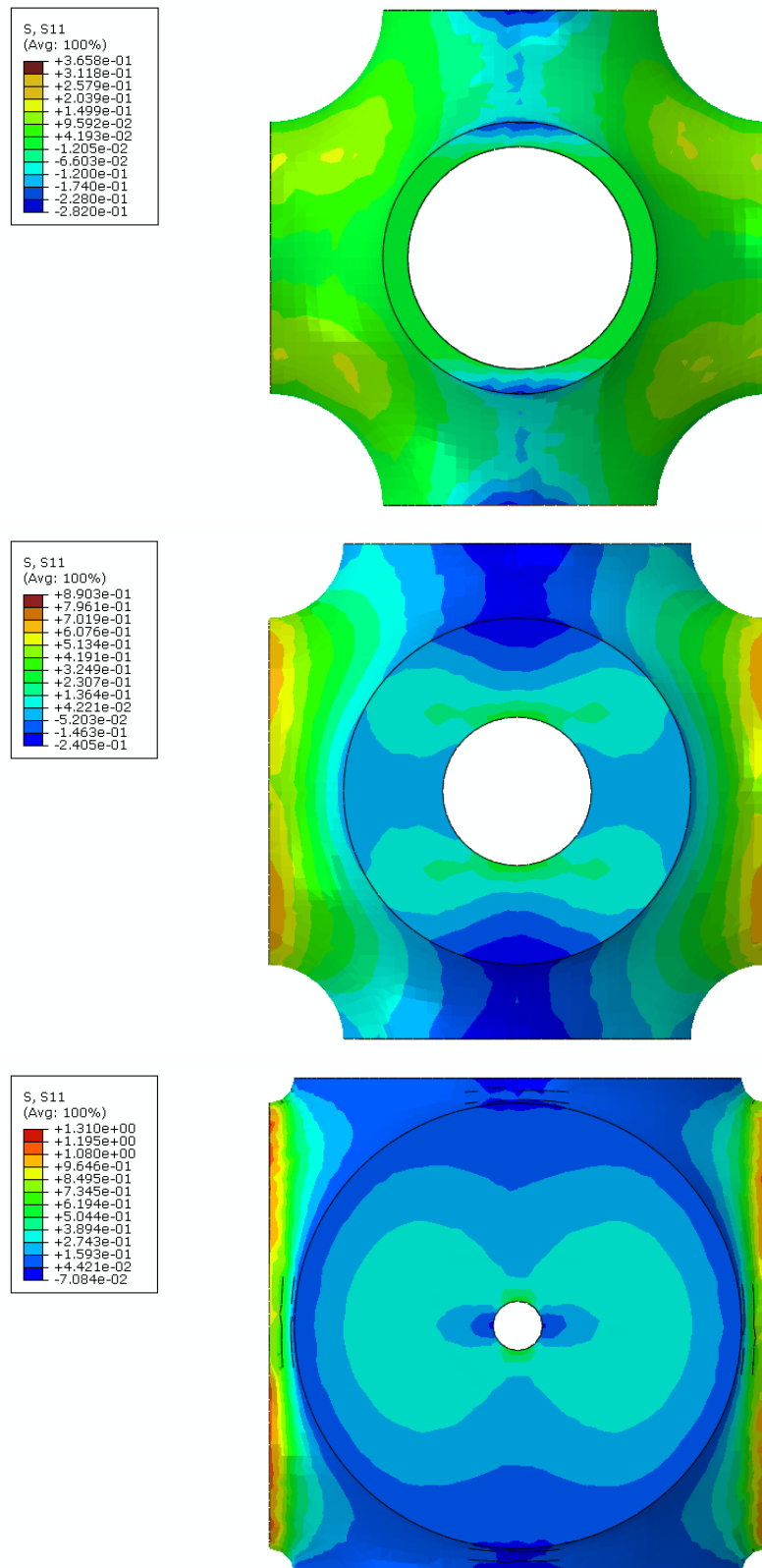


Figure 4.28 – Schwartz surface: variation of the scaffold's tensile stress with the surface thickness.

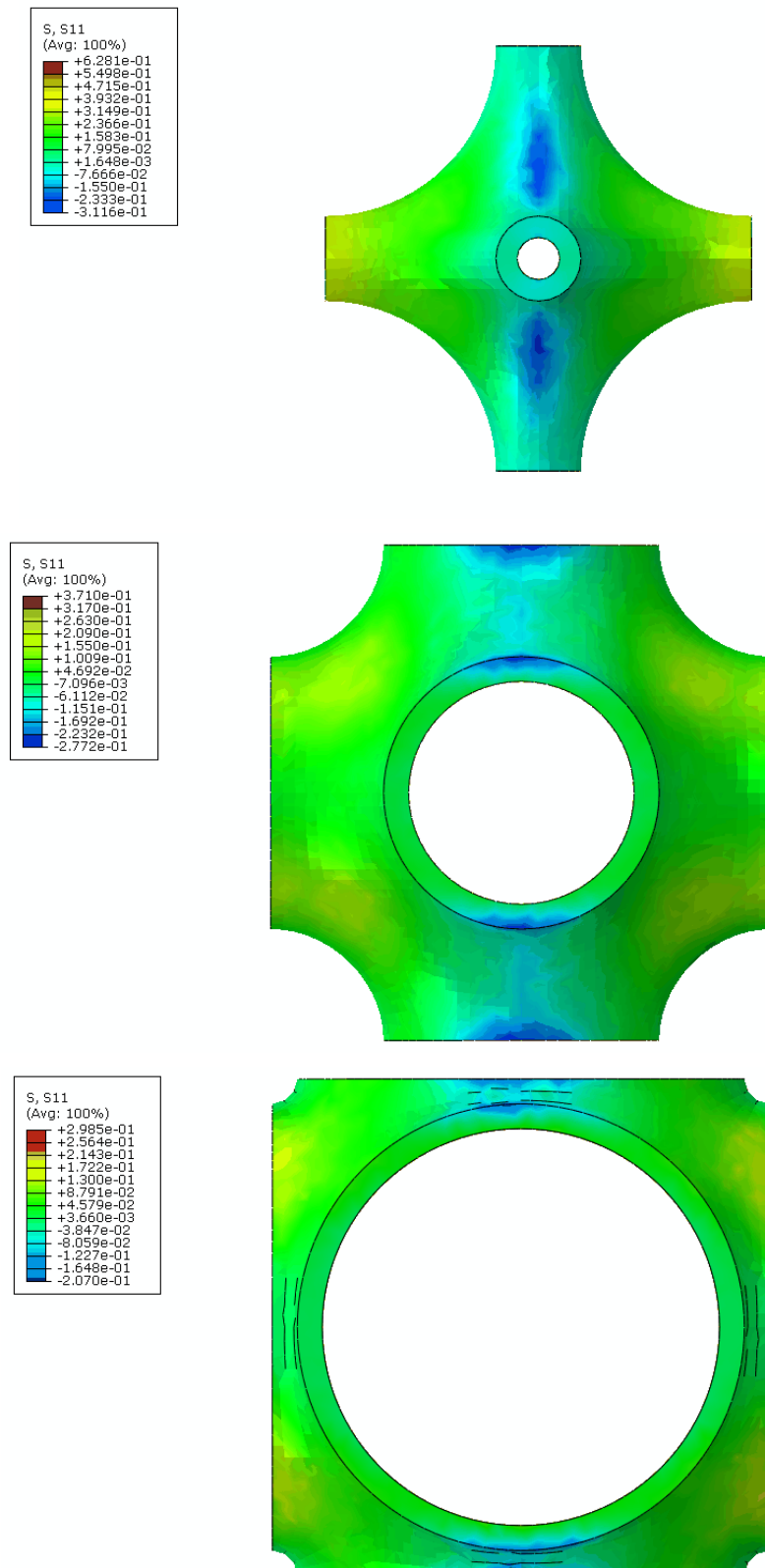


Figure 4.29 – Schwartz surface: variation of the scaffold's tensile stress with the surface radius.

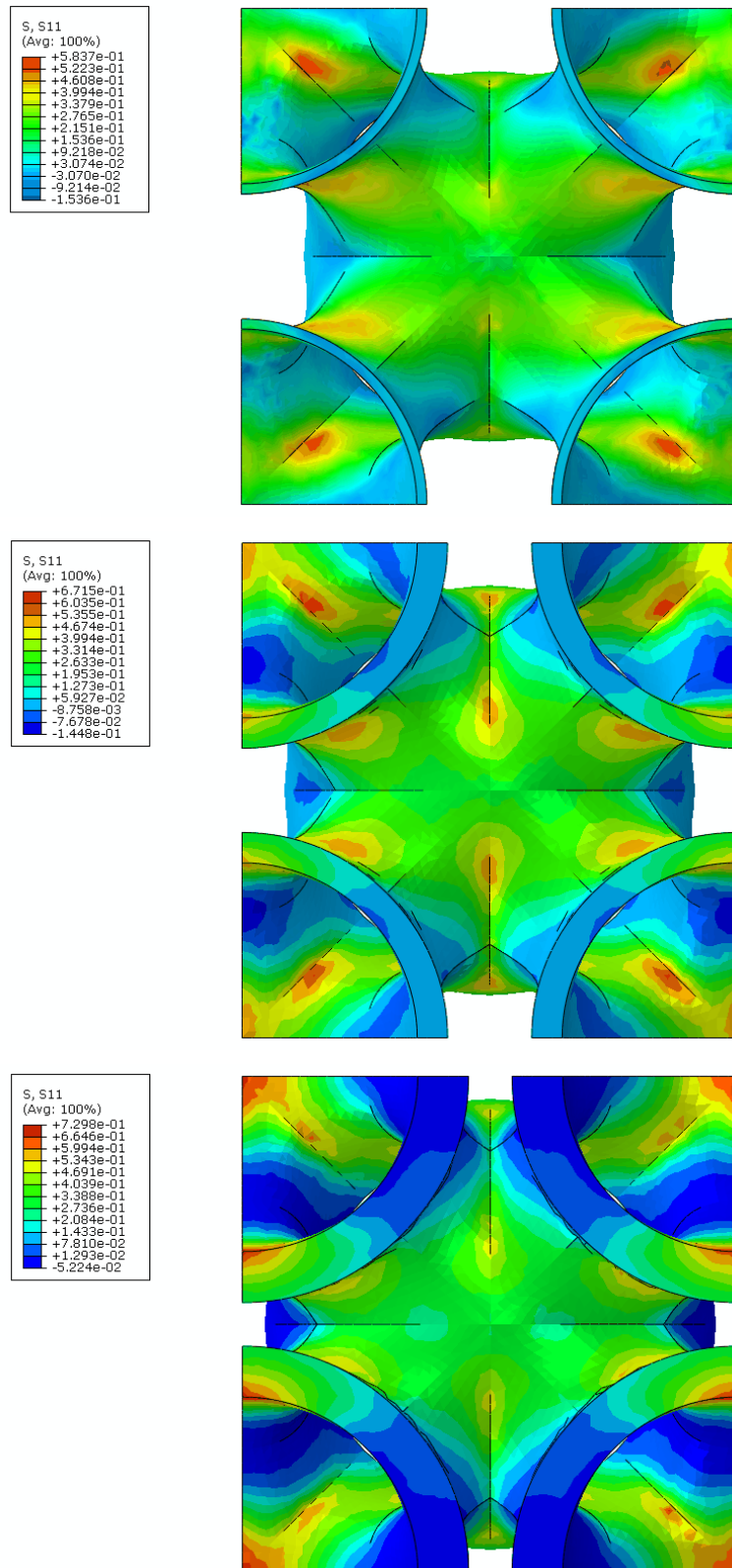


Figure 4.30 – Schoen surface: variation of the scaffold's tensile stress with the surface thickness.

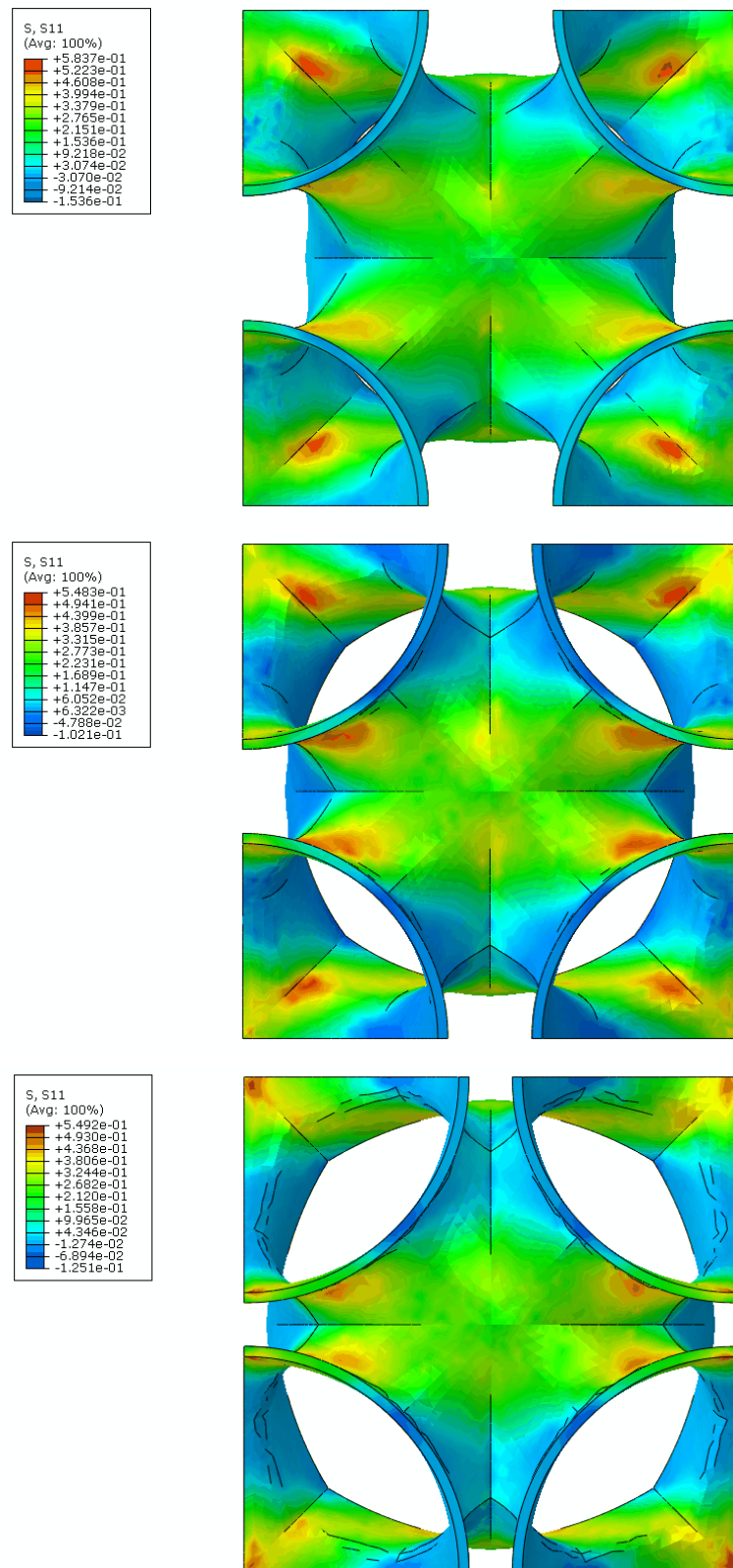


Figure 4.31 – Schoen surface: variation of the scaffold's tensile stress with the surface radius.

(c) Summary

From the numerical results, it is possible to observe that the Triple periodic minimal surface scaffolds have higher versatility of these structures and better mechanical performance for higher levels of porosity. For instance, with the same level of porosity, one may define two different Schwartz structures with two levels of mechanical behaviour. In other words, they are more advantageous for scaffold modelling. Within the triple periodic minimal surfaces, the Schwartz and Schoen surfaces have similar mechanical behaviour, in spite of the Schwartz ones that present a higher number of geometric variations for both radius and thickness variations.

4.4.2. Crushable Foam Simulations

In order to undergo the numerical compressive simulations, in addition to the material properties listed in Table 4.1, other properties were introduced along with a stress-strain curve of each material. The “Rate sensitivity via damping coefficient” is a material parameter that must be defined, in spite of not being necessary for the performed simulations. This parameter would only be used in the case of impact simulations, which is not the case being investigated.

Table 4.1 – Material compressive properties.

Pore Size [μm]	Mass Density [g/mm^3]	Bulk Modulus [MPa]	Poisson ratio	Maximum Stress [MPa]	Rate sensitivity via damping coefficient
450	0.0011	54.218	0.33	13.200	0.275 (0.05<recommended value<.50)
550		85.165		13.003	
660		51.857		9.473	

For simulation purposes, scaffolds were assumed to be rectangular structures with the following dimensions:

- length (l): 2.5 mm;
- width (w): 2.5 mm;
- height (h_0): 4.0 mm.

Additionally, it was considered a rigid body attached to the scaffold simulating the machine’s clamp (see Figure 4.32). A constant velocity of 0.1667 mm/ms was defined for the movement of the rigid block for the compression of the scaffolds. This value is 10000 higher than the experimental value (0.00001667 mm/ms). The reason for this velocity is related to computational time, as it was not possible to undergo the simulations with the real compression velocity.

The mechanical properties for the rigid body were defined in such a way that the rigid body had sufficient strength to perform the scaffold's compression without suffering any kind of deformation. The use of rigid body element is to impose deformation on another body tested without suffering deformation. A limit displacement value was also defined for the rigid body. Once it reaches 50 % of the scaffold's height, the compressive simulation is complete as the strain value reaches the value of 1.

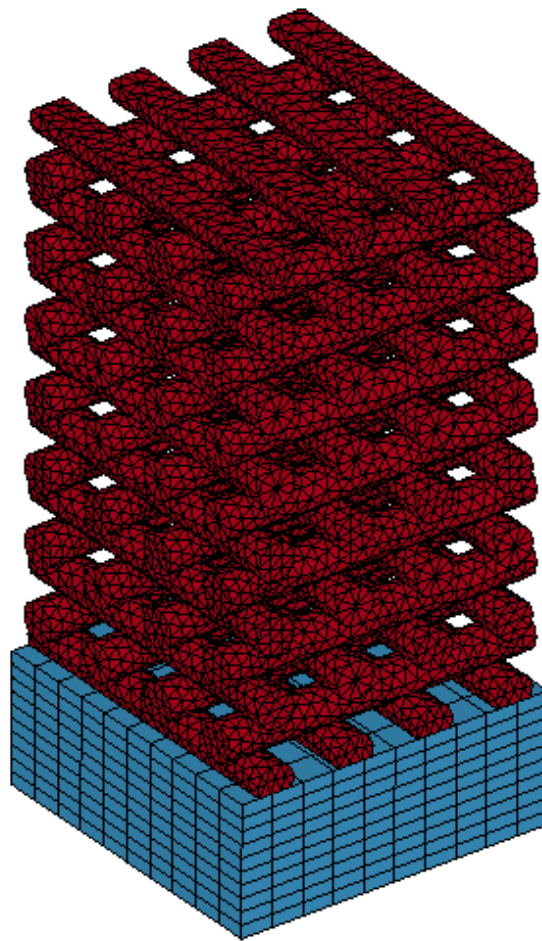


Figure 4.32 – Rigid body for compressive solicitation upon the scaffold.

Scaffolds with three different dimensions of pore sizes were considered (450, 550 and 650 μm). Figure 4.33 illustrates the numerical compressive stress-strain behaviours for the different scaffolds. It is possible to observe that as the pore size increases, the compressive strengths of the scaffolds decrease.

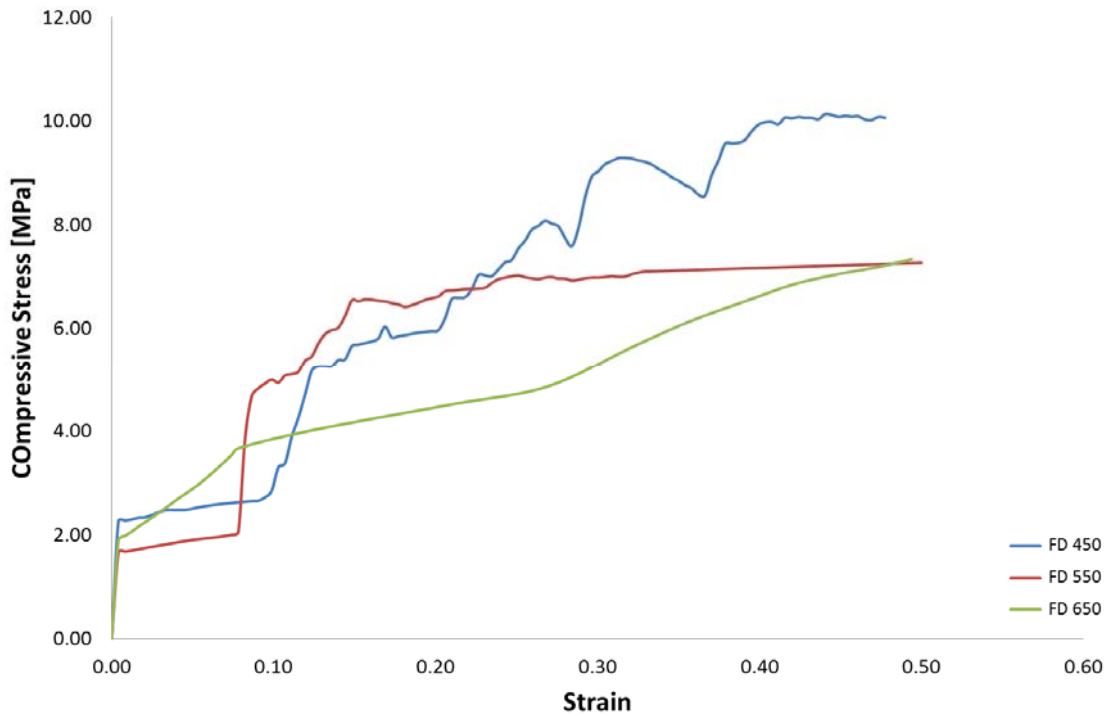


Figure 4.33 – Numerical compressive stress-strain curves for the three different pore sizes.

Figures 4.34 to 4.36 illustrate the obtained numerical stress-strain curves with the sigmoid fitted curves, while Figures 4.37 to 4.39 shows the obtained fitted stress-strain curves with the average experimental stress-strain curves. From the obtained curves, it is possible to observe that the densification phenomenon is not considered in the numerical calculations, so that the numerical calculations for the compressive simulations need to be optimised. From the comparisons of the experimental results and the fitted curves, it is possible to observe that the scaffold with a pore size of 550 μm presents the most significant deviation, at the end of the compression cycle.

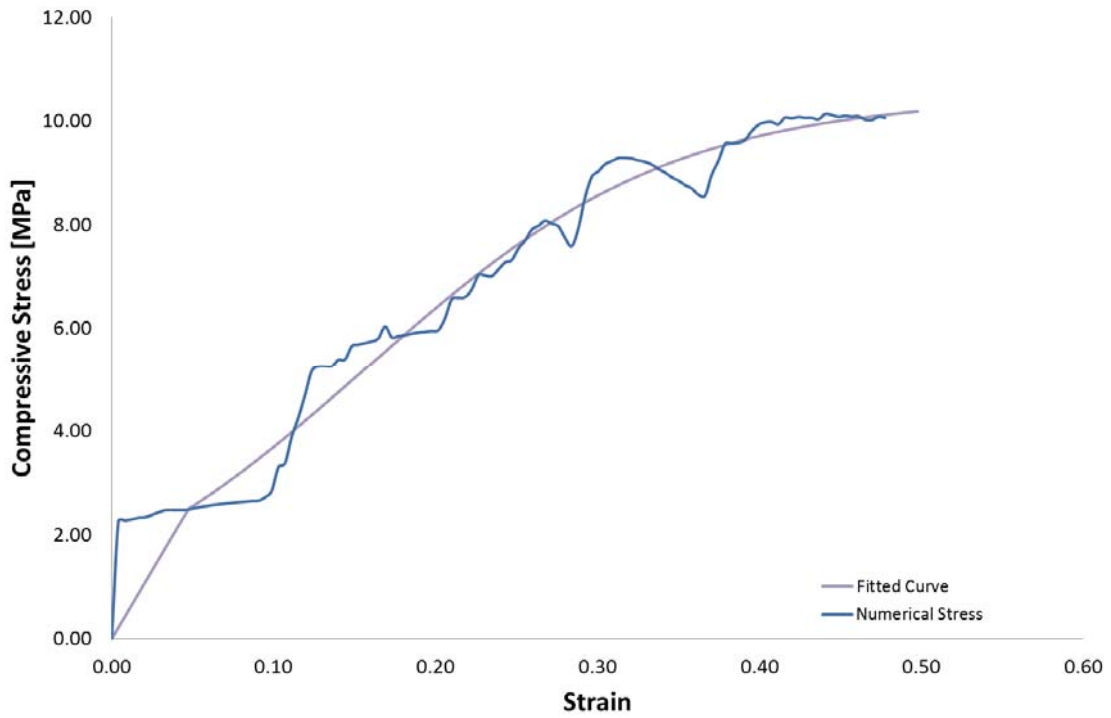


Figure 4.34 – Comparison between the numerical stress-strain curve and the sigmoid fitted curve for the scaffold with a pore size of 450 μm .

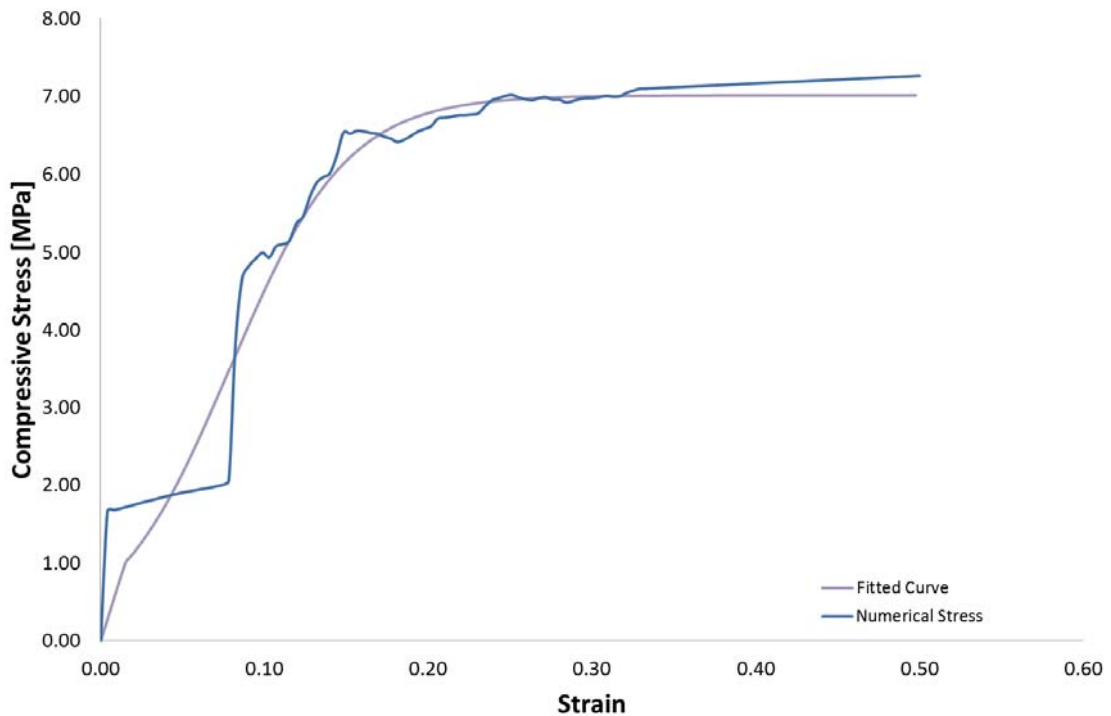


Figure 4.35 – Comparison between the numerical stress-strain curve and the sigmoid fitted curve for the scaffold with a pore size of 550 μm .

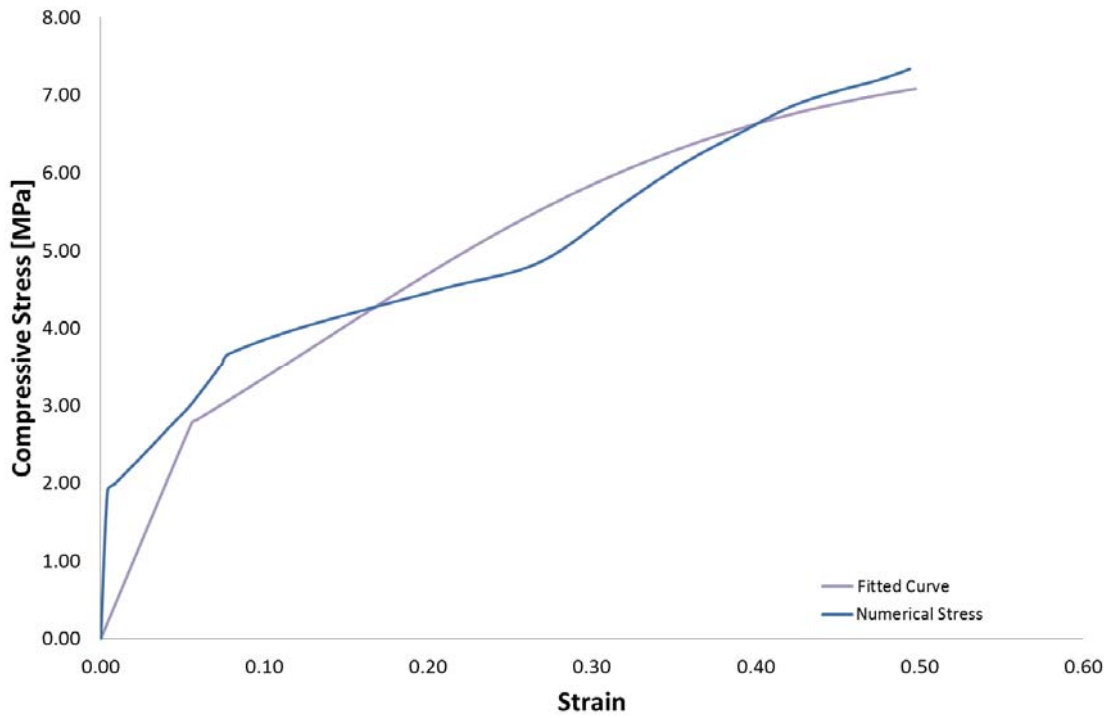


Figure 4.36 – Comparison between the numerical stress-strain curve and the sigmoid fitted curve for the scaffold with a pore size of 650 μm .

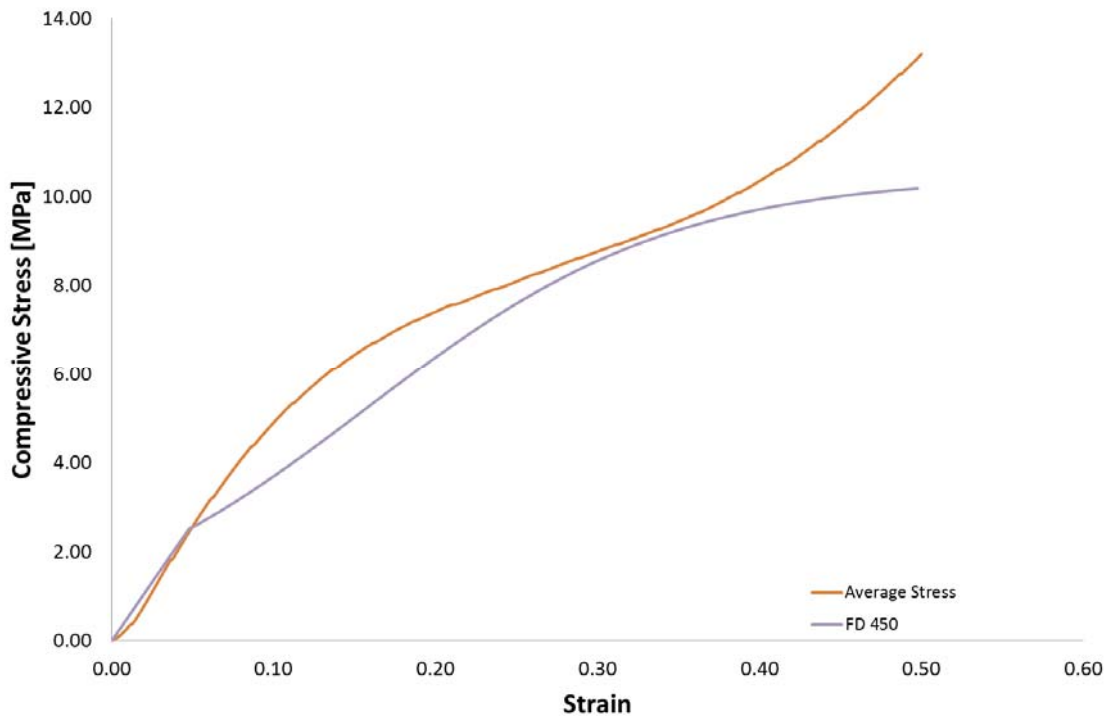


Figure 4.37 – Comparison between the numerical stress-strain curve and the sigmoid curve fitting for the scaffold with a pore size of 450 μm .

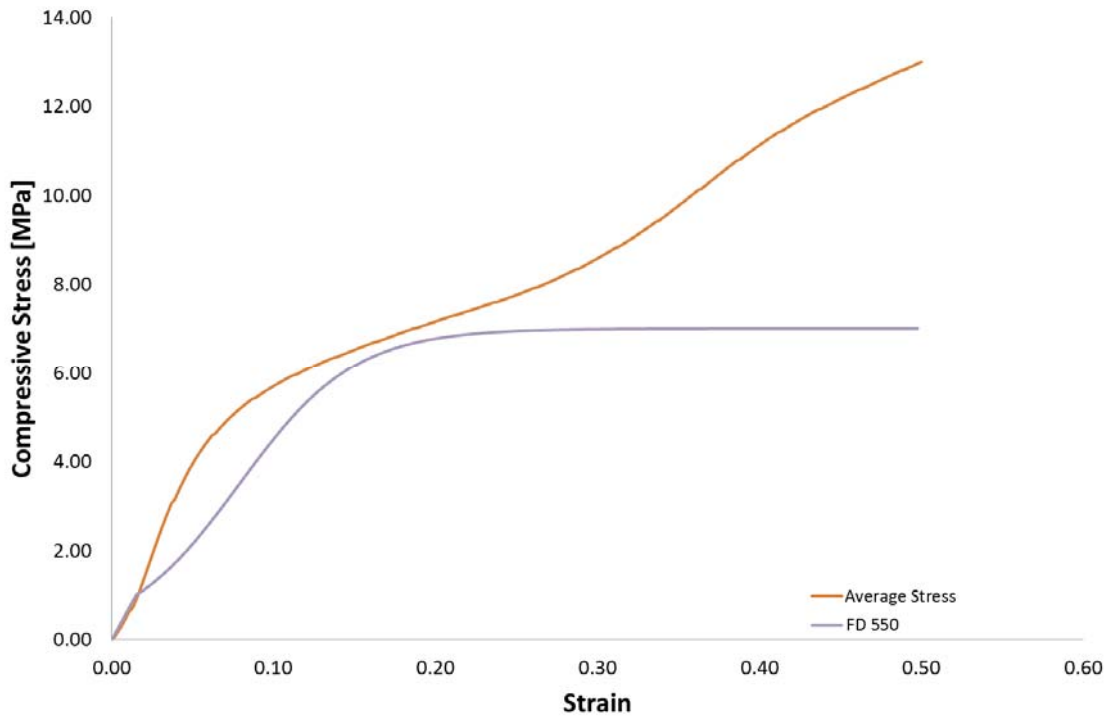


Figure 4.38 – Comparison between the average stress-strain curve and the sigmoid curve fitting for the scaffold with a pore size of 550 μm .

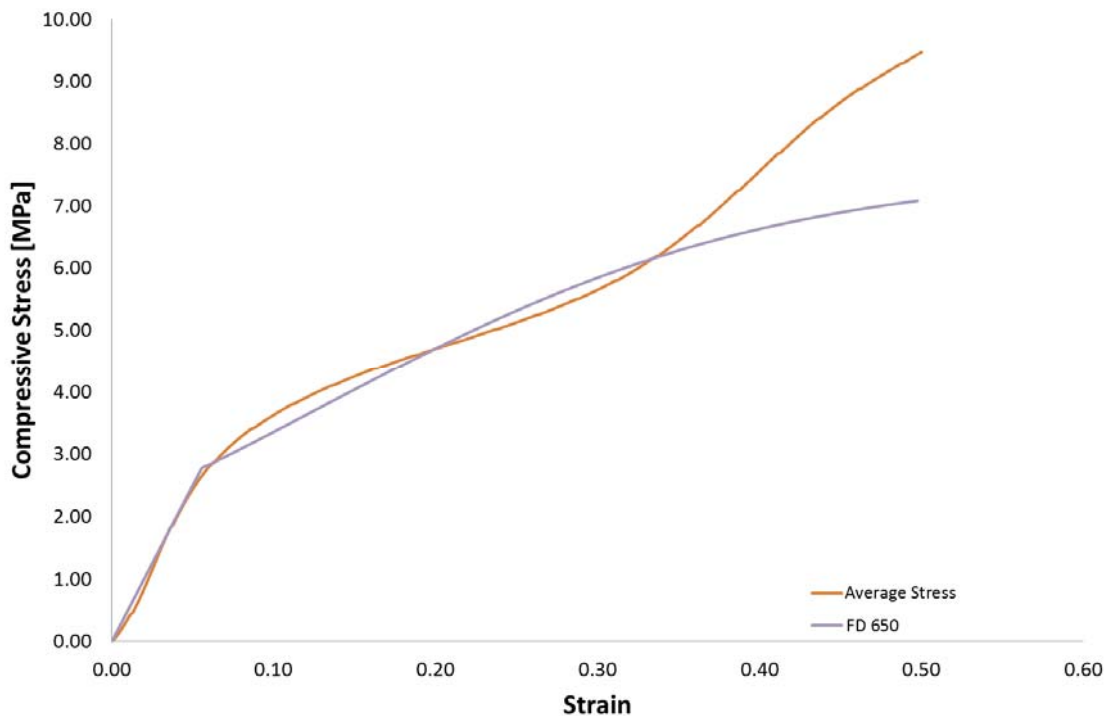


Figure 4.39 – Comparison between the average stress-strain curve and the sigmoid curve fitting for the scaffold with a pore size of 650 μm .

Using numerical simulations, it is possible to visualize the compressive testing during the calculation time cycle. From these numerical simulations, stress and strain plots were obtained at the following time steps of the compressive testing: 20 %, 40 %, 60 %, 80 % and 100 %. Figures 4.40, 4.41 and 4.42 illustrate the strain behaviour for each scaffold pore size. Figures 4.43, 4.44 and 4.45 illustrate the stress behaviour for each scaffold pore size.

Results show that the scaffold with a pore size of 450 μm presents the highest densification, presenting the smallest deviation between the numerical and experimental stress-strain curves. Regarding the scaffold with a pore size of 550 μm , since the scaffold's filaments tend to bulge outwards of the scaffold, which results in a structure that presents the lowest densification compared to the other scaffolds and the experimental results, that's why the numerical stress-strain curve for the scaffold with a pore size of 550 μm presents the biggest deviation between the numerical and experimental stress-strain curves. Regarding the scaffold with a pore size of 650 μm , Figures 4.44 and 4.45 illustrate a more balanced compression, except in the centre of the scaffold, when compared to the other scaffold structures. The three structures tend to bulge outwards when undergoing the compressive simulations, the smaller is the bulge phenomenon, the higher is the densification, presenting a good agreement between the numerical curves and the experimental curves.

In order to optimise the numerical simulations, two aspects need to be addressed. One regards the filament's contact and penetration parameters. The other one aspect relates to the mesh elements of the scaffolds. The CAD models present 100 % symmetry in all three axes, although the obtained meshed body do not present 100 % symmetry resulting in an unbalanced bulge phenomenon, during the compressive testing. In the case of the meshed elements present 100 % symmetry within the meshed body, the densification phenomenon could be more significant in all three scaffolds, due to a higher balanced compression process of the structures. Nonetheless, due to the complexity of the structures, a mesh with 100% symmetry is difficult to obtain.

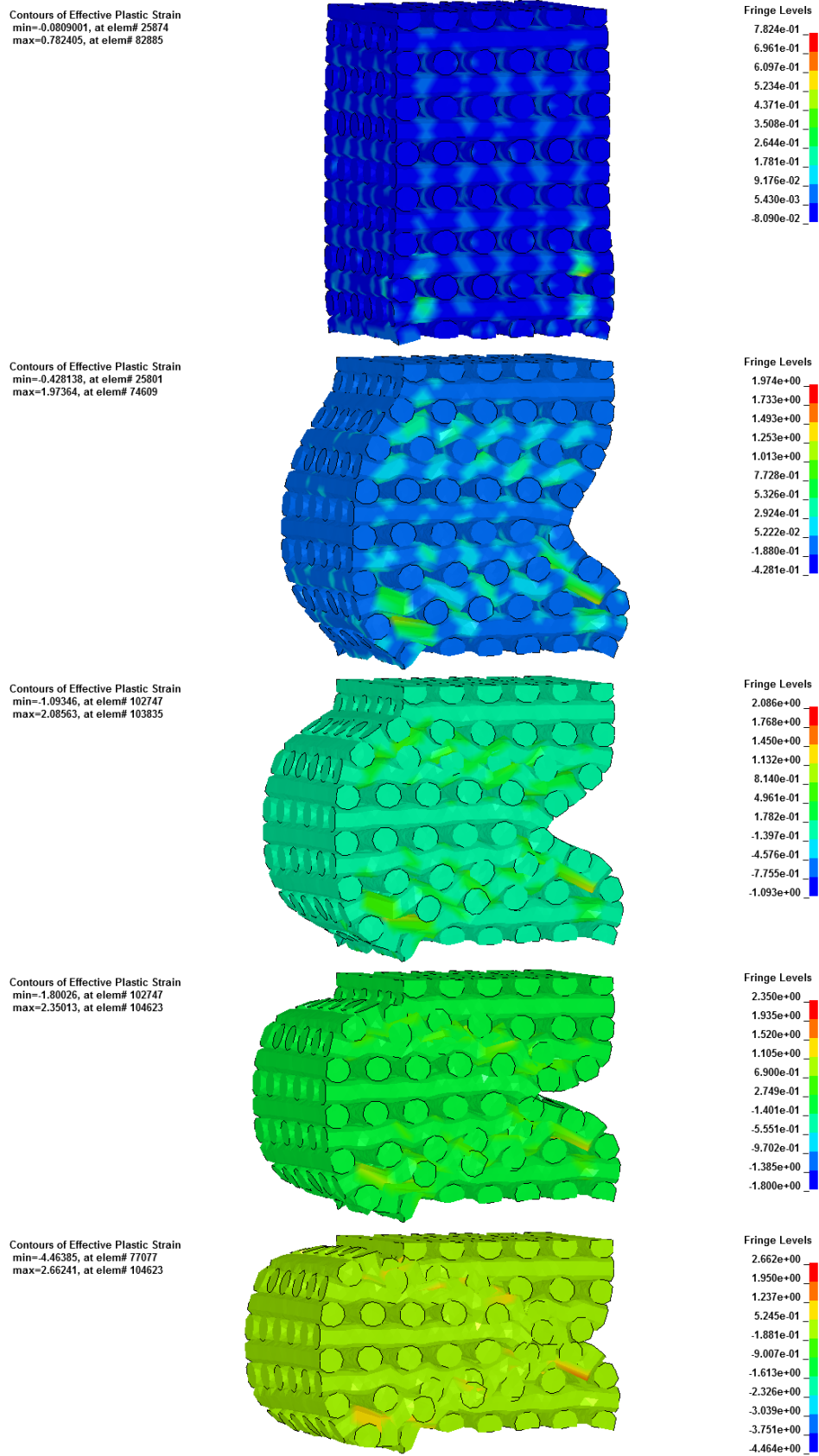


Figure 4.40 – Strain variation regarding increments of 20% of compression for the scaffold with a pore size of 450 μm .

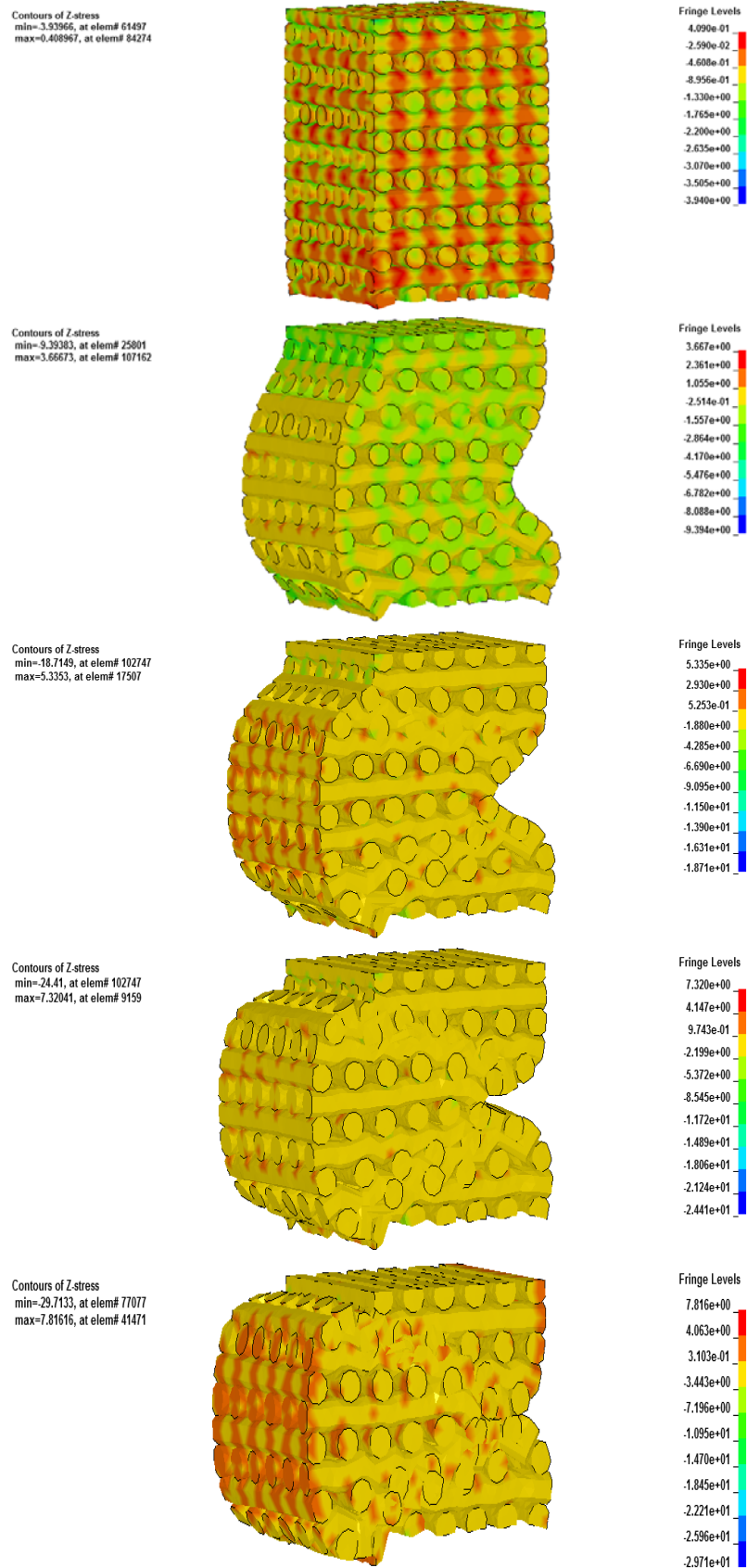


Figure 4.41 – Stress variation regarding increments of 20% of compression for the scaffold with a pore size of 450 μm .

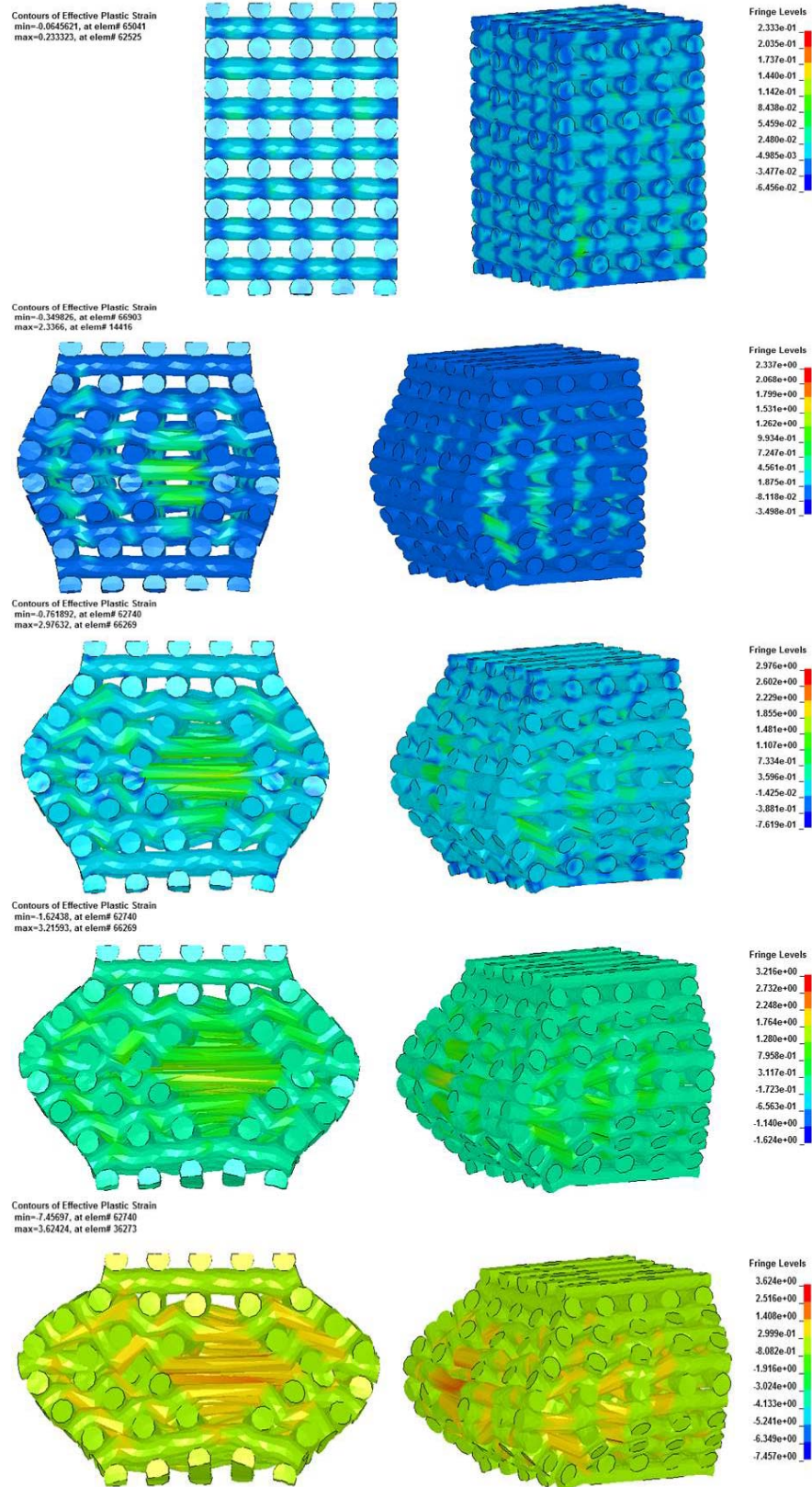


Figure 4.42 – Strain variation regarding increments of 20% of compression for the scaffold with a pore size of 550 μm .

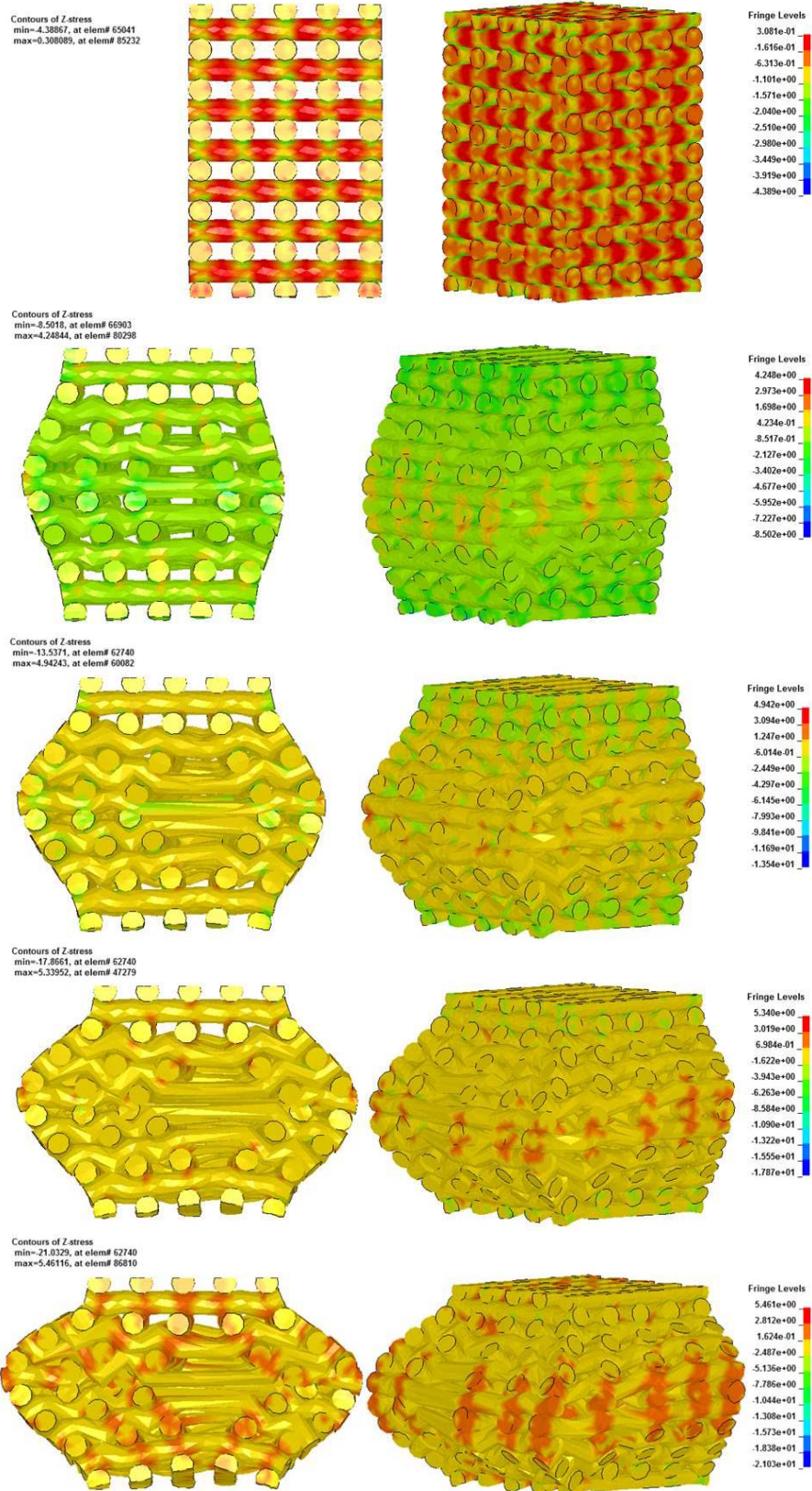


Figure 4.43 – Stress variation regarding increments of 20% of compression for the scaffold with a pore size of 550 μm .

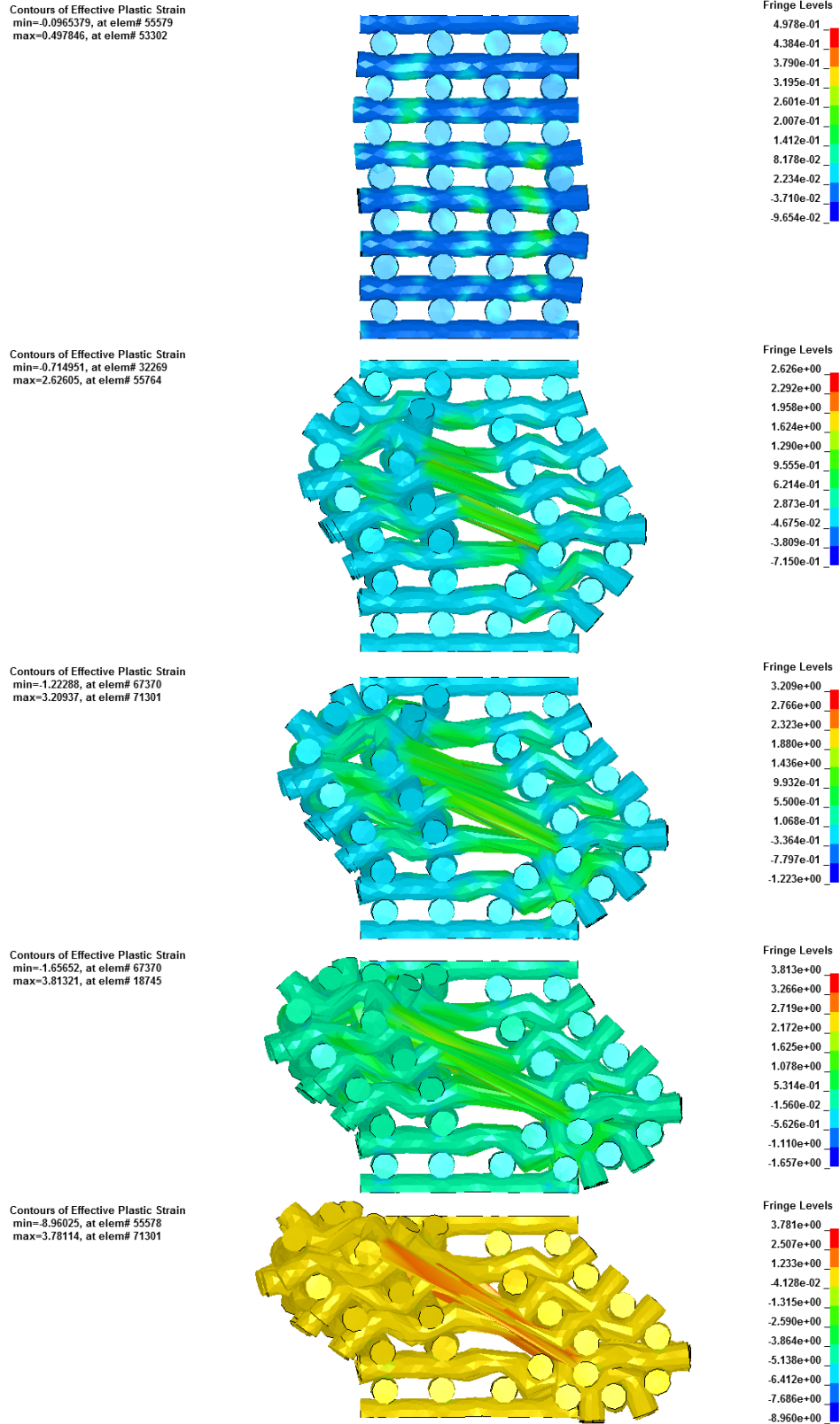


Figure 4.44 – Strain variation regarding increments of 20% of compression for the scaffold with a pore size of 650 μm .

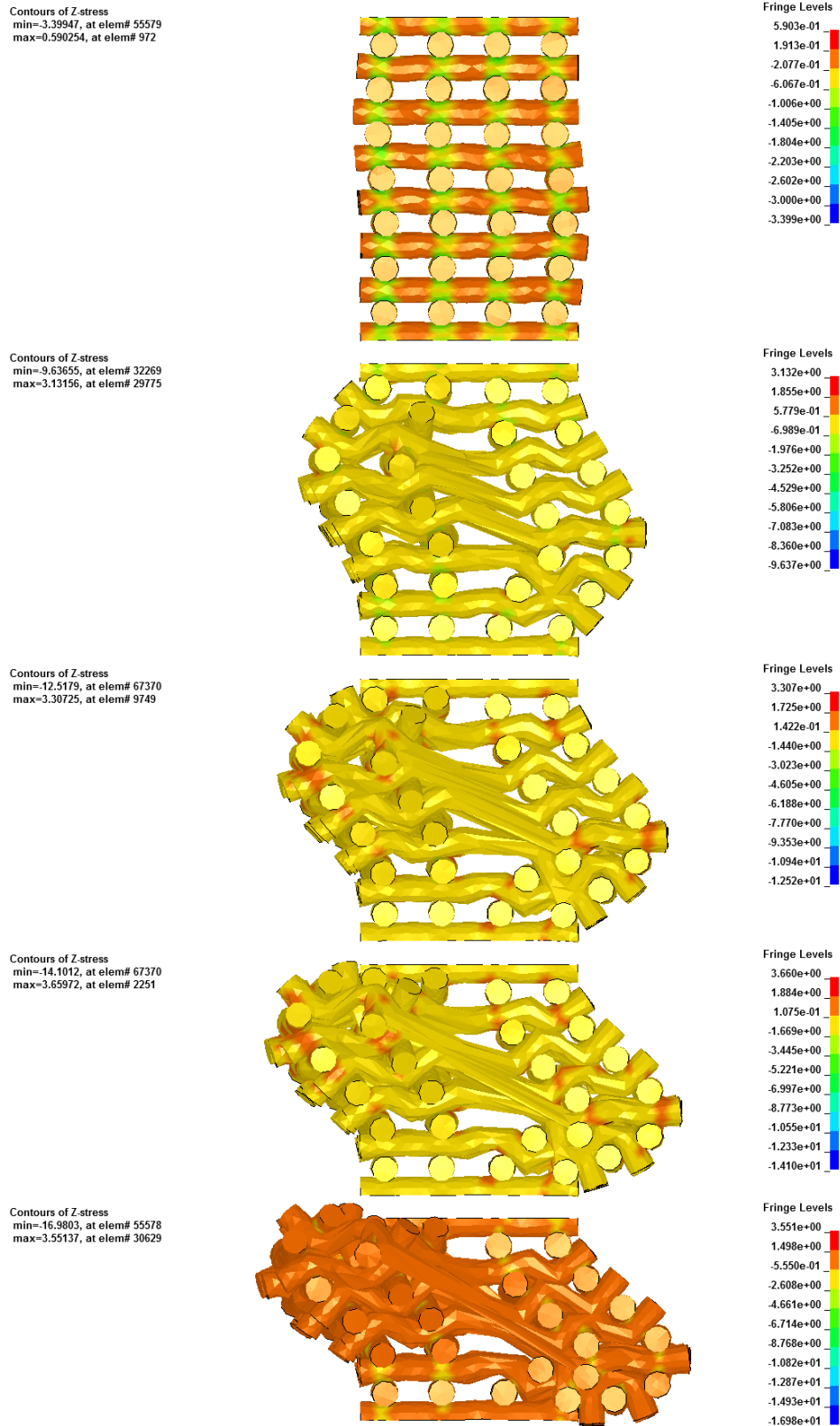


Figure 4.45 – Stress variation regarding increments of 20% of compression for the scaffold with a pore size of 650 μm .

(a) Summary

For the crushable foam simulations, the scaffold with a pore size of 450 μm presented the best numerical results when compared to the experimental data. In order to present a better agreement between the numerical stress-strain curves and the experimental ones, the numerical parameters of all three structures need to be optimised. Moreover, a symmetric meshed body also needs to be defined.

Chapter 5 – Vascular Analysis of Scaffolds for Tissue Engineering

5.1. Vascular Behaviour of Scaffolds in Tissue Engineering

Most tissues in the body rely on blood vessels to supply the individual cells with nutrients and oxygen. For a tissue to grow beyond 100-200 μm (the diffusion limit of oxygen), new blood-vessel formation is required (Carmeliet and Jain, 2000), and this is also true for tissue-engineered constructs. During *in vitro* culture, larger tissue-engineered constructs can be supplied with nutrients, for instance in perfusion bioreactors (Janssen *et al*, 2006; Portner *et al*, 2005). However, after implantation of tissue constructs, the supply of oxygen and nutrients to the implant is often limited by diffusion processes that can only supply cells in a proximity of 100-200 μm from the next capillary. In order for implanted tissues of greater size to survive, the tissue has to be vascularised, which means that a capillary network capable of delivering nutrients to the cells is formed within the tissue. After implantation, blood vessels from the host generally invade the tissue to form such a network, in part in response to signals that are secreted by the implanted cells as a reaction to hypoxia (Rouwkema *et al*, 2008).

However, this spontaneous vascular ingrowth is often limited to several tenths of micrometres per day (Clark and Clark, 2005), meaning that the time needed for complete vascularisation of an implant of several millimetres is in the order of weeks. During this time, insufficient vascularisation can lead to nutrient deficiencies and/or hypoxia deeper in the tissue. Moreover, nutrient and oxygen gradients will be present in the outer regions of the tissue, which could result in non-uniform cell differentiation and integration and thus decreased tissue function (Malda *et al*, 2004).

As an attempt to overcome this issue, Mironov *et al* (2009) used an additive manufacturing technique based on organ printing of tissue spheroids as building blocks for the biofabrication of living organs composed of both functional organ tissue and an internal branched vascular tree. Closely placed tissue spheroids undergo tissue fusion, a process that represents a fundamental biological and biophysical principle of developmental biology-inspired directed tissue self-assembly. It is possible to engineer small segments of an intra-organ branched vascular tree by using solid and lumenized vascular tissue spheroids. By using two types of spheroids, one for the organ tissue and the other for the vascular tree, and with the aid of the tissue fusion process, it is possible to obtain an organ fully vascularised. Figure 5.1 represents a roadmap proposed by Mironov *et al* (2009) for the biofabrication of vascularised organs.

Because the speed of vascularisation after implantation is a major problem in tissue engineering, the successful use of tissue-engineered constructs is currently limited to thin or avascular tissues, such as skin or cartilage, for which post-implantation neovascularisation from the host is sufficient to meet the demand for oxygen and nutrients (Jain *et al*, 2005). To succeed in the application of tissue engineering for bigger tissues, such as bone and muscle, the problem of vascularisation has to be solved (Johnson *et al*, 2007).

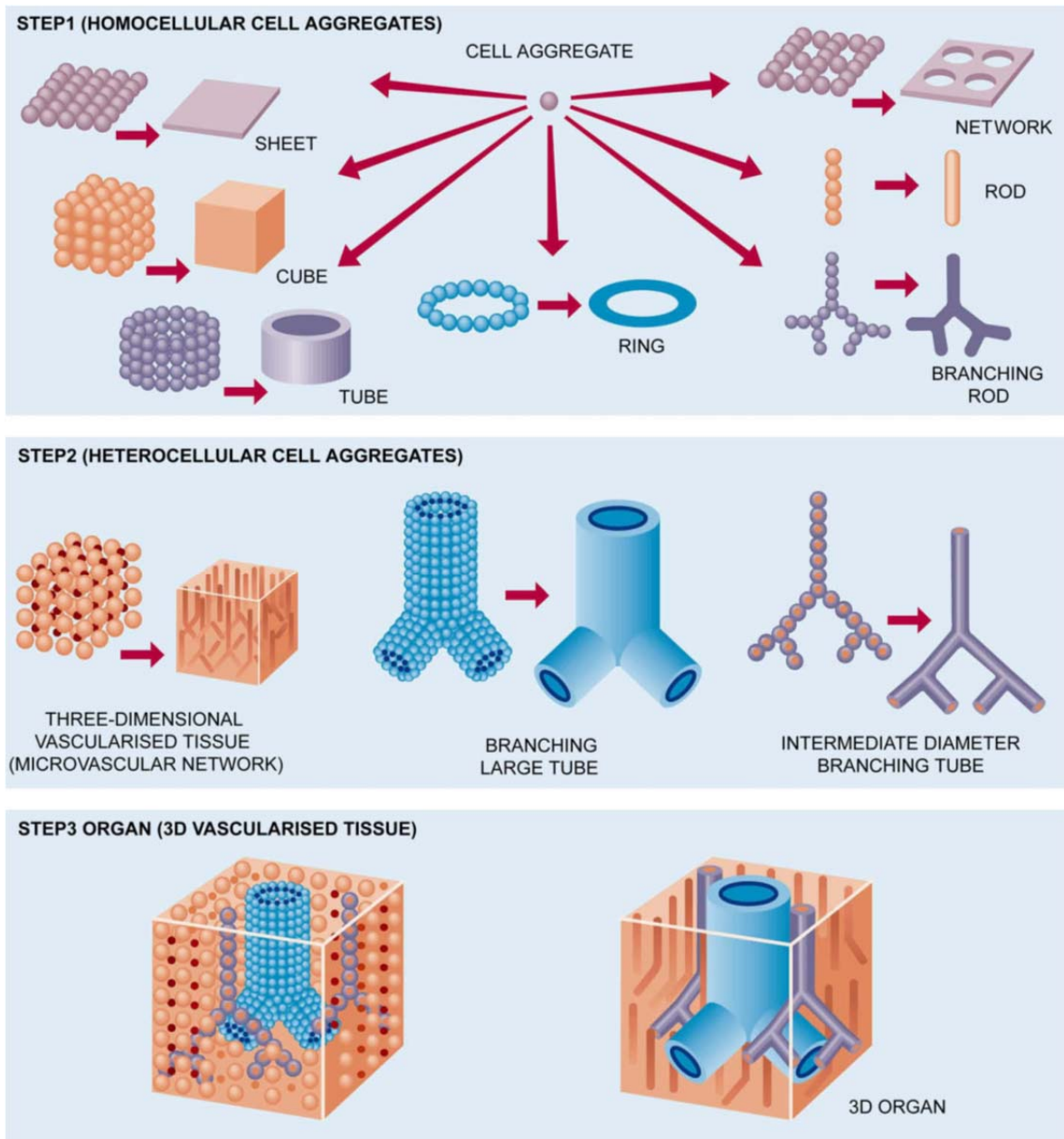


Figure 5.1 – Roadmap for the biofabrication of organs fully vascularised (Mironov *et al*, 2009).

5.2. Blood Characteristics

Blood is a specialized bodily fluid composed of a liquid called blood plasma and blood cells suspended within the plasma. The blood cells present in blood are red blood cells (also called erythrocytes), white blood cells (including both leukocytes and lymphocytes) and platelets (also called thrombocytes). Plasma is predominantly water containing dissolved proteins, salts and many other substances, which amounts up to 55% of blood by volume (Humphrey and Delange, 2003).

The most abundant cells in blood are by far red blood cells. These cells contain hemoglobin, an iron-containing protein, which facilitates transportation of oxygen by reversibly binding to this respiratory gas and greatly increasing its solubility in blood. In contrast, carbon dioxide is almost entirely transported extracellularly dissolved in plasma as bicarbonate ion. White blood cells help to resist infections and parasites, and platelets are important in blood clotting (Humphrey and Delange, 2003).

Blood is circulated around the body through blood vessels by the pumping action of the heart. Arterial blood carries oxygen from inhaled air to the body tissues and venous blood carries carbon dioxide, a waste product of metabolism produced by cells, from the tissues to the lungs to be exhaled. One aspect that must always be taken into account is that blood properties vary with factors such as age, gender, race and health. All these make it impossible to define a specific value for a certain blood property, for instance its density (Humphrey and Delange, 2003).

Blood pressure refers to the force exerted by circulating blood within the walls of blood vessels. The pressure of the circulating blood decreases as blood moves through arteries, arterioles, capillaries, and veins. Usually, blood pressure refers to arterial pressure, i.e., the pressure in the larger arteries, where arteries are the blood vessels taking blood away from the heart. Arterial pressure is most

commonly measured via a sphygmomanometer, which uses the height of a column of mercury to determine the circulating pressure. Although many modern vascular pressure devices no longer use mercury, vascular pressure values are still universally reported in millimetres of mercury (mmHg) (Humphrey and Delange, 2003).

The systolic arterial pressure is defined as the peak pressure in the arteries, which occurs near the beginning of the cardiac cycle, while the diastolic arterial pressure is the lowest pressure at the resting phase of the cardiac cycle. The average pressure throughout the cardiac cycle is a mean arterial pressure, while the pulse pressure reflects the difference between the maximum and minimum pressures measured (Humphrey and Delange, 2003).

Typical values for a resting, healthy adult human are approximately 120 mmHg (16 kPa) systolic and 80 mmHg (11 kPa) diastolic with large individual variations. These measures of arterial pressure are not static, but undergo natural variations from one heartbeat to another, as well throughout the day in a circadian rhythm. They also change in response to stress, nutritional factors, drugs, or disease. Hypertension refers to arterial pressure being abnormally high, as opposed to hypotension, when it is abnormally low. Blood pressure measurements are the most commonly measured physiological parameters along with body temperature (Humphrey and Delange, 2003).

5.3. Constitutive Equation of Blood Flow

Blood is not a homogeneous medium mainly consisting of plasma and a suspension of red blood cells. White cells, or leukocytes, and platelets present in smaller concentrations, play an important role in biochemical processes, like immune response, inflammation, and coagulation (Humphrey and Delange, 2003). Whole blood has a pseudoplastic flow behaviour (Figure 5.2), characterized by a viscosity (resistance to flow) that is lower at higher shear rates than at lower shear rates. A pseudoplastic behaviour is also called shear thinning, mainly due to particles within the fluid aggregating at low shear rates but "breaking" at higher shear rates, which lowers the viscosity (Humphrey and Delange, 2003). Red blood cells tend to aggregate at lower shear rates, a phenomenon known as rouleaux (Figure 5.3), which depends on the presence of fibrinogen and globulins (Humphrey and Delange, 2003). In the limit, as the shear rate goes to zero, the blood will tend to further aggregate, eventually leading to a process known as clotting, which involves additional mechanisms, including platelet activation and the conversion of fibrinogen to fibrin, an essential component of a clot. As the shear rate increases from low, but nonzero values, the rouleaux break up and blood behaves like a Newtonian fluid. The latter is often assumed in large arteries with a viscosity $\mu \sim \text{constant}$ (often cited to be ~ 3.5 cP, or centiPoise) and the Navier–Poisson equations to describe most blood flows. Plasma (whole blood minus cells) always behaves as a Newtonian fluid, with a viscosity $\mu \sim 1.2$ cP (Humphrey and Delange, 2003). In capillaries, which are $\sim 5\text{--}8$ μm in diameter, the red blood cells go through one at a time, with plasma in between. In this case, the blood should be treated as a two-phase flow – a solid and a fluid mixture (Humphrey and Delange, 2003).

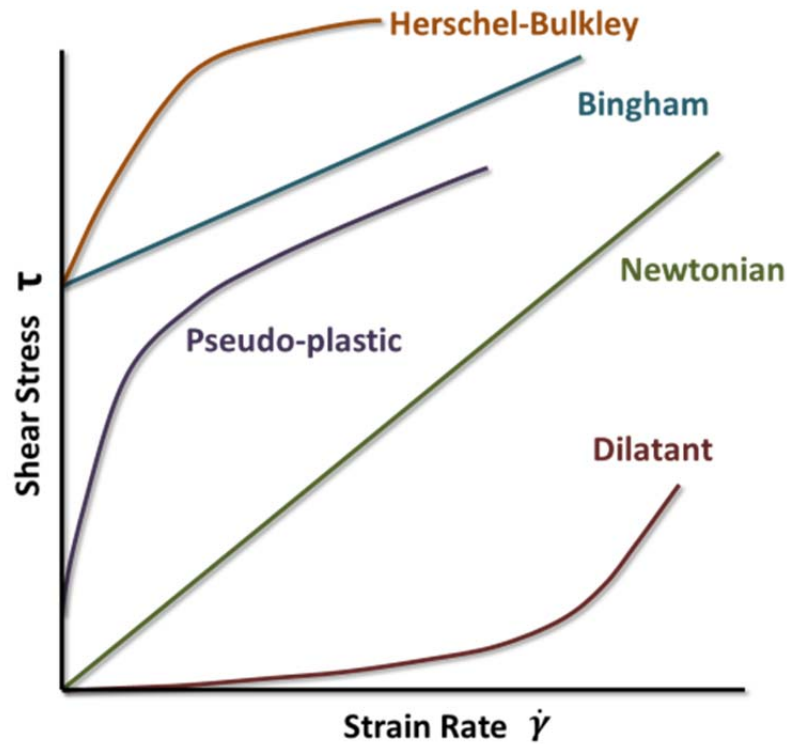


Figure 5.2 – Illustration of Newtonian and Non-newtonian fluid behaviour.

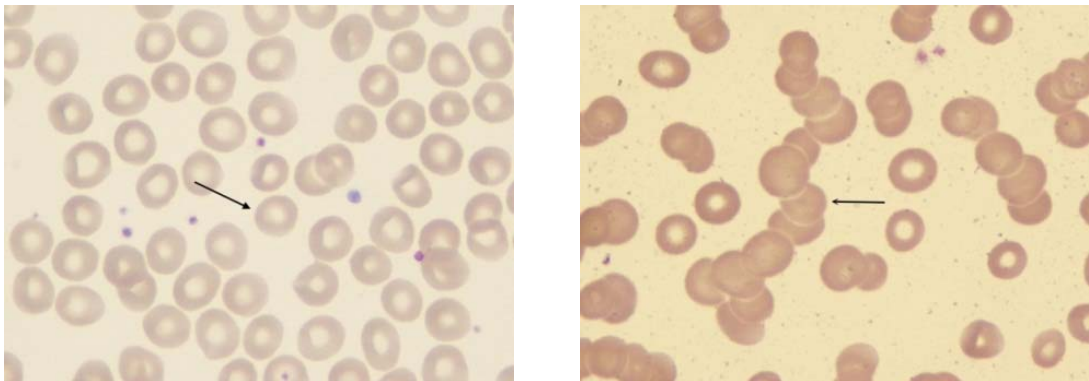


Figure 5.3 – Illustration of single red blood cells and an aggregate of red blood cells, rouleaux phenomenon.

Because of its non-Newtonian behaviour, whole blood has been modelled using various relations. For example, Fung (1990) advocates the following blood model:

$$\begin{aligned}
 \sigma_{xx} &= -p + 2\eta(J_2)D_{xx} & \sigma_{xy} &= 2\eta(J_2)D_{xy} \\
 \sigma_{yy} &= -p + 2\eta(J_2)D_{yy} & \sigma_{yz} &= 2\eta(J_2)D_{yz} \\
 \sigma_{zz} &= -p + 2\eta(J_2)D_{zz} & \sigma_{xz} &= 2\eta(J_2)D_{xz}
 \end{aligned} \tag{5.1}$$

where

$$\eta(J_2) = \frac{1}{\sqrt{J_2}} \left((\mu^2 J_2)^{1/4} + \frac{1}{\sqrt{2}} \sqrt{\tau_y} \right)^2 \quad (5.2)$$

$$J_2 = \frac{1}{2} (D_{xx} + D_{yy} + D_{zz} + 2D_{xy}D_{yx} + 2D_{xz}D_{zx} + 2D_{yz}D_{zy}) \quad (5.3)$$

and μ is a viscosity at a high shear rate and τ_{xy} is a solid-like yield stress at low shear rates.

Plasma is considered to have a Newtonian behaviour as mentioned before, D_{xy} is nonzero and all other components of $[D]$ are zero. Hence, Fung's relation reduces to

$$\sigma_{xy} = 2\eta(J_2)D_{xy} \quad (5.4)$$

when

$$\eta(J_2) = \frac{1}{\sqrt{D_{xy}^2}} \left((\mu^2 D_{xy}^2)^{1/4} + \frac{1}{\sqrt{2}} \sqrt{\tau_y} \right)^2 \quad (5.5)$$

When D_{xy} is very small, η tends to become large, its value depending largely on the values of $\tau/2D_{xy}$; τ_y is also small, usually on the order of 0.005 Pa. Conversely, when D_{xy} is large, the yield stress becomes negligible and $\eta \cong \mu$, the Newtonian case wherein $\sigma_{xy} = 2\mu D_{xy}$. Hence, Fung's relation accounts for the pseudoplastic character illustrated in Figure 5.2, including Newtonian behaviour at high shear rates (Humphrey and Delange, 2003; Fung, 1990).

5.4. Scaffold Vascularisation

The architecture and design of a scaffold has a profound effect on the rate of vascularisation after implantation (Almeida and Bártolo, 2008; 2007). First, the pore size of the scaffold is a critical determinant of blood-vessel ingrowth. Druecke *et al* (2004) showed that vessel ingrowth was significantly faster in scaffolds with pores greater than 250 μm than in those with smaller pores. However, it is not only the pore size that is important for vascularisation: the interconnectivity of the pores is also significant because cell migration, and thus vascularisation, will be inhibited if pores are not interconnected, even if the scaffold porosity is high (Laschke *et al*, 2006; Karageorgiou and Kaplan, 2005; Yang *et al*, 2001).

The flow of the biological medium through the scaffold is necessary to provide the cells with nutrients and oxygen and flush out the metabolic products (Vossenber *et al*, 2009). The success of cell attachment to the scaffold depends on the flow regime. High flows cause high shear stress (Martin and Vermette, 2005) and prevent attachment of cells to the scaffold surface, already attached cells may be damaged or hindered in proliferation. Shear stress is also considered as an important parameter for *in vivo* systems. Wang and Tarbell (2000) found by experiments for smooth-muscle cells that with increasing shear stress the production of prostaglandins increased. The results of Wang and Tarbell (2000) indicate that the blood flow rate plays an important role in the signal communication system from the blood vessels to the smooth muscle cells.

When designing a scaffold, the shear stress that acts on the fibres of the scaffold on which the cells grow must therefore be considered as a design parameter. Shear stress is proportional to the velocity gradient and is a function of design parameters such as fibre diameter and distance between the fibre centres and operational variables such as fluid velocity (Vossenber *et al*, 2009).

For *in vitro* cultures such as in bioreactors, the cells are subjected to a continuous fluid flow of nutrients. It has been proven that the fluid flow induces a stress upon the cells that are attached to the walls of the scaffolds, namely the wall shear stress. Higher values of wall shear stress decrease the cell's ability to attach to the wall of the scaffold, or eventually it also removes the attached cells and may kill them when the values are too high. Lower values also don't offer the necessary stimuli that the cells need for a healthy proliferation and/or differentiation. In other words, each cell type has its appropriate shear stress value. In the following table, shear stresses regarding optimum, critical and death values for several cell types are presented. Table 5.1 presents several Shear Stress values that are optimum, natural or even lethal for cell cultures within bioreactors.

Table 5.1 – Shear Stress values for cell cultures within bioreactors.

Cell Type	Process	Shear Stress (Pa)	References
Osteoblasts	Osteogenesis	5×10^{-5} – optimum	Cartmell <i>et al</i> (2003)
		5.7×10^{-2} – death	Porter <i>et al</i> (2005)
Osteocytes		0.5 a 1.5 – optimum	Godara <i>et al</i> (2008)
Chondrocytes	Chondrogenesis	0.1 – natural	Schinagl <i>et al</i> (1999)
Smooth Muscle Cells	Myogenesis	0.5 a 2.5 - optimum	Martin and Vermette (2005)
Cardiomyocytes		0.24 – death	Radisic <i>et al</i> (2008)
Hepatocytes	Others	0.033 – optimum	Park <i>et al</i> (2008)
		0.5 – critical	
Cardiac Valve Cells		2.2 – optimum	Martin and Vermette (2005)

5.5. Vascular Simulation

The main goal for simulating the scaffold vascular behaviour is to evaluate the porosity dependence on both Wall Shear Stress and Shear Stress Rates on the surface of the scaffold. These two parameters are the most critical due to the fact that they contribute to the cell's performance regarding their proliferation and differentiation along the scaffold structure internally and externally.

If the scaffold is hosted within a biofluid rich environment, the first step is to obtain the geometric representation the existing biofluid, in other words, the empty space within the scaffold unit (Figure 5.4). Figure 5.5 illustrates the unfilled volumes of the scaffold units, which represents the biofluid volume.

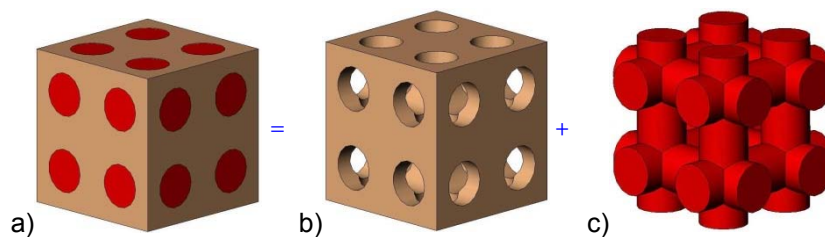


Figure 5.4 – Illustration of a scaffold hosted within a biofluid environment and the resulting volumes
a) scaffold with biofluid b) scaffold and c) biofluid geometry.

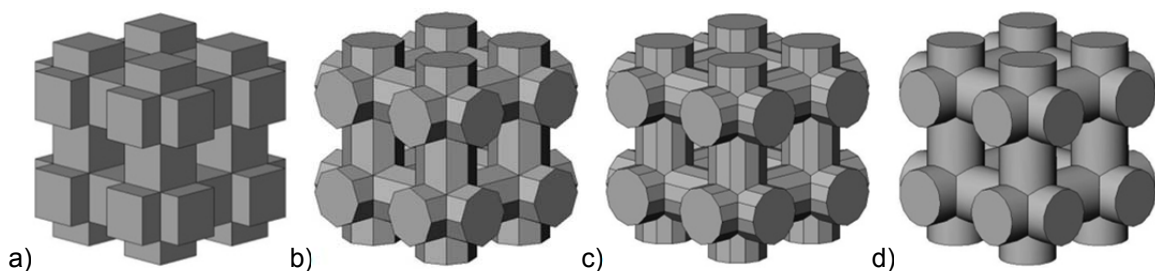


Figure 5.5 – The family of scaffolds representing the volume related with the flow of biofluids inside the human body, which is classified according to the number of faces per pore. a) 4f unit, b) 8f unit, c) 12f unit and d) cf unit.

Flow simulation enables to study biofluid mass flow, pressure and fluid velocity for different scaffold topologies. For simulation purposes, it was considered for the biofluid a density of 1080 kg/m^3 and a dynamic viscosity of 0.0035 Pa s . The inlet and outlet values correspond to a blood pressure flow of 100 mm Hg . The inlet and outlet of the biofluid flow within a scaffold is illustrated in Figure 5.6.

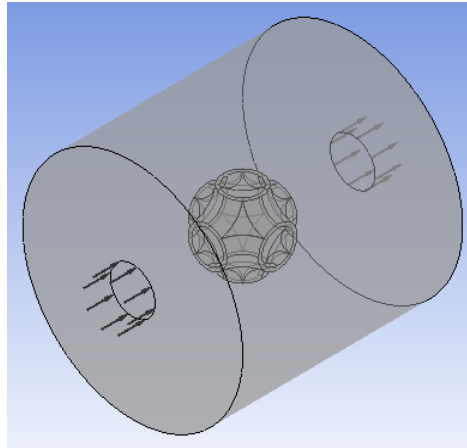


Figure 5.6 – Biofluid flow within the scaffold illustrating the chamber's inlet and outlet.

5.6. Vascular Results and Discussion

(a) Non-Triple Periodic Minimal Surfaces

Figure 5.7 and 5.8 illustrate the variation of the Shear Strain Rate and Wall Shear Stress with the increase of the pore size of the scaffold. For both parameters, the scaffolds with “CF” present a sinusoidal behaviour with the increase of the pore size of the scaffold, maintaining its average value constant. Regarding the Shear Strain Rate, as the pore size increases, the Shear Strain Rate increases initially and then decreases (“4F” pores), decreases and then begins to increase (“12F” pores), while the “8F” pores also present a sinusoidal behaviour with a higher amplitude and higher values compared with the Circular Pores. Regarding the Wall Shear Stress, both the “4F” and “12F” pores present an almost linear decreasing behaviour, having the “12F” pores higher values of Wall Shear Stress. The “8F” pores presents a sinusoidal behaviour with both less amplitude and value of Wall Shear Stress compared to the “CF” pores.

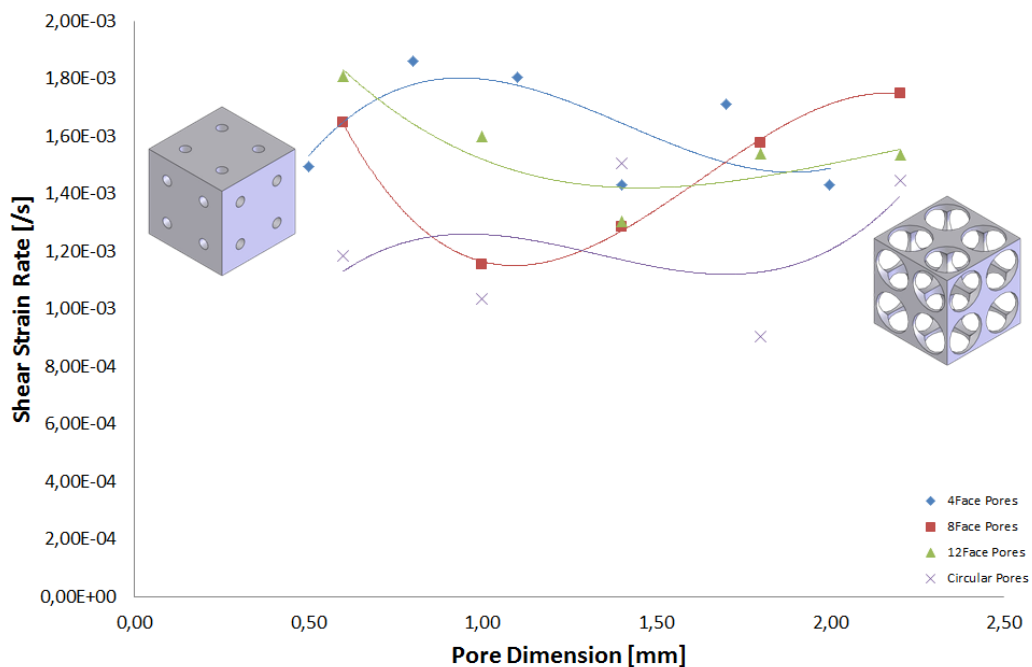


Figure 5.7 – Regular geometric scaffolds: variation of the Shear Strain Rate with the pore’s dimensions.

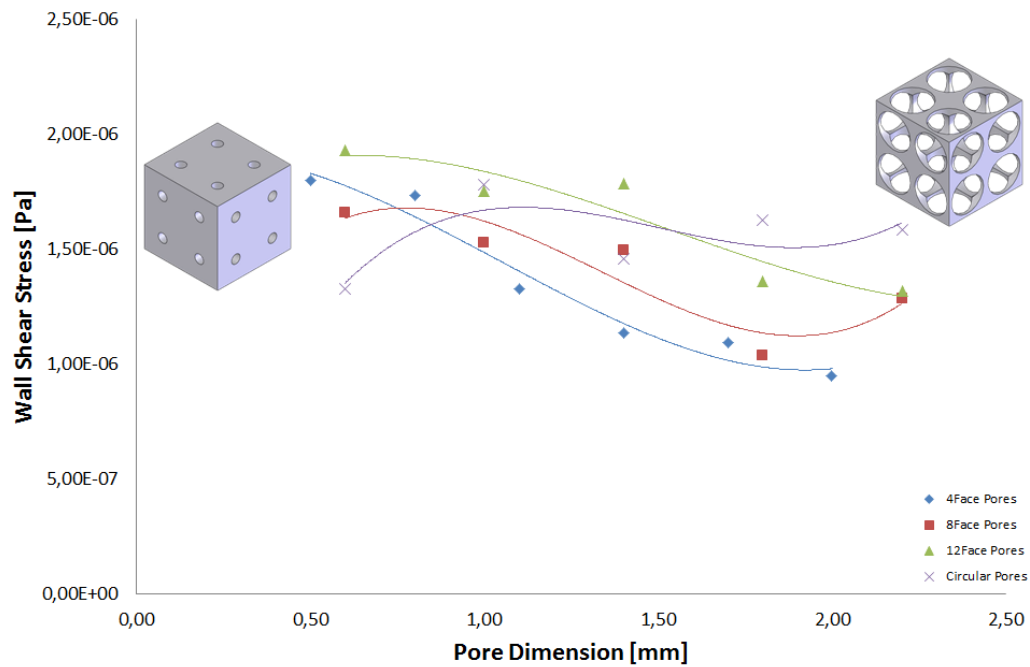


Figure 5.8 – Regular geometric scaffolds: variation of the Wall Shear Stress with the pore's dimensions.

Figures 5.9 and 5.10 illustrate a micro-scale analysis of the Shear Strain Rate and Wall Shear Stress for the regular geometric scaffolds with the increase of pore size. On a micro-scale level, all 4 pore types have a similar behaviour regarding the Shear Strain Rate and Wall Shear Stress. Figure 5.9 illustrates the variation of the Shear Strain Rate for scaffolds with “8F” pores. Regarding this issue, no particular superficial variation is observed, only that the higher values of Shear Strain Rate are located on the exterior of the scaffold. The lower values are verified in its interior. For the Wall Shear Stress for scaffolds with “4F”, the difference in values between the interior and exterior of the scaffold are more significant (Figure 5.10). In other words, the cells located on the exterior surface of the scaffold have a higher mechanobiological stimulation compared to the cells in the interior of the scaffold. This will result in a low cell proliferation and differentiation inside the scaffold due to the lack of stimulation.

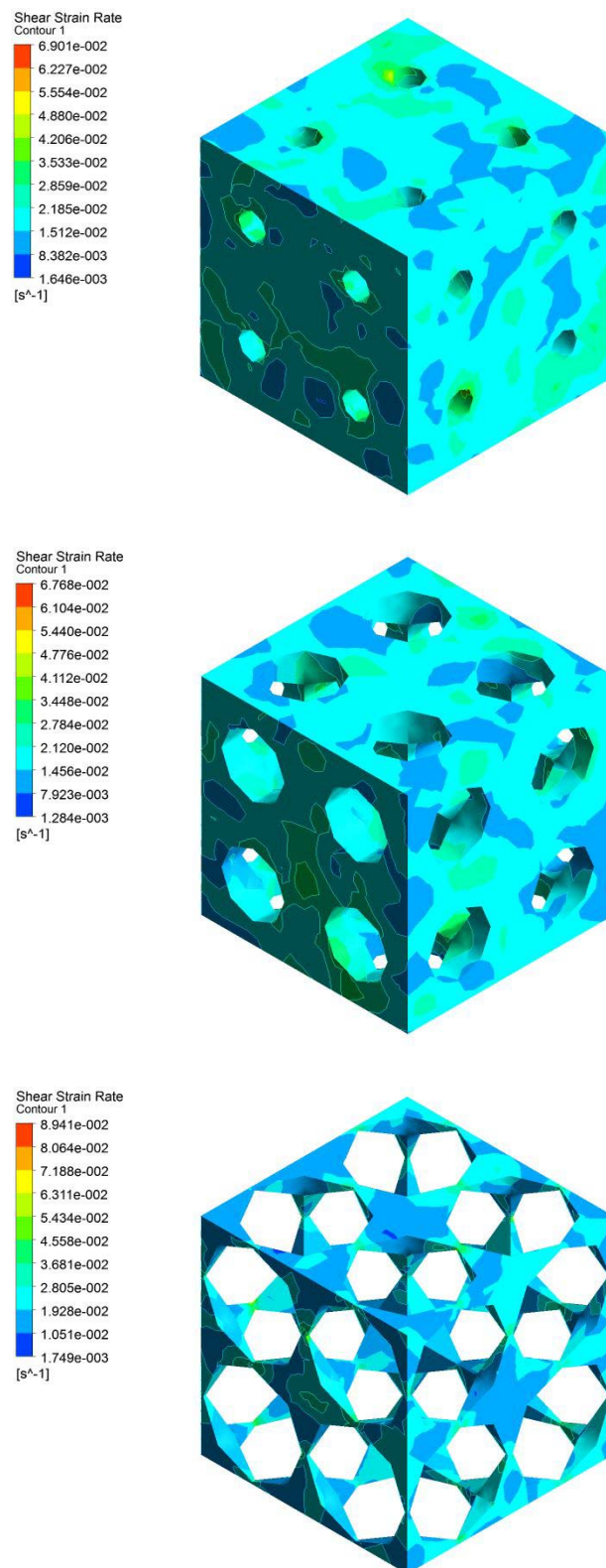


Figure 5.9 – Regular geometric scaffolds: variation of the Shear Strain Rate with the pore's dimensions.

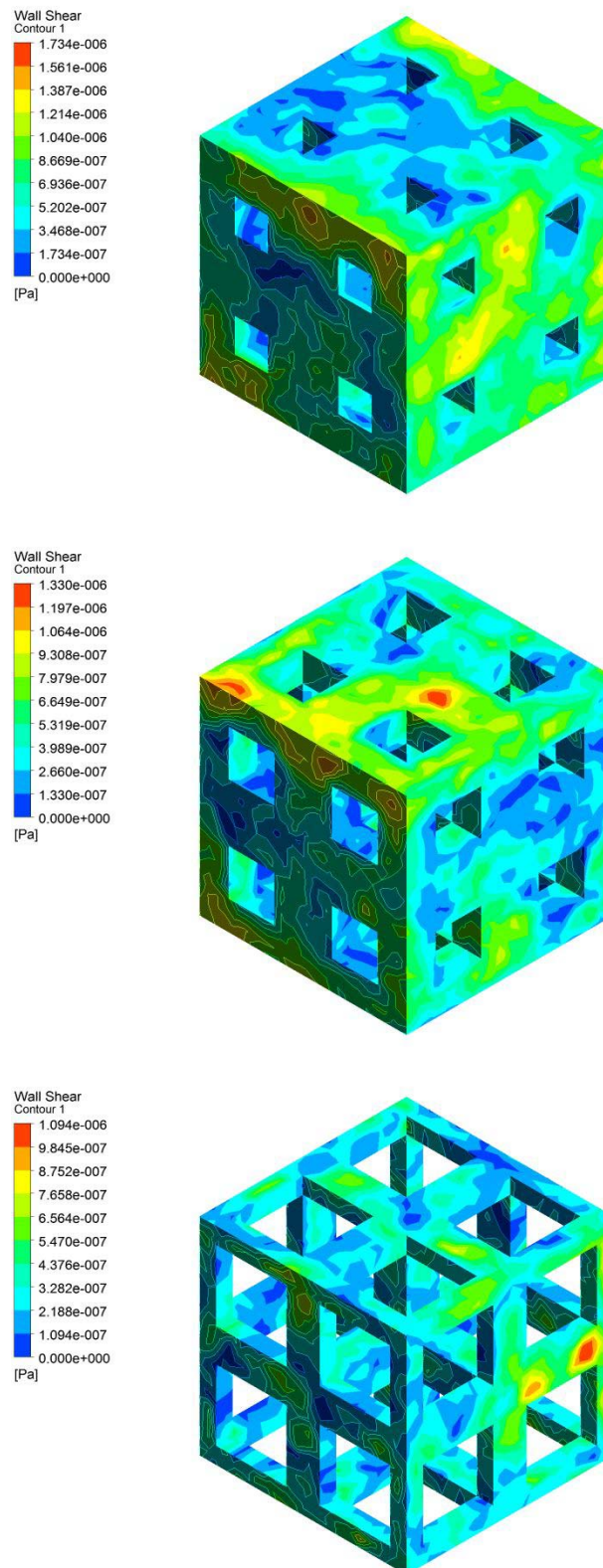


Figure 5.10 – Regular geometric scaffolds: variation of the Wall Shear Stress with the pore's dimensions.

The scaffold structures that were used for the Crushable Foam Simulations were also subjected to vascular simulations. Bearing in mind, that only three geometries were analysed, the present data isn't enough to present a behaviour curve of the Shear Strain Rate and Wall Shear Stress as a function of pore size. Therefore only a micro analysis was performed on the superficial behaviour of the scaffolds. Similarly to the *n faces per pore* scaffolds, the Shear Strain Rate and Wall Shear Stress aren't homogenous throughout the scaffold, presenting higher values on the outer regions of the scaffold compared to the interior regions.

Regarding the pore size variation, the results demonstrate that as the pore size increases, lower is the difference in value for the Shear Strain rate and the Wall Shear Stress between the outer and inner regions of the scaffold due to the decrease in difficulty of the fluid flow to the interior of the scaffold. In this case, for the 0/90° lay-down scaffolds, as the pore size increases, so does the vascular behaviour of the scaffolds in spite of the decrease in mechanical performance, improving the balance between the interior and exterior cellular stimulations. Figure 5.11 illustrates the variation of the Shear Strain Rate as the pore size increases from 450 µm to 550 µm to 650 µm. Figure 5.12 illustrates the variation of the Wall Shear Stress as the pore size increases from 450 µm to 550 µm to 650 µm.

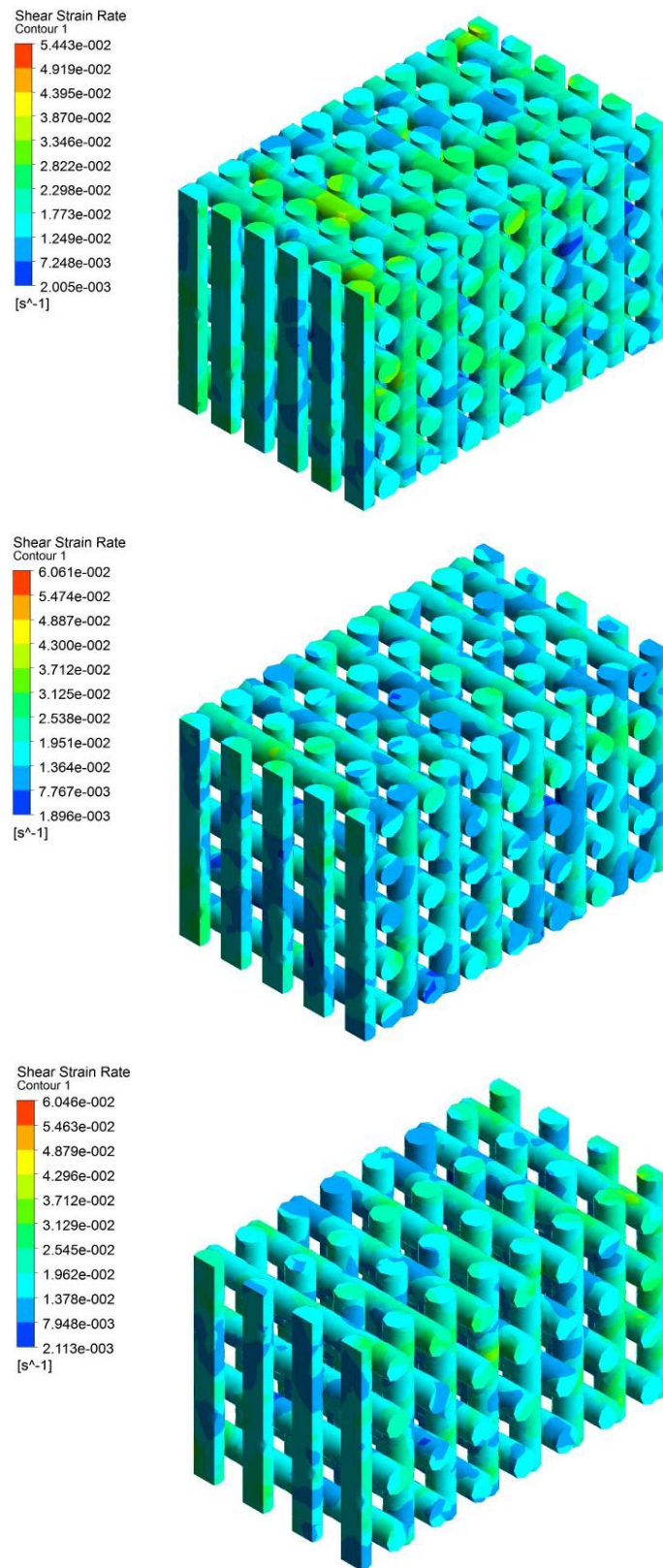


Figure 5.11 – Filament orientated 0/90° scaffolds: variation of the Shear Strain Rate with the variation of the pore size.

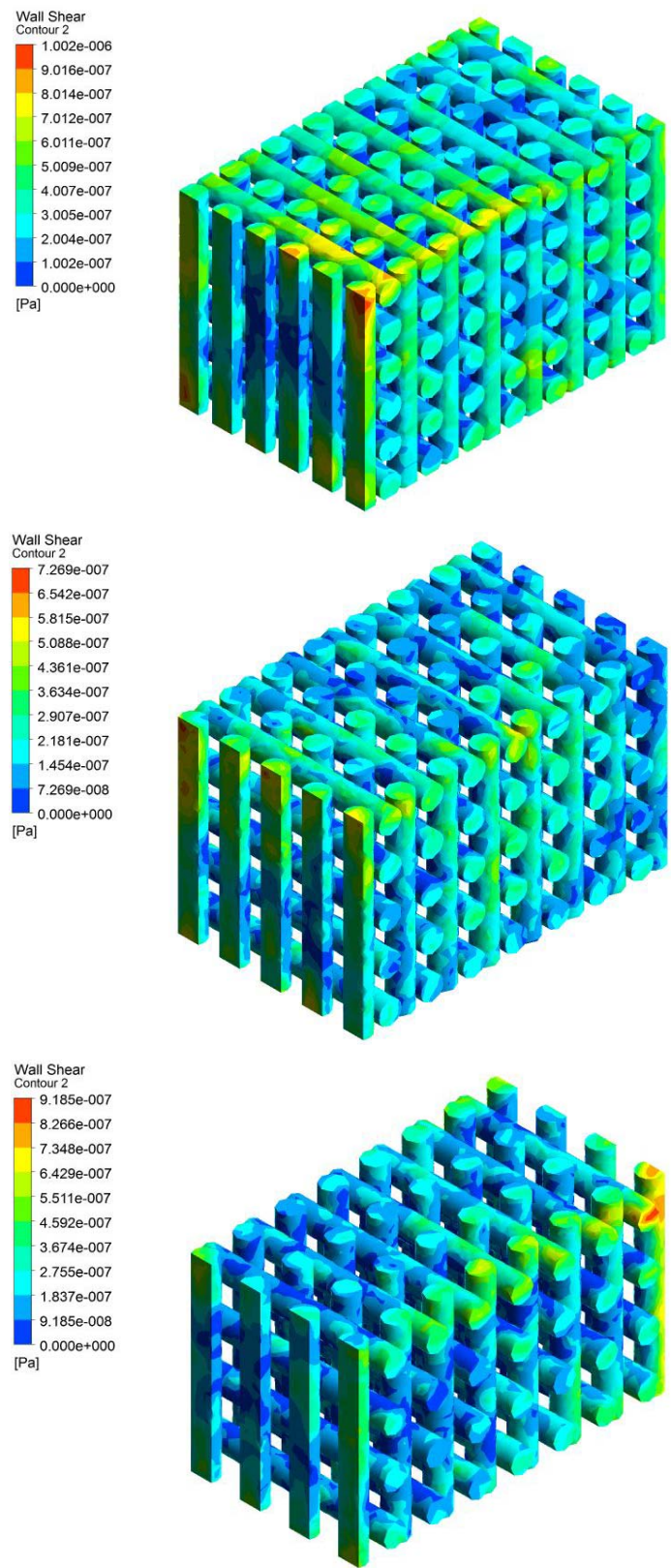


Figure 5.12 – Filament orientated 0/90° scaffold: variation of the Wall Shear Stress with the variation of the pore size.

(b) *Triple Periodic Minimal Surfaces*

Figures 5.13 and 5.14 illustrate the variation of the Shear Strain Rate variation of the Schoen geometry. Figure 5.13 illustrates the variation of the Shear Strain Rate due to the increase of thickness while Figure 5.14 illustrates the variation of the Shear Strain Rate due to the increase of radius. From the figures, it is possible to verify that the Shear Strain Rate decreases with the geometries' thickness and increases with the radius. In this case, it is possible to conclude that the increase of thickness lowers the Shear Strain Rate, resulting in a higher probability of occurring the rouleaux phenomenon. Regarding the radius variation, the probability of occurring the rouleaux phenomenon decreases with the increase of radius. The Schwartz geometries have a similar behaviour for the Shear Strain Rate. In conclusion, the best geometric option is to work with lower thicknesses and higher radius values.

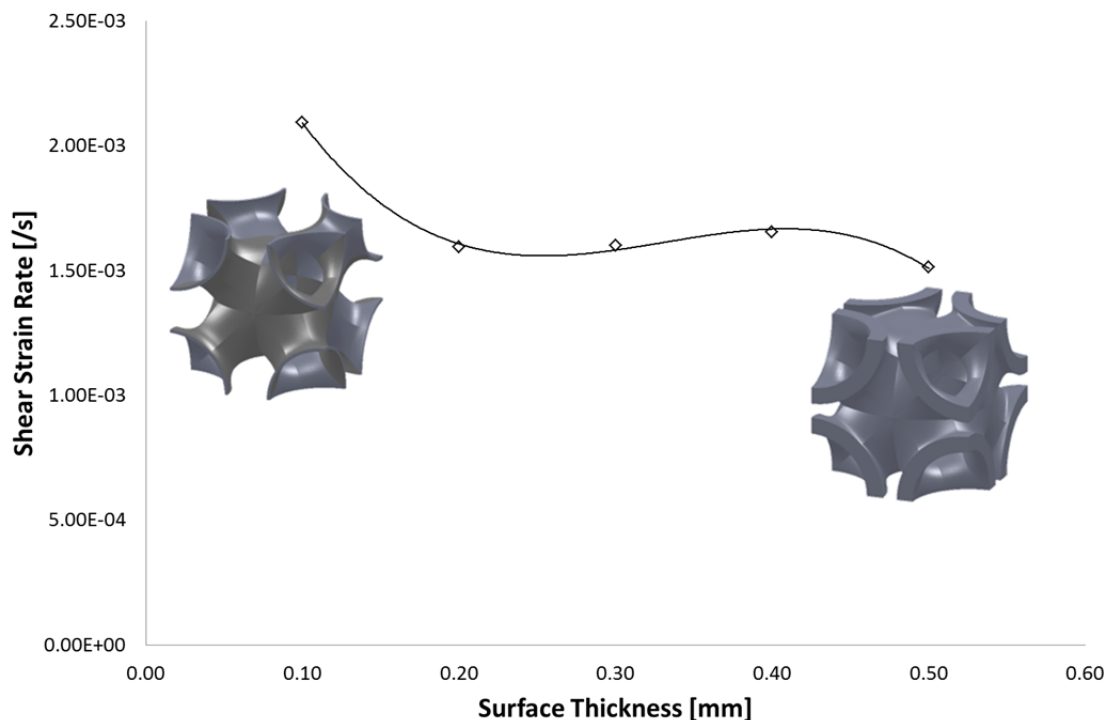


Figure 5.13 – Schoen surface: variation of the Shear Strain Rate with the variation of the thickness.

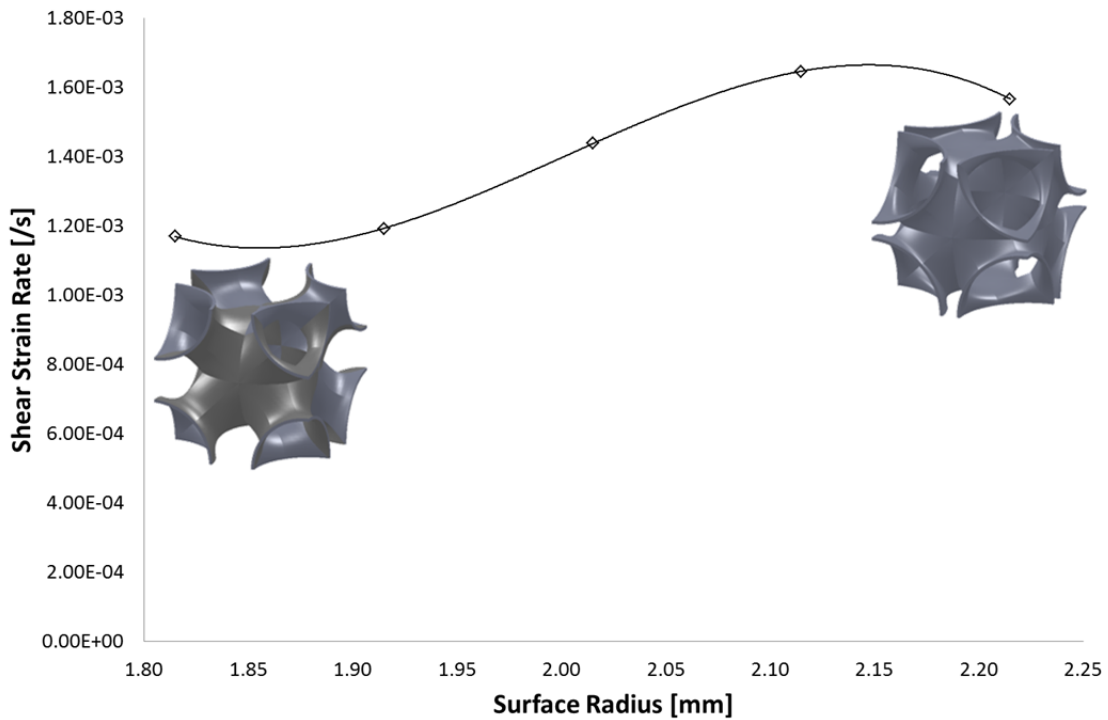


Figure 5.14 – Schoen surface: variation of the Shear Strain Rate with the variation of the radius.

Figures 5.15 and 5.16 illustrate the variation of the Wall Shear Stress in function of the thickness variation of the geometries. Figure 5.15 illustrates the variation of the Schwartz geometry and Figure 5.16 illustrates the variation of the Schoen geometry. From the figures illustrated below, it is possible to verify that the Wall Shear Stress increases for the Schwartz geometry and decreases for the Schoen geometries. The geometric variation regarding the radius variation has a similar behaviour for the Wall Shear Stress. In conclusion, once the cell's shear stress is known, it is possible to design the scaffolds with the ideal value so that neither do the cells lack the adequate stimuli or are harmed due to the values being too high.

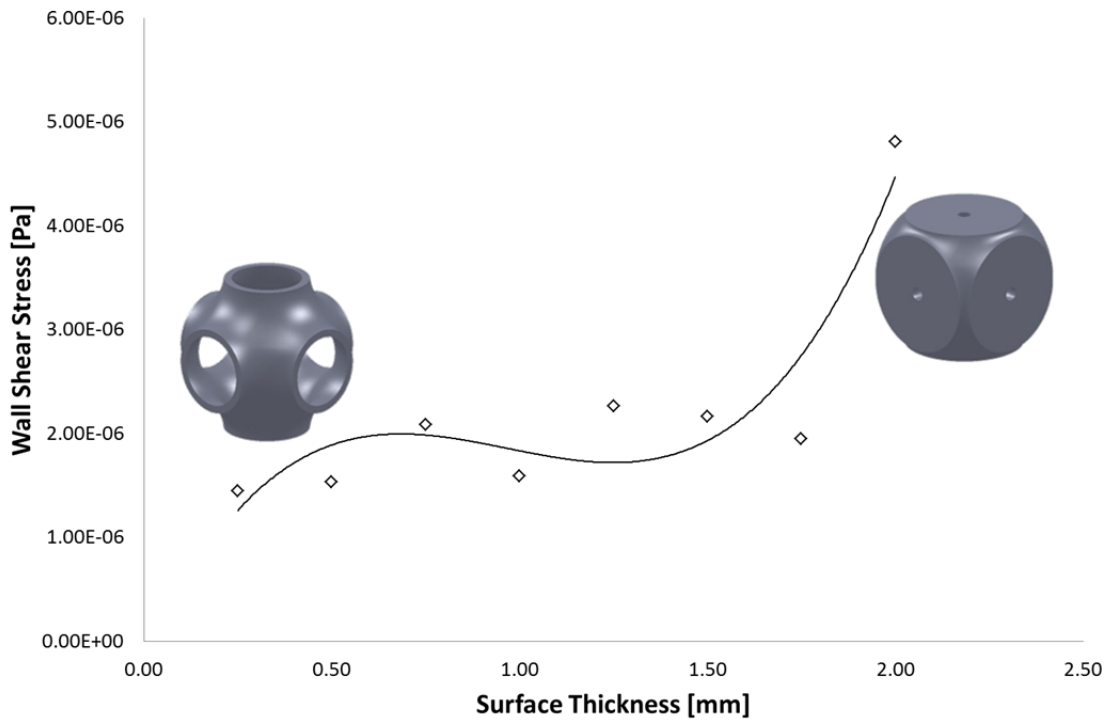


Figure 5.15 – Schwartz surface: variation of the Wall Shear Stress with the variation of the thickness.

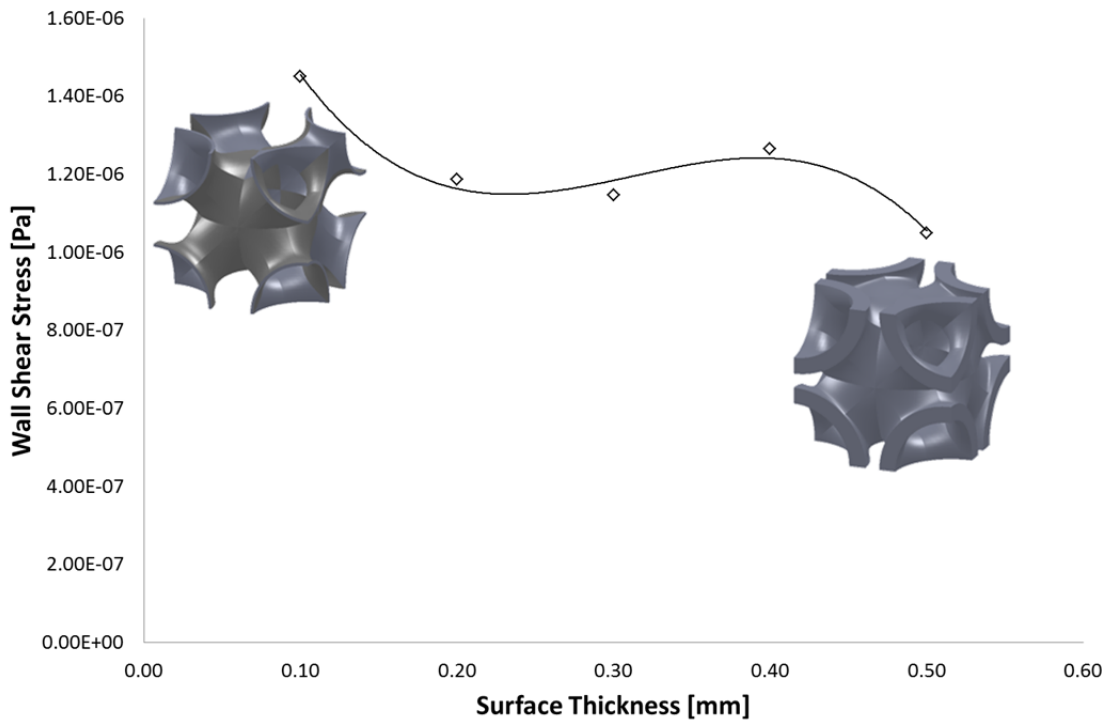


Figure 5.16 – Schoen surface: variation of the Wall Shear Stress with the variation of the thickness.

A micro-scale analysis of both geometries was also performed for the vascular simulations. Figures 5.17 and 5.18 illustrate the variation of the Shear Strain Rate variation of the Schoen geometry. Figure 5.17 illustrates the variation of the Shear Strain Rate due to the increase of thickness and Figure 5.18 illustrates the variation due to the increase of radius. Both figures illustrate that both geometries present a more homogenous Shear Strain Rate variation with lower values.

Figures 5.19 and 5.20 illustrate the variation of the Wall Shear Stress in function of the thickness variation of the Schwartz and Schoen geometry respectively. Regarding the Wall Shear Stress, the Schoen geometries present a more homogenous variation with lower thickness values, for both interior and exterior regions of the scaffold. The most significant variation is presented with the thickness variation of the Schwartz geometries. The Wall Shear Stress increases with the increase of thickness maintaining a homogenous distribution on the exterior region of the scaffold. Regarding the interior region of the scaffold, it tends to decrease with a homogenous distribution.

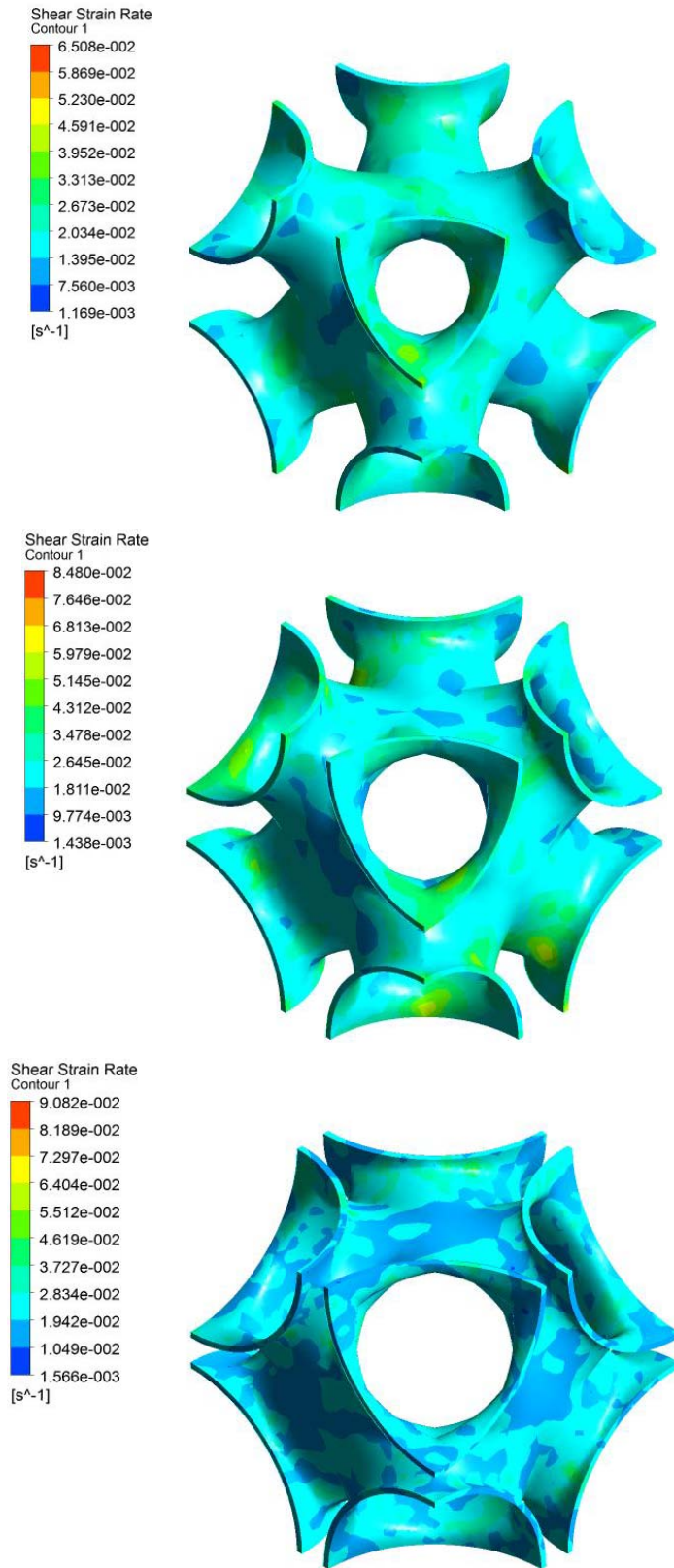


Figure 5.17 – Schoen surface: variation of the Shear Strain Rate with the variation of the radius.

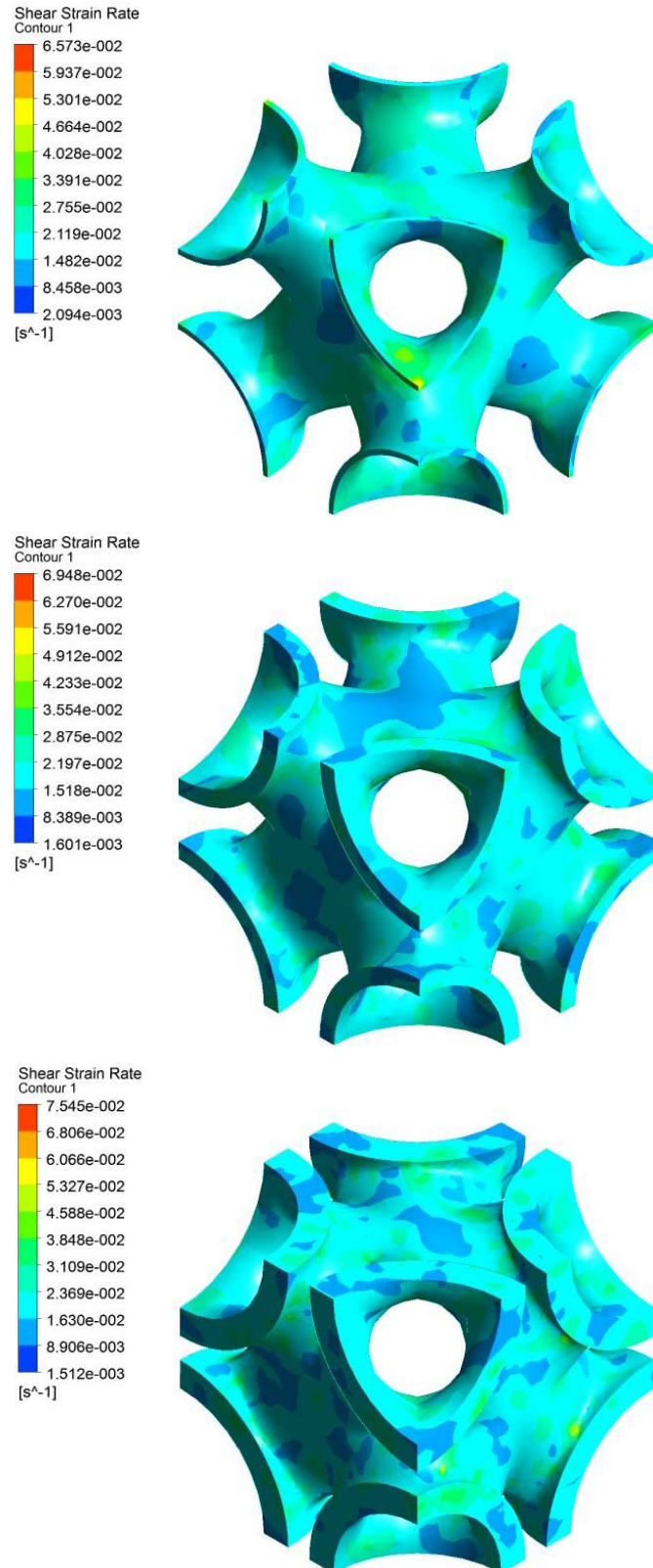


Figure 5.18 – Schoen surface: variation of the Shear Strain Rate with the variation of the thickness radius.

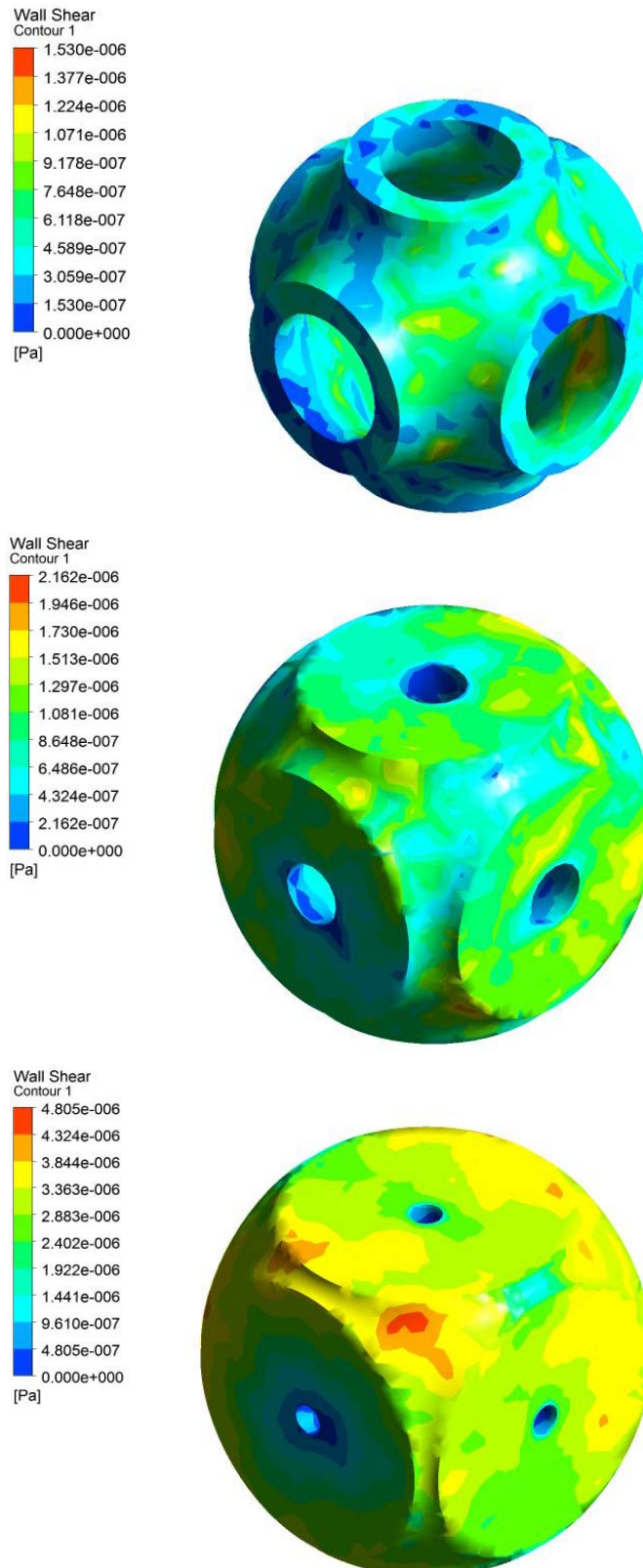


Figure 5.19 – Schwartz surface: variation of the Wall Shear Stress with the variation of the thickness.

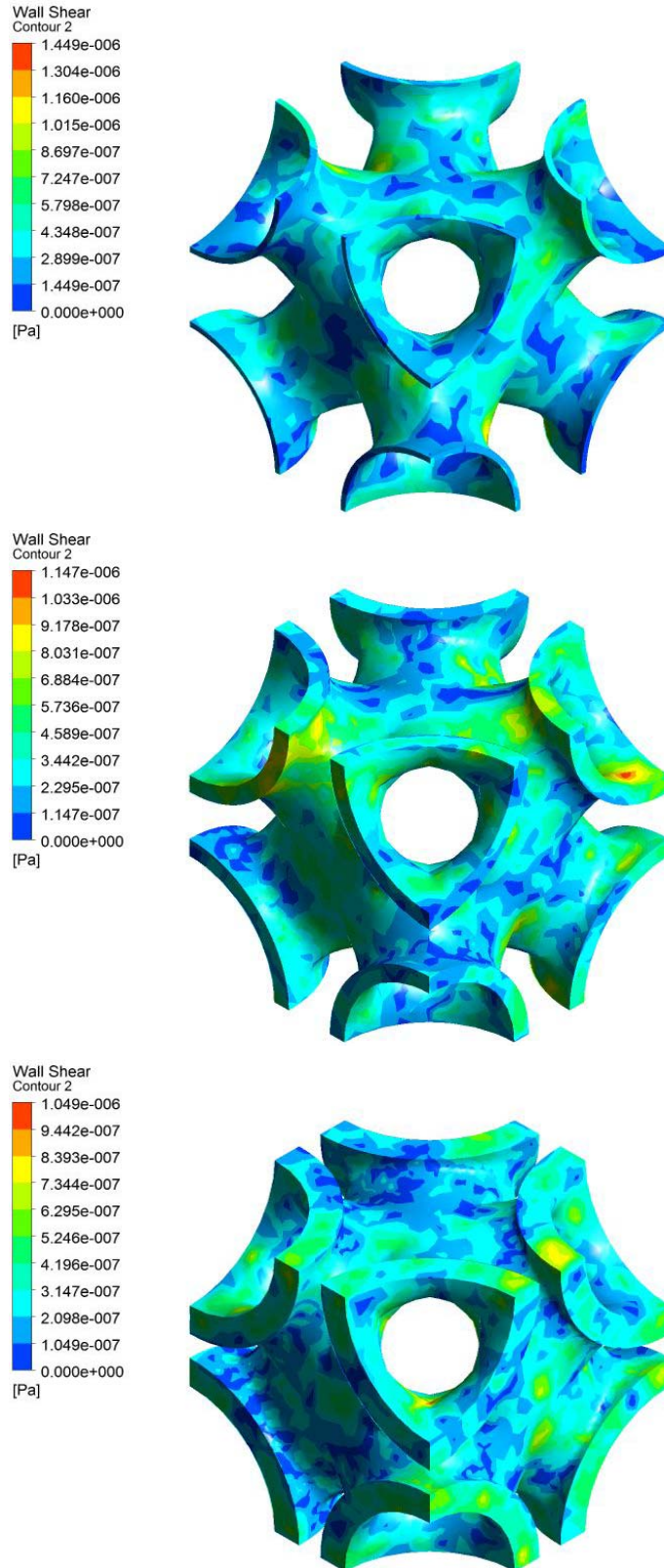


Figure 5.20 – Schoen surface: variation of the Wall Shear Stress with the variation of the thickness.

(c) Summary

The vascular simulation results demonstrate that the Triple periodic minimal surfaces present higher vascular properties when compared to the Non-triple periodic surfaces. Results of both geometries show that the Shear Strain Rate decreases with the geometries' thickness and increases with the radius. Regarding the Wall Shear Stress, it increases for the Schwartz geometry and decreases for the Schoen geometries as the geometries' thickness increases. The geometric variation regarding the radius variation has a similar behaviour for the Wall Shear Stress. Results of the variation of the Shear Strain Stress on the scaffold's surface show that both geometries present a more homogenous variation with lower geometric values. Regarding the Wall Shear Stress, the Schoen geometries present a more homogenous variation with lower thickness values. The most significant variation is presented with the thickness variation of the Schwartz geometries. The Wall Shear Stress increases with the increase of thickness maintaining a homogenous distribution on the scaffold.

Chapter 6 – Topological Optimisation of Scaffolds for Tissue Engineering

6.1. Design Optimisation of Scaffolds in Tissue Engineering

The classical problem in engineering design consists in finding the optimum geometric configuration of a structure that maximizes a given cost objective function with boundary conditions and constraints. Structural optimisation can be classified as follows (Lee, 2007; Hsu and Hsu, 2005):

- Size optimisation;
- Shape optimisation;
- Topology optimisation.

In size optimisation (Figure 6.1.b), only the cross section of a structure is optimised. A typical size feature of a given structure, such as the thickness of a beam, is either increased or decreased in order to improve its performance. In shape optimisation (Figure 6.1.c), the shape of the structure is obtained by changing the shape of the used components with other components of different shape, in order to improve a desired variable within a system. In topology optimisation (Figure 6.1.d), the shape and connectivity of the domain are both design variables.

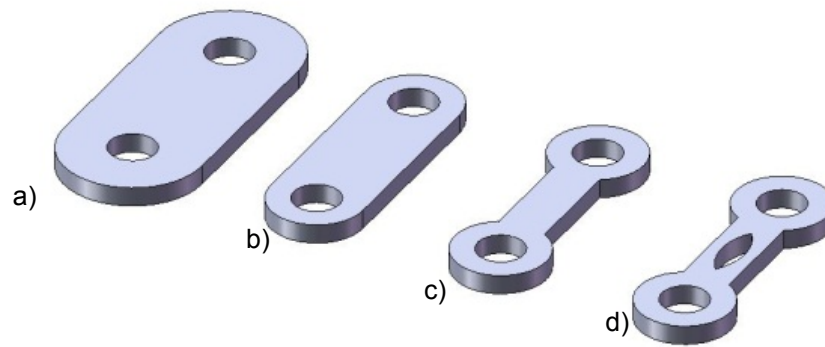


Figure 6.1 – Types of engineering optimisations: a) original part b) part after size optimisation c) part after shape optimisation and d) part after topological optimisation.

Topology optimisation provides the first design concept of the structure's materials distribution. Its goal is to minimise the structure compliance while satisfying the constraints of volume removal. As the structure compliance is twice the strain energy, the objective function of minimising structure compliance is equivalent to minimising strain energy (Kruijf *et al*, 2007; Rozvany, 2001).

In spite of several attempts to define optimised scaffolds (Podshivalov *et al*, 2009; 2008; Holdstein and Fischer, 2008; Wettergeen *et al*, 2008; 2005a; 2005b), there is no work correlating both porosity and mechanical properties with topological information. As described in Chapter 2, scaffolds must be highly porous structures but also effective from a mechanical point of view. This is a complex issue, fundamental for tissue engineering applications and not yet fully addressed. This chapter proposes an optimised strategy to obtain scaffolds with an appropriate topology maximizing both porosity and mechanical behaviour. The methodology proposed in this chapter is of simple implementation and does not require high computational calculation time.

6.2. Topological Optimisation

Topological optimisation, aiming to find the best use of material according to a “maximum-stiffness” design, requires neither parameters nor the explicit definition of optimisation variables. The objective function is predefined, as are the state variables (constrained dependent variables), and the design variables (independent variables to be optimised). The topological optimisation problem requires the problem definition (material properties, model and loads), the objective function (the function to be minimized or maximized), and the state variables corresponding to the percentage of material to be removed (Neches and Cisilino, 2008; Ansola *et al*, 2007; Kruijf *et al*, 2007; Hsu and Hsu, 2005; Bendsøe and Sigmund, 2003; Rozvany, 2001; Bendsøe, 1989; Bendsøe and Kikuchi, 1988).

From a mechanical point of view, the goal of topological optimisation is to minimise the total compliance, which is proportional to the strain energy. Figure 6.2 illustrates the general topology optimisation scheme considered in this work.

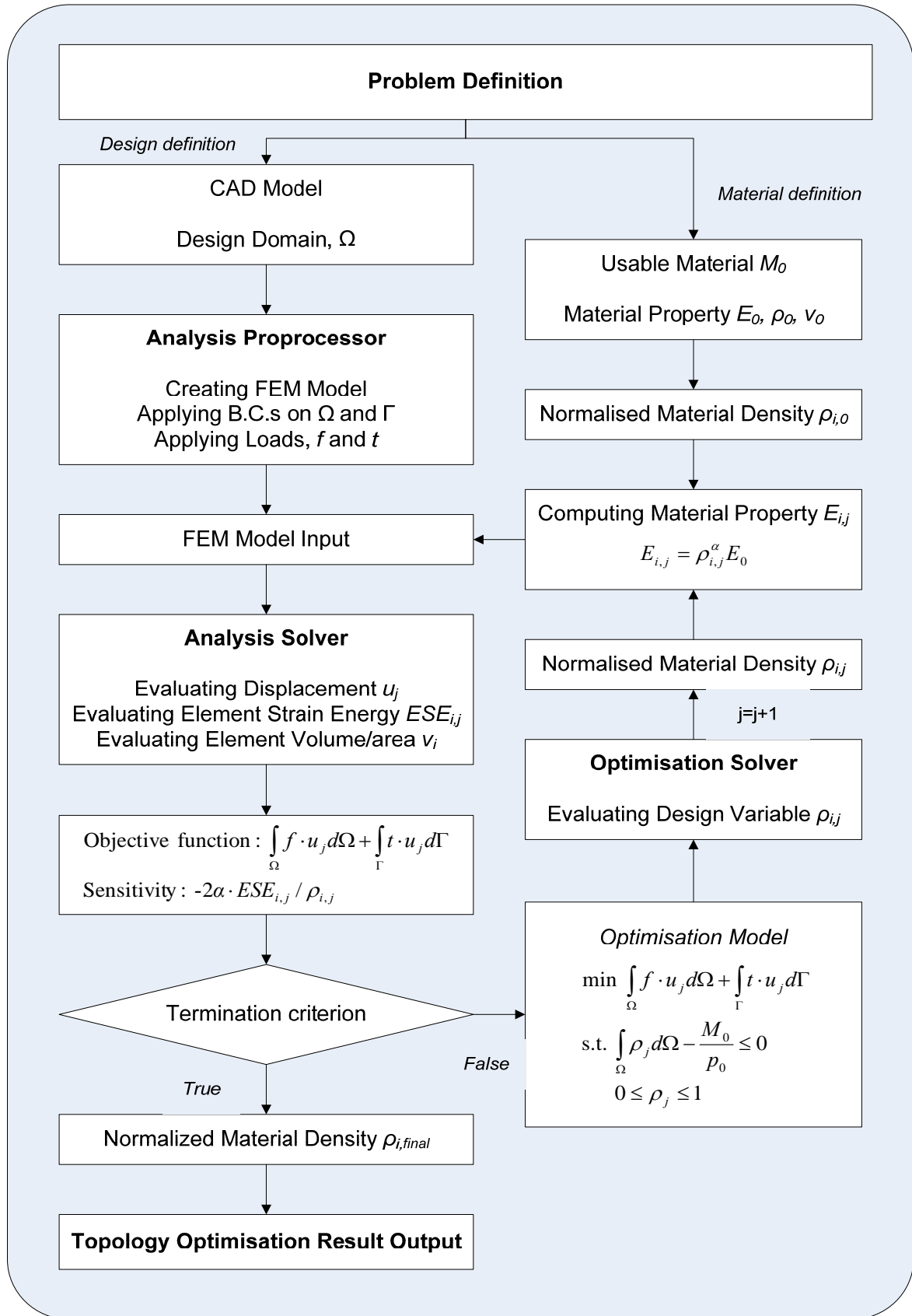


Figure 6.2 – A general topological optimisation process.

The design variables are internal, pseudo-densities that are assigned to each finite element in the topological problem. The pseudo-density for each element varies from 0 to 1, where $\eta_i \approx 0$ represents material to be removed, and $\eta_i \approx 1$ represents material that should be (Figure 6.3).

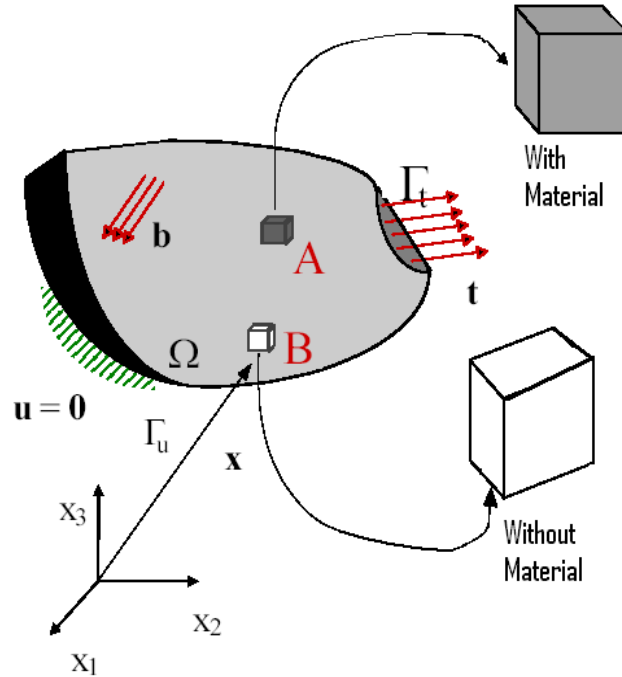


Figure 6.3 – Illustration of a topological optimisation.

For a given domain $\Omega \subseteq \mathcal{R}^2(\mathcal{R}^3)$, regions $\Omega(\Gamma_t)$ and fixed boundaries, the optimisation goal is to find the optimal elasticity tensor $E_{ijkl}(x)$, which takes the form (Mlejnek and Schirmacher, 1993; Mlejnek, 1992):

$$E_{ijkl}(x) = \eta(x) \bar{E}_{ijkl} \quad (6.1)$$

where \bar{E}_{ijkl} is the constant rigidity tensor for the considered material and $\eta(x)$ is an indicator function for a region $\Omega^* \subseteq \Omega$ that is occupied by material:

$$\eta(x) = \begin{cases} 1 & , \text{ if } x \in \Omega^* \\ 0 & , \text{ if } x \notin \Omega^* \end{cases} \quad (6.2)$$

Considering the energy bilinear form

$$a(u, v) = \int_{\Omega} \sum_{i,j,k,l=1}^3 E_{ijkl} \varepsilon_{ij}(u) \varepsilon_{kl}(v) dx \quad (6.3)$$

with linearized strains

$$\varepsilon_{ij} = \frac{1}{2} \left(\frac{\partial u_i}{\partial x_j} + \frac{\partial u_j}{\partial x_i} \right) \quad , i, j = 1, 2, 3 \quad (6.4)$$

and the load linear form

$$l(u) = \int_{\Omega} fu \, dx + \int_{\Gamma_t} tu \, ds \quad (6.5)$$

The optimisation problem considered here is defined as follows:

$$\min_{\eta^*(x_e), i=1, \dots, n} l(u) = \int_{\Omega} fu \, dx + \int_{\Gamma_t} tu \, ds$$

subjected to constraints:

$$\begin{aligned} (i) \quad & \int_{\Omega} \sum_{i,j,k,l=1}^3 \tilde{E}_{ijkl} (\eta(x)) \varepsilon_{ij}(u(x)) \varepsilon_{kl}(v(x)) dx = l(v) \quad \forall v \in U \quad (6.6) \\ (ii) \quad & 0 \leq \eta(x) \leq 1 \quad \forall x \in \Omega \\ (iii) \quad & \int_{\Omega} \eta(x) dx \leq Vol \end{aligned}$$

(a) Finite Element Discretisation for the Optimisation Problem

The domain Ω is represented as a collection of a finite number of subdomains. This is called discretisation of the domain. Each subdomain is called an element and the collection of elements is called the finite element mesh. In this case, $\eta(x)$ was discretised by assigning a constant value on each element of the finite element model, establishing a suitable piecewise constant function $\eta^*(x)$ to approximate $\eta(x)$

(b) *Topological Optimisation Algorithm*

The algorithm considered to obtain the solution of the minimum compliance problem is based on the following update strategy (Vogel, 1997):

For $e=1, \dots, n$:

$$\eta_e^{k+1} = \begin{cases} \max\{(1-\zeta)\eta_e^k, eps\} & , \text{if } \eta_e^k (D_e^{k+1})^\alpha \leq \max\{(1-\zeta)\eta_e^k, eps\} \\ \eta_e^k (D_e^{k+1})^\alpha & , \text{if } \max\{(1-\zeta)\eta_e^k, eps\} \leq \eta_e^k (D_e^{k+1})^\alpha \leq \min\{(1+\zeta)\eta_e^k, 1\} \\ \min\{(1+\zeta)\eta_e^k, 1\} & , \text{if } \min\{(1+\zeta)\eta_e^k, 1\} \leq \eta_e^k (D_e^{k+1})^\alpha \end{cases} \quad (6.7)$$

with an appropriate weighing factor α , a move limit ζ and an upper limit $eps > 0$.

To perform the update strategy in Equation 6.7 for a given data η_e^k , $e=1, \dots, n$, eps , ζ , α it is necessary first to compute D_e^{k+1} , $e=1, \dots, n$ which is given by the following equation:

$$D_e^{k+1} = (\Lambda^{k+1})^{-1} E \sum_{i,j,k,l=1}^3 \frac{\partial \tilde{E}_{ijkl}(\eta_e^k)}{\partial \eta} \varepsilon_{ij}^k(u(x_e)) \varepsilon_{kl}^k(u(x_e)) \quad (6.8)$$

The Lagrange parameter Λ is updated by solving the equation:

$$V(\Lambda) := \sum_{e=1}^n \eta_e^{k+1}(\Lambda) - Vol = 0 \quad (6.9)$$

in an inner interaction using an appropriate root finding algorithm (Bisection Method, Newton's Method, Secant Method, False Position Method). The selected method was the Bisection Method which is less efficient than Newton's Method but it is also much less prone to odd behaviour.

6.3. Topological Results and Discussion

Two different analyses were carried out:

- Topological optimisation of an initial solid block under different constraints;
- Topological optimisation of an initial solid block with loading and constraint surfaces defined based on geometrical information obtained from real biological tissues (Bio-surface constrained optimisation of a solid block element).

Each block was assumed to be made of PCL (elastic modulus of 400 MPa and Poisson's ratio of 0.33). The optimisation scheme described in the previous sections was implemented using the finite element software Ansys. A total number 100 iterations for each calculation was considered and the convergence tolerance parameter for each calculation was assumed to be 1E-4.

(a) Topological optimisation of an initial solid block

A solid cubic block with 5 mm of size was considered. A mesh of 15625 cubic solid elements of 0.2 mm of size was used to model the block (Figure 6.4). The optimisation goal is to obtain the best material distribution within the geometric space that corresponds to the solid block, maximizing the mechanical behaviour of the construct based on an imposed porosity value. Different levels of porosity were considered (10 % to 90 % with increments of 10). The block element was assumed to have a linear elastic behaviour, so strain values of 0.1 were simulated by imposing a corresponding displacement according to the strain direction considered.

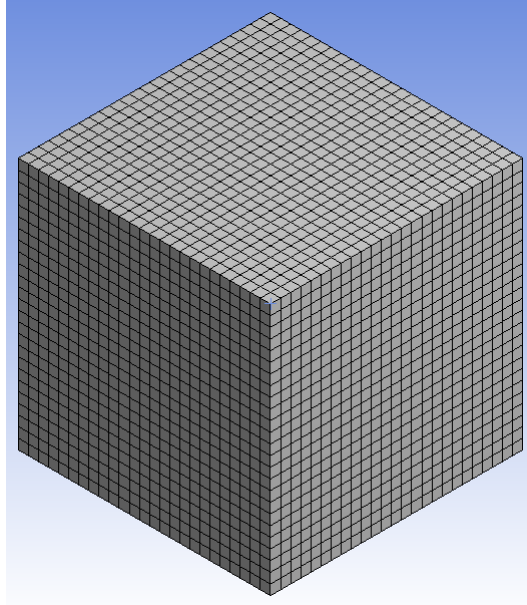


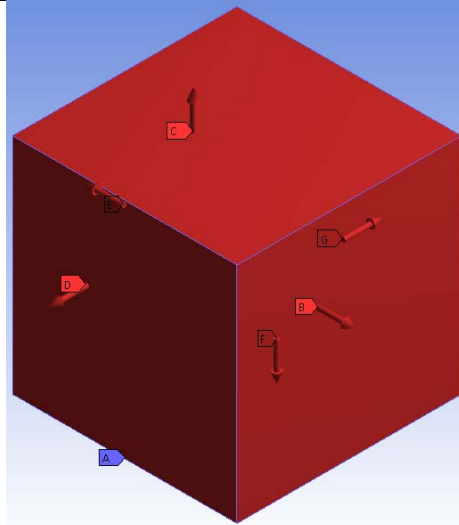
Figure 6.4 – Illustration of the Meshed model of the scaffold.

Based on the strain locations, different optimisation scenarios were considered as follows (Figure 6.5):

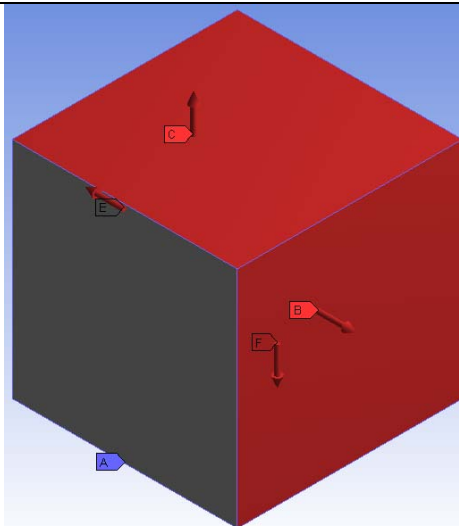
- Scenario 1: all the edges of the block were constrained (no displacements or rotations in the X, Y, Z plane) and the block faces were submitted to strains in all directions (ϵ_{xx} , ϵ_{yy} , ϵ_{zz}).
- Scenario 2: all the edges of the block were constrained (no displacements or rotations in the X, Y, Z plane) and the faces were submitted to strains in two directions (ϵ_{xx} , ϵ_{yy}), (ϵ_{xx} , ϵ_{zz}), (ϵ_{yy} , ϵ_{zz}).
- Scenario 3: all the edges of the block were constrained (no displacements or rotations in the X, Y, Z plane) and the faces were submitted to a strain in one direction (ϵ_{xx} , ϵ_{yy} or ϵ_{zz}).
- Scenario 4: all the vertices of the block were constrained (no displacements or rotations in the X, Y, Z plane) and the faces were submitted to strains in all directions (ϵ_{xx} , ϵ_{yy} , ϵ_{zz}).
- Scenario 5: all the vertices of the block were constrained (no displacements or rotations in the X, Y, Z plane) and the faces were submitted to strains in two directions (ϵ_{xx} , ϵ_{yy}), (ϵ_{xx} , ϵ_{zz}), (ϵ_{yy} , ϵ_{zz}).

- Scenario 6: all the vertices of the block were constrained (no displacements or rotations in the X, Y, Z plane) and the faces were submitted to a strain in one direction (ϵ_{xx} , ϵ_{yy} or ϵ_{zz}).
- Scenario 7: all the vertices of the block were constrained (no displacements or rotations in the X, Y, Z plane) and the edges were submitted to strains in all directions (ϵ_{xx} , ϵ_{yy} , ϵ_{zz}).
- Scenario 8: all the vertices of the block were constrained (no displacements or rotations in the X, Y, Z plane) and the edges were submitted to strains in two directions (ϵ_{xx} , ϵ_{yy}), (ϵ_{xx} , ϵ_{zz}), (ϵ_{yy} , ϵ_{zz}).
- Scenario 9: all the vertices of the block were constrained (no displacements or rotations in the X, Y, Z plane) and the edges were submitted to a strain in one direction (ϵ_{xx} , ϵ_{yy} or ϵ_{zz}).
- Scenario 10: faces were submitted to strains in a single direction (ϵ_{xx} , ϵ_{yy} or ϵ_{zz}) and the remaining faces were constrained.
- Scenario 11: faces were submitted to strains in two directions (ϵ_{xx} , ϵ_{yy}), (ϵ_{xx} , ϵ_{zz}), (ϵ_{yy} , ϵ_{zz}) and the remaining faces were constrained.
- Scenario 12: edges were submitted to strains in a single direction (ϵ_{xx} , ϵ_{yy} or ϵ_{zz}) and the remaining edges were constrained.
- Scenario 13: edges were submitted to strains in two directions (ϵ_{xx} , ϵ_{yy}), (ϵ_{xx} , ϵ_{zz}), (ϵ_{yy} , ϵ_{zz}) and the remaining edges were constrained.

Scenario 1



Scenario 2



Scenario 3

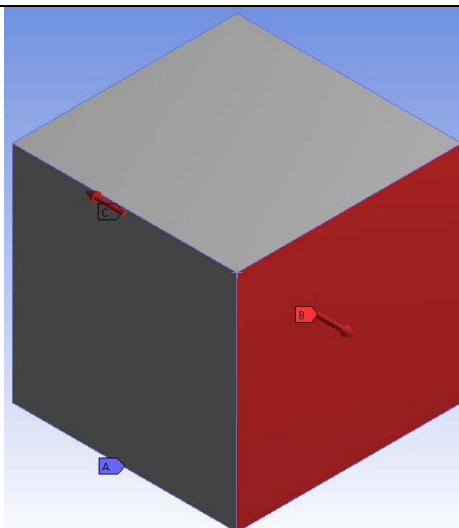


Figure 6.5 – Simulation scenarios considered for topological optimisation.

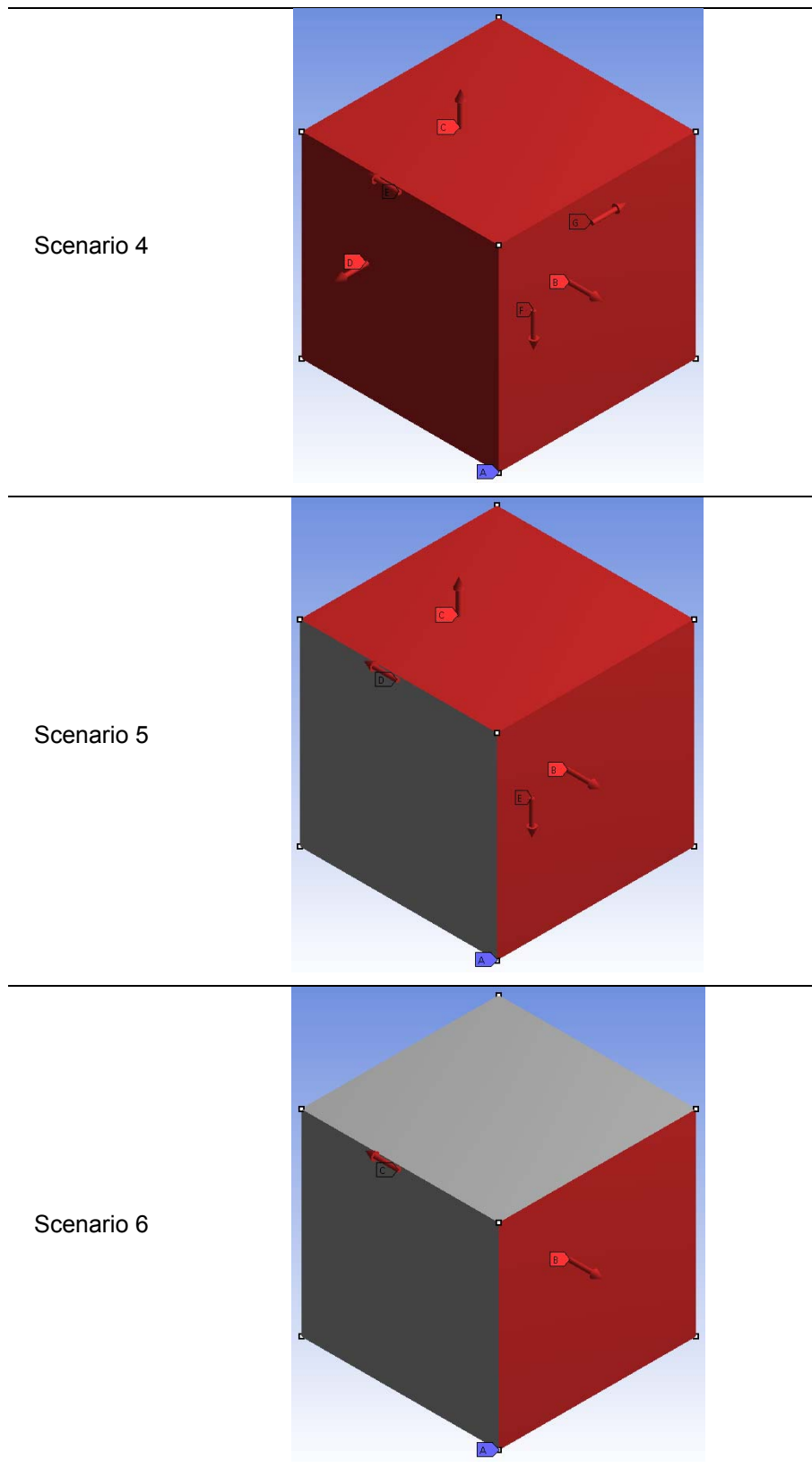
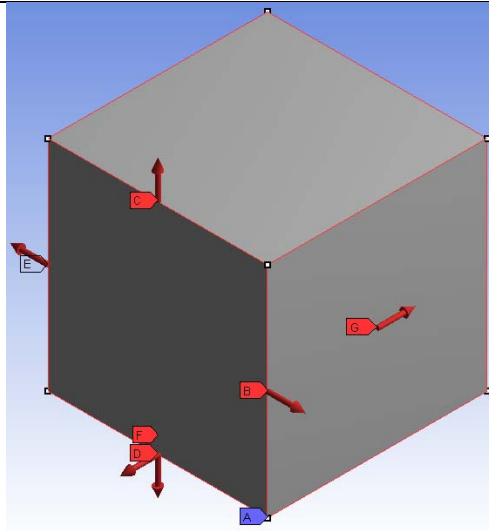
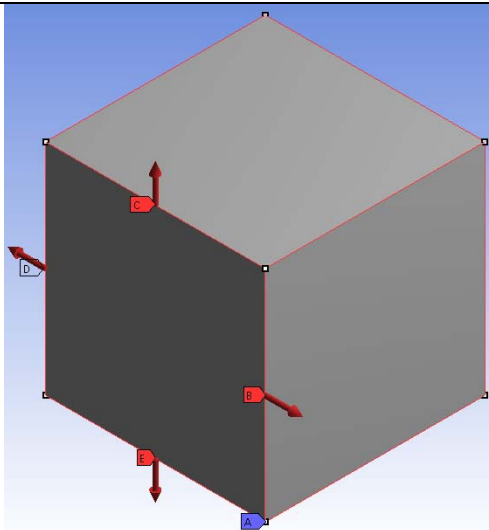


Figure 6.5 – Continuation.

Scenario 7



Scenario 8



Scenario 9

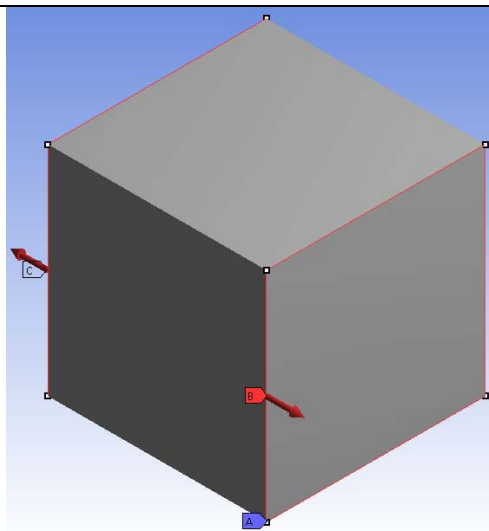
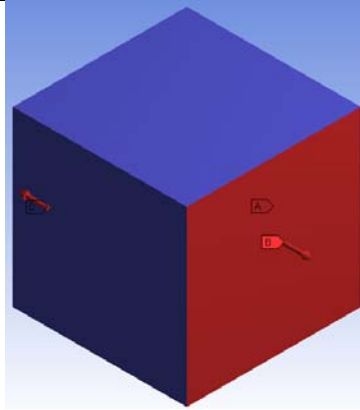
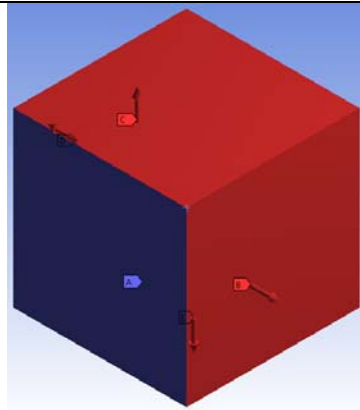


Figure 6.5 – Continuation.

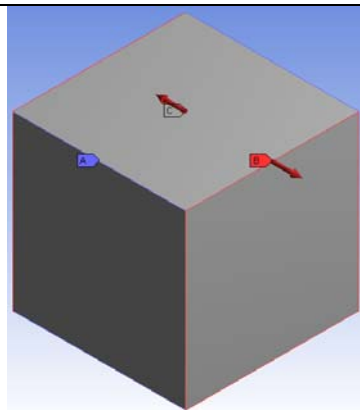
Scenario 10



Scenario 11



Scenario 12



Scenario 13

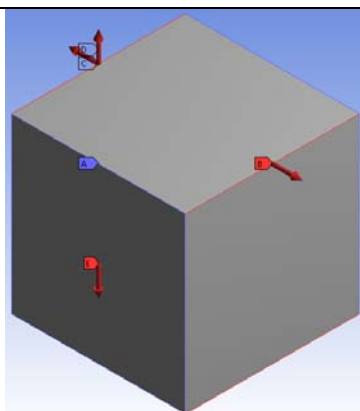


Figure 6.5 – Continuation.

The obtained results were:

- Scenario 1: No valid topological scaffold models were obtained in this simulation scenario, either due to a shell or non-interconnected models.
- Scenario 2: Figure 6.6 presents 2 valid topological scaffold models were obtained in this simulation scenario.
- Scenario 3: Figure 6.7 presents 2 valid topological scaffold models were obtained in this simulation scenario.
- Scenario 4: No valid topological scaffold models were obtained in this simulation scenario, either due to a shell or non-interconnected models.
- Scenario 5: No valid topological scaffold models were obtained in this simulation scenario, either due to a shell or non-interconnected models.
- Scenario 6: No valid topological scaffold models were obtained in this simulation scenario, either due to a shell or non-interconnected models.
- Scenario 7: No valid topological scaffold models were obtained in this simulation scenario, either due to a shell or non-interconnected models.
- Scenario 8: Figure 6.8 presents 5 valid topological scaffold models were obtained in this simulation scenario.
- Scenario 9: Figure 6.9 presents 4 valid topological scaffold models were obtained in this simulation scenario.
- Scenario 10: No valid topological scaffold models were obtained in this simulation scenario, either due to a shell or non-interconnected models.
- Scenario 11: No valid topological scaffold models were obtained in this simulation scenario, either due to a shell or non-interconnected models.
- Scenario 12: Figure 6.10 presents 4 valid topological scaffold models were obtained in this simulation scenario.
- Scenario 13: Figure 6.11 presents 7 valid topological scaffold models were obtained in this simulation scenario.

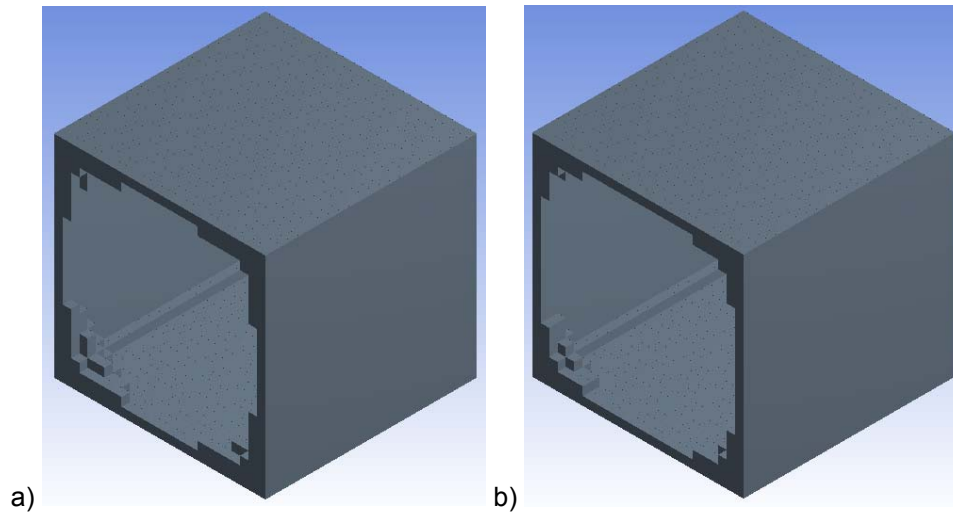


Figure 6.6 – Illustration of topologically optimised scaffold models from Scenario 2 with a porosity of a) 80 % b) 90 %.

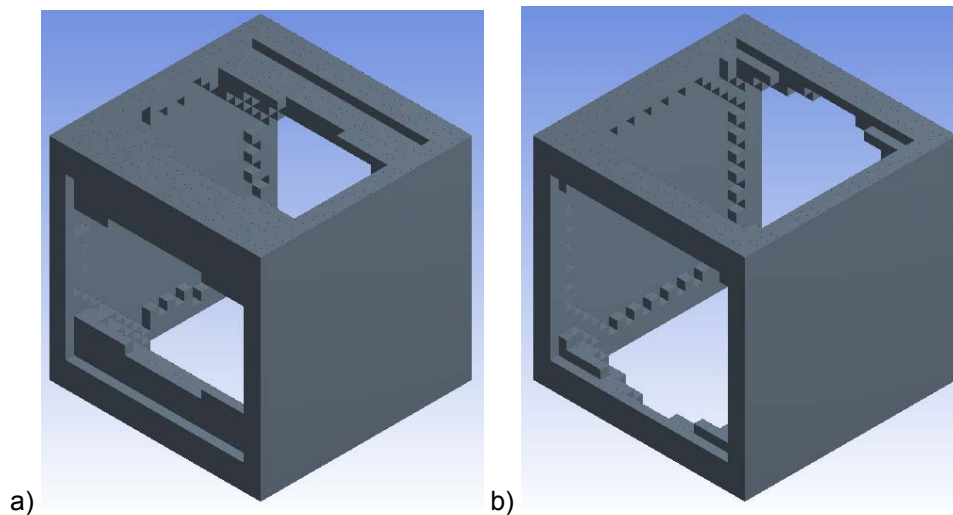


Figure 6.7 – Illustration of topologically optimised scaffold models from Scenario 3 with a porosity of a) 80 % b) 90 %.

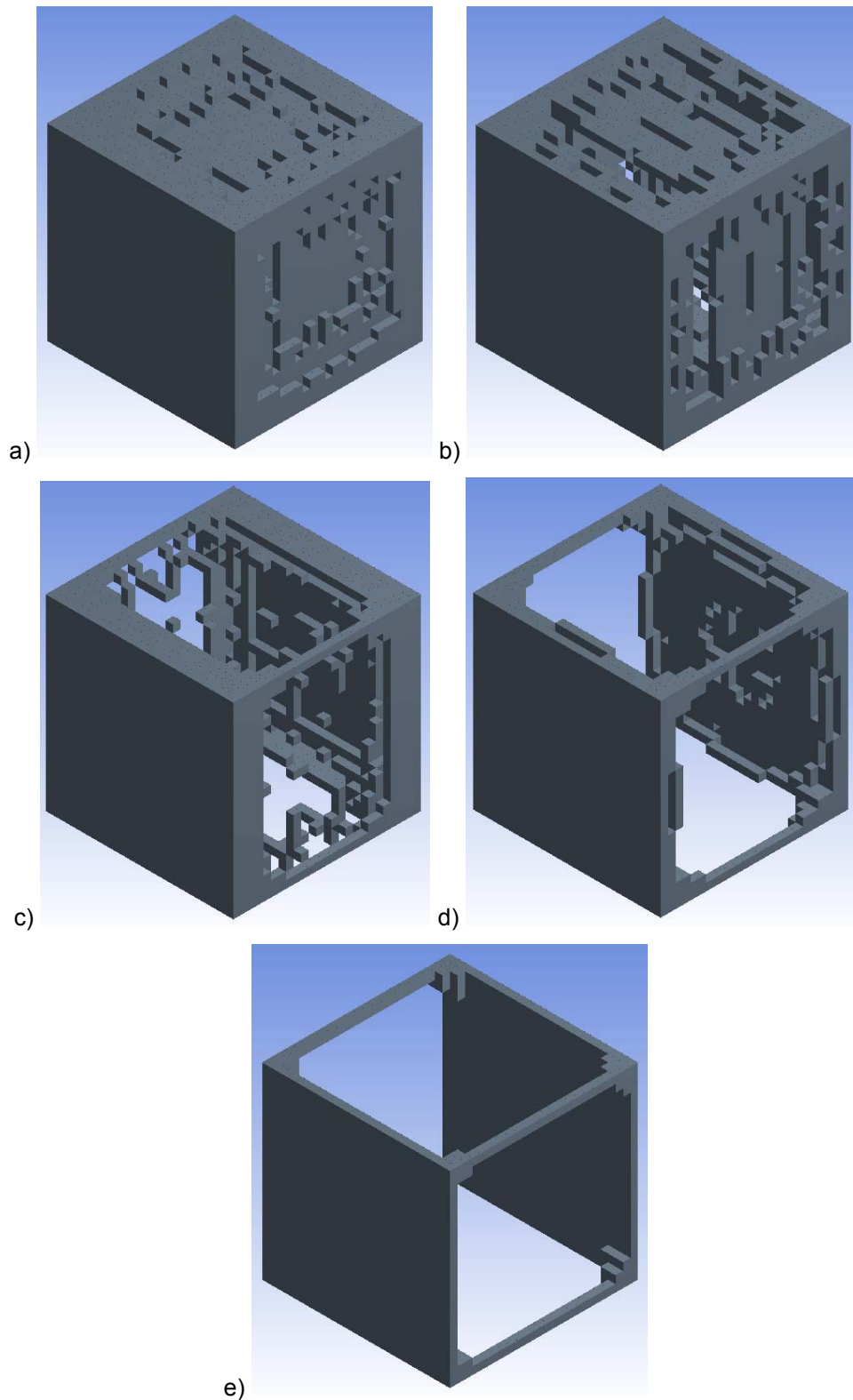


Figure 6.8 – Illustration of topologically optimised scaffold models from Scenario 8 with a porosity of a) 50 % b) 60% c) 70 % d) 80 % e) 90 %.

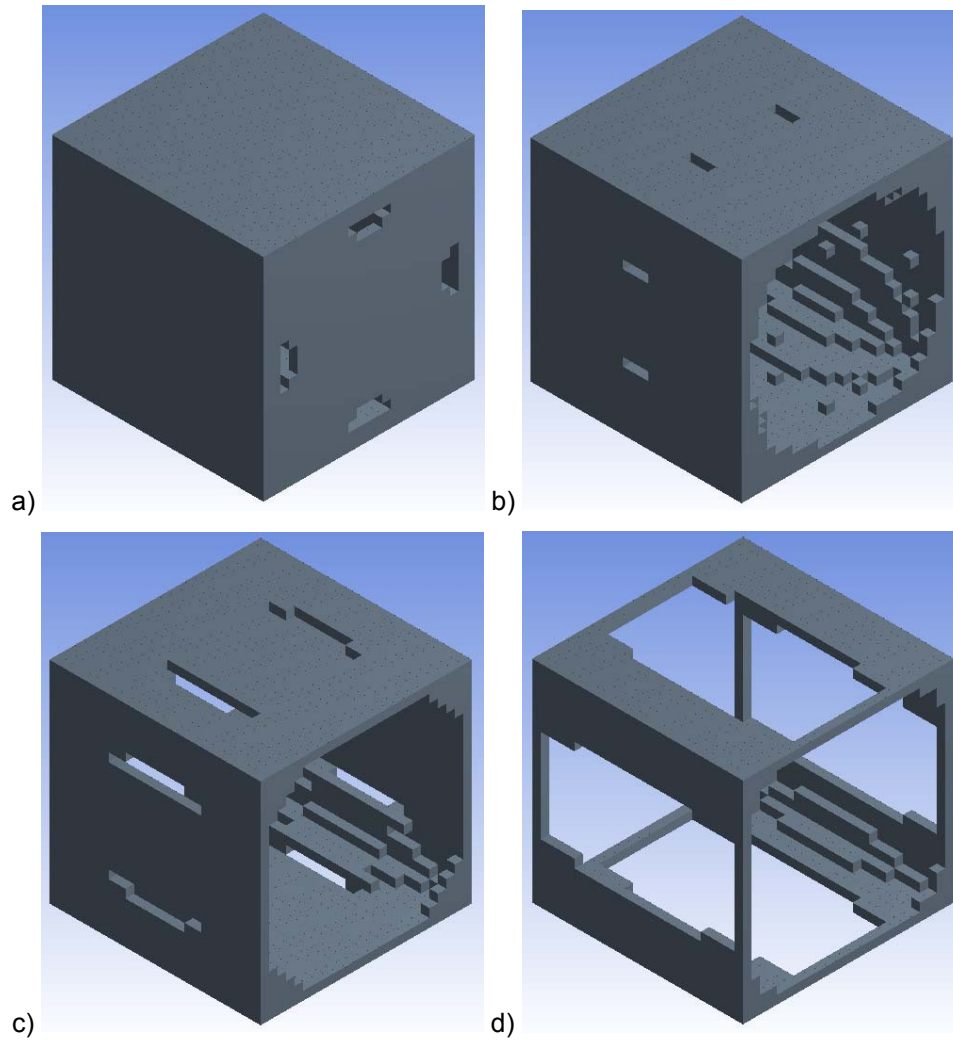


Figure 6.9 – Illustration of topologically optimised scaffold models from Scenario 9 with a porosity of a) 60 % b) 70% c) 80 % d) 90 %.

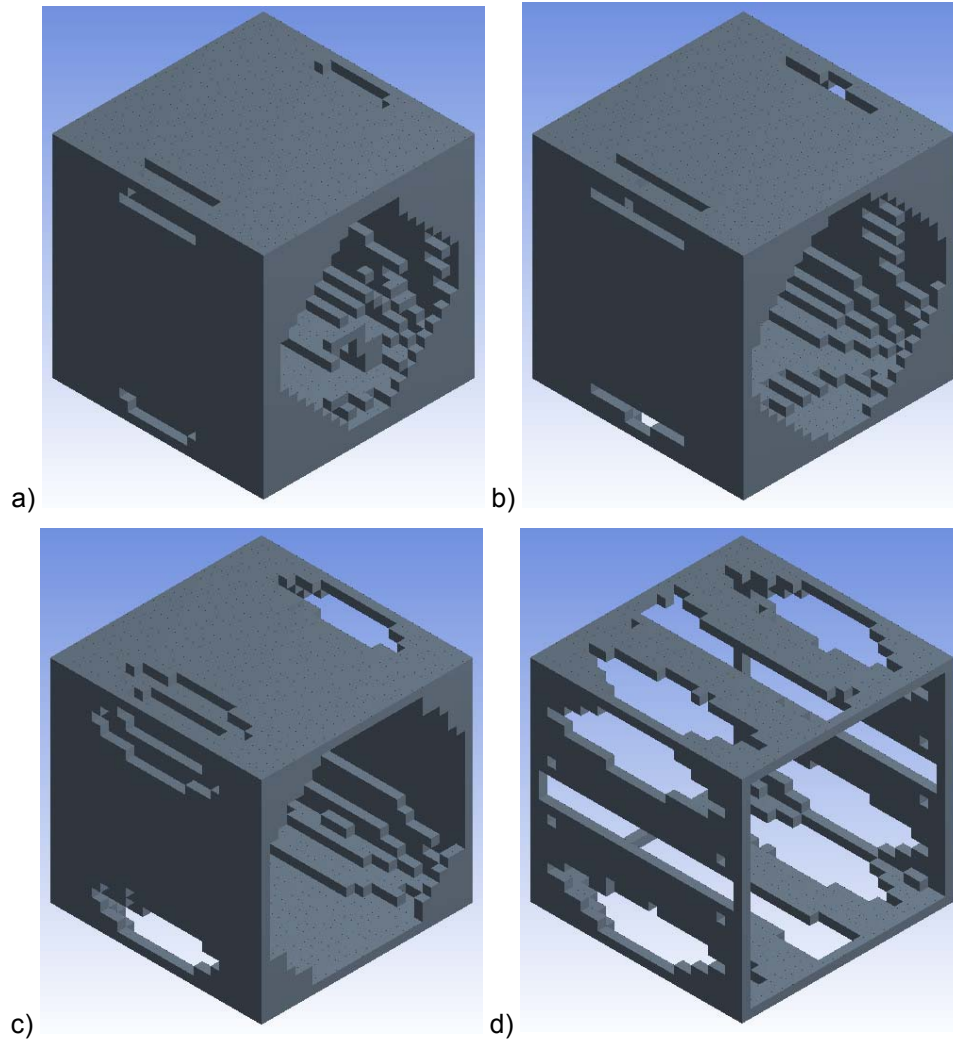


Figure 6.10 – Illustration of topologically optimised scaffold models from Scenario 12 with a porosity of a) 60 % b) 70% c) 80 % d) 90 %.

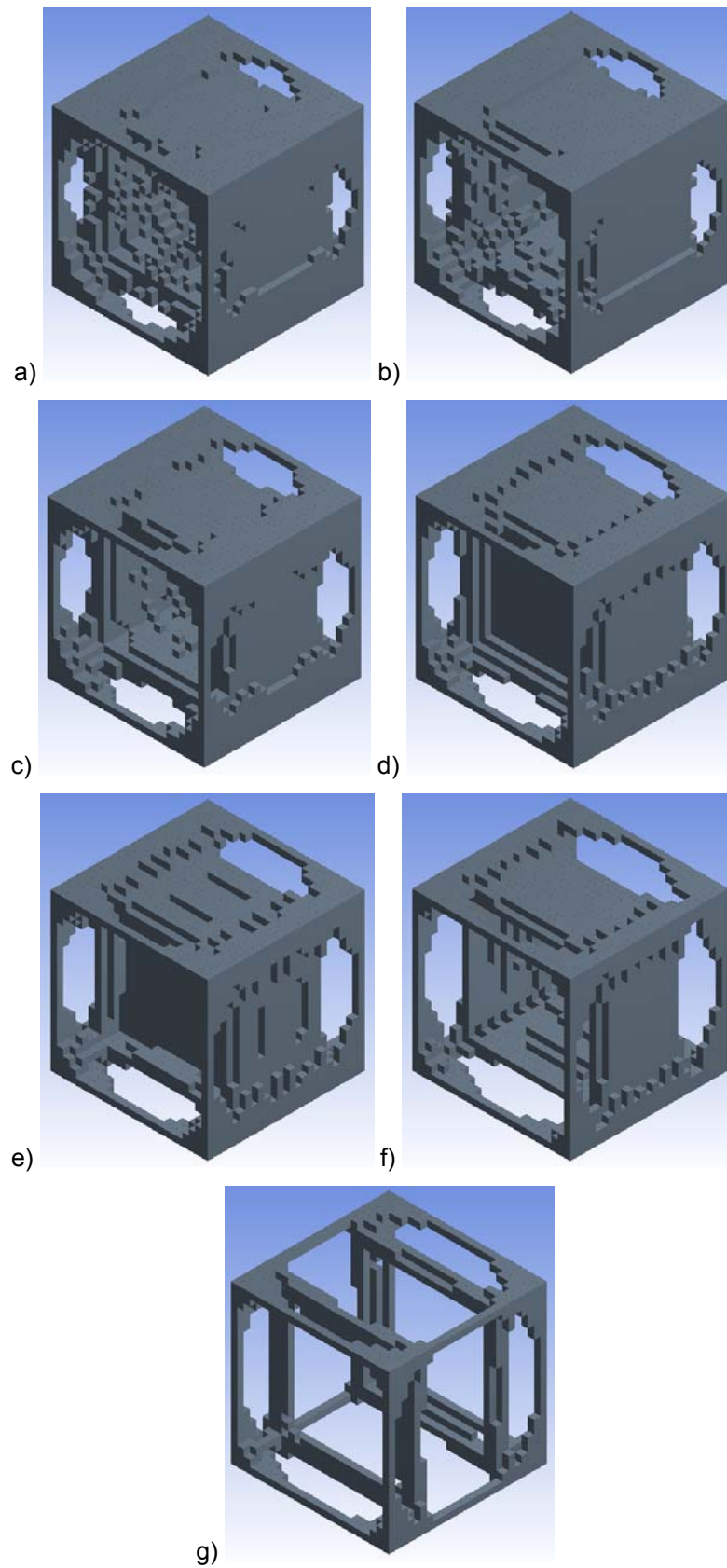


Figure 6.11 – Illustration of topologically optimised scaffold models from Scenario 6 with a porosity of a) 30 % b) 40% c) 50 % d) 60 % e) 70 % f) 80 % g) 90 %.

Figures 6.6 and 6.7 illustrate the solution for scenarios 2 and 3. Both scenarios only present 2 valid topological solutions for 80 % and 90 % porosity. By comparing both, the first scenario presents higher biological performance due to its interconnectivity in 2 directions instead of just 1 in the second scenario.

Figures 6.9 and 6.10 illustrate the results for scenarios 9 and 12. These 2 scenarios present 4 valid topological solutions for 60 %, 70 %, 80 % and 90 % of porosity. In this case, scenario 12 presents the best results due to the fact that all 4 solutions present pore interconnectivity in all 3 directions, when compared to scenario 9 which only 3 present pore interconnectivity in all directions.

Figure 6.8 presents 5 valid topological solutions for scenario 8, ranging from 50 % to 90 % in porosity. All 5 solutions present pore interconnectivity in all 3 directions.

The scenario 13 is the scenario that presents the highest number valid topological solutions (Figure 6.11). In this case, all solutions present pore interconnectivity in all 3 directions ranging from 30 % to 90 %.

From the results, it is possible to conclude that the best given topological optimised scenario is the 6th, which corresponds to the scenario with constraints on the edges in 1 direction and the displacements on the edges but in 2 directions.

(b) Bio-surface constrained optimisation of a solid block element

This approach is based on μ CT data of real biological tissues to create the loading and constraint surfaces of the scaffold during the topological optimisation process. Contrary to the previous case, where all faces of a block were considered as admissible loading and constraint surfaces, in this approach only specific regions are considered. The goal of this approach is to obtain biomimetic optimised elements. In order to perform this kind of optimisation, a trabecular bone region was considered. The corresponding STL model is shown in Figure 6.12.a. The STL file model obtained from the μ CT data was analysed and non-valid triangles were removed and errors (overlapping, degenerated triangles, etc.) corrected (Figure 6.12.b). Once analysed and corrected, datum plane boundaries were created in order to define the scaffold element boundary space (Figure 6.13). The following step involves the intersection between the datum planes and the STL model to define the loading and constraint curves (Figure 6.14) to define the surfaces for optimisation (Figure 6.15). The scaffold block element considered indicated in Figure 6.16.

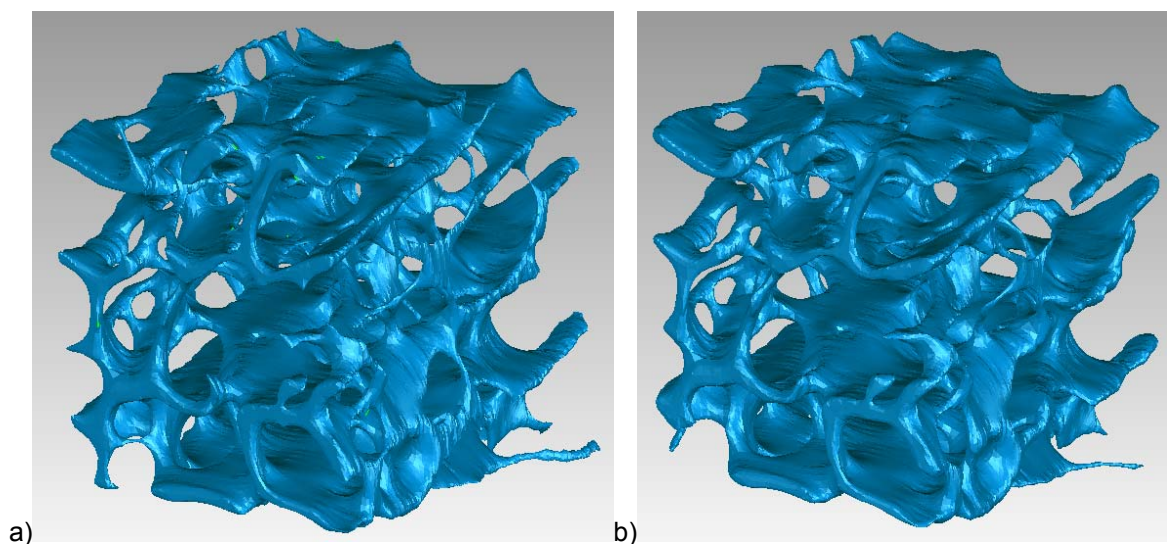


Figure 6.12 – a) μ CT STL file and b) STL file after removing the triangular imperfections.

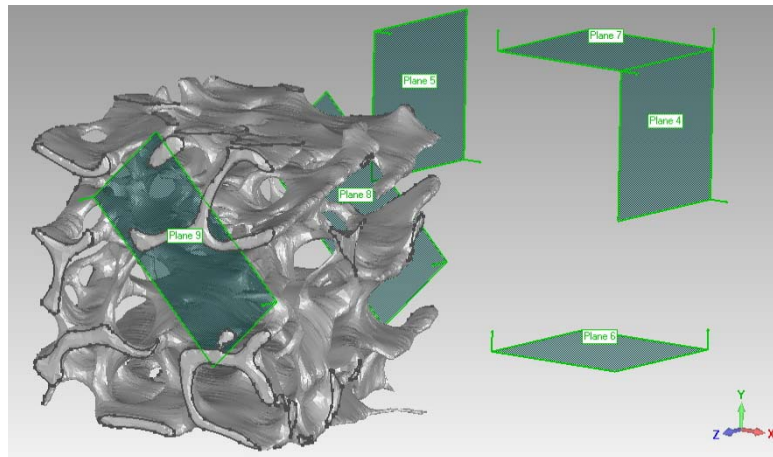


Figure 6.13 – Definition of the datum planes on the STL model limiting the scaffold's boundary.

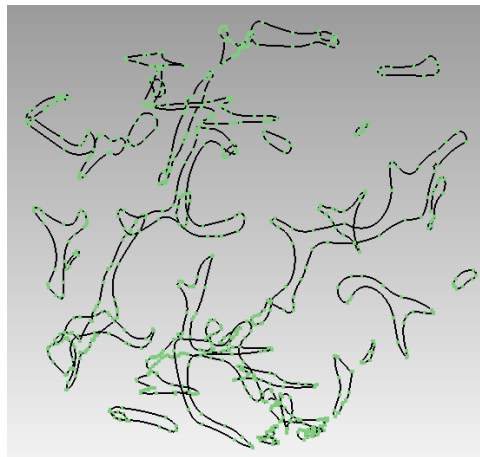


Figure 6.14 – Illustration of the curves obtained from the intersection between the datum planes and the STL model.

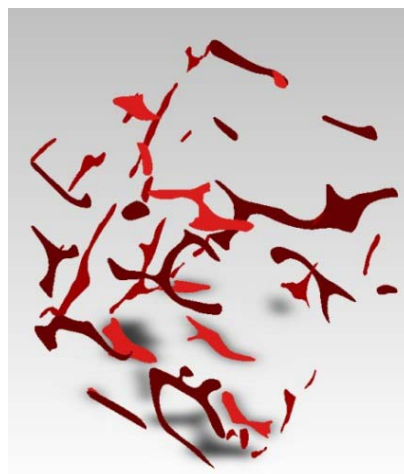


Figure 6.15 – Illustration of the a) Loading and constraint surfaces and b) free non-solicited surfaces.

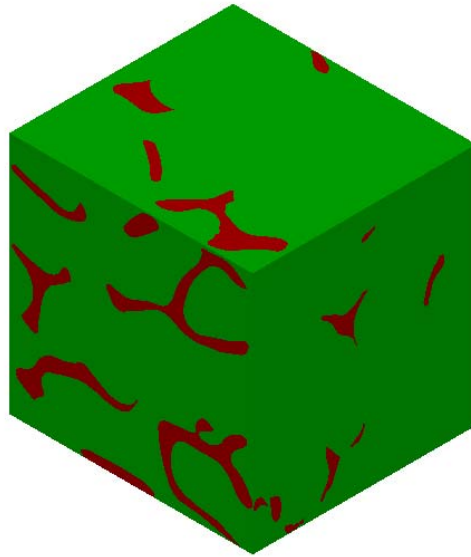


Figure 6.16 – Illustration of the scaffold block element considered for the topological simulations. Red – regions subjected to either loading or constraint conditions; Green – regions free of either loading or constraint conditions.

The porosity of the original μ CT model within the STL file is 84 %, this was also the considered value for simulation purposes. The block element was assumed to have a linear elastic behaviour, so strain values of 0.1 were simulated by imposing a corresponding displacement according to the strain direction considered (0.2 mm along both X and Y directions, and 0.184 along the Z direction). A mesh of 98535 solid tetrahedral elements was considered (Figure 6.17).

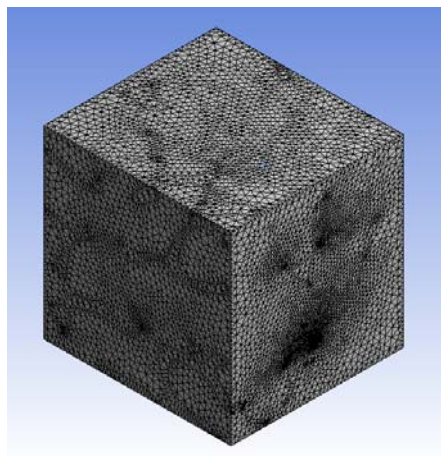


Figure 6.17 – Illustration of the Meshed model of the scaffold.

The following scenarios were considered (Figures 6.18 and 6.19):

- Scenario 1: specific regions of the block faces were submitted to strains in a single direction ϵ_{xx} and the remaining specific regions were constrained.
- Scenario 2: specific regions of the block faces were submitted to strains in a single direction ϵ_{yy} and the remaining specific regions were constrained.
- Scenario 3: specific regions of the block faces were submitted to strains in a single direction ϵ_{zz} and the remaining specific regions were constrained.
- Scenario 4: specific regions of the block faces were submitted to strains in a two directions (ϵ_{yy} , ϵ_{zz}) and the remaining specific regions were constrained.
- Scenario 5: specific regions of the block faces were submitted to strains in a two directions (ϵ_{xx} , ϵ_{zz}) and the remaining specific regions were constrained.
- Scenario 6: specific regions of the block faces were submitted to strains in a two directions (ϵ_{xx} , ϵ_{yy}) and the remaining specific regions were constrained.

In Figures 6.18 and 6.19, the Red are subjected to a loading condition while the Blue regions are constraint. The Gray regions are free of either loading or constraint conditions.

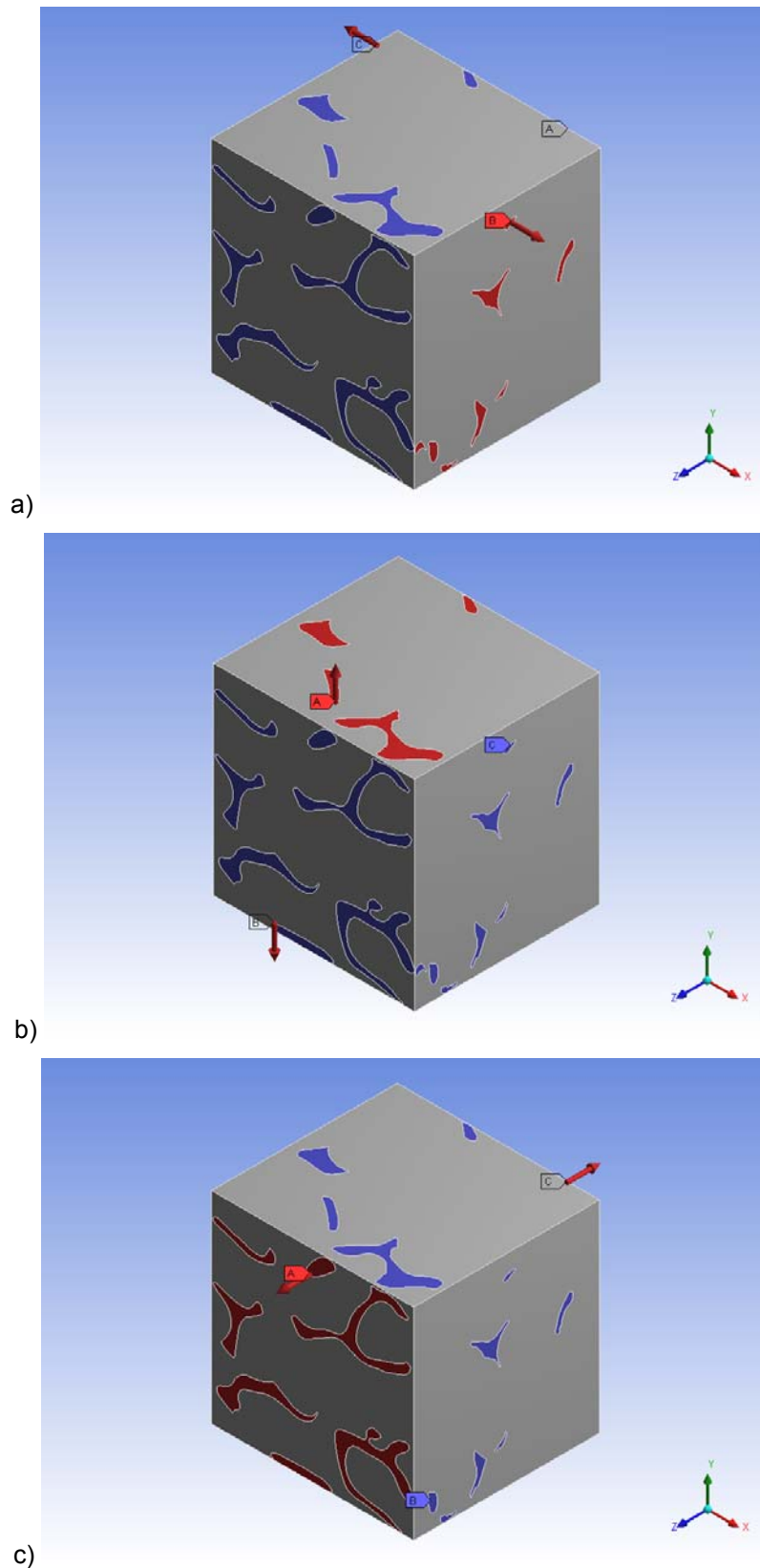


Figure 6.18 – Illustration the variation of the solicitations according to each direction, maintaining the other two directions constrained: a) DX - Displacement in the XX direction b) DY - Displacement in the YY direction c) DZ - Displacement in the ZZ direction.

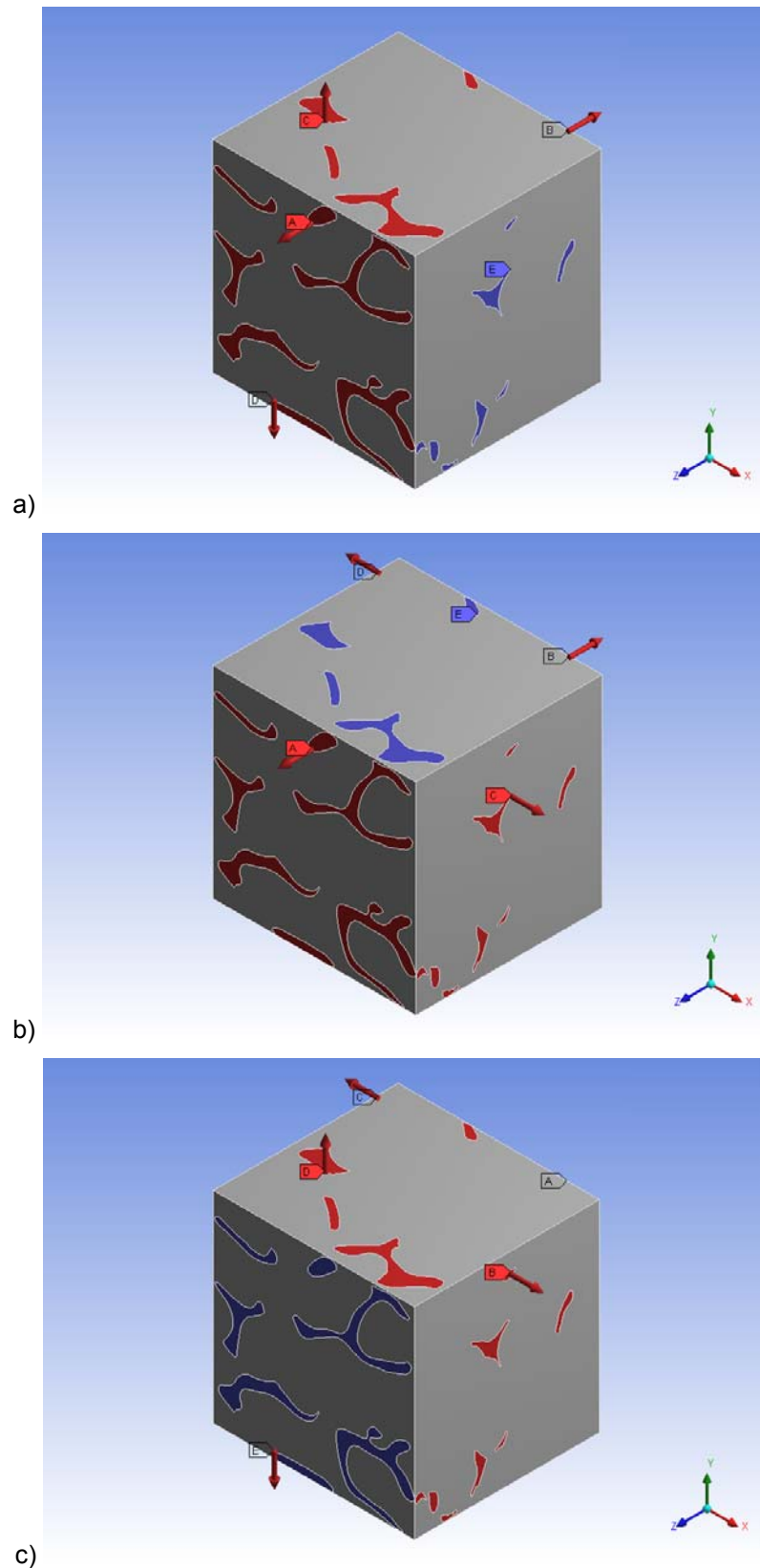


Figure 6.19 – Illustration the variation of the constraints according to each direction, maintaining the other two directions under displacement: a) CX - Constraint in the XX direction b) CY - Constraint in the YY direction c) CZ - Constraint in the ZZ direction.

The obtained results were:

- Scenario 1: Figure 6.20.a presents a valid topological scaffold model in 2 different positions.
- Scenario 2: Figure 6.20.b presents a valid topological scaffold model in 2 different positions.
- Scenario 3: Figure 6.20.c presents a valid topological scaffold model in 2 different positions.
- Scenario 4: Figure 6.21.a presents a valid topological scaffold model in 2 different positions.
- Scenario 5: Figure 6.21.a presents a valid topological scaffold model in 2 different positions.
- Scenario 6: Figure 6.21.a presents a valid topological scaffold model in 2 different positions.

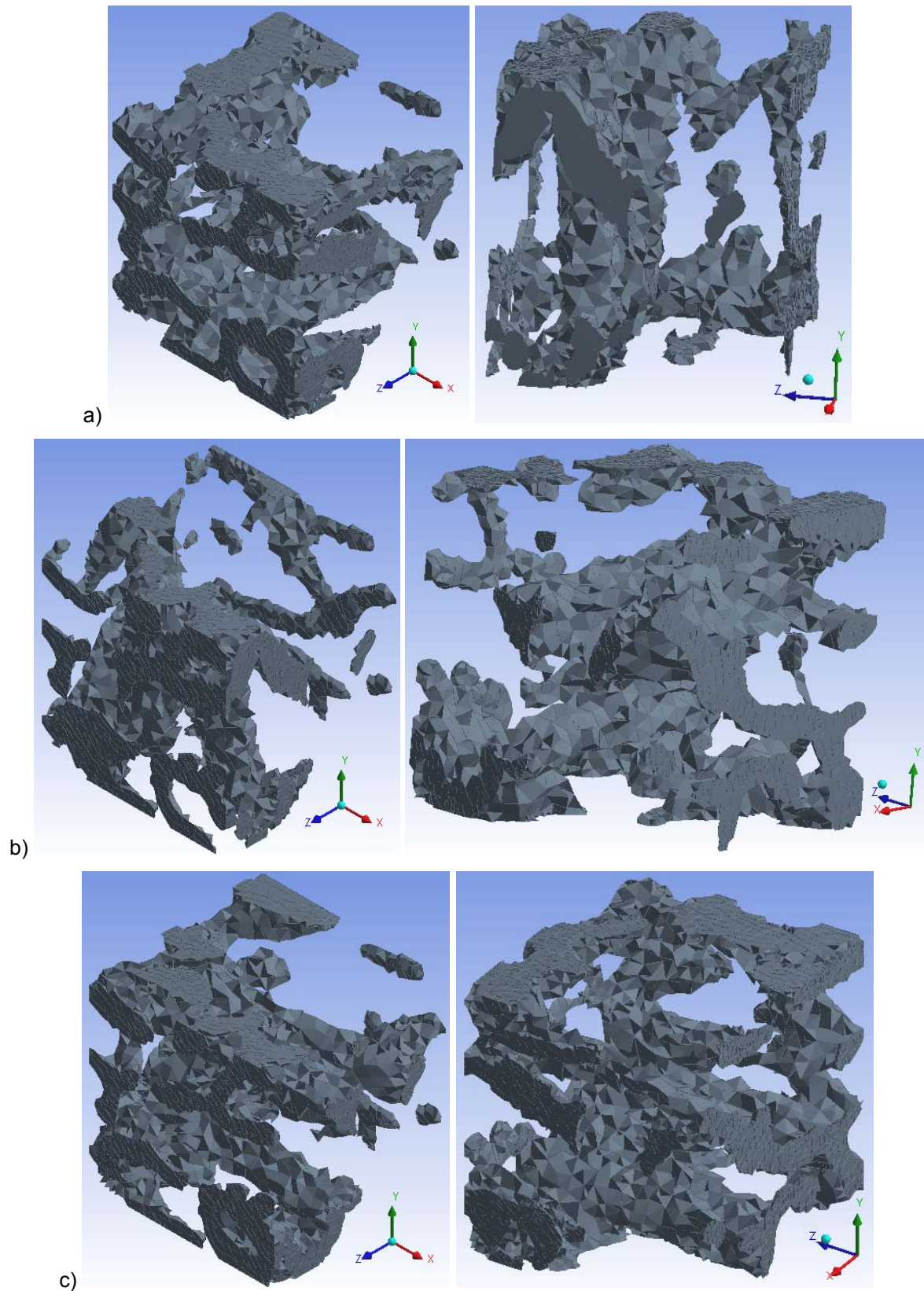


Figure 6.20 – Illustration the topological optimisation results according to each displacement direction: a) DX - Displacement in the XX direction b) DY - Displacement in the YY direction c) DZ - Displacement in the ZZ direction.

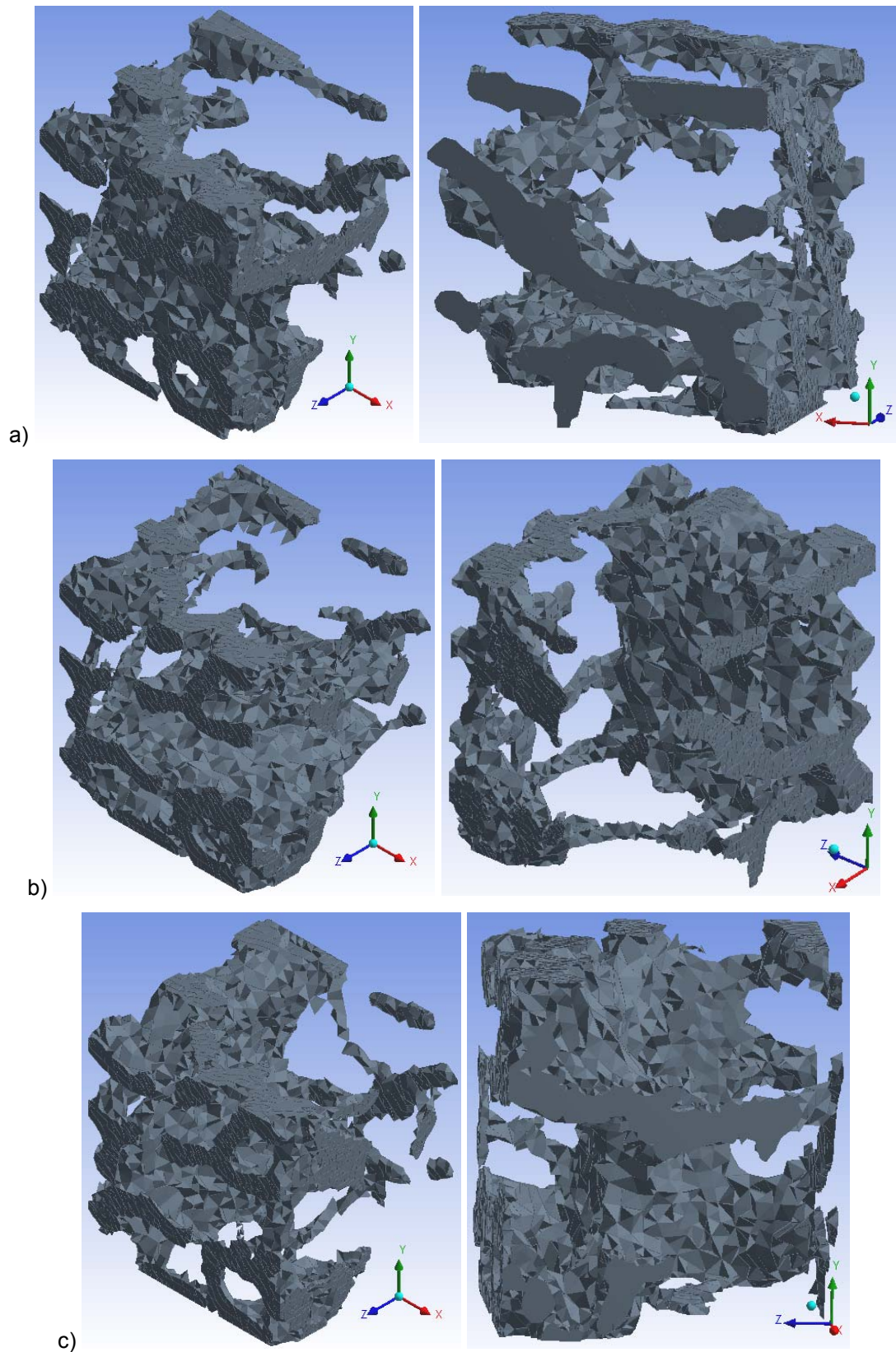


Figure 6.21 – Illustration the topological optimisation results according to each constraint direction:
a) CX - Constraint in the XX direction b) CY - Constraint in the YY direction c) CZ - Constraint in the ZZ direction.

After performing the six topological optimisation scenarios for the given objective function of 84 % porosity, the following results were obtained. Figures 6.20 and 6.21 illustrate the topological results for each case study. Figure 6.20 illustrate the results according to the variation of the solicitations in each direction, maintaining the other two directions constrained. Figure 6.21 illustrates the results according to the variation of the constraints in each direction, maintaining the other two directions under displacement.

These results permit to conclude that this approach enables to produce more biomimetic topologies. The initial external topology of the μ CT data, which corresponds to a structure of a well-defined mechanical behaviour and porosity level is the starting point of an optimisation scheme that enables us to obtain, based on a biomimetic external surfaces, constructs with different levels of porosity and mechanical properties according to the required applications. The goal is not to obtain similar structures as the starting model by instead to use the starting configuration to produce novel models with different characteristics.

Chapter 7 – Conclusions and Future Works

7.1. Concluding Remarks

Scaffolds are critical elements for tissue engineering applications, as they provide the necessary support for tissue regeneration in an organised way. As described in Chapter 1, scaffolds should be biocompatible, biodegradable, with appropriate porosity, pore structure and pore distribution, on top of presenting both surface and structural compatibility. These characteristics are usually difficult to achieve, i.e., it is quite difficult to design a construct with both high porosity (a critical property for vascularisation purposes) and high mechanical properties.

Design strategies to produce optimized scaffolds represent a critical topic of research in the field of tissue engineering. This is an emergent domain covered by this research study.

The state-of-the-art in tissue engineering, biofabrication and scaffold design, based on numerical simulations to determine optimum scaffold design parameters, is fully addressed. The knowledge gathered through this literature review (Chapters 1, 2 and 3) was fundamental to develop a computational strategy for Computer Aided Design of Scaffolds based on CAD data, the mechanical models, and the finite element method, in order to investigate the following issues: the mechanical behaviour (Chapter 4), the vascular behaviour (Chapter 5) and to optimise the scaffold's topology (Chapter 6).

Scaffolds can be considered as a LEGO structure formed by an association of small elementary units or blocks. Two families of elementary scaffold units were considered: i) Non-triple periodic minimal surfaces, and ii) Triple periodic minimal

surfaces (Schwartz and Schoen surfaces). Both families of scaffold topologies were evaluated as a function of porosity, in terms of mechanical and vascular performance. Additionally, all families were experimentally validated from a manufacturing view. The use of these different scaffold families enables the fabrication of fully interconnected scaffolds through additive biofabrication techniques. Non-triple periodic minimal surfaces were evaluated in terms of pore topology and pore distribution, while the Triple periodic minimal surfaces were evaluated in terms of two geometric design parameters (radius and thickness values).

From a mechanical point of view, it is possible to observe that:

- By increasing the porosity, the mechanical properties decrease in a non-linear way.
- The influence of the number of pores per face, on the mechanical properties of Non-triple periodic minimal surfaces, was also determined. For a given level of porosity, by increasing the number of pores per face, the mechanical properties increase in a non-linear way.
- The relationship between porosity and mechanical properties depends on the architecture of the pore. Non-triple periodic minimal surfaces that present better behaviour are the scaffolds with “CF” pores below a critical value of 50 % porosity, and the scaffolds with “4F” pores above 50 % porosity. On the other way, the Triple periodic minimal surface scaffolds presenting the best results are the ones obtained with the Schwartz surfaces. These surfaces, for the same level of porosity and different radius values, enable to produce structures either with high mechanical behaviour or low mechanical behaviour.
- A relationship between the geometric parameters (radius and thickness) of Triple periodic minimal surfaces and its mechanical properties was obtained on a macro-scale level. For both Schwartz and Schoen surfaces, the mechanical properties improve with the increase in its thickness in a non-linear way. Regarding the radius variation for the Schoen surfaces the

mechanical properties decrease in a non-linear way as the radius increases.

- On a micro-scale level, for both Schwartz and Schoen surfaces, the scaffold structures present a more homogenous tensile distribution for lower thickness values. Regarding the radius variation for Schwartz surfaces, there is no significant tensile stress variation with an increase of radius, while Schoen geometries present a more homogenous tensile distribution for lower radius values.
- On another level, the Von Misses tensile stresses and the normal σ_{xx} stress variation, according to the node's geometric "X" position in the Schoen surface, was determined. Results show that both tensile stresses are similar, which means that the other tensile or shear stresses are less significant. It is also possible to observe that the geometric transition, from the corner channel to the central sphere, is characterized by a decrease on the average tensile stresses.
- In order to validate the proposed mechanical simulations, a comparison between numerical and experimental data was performed. In this case, a crushable foam behaviour was adopted for the numerical simulations. This comparison was undertaken for three pore sizes (450 μm , 550 μm and 650 μm). Results demonstrate that the scaffold with a pore size of 450 μm presents the best numerical results when compared to the experimental compressive data. The plots from the numerical simulations illustrate that an unbalanced meshed body results in an unbalanced bulging phenomenon, which influences the densification process. This phenomenon can justify the deviations verified between the numerical stress-strain curves and the experimental ones. In order to obtain a better agreement between the numerical stress-strain curves and the experimental ones, the numerical parameters of all three structures need to be optimised and a symmetric meshed body needs to be defined.

Two critical parameters were considered in the vascular simulations for both scaffold families, the Shear Stress Rate and the Wall Shear Stress. From the results, it is possible to observe that:

- For Non-triple periodic minimal surfaces, on a macro-scale level, both parameters present a sinusoidal behaviour with the increase of the pore size, maintaining its average value constant.
- For Non-triple periodic minimal surfaces, on a micro-scale level, both parameters present a similar behaviour with the increase in pore size, being more significant for the Wall Shear Stress. With the increase in the pore size, both structures present a more homogenous distribution of values with smaller deviations between the highest and lowest values. It is also possible to observe that higher values are located on the exterior of the scaffold and lower values in its interior.
- For the scaffold structures with pore sizes of 450 μm , 550 μm and 650 μm , both parameters present a similar behaviour. Results demonstrate that as the pore size increases, the difference is lower in value for the Shear Strain rate, and the Wall Shear Stress between the outer and inner regions of the scaffold, due to the decrease in the difficulty of the fluid to flow to the interior of the scaffold.
- For the Shear Strain Rate of Triple periodic minimal surfaces, it is possible to observe that the Shear Strain Rate decreases with the geometries' thickness and increases with the radius, for the Schoen surfaces. The Schwartz geometries have a similar behaviour for the Shear Strain Rate. In conclusion, the best geometric option is the scaffold with lower thickness and higher radius values.
- For the Wall Shear Stress of Triple periodic minimal surfaces, it is possible to observe that the Wall Shear Stress increases for the Schwartz geometry and decreases for the Schoen geometries, with the increase in thickness. The geometric variation regarding the radius variation has a similar behaviour compared to the thickness.

- Regarding the Wall Shear Stress of Triple periodic minimal surfaces on a micro-scale, the Schoen geometries present a more homogenous variation with lower thickness values, for both interior and exterior regions of the scaffold. The most significant variation is presented with the thickness variation of the Schwartz geometries, so the Wall Shear Stress increases with the increase of thickness maintaining a homogenous distribution on the exterior region of the scaffold. Regarding the interior region of the scaffold, it tends to decrease with a homogenous distribution.

Regarding the topological optimizations, two types of analysis were carried out:

- The topological optimisation of an initial solid block element:

In this analysis, several scenarios were considered, combining loading and constraint conditions on vertices, edges and faces. In this case, two types of design models were obtained, invalid and valid scaffold models. Design models that present a shell structure or non-interconnected designs are considered invalid scaffold models, while design models that present interconnectivity in 1, 2 or 3 directions are considered valid scaffold models.

From the results, it is possible to conclude that the best topological scenario corresponds to a scenario with constraints on the edges in 1 direction and displacements on the edges in the other 2 directions, obtaining 7 valid scaffold design models with interconnectivity in all 3 directions.
- The bio-surface constrained optimisation of a solid block element:

The initial external topology of the μ CT data, which corresponds to a structure of a well-defined mechanical behaviour and porosity level, is the starting point of an optimisation scheme that enables to obtain constructs with different levels of porosity and mechanical properties, according to the required applications, based on biomimetic external surfaces.

This particular topological optimisation scheme uses the surface boundaries to produce novel models with different characteristics, which are different from the initial μ CT models. This approach enables to produce valid biomimetic scaffold topologies for tissue engineering applications.

7.2. Future Works

Possible future directions for research following on this thesis can be undertaken in two main areas, namely numerical and experimental.

The numerical work that needs further investigation:

- Including viscoelastic behaviour models in the numerical simulations;
- Introducing degradation models in both the mechanical and vascular simulations;
- Combining both mechanical and vascular simulations in order to obtain a more complete understanding of tissue engineering scaffolds for specific domains, such as in perfusion bioreactors;
- Including cellular proliferation and behaviour models allowing numerical simulations of both cells and constructs. In this case, the degradation effect upon the polymeric and/or ceramic scaffolds should be considered.

The experimental work to be carried out:

- Validate the vascular simulations undertaken in this research work;
- Undergoing combined experimental mechanical and vascular stimulations upon the scaffolds in order to validate the numerical simulations;
- Develop cellular proliferation and behaviour models to be used in numerical simulations.

During this work, new research directions started to be explored and implemented at Centre for Rapid and Sustainable Product Development, with support of the Portuguese Foundation for Science and Technology (FCT), the Portuguese Agency for Innovation (ADI), the Ciencia Y Tecnologia Para El Desarrollo (CYTED) and the Marie Curie European Projects (FP7), as stated before. These projects are based in the deep understanding achieved during this thesis.

Several questions have been answered through this thesis, but several others have been proposed and must be solved in the future by further research studies. In other words, a PhD thesis is just another step in one's academic life in order to continue undergoing research and investigation at a different level.

References

- Adachi, T., Osako, Y., Tanaka, M., Hojo, M. and Hollister, S.J. (2006) "Framework for optimal design of porous scaffold microstructure by computational simulation of bone regeneration", *Biomaterials*, 27(21):3964-3972.
- Allan, I., Newman, H. and Wilson M. (2001) "Antibacterial activity of particulate Bioglass against supra- and subgingival bacteria", *Biomaterials*, 22:1683-1687.
- Almeida, H.A. and Bártolo, P.J. (2007) "Topological Optimization of Rapid Prototyping Scaffolds", International Conference on Manufacturing Automation (ICMA2007) National University of Singapore, Singapore.
- Almeida, H.A. and Bártolo, P.J. (2008) "Computer Simulation and Optimisation of Tissue Engineering Scaffolds: Mechanical and Vascular Behaviour", 9th Biennial ASME Conference on Engineering Systems Design and Analysis (ESDA2008) Y. Halevi and A. Fischer (Eds.) Haifa Isreal.
- Almeida, H.A., Mota, C.M., Mateus, A.J., Bártolo, P.J., Ferreira, N., Domingos, M. & N.M. Alves (2010) "Prototipagem Rápida por Bio-Extrusão", Portuguese Patent N° 104247.
- Alves, N.M.F. and Bártolo, P.J. (2006) "Integrated computational tools for virtual and physical automatic construction", *Automation in Construction*, 15:257-271.
- Alves, N.M.F. and Bártolo, P.J. (2008) "Automatic 3D shape recovery for rapid prototyping", *Virtual and Physical Prototyping*, 3(2):123-137.
- Alves, N.M.F., Bártolo, P.J. and Almeida, H.A. (2012) "Bioreverse engineering", in: *Reverse Engineering for Medical, Manufacturing and Security Applications*; P.J. Bártolo & B. Bidanda (Eds.), Springer (in press).
- Andersson S. (1983) "On the description of complex inorganic crystal structures", *Angew Chem Int Edit*, 22(2):69-81.
- Ang, T.H., Sultana, F.S.A., Hutmacher, D.W., Wong, Y.S., Fuh, J.Y.H., Mo, X.M., Loh, H.T., Burdet, E. and Teoh, S.H. (2002) "Fabrication of 3D chitosan-hydroxyapatite scaffolds using a robotic dispersing system", *Materials Science and Engineering C*, 20:35-42.
- Angelova, N. and Hunkeler, D. (1999) "Rationalizing the design of polymeric biomaterials", *Trends in Biotechnology*, 17(10):409-421.
- Ansola, R., Veguería, E., Canales, J. and Tárrago, J. (2007) "A simple evolutionary topology optimization procedure for compliant mechanism design", *Finite Elements in Analysis and Design*, 44:53-62.
- Badylak, S., Freytes, D.O. and Gilbert, T.W. (2009) "Extracellular matrix as a biological scaffold material: structure and function", *Acta Biomaterialia*, 5:1-13.
- Bag, R., Suleman, N. and Guntupalli, K.K. (2004) "Respiratory failure in interstitial lung disease", *Curr Opin Pulm Med*, 10(5):412-418.

- Bártolo, P., Mendes, A. and Jardini, A. (2004) "Bio-prototyping", in: *Design and Nature II*; M.W. Collins and C.A. Brebbia (Eds.) WIT Press, Southampton, UK, 535-543.
- Bártolo, P.J. (2006) "State of the art of solid freeform fabrication for soft and hard tissue engineering", in: *Design and Nature III: Comparing design in nature with science and engineering*; C.A. Brebbia (Ed.) WIT Press, Wessex Institute of Technology, UK, 233-243.
- Bártolo, P.J. (2011) "Stereolithographic Processes", in: *Stereolithography - Materials, Processes and Applications*, P.J. Bártolo (Ed.), Springer.
- Bártolo, P.J. and Mitchell, G. (2003) "Stereo-thermal-lithography", *Rapid Prototyping Journal*, 9:150–156.
- Bártolo, P.J., Almeida H. and Laoui, T. (2009a) "Rapid prototyping & manufacturing for tissue engineering scaffolds", *International Journal of Computer Applications in Technology*, 36(1):1-9.
- Bártolo, P.J., Almeida, H.A., Rezende, R.A., Laoui, T. and Bidanda, B. (2008) "Advanced Processes to Fabricate Scaffolds for Tissue Engineering", in: *Virtual Prototyping & Bio-Manufacturing in Medical Applications*; B. Bidanda and P.J. Bártolo (Eds.) Springer, New York, 151-174.
- Bártolo, P.J., Chua, C.K., Almeida, H.A., Chou, S.M. and Lim, A.S.C. (2009b) "Biomanufacturing for Tissue Engineering: Present and Future Trends", *Virtual and Physical Prototyping*, 4(4):203-216.
- Bártolo, P.J., Kruth, J.P., Silva, J., Levy, G., Malshe, A., Rajurkar, K., Mitsuishi, M., Ciurana, J. and Leu, M. (2012) "Biomedical production of implants by additive electro-chemical and physical processes", *CIRP Annals – Manufacturing Technology*, in press.
- Bártolo, P.J., Lagoa, R. and Mendes, A. (2003) "Rapid prototyping system for tissue engineering", in: *Proceedings of the International Conference on Advanced Research in Virtual and Physical Prototyping*; P.J. Bártolo et al (Eds.) Leiria, 419-426.
- Beckstead, B.L., Pan, S., BrattLeal, A.M., Ratner, B.D., Giachelli, C.M. and Bhrany, A.D. (2005) "Esophageal epithelial cell interaction with synthetic and natural scaffolds for tissue engineering", *Biomaterials*, 26:6217-6228.
- Bendsøe, M. P. and Sigmund, O. (2003) "Topology optimization: theory, methods and applications", Springer.
- Bendsøe, M.P. (1989) "Optimal shape design as a material distribution problem", *Structural and Multidisciplinary Optimization*, 1:193-202.
- Bendsøe, M.P. and Kikuchi, N. (1988) "Generating optimal topologies in structural design using homogenization method", *Computer Methods in Applied Mechanics and Engineering*, 71:197-244.
- Berry, C.C., Campbell, G., Spadicino, A., Robertson, M. and Curtis, A. (2004) "The influence of microscale topography on fibroblast attachment and motility", *Biomaterials*, 25:5781-5788.
- Bertsch, A., Jiguet, S., Bernhard, P. and Renaud, P. (2003) "Microstereolithography: a review", *Mat Res Soc Symp Proc*, 758:LL.1.1.1-13.

- Bhumiratana, S. and Vunjak-Novakovic, G. (2012) "Concise Review: Personalized Human Bone Grafts for Reconstructing Head and Face", *Stem Cells Translational Medicine*, 1:64-69.
- Bignon, A., Chouteau, J., Chevalier, J., Fantozzi, G., Carret, J.P., Chavassieux, P., Boivin, G., Melin, M. and Hartmann, D. (2003) "Effect of microand macroporosity of bone substitutes on their mechanical properties and cellular response", *Journal of Materials ScienceMaterials in Medicine*, 14:1089-1097.
- Billiet, T., Vandenhaute, M., Schelfhout, J., Van Vlierberghe, S. and Dubruel, P. (2012) "A review of trends and limitations in hydrogel-rapid prototyping for tissue engineering", *Biomaterials*, 33(26):6020-6041.
- Boland, T., Tao, X., Damon, B.J., Manley, B. and Kesari, P. (2007) "Drop-on-demand printing of cells and materials for designer tissue constructs", *Mater Sci Eng: C*, 27(3):372-376.
- Boonthekul, T. and Mooney, D.J. (2003) "Protein-based signalling systems in tissue engineering", *Current Opinion in Biotechnology*, 14:559-565.
- Borer, J.S., Truter, S.L., Gupta, A., Herrold, E.M., Carter, J.N., Lee, E. and Pittlor, L. (2004) "Heart failure in aortic regurgitation: the role of primary fibrosis and its cellular and molecular pathophysiology", *Adv Cardiol*, 41:16-24.
- Brekke, J.H. (1996) "A rationale delivery of osteoconductive proteins (A review)", *Tissue Eng*, 2:97.
- Bryant, S. and Anseth, K.S. (2001) "The effects of scaffold thickness on tissue engineered cartilage in photocrosslinked poly(ethyleneoxide) hydrogels", *Biomaterials*, 22:619-626.
- Bucklen, B., Wettergreen, W., Yuksel, E. and Liebschner, M. (2008) "Bone-derived CAD library for assembly of scaffolds in computer-aided tissue engineering", *Virtual and Physical Prototyping*, 3(1):13-23.
- Byrne, D.P., Lacroix, D., Planell, J.A., Kelly, D.J. and Prendergast, P.J. (2007) "Simulation of tissue differentiation in a scaffold as a function of porosity, Young's modulus and dissolution rate: application of mechano-biological models in tissue engineering", *Biomaterials*, 28(36):5544-5554.
- Carmeliet, P. and Jain, R.K. (2000) "Angiogenesis in cancer and other diseases", *Nature*, 407:249-257.
- Carter, D.R., Blenman, P.R. and Beaupre, G.S. (1988) "Correlations between mechanical-stress history and tissue differentiation in initial fracture-healing", *J Orthop Res*, 6(5):736-748.
- Cartmell, S., Porter, B., García, A., and Guldberg, R. (2003) "Effects of Medium Perfusion Rate on Cell-Seeded Three-Dimensional Bone Constructs in Vitro", *Tissue Engineering*, 9(6):1197-1203.
- Carvalho, C., Landers, R., Mulhaupt, R., Hubner, U. and Schmelzeisen, R. (2005) "Fabrication of soft and hard biocompatible scaffolds using 3D-Biplotting", in: *Virtual Modelling and Rapid Manufacturing – Advanced Research in Virtual and Rapid Prototyping*, P.J. Bártolo et al (Eds.), Taylor & Francis, London, UK, 97-102.

- Cheah, C.M., Chua, C.K., Leong, K.F., Cheong, C.H. and Naing, M.W. (2004) "Automatic algorithm for generating complex polyhedral scaffold structures for tissue engineering", *Tissue Eng*, 10(3-4):595-610.
- Chen, C.S., Mrksich, M., Huang, S., Whitesides, G.M. and Ingber, D.E. (1997) "Geometric control of cell life and death", *Science*, 276:1425-1428.
- Chen, Y., Zhou, S. and Li, Q. (2011) "Microstructure design of biodegradable scaffold and its effect on tissue regeneration", *Biomaterials*, 32:5003-5014.
- Chen, Y.H., Ng, C.T. and Wang, Y.Z. (1999) "Data reduction in integrated reverse engineering and rapid prototyping", *International Journal of Computer Integrated Manufacturing*, 12:97-103.
- Cheng, Z. and Teoh, S.H. (2004) "Surface modification of ultra thin poly (ϵ -caprolactone) films using acrylic acid and collagen", *Biomaterials* 25:1991-2001.
- Chen-Yang, Y.W., Liao, J.D., Kau, J.Y., Huang, J., Chang, W.T. and Chen, C.W. (2000) "Surfacemodifications of expanded poly(tetrafluoroethylene) sheets assisted by CO₂ antenna coupling microwave plasma", *Macromol*, 33:5638-5643.
- Chicurel, M.E., Chen, C.S. and Ingber, D.E. (1998) "Cellular control lies in the balance of forces", *Curr Opin Cell Biol*, 10(2):232-239.
- Chong, A.K.S. and Chang, J. (2006) "Tissue engineering for the hand surgeon: A clinical perspective", *The Journal of Hand Surgery*, 31A:349-358.
- Chu, T.M., Halloran, J.W., Hollister, S.J. and Feinberg, S.E. (2001) "Hydroxyapatite implants with designed internal architecture", *Journal of Materials Science-Materials in Medicine*, 12(6):471-478.
- Chua, C.K., Leong, K.F. and Lim, C.S. (2003) "Rapid Prototyping: Principles and Applications", World Science Publishing, Singapore.
- Clark, E.R. and Clark, E.L. (2005) "Microscopic observations on the growth of blood capillaries in the living mammal", *American Journal of Anatomy*, 64:251-301.
- Cooke, M.N., Fisher, J.P., Dean, D., Rimnac, C. and Mikos, A.G. (2002) "Use of stereolithography to manufacture critical-sized 3D biodegradable scaffolds for bone ingrowth", *Journal of Biomedical Materials Research Part B: Applied Biomaterials* 64B:65-69.
- de Bartolo, L., Leindlein, A., Hofmann, D., Bader, A., de Grey, A., Curcio, E. and Drioli, E. (2012) "Bio-hybrid organs and tissues for patient therapy: a future vision for 2030", *Chemical Engineering and Processing: Process Intensification*, 51:79-87.
- Deshpande, V.S. and Fleck, N.A. (2000) "Isotropic Constitutive Model for Metallic Foams," *Journal of the Mechanics and Physics of Solids*, 48:1253-1276.
- Dias, J.R. (2010) "Nanofibres development for cartilage tissue regeneration through electrospinning process", MSc Thesis, Master in Engineering Design and Product Development, Polytechnic Institute of Leiria.
- Dias, J.R., Antunes, F.E., Mitchell, G.R. and Bártoło, P.J. (2012) "PCL nanofibre meshes produced by electrospinning for cartilage tissue regeneration", *Proceedings of the 1st International*

- Conference on Design and Processes for Medical Devices (PROMED), E. Cerretti *et al*, Neos Edizioni:171-175.
- Dougherty, C. (2006) "Prometheus (Gods and Heroes of the Ancient World)", Taylor & Francis, London & New York.
- Druecke, D., Langer, S., Lamme, E., Pieper, J., Ugarkovic, M., Steinau, H.U. and Homann, H.H. (2004) "Neovascularization of poly(ether ester) block-copolymer scaffolds in vivo: long-term investigations using intravital fluorescent microscopy", *Biomedical Materials Research Part A*, 68:10-18.
- Eckes, B. and Krieg, T. (2004) "Regulation of connective tissue homeostasis in the skin by mechanical forces", *Clin Exp Rheumatol*, 22(3 Suppl 33):S73-76.
- Ellison, C.J., Phatak, A., Giles, D.W., Macosko, C.W., and Bates, F.S. (2007) "Melt blown nanofibers: Fiber diameter distributions and onset of fiber breakup", *Polymer*, 48:3306-3316.
- Eshraghi, S. and Das, S. (2010) "Mechanical and microstructural properties of polycaprolactone scaffolds with one-dimensional, two-dimensional, and three-dimensional orthogonally oriented porous architectures produced by selective laser sintering", *Acta Biomaterialia*, 6(7):2467-2476.
- Feder-Mengus, C., Ghosh, S., Reschner, A., Martin, I. and Spagnoli, G.C. (2008) "New dimensions in tumor immunology: what does 3D culture reveal?", *Trends in Molecular Medicine*, 14(8):333-340.
- Ferreira, J.M. (2011) "Degradação enzimática in vitro de estruturas 3D em Poli(ϵ -caprolactona)", MSc Thesis, Master in Engineering Design and Product Development, Polytechnic Institute of Leiria.
- Fischbach, C., Tessmar, J., Lucke, A., Schnell, E., Schmeer, G., Blunk, T. and Gopferich, A. (2001) "Does UV radiation affect polymer properties relevant to tissue engineering?", *Surface Science*, 491:333-345.
- Fischer, J.P., Dean, D., Engel, P.S. and Mikos, A. (2001) "Photoinitiated polymerization of biomaterials", *Annu Rev Mater Res*, 31:171-181.
- Freyman, T.M., Yannas, I.V. and Gibson, L.J. (2001) "Cellular materials as porous scaffolds for tissue engineering", *Progress in Mater Sci*, 46:273-282.
- Fuchs, J.R., Nasser, B.A. and Vacanti, J.P. (2001) "Tissue engineering: a 21st century solution to surgical reconstruction", *Ann Thorac Surg*, 72, 577-581, 2001.
- Fung, Y.C. (1990) "Biomechanics: Motion, Flow, Stress and Growth", Springer – Verlag, New York.
- Galarnau, L., Loranger, A., Gilbert, S. and Marceau, N. (2007) "Keratins modulate hepatic cell adhesion, size and G1/S transition", *Experimental Cell Research*, 313:179-194.
- Gandy, P.J.F., Bardhan, S., Mackay, A.L. and Klinowski, J. (2001) "Nodal surface approximations to the P, G, D and I-WP triply periodic minimal surfaces," *Chemical Physics Letters*, 336(3):187-195.
- Gibson, L.J. (2005) "Biomechanics of cellular solids", *Journal of Biomechanics* 38:377-399.

- Gibson, L.J. and Ashby, M.F. (1982) "The Mechanics of Three-Dimensional Cellular Materials," Proceedings of the Royal Society, London, A 382:43-59.
- Gibson, L.J. and Ashby, M.F. (1997) "Cellular Solids: Structure and Properties", Second Edition, Cambridge University Press, Cambridge, U.K.
- Gibson, L.J., Ashby, M.F., Karam, G.N., Wegst, U., Shercliff, H.R. (1995) "The mechanical properties of natural materials II: Microstructures for mechanical efficiency", Proceedings of the Royal Society of London A450, 141-162.
- Gibson, L.J., Ashby, M.F., Schajer, G.S. and Robertson, C.I. (1982) "The Mechanics of Two-Dimensional Cellular Materials", Proceedings of the Royal Society, London, A 382:25-42.
- Godara, P., McFarland, C. D., and Nordon, R. E. (2008) "Design of bioreactors for mesenchymal stem cell tissue engineering (Mini Review)", Journal of Chemical Technology and Biotechnology, 83(4):408-420.
- Gomes, M.E. and Reis, R.L. (2004) "Biodegradable polymers and composites in biomedical applications: from catgut to tissue engineering. Part 2 Systems for temporary replacement and advanced tissue regeneration", Int Materials Rev, 49:274-285.
- Grace, J.M. and Gerenser, L.J. (2003) "Plasma treatment of polymers", J Disper Sci Technol, 24:305-341.
- Greene, G., Yao, G. and Tannenbaum, R. (2003) "Wetting characteristics of plasma-modified porous polyethylene", Langmuir, 19:5869-5874.
- Greiner, A. and Wendorff, J.H. (2007) "Electrospinning of nanofibres: Towards new techniques, functions, and applications", Angewandte Chemie International Edition, 46:5670-5703.
- Griffith, M.L. and Halloran, J.W. (1996) "Freeform fabrication of ceramics via stereolithography", Journal of the American Ceramic Society 79:2601-2608.
- Grodzinsky, A.J., Levenston, M.E., Jin, M. and Frank, E.H. (2000) "Cartilage tissue remodeling in response to mechanical forces", Ann Rev Biomedical Engineering, 2:691-713.
- Gross, K.A. and Rodríguez-Lorenzo, L.M. (2004) "Biodegradable composite scaffolds with an interconnected spherical network for bone tissue engineering", Biomaterials 25:4955-4962.
- Gualandi, C. (2011) "Porous Polymeric Bioresorbable Scaffolds for Tissue Engineering", Springer Theses, Springer-Verlag Berlin Heidelberg.
- Guillotin, B. and Guillemot, F. (2011) "Cell patterning technologies for organotypic tissue fabrication", Trends in Biotechnology, 29(4):183–190.
- Gupta, B., Hilborn, J., Hollenstein, C., Plummer, C.J.G., Houriet, R. and Xanthopoulos, N.J. (2000) "Surfacemodification of polyester films by RF plasma", Appl Polym Sci, 78:1083-1091.
- Hao, L., Savalani, M.M. and Harris, R.A. (2005) "Layer manufacturing of polymer/bioceramic implants for bone replacement and tissue growth", in: Virtual Modelling and Rapid Manufacturing – Advanced Research in Virtual and Rapid Prototyping, P.J. Bártolo et al (Eds.), Taylor & Francis, London, UK, 127-131.
- Healy, K.E., Tsai, D. and Kim, J.E. (1992) "Osteogenic cell attachment to biodegradable polymers", Mater Res Soc Symp Proc, 252:109.

- Ho, M.H., Kuo, P.Y., Hsieh, H.J., Hsien, T.Y., Hou, L.T., Lai, J.Y. and Wang, D.W. (2004) "Preparation of porous scaffolds by using freeze-extraction and freeze-gelation methods", *Biomaterials*, 25:129-138.
- Holdstein, Y. and Fischer, A. (2008) "Modelling micro-scaffold-based implants for bone tissue engineering", 9th Biennial ASME Conference on Engineering Systems Design and Analysis (ESDA2008) Y. Halevi and A. Fischer (Eds.) Haifa Isreal.
- Hollister, S.J. (2005) "Porous scaffold design for tissue engineering", *Nature Materials*, 4(7):518-524.
- Hollister, S.J., Maddox, R.D., and Taboas, J.M. (2002) "Optimal design and fabrication of scaffolds to mimic tissue properties and satisfy biological constraints", *Biomaterials*, 23(20):4095-4103.
- Hsu, M.H. and Hsu, Y.L. (2005) "Generalization of two and three-dimensional structural topology optimization", *Engineering Optimization*, 37:83-102.
- Huiskes, R., Ruimerman, R., van Lenthe, G.H. and Janssen, J.D. (2000) "Effects of mechanical forces on maintenance and adaptation of form in trabecular bone", *Nature*, 405(6787):704-706.
- Humphrey, J.D. and Delange, S.L. (2003) "An introduction to Biomechanics – Solids and Fluids, Analysis and Design", Springer, New York.
- Hutmacher, D., Woodfield, T., Dalton, P. and Lewis, J. (2008) "Scaffold design and fabrication", in: *Tissue Engineering*, Clemens van Blitterswijk, Elsevier.
- Hutmacher, D.W. (2001) "Scaffold design and fabrication technologies for engineering tissues--state of the art and future perspectives", *J Biomater Sci Polym Ed.*, 12(1):107-124.
- Hutmacher, D.W., Schantz, .JT., Lam, C.X.F., Tan, K.C. and Lim, T.C. (2007) "State of the art and future directions of scaffold-based bone engineering from a biomaterials perspective", *J. Tissue Eng. Regen. Med.*, 1:245-260.
- Hutmacher, D.W., Sittering, M. and Risbud, M.V. (2004) "Scaffold-based tissue engineering: rationale for computer-aided design and solid free-form fabrication systems", *Trends in Biotechnology*, 22:354-362.
- Hyde, S. (1996) "Bicontinuous structures in lyotropic liquid crystals and crystalline hyperbolic surfaces", *Current Opinion in Solid State & Materials Science*, 1:653-662.
- Hynes, R.O. (1992) "Integrins, versatility, modulation, and signalling in cell adhesion", *Cell*, 69:11-25.
- Ingber, D.E. (2003) "Mechanobiology and diseases of mechanotransduction". *Ann Med*, 35(8):564-577.
- Ireland, D., Harrall, R., Curry, V., Holloway, G., Hackney, R., Hazleman, B. and Riley, G. (2001) "Multiple changes in gene expression in chronic human Achilles tendinopathy". *Matrix Biology*, 20(3):159-169.
- Jacobs, C.R., Temiyasathit, S. and Castillo, A.B. (2010) "Osteocyte mechano-biology and pericellular mechanics", *Annu Rev Biomed Eng*, 369-400.

- Jain, R.K., Au, P., Tam, J., Duda, D.G. and Fukumura, D. (2005) "Engineering vascularized tissue", *Nature Biotechnology*, 23:821-823.
- Janssen, F.W., Oostra, J., Oorschot, A. and van Blitterswijk, C.A. (2006) "A perfusion bioreactor system capable of producing clinically relevant volumes of tissue-engineered bone: in vivo bone formation showing proof of concept", *Biomaterials*, 27:315-323.
- Jeong, J.H., Kima, S.W. and Park, T.G. (2007) "Molecular design of functional polymers for gene therapy", *Progress in Polymer Science*, 32(11):1239-1274.
- Johnson, P.C., Mikos, A.G., Fisher, J.P. and Jansen, J.A. (2007) "Strategic directions in tissue engineering", *Tissue Engineering*, 13:2827-2837.
- Jones, A.C., Arns, C.H., Hutmacher, D.W., Milthorpe, B.K., Sheppard, A.P. and Knackstedt, M.A. (2009) "The correlation of pore morphology, interconnectivity and physical properties of 3D ceramic scaffolds with bone ingrowth", *Biomaterials*, 30:1440-1451.
- Jung, Y., Chu, K.T. and Torquato, S. (2007) "A variational level set approach for surface area minimization of triply-periodic surfaces," *Journal of Computational Physics*, 223(2):711-730.
- Karageorgiou, V. and Kaplan, D. (2005) "Porosity of 3D biomaterial scaffolds and osteogenesis", *Biomaterials*, 26:5474-5491.
- Kelly, D.J. and Jacobs, C.R. (2010) "The role of mechanical signals in regulating chondrogenesis and osteogenesis of mesenchymal stem cells", *Birth Defects Res Part C - Embryo Today-Rev*, 90(1):75-85.
- Kelly, D.J. and Prendergast, P.J. (2005) "Mechano-regulation of stem cell differentiation and tissue regeneration in osteochondral defects", *J Biomech*, 38(7):1413-1422.
- Kim, B.S. and Mooney, D.J. (2001) "Development of biocompatible synthetic extracellular matrices for tissue engineering", *Trends Biotechnol*, 16:224-230.
- Kim, K.S., Ryu, C.M., Park, C.S., Sur, G.S. and Park, C.E. (2003a) "Investigation of crystallinity effects on the surface of oxygen plasma treated low density polyethylene using X-ray photoelectron spectroscopy", *Polymer*, 44:6287-6295.
- Kim, S.S., Utsunomiya, H., Koski, J.A., Wu, B.M., Cima, M.J., Sohn, J., Mukai, K., Griffith, L.G. and Vacanti, J.P. (1998) "Survival and function of hepatocytes on a novel three-dimensional synthetic biodegradable polymer scaffolds with an intrinsic network of channels", *Annals of Surgery* 228:8-13.
- Kim, T.K., Sharma, B., Williams, C.G., Ruffner, M.A., Malik, A., McFarland, E.G. and Elisseeff, J.H. (2003b) "Experimental model for cartilage tissue engineering to regenerate the zonal organization of articular cartilage", *Osteoarthritis and Cartilage*, 11:653-664.
- Koberstein, J.T., Duch, D.E., Hu, W., Lenk, T.J., Bhatia, R., Brown, H.R., Lingelser, J.P. and Gallot, Y. (1998) "Creating smart polymer surfaces with selective adhesion properties", *J Adhes*, 66:229-249.
- Kowata, S. and Sun, H.B. (2003) "Two-photon photopolymerization as a tool for making micro-devices", *Appl Surf Sci*, 208/209:153-158.

- Kreeger, P.K. and Shea, L.D. (2002) "Scaffolds for Directing Cellular Responses and Tissue Formation in Biomimetic Materials and Design", in: *Biomimetic Materials and Design: Biointerfacial Strategies, Tissue Engineering and Targeted Drug Delivery*; A.K. Dillow and A.M. Lowman (Eds.) Marcel Dekker, Inc, New York, 283-309.
- Kreke, M.R., Huckle, W.R., Goldstein, A.S. (2005) "Fluid flow stimulates expression of osteopontin and bone sialoprotein by bone marrow stromal cells in a temporally dependent manner", *Bone* 36:1047-1055.
- Kruijff, N., Zhou, S., Li, Q. and Mai, Y.W. (2007) "Topological design of structures and composite materials with multiobjectives", *International Journal of Solids and Structures*, 44(22-23):7092-7109.
- Kuboki, Y., Takita, H., Kobayashi, D., Tsuruga, E., Inoue, M. and Murata, M. (1998) "BMP-induced osteogenesis on the surface of hydroxyapatite with geometrically feasible and nonfeasible structures: topology of osteogenesis", *J Biomed Mater Res.*, 39:190-199.
- Kulkarni, P., Marsan, A. and Dutta, A. (2000) "A review of process planning techniques in layered manufacturing", *Rapid Prototyping Journal*, 6(1):18-35.
- Kuppan, P., Sethuraman, S. and Krishnan, U.M. (2012) "Tissue engineering interventions for esophageal disorders — Promises and challenges", *Biotechnology Advances* (in press).
- Lam, C.X.F., Mo, X.M., Teoh, S.H. and Hutmacher, D.W. (2002) "Scaffold development using 3D printing with a starch-based polymer", *Materials Science & Engineering C-Biomimetic and Supramolecular Systems* 20:49-56.
- Lammerding, J., Kamm, R.D. and Lee, R.T. (2004) "Mechanotransduction in cardiac myocytes". *Ann N Y Acad Sci*, 1015:53-70.
- Lan, P.X., Lee, J.W., Seol, Y.J. and Cho, D.W. (2009) "Development of 3D PPF/DEF scaffolds using micro-stereolithography and surface modification", *J Mater Sci: Mater Med*, 20:271-279.
- Langer, R. (1997) "Tissue engineering: a new field and its challenges", *Pharm Res*, 14:840-841.
- Langer, R. and Vacanti, J.P. (1993) "Tissue engineering", *Science* 260:920-926.
- Larsson M., Terasaki, O. And Larsson, K. (2003) "A solid state transition in the tetragonal lipid bilayer structure at the lung alveolar surface", *Solid State Sci*, 5(1):109-14.
- Laschke, M.W., Harder, Y., Amon, M., Martin, I., Farhadi, J., Ring, A., Torio-Padron, N., Schramm, R., Rücker, M., Junker, D., Häufel, J.M., Carvalho, C., Heberer, M., Germann, G., Vollmar, B. and Menger, M.D. (2006) "Angiogenesis in tissue engineering: breathing life into constructed tissue substitutes", *Tissue Engineering*, 12:2093-2104.
- Lee, G. and Barlow, J.W. (1996) "Selective laser sintering of bioceramic materials for implants", *Proceedings of the '96 SFF Symposium*, Austin, TX, August 12–14.
- Lee, J., Cuddihy, M.J. and Kotov, N.A. (2008) "Three-Dimensional Cell Culture Matrices: State of the Art", *Tissue Engineering Part B*, 14:61-86.
- Lee, T. H. (2007) "Optimisation of Structural and Mechanical Systems", J.S. Arora (Ed.) World Scientific, Singapore.

- LeGeros, R.Z. and LeGeros, J.P. (1995) "Calcium phosphate biomaterials: preparation, properties, and biodegradation", in: Encyclopedia handbook of biomaterials and bioengineering part A: materials, vol. 2.; D.L. Wise, D.J. Trantolo, D.E. Altobelli, M.J. Yaszemski, J.D. Gresser, E.R. Schwartz (Eds.), New York: Marcel Dekker, 1429-1463.
- Lemercier, G., Mulatier, J.C., Martineau, C., Anémian, R., Andraud, C., Wang, I., Stéphan, O., Amari, N. and Baldeck, P. (2005) "Two-photon absorption: from optical limiting to 3D microfabrication", *Comptes Rendus Chimie*, 8:1308-1316.
- Leong, K.F., Cheah, C.M. and Chua, C.K. (2003) "Solid freeform fabrication of three-dimensional scaffolds for engineering replacement tissues and organs", *Biomaterials*, 24:2363-2378.
- Leong, K.F., Chua, C.K., Sudarmadja, N. and Yeong, W.Y. (2008) "Engineering functionally graded tissue engineering scaffolds", *Journal of Mechanical Behaviour of Biomedical Materials*, 1:140-152.
- Leukers, B., Gulkan, H., Irsen, S.H., Milz, S., Tille, C., Schieker, M. and Seitz, H. (2005) "Hydroxyapatite scaffolds for bone tissue engineering made by 3D printing", *J Mater Sci Mater Med*, 16:1121-1124.
- Levy, R.A., Chu, T.G.M., Holloran, J.W., Feinberg, S.E. and Hollister, S. (1997) "CT-generated porous hydroxyapatite orbital floor prosthesis as a prototype bioimplant", *Am J Neuroradiol*, 18:1522-1525.
- Limpanuphap, S. and Derby, B. (2002) "Manufacture of biomaterials by a novel printing process", *J Mater Sci Mater Med*, 13:1163-1166.
- Liu, C.Z. and Czernuszka, J.T. (2006) "On the development of biodegradable scaffolds for tissue engineering: a perspective", *Materials Science and Technology*, 12:2479-2488.
- Liu, V.A and Bhatia S.N. (2002) "Three-dimensional patterning of hydrogels containing living cells", *Biomed. Microdevices*, 4:257-266.
- Ma, P.X. (2004) "Scaffolds for tissue fabrication", *Materials Today*, 7:30-40.
- Mahajan, H. P. (2005) "Evaluation of chitosan gelatine complex scaffolds for articular cartilage tissue engineering", MSc Thesis, Mississippi State University, USA.
- Maiti, S.K., Gibson, L.J. and Ashby, M.F. (1984) "Deformation and Energy Absorption Diagrams for Cellular Solids" *Acta Metallurgica*, 32(11):1963-1975.
- Malda, J., Rouwkema, J., Martens, D.E., le Comte, E.P., Kooy, F.K., Tramper, J., van Blitterswijk, C.A. and Riesle, J. (2004) "Oxygen gradients in tissue-engineered PEGT/PBT cartilaginous constructs: measurement and modelling", *Biotechnology and Bioengineering*, 86:9-18.
- Marler, J.J., Upton, J., Langer, R. and Vacanti, J.P. (1998) "Transplantation of cells in matrices for tissue regeneration", *Adv Drug Del Rev*, 33:165-182.
- Martin, I., Wendt, D. and Heberer, M. (2004) "The role of bioreactors in tissue engineering", *Trends in Biotechnology*, 22:80-86.
- Martin, Y., and Vermette, P. (2005) "Bioreactors for tissue mass culture: Design, characterization, and recent advances", *Biomaterials*, 26(35):7481-7503.

- Mateus, A.J., Almeida, H.A., Ferreira, N.M., Alves, N.M., Bártolo, P.J., Mota C. and Sousa, J.P. (2008) "Bioextrusion for tissue engineering applications", in: *Virtual and Rapid Manufacturing – Advanced Research in Virtual and Rapid Prototyping*, P.J. Bártolo et al (Eds.), Taylor&Francis, London, 171-175.
- Matsuda, T. and Mizutani, M. (2002) "Liquid acrylate-endcapped poly(ϵ -caprolactone-cotrimethylene carbonate). II. Computer-aided stereolithographic microarchitectural surface photoconstructs", *Journal of Biomedical Materials Research*, 62:395-403.
- Matsumoto, T. and Mooney, D.J. (2006) "Cell instructive polymers", *Adv Biochem Engin/Biotechnol*, 102:113-137.
- McClary, K.B., Ugarova, T. and Grainger, D.W. (2000) "Modulating fibroblast adhesion, spreading and proliferation using self-assembled monolayer films of alkylthiolates on gold", *J Biomed Mater Res*, 50(3):429-439.
- Melchels, F.P., Feijen, J. and Grijpma, D.W. (2009) "A poly(D,L-lactide) resin for the preparation of tissue engineering scaffolds by stereolithography", *Biomaterials*, 30:3801-3809.
- Meyers, M.A., Chen, P.Y., Lin, A.Y.M. and Seki, Y. (2008) "Biological materials: Structure and mechanical properties", *Progress in Materials Science*, 53(1):1-206.
- Mikos, A.G., Sarakinos, G., Lyman, M.D., Ingber, D.E., Vacanti, J.P. and Langer, R. (1993) "Prevascularization of porous biodegradable polymers", *Biotechnol Bioeng*, 42:716-723.
- Miot, S., Woodfield, T., Daniels, A.U., Suetterlin, R., Peterschmitt, I., Heberer, M., Blitterswijk, C.A.v., Riesle, J. and Martin, I. (2005) "Effects of scaffold composition and architecture on human nasal chondrocyte redifferentiation and cartilaginous matrix deposition", *Biomaterials*, 26:2479-2489.
- Miranda, P., Saiz, E., Gryn, K. and Tomsia, A.P. (2006) "Sintering and robocasting of β -tricalcium phosphate scaffolds for orthopaedic applications", *Acta Biomaterialia*, 2:457-466.
- Mironov, V., Boland, T., Trusk, T., Forgacs, G. and Markwald, R.R. (2003) "Organ printing: computer-aided jet-based 3D tissue engineering", *Trends in Biotechnology*, 21:157-161.
- Mironov, V., Visconti, R.P., Kasyanov, V., Forgacs, G., Drake, C.J. and Markwald, R.R. (2009) "Organ printing: Tissue spheroids as building blocks", *Biomaterials*, 30:2164–2174.
- Mistry, A.S. and Mikos A.G. (2005) "Tissue engineering strategies for bone regeneration", *Adv Biochem Engin/Biotechnol*, 94:1-22.
- Mitchell, G.R. and Davis, F.J. (2011) "Electrospinning and tissue engineering", in: *Advances on modelling in tissue engineering*; P.J. Bartolo and P.R. Fernandes (Eds.), New York: Springer, 111-136.
- Mitchell, G.R., Ahn, K. and Davis, F.J. (2011) "The potential of electrospinning in rapid manufacturing processes", *Virtual and Physical Prototyping*, 6(2):63-77.
- Mlejnek H.P. and Schirmacher, R. (1993) "An Engineering Approach to Optimal Material Distribution and Shape Finding", *Computational Methods Applied to Mechanical Engineering*, 106:1-26.

- Mlejnek, H.P. (1992) "Some aspects of the genesis of structures", *Structural and Multidisciplinary Optimization*, 5:64-69.
- Mooney, D.J., Cima, L.G., Langer, R., Johnson, L., Hansen, L.K., Ingber, D.E. and Vacanti, J.P. (1992) "Principles of tissue engineering and reconstruction using polymer-cell constructs", *Mater Res Soc Symp Proc*, 252:345.
- Moroni, L., Schotel, R., Sohler, J., Wijn, J.R. and Blitterswijk, C.A. (2006) "Polymer hollow fiber three-dimensional matrices with controllable cavity and shell thickness", *Biomaterials*, 27:5918-5926.
- Morsi, Y.S., Wong, C.S. and Patel, S.S. (2008) "Virtual prototyping of biomanufacturing in medical applications – conventional manufacturing processes for three-dimensional scaffolds", in: *Virtual Prototyping & Bio-Manufacturing in Medical Applications*; B. Bidanda and P.J. Bártolo (Eds.) Springer, New York, 129-148.
- Moura, C.S., Bártolo, P.J. and Almeida, H.A. (2010) "Intelligent Biopolymer Selector System for Medical Applications", in: *Innovative Developments in Design and Manufacturing – Advanced Research in Virtual and Rapid Prototyping*; P.J. Bártolo et al (Eds.) Taylor&Francis, 81-86.
- Mullender, M., ElHaj, A.J., Yang, Y., van Duin, M.A., Burger, E.H. and Klein-Nulend, J. (2004) "Mechanotransduction of bone cells in vitro: mechanobiology of bone tissue", *Med Biol Eng Comput*, 42(1):14-21.
- Murakami, T., Kuroda, S.I. and Osawa, Z. (1998) "Dynamics of polymeric solid surfaces treated with oxygen plasma: effect of aging media after plasma treatment", *J Colloid Interface Sci*, 202:37-44.
- Mustafa, K., Oden, A., Wennerberg, A., Hultenby, K. and Arvidson, K. (2005) "The influence of surface topography of ceramic abutments on the attachment and proliferation of human oral fibroblasts", *Biomaterials*, 26:373-381.
- Mutel, B., Grimblot, J., Dessaux, O. and Goudmand, P. (2000) "XPS investigations of nitrogen-plasma-treated polypropylene in a reactor coupled to the spectrometer", *Surf Interface Anal*, 30:401-406.
- Naing, M.W., Chua, C.K. and Leong, K.F. (2008) "Computer Aided Tissue Engineering Scaffold Fabrication", in: *Virtual Prototyping & Bio-Manufacturing in Medical Applications*; B. Bidanda & P.J. Bártolo (Eds.) Springer USA, 67-85.
- Naing, M.W., Chua, C.K., Leong, K.F. and Wang, Y. (2005) "Fabrication of customized scaffolds using computer-aided design and rapid prototyping techniques", *Rapid Prototyping Journal*, 11(4):249-259.
- Nathan, C. and Sporn, M. (1991) "Cytokines in context", *J Cell Biol*, 113:981-986.
- Neches, L. and Cisilino, A. (2008) "Topology optimization of 2D elastic structures using boundary elements", *Engineering Analysis with Boundary Elements*, 32:533-544.

- Nehrer, S., Breinan, H.A., Ramappa, A., Young, G., Shortkroff, S., Louie, L.K., Sledge, C.B., Yannas, I.V. and Spector, M. (1997) "Matrix collagen type and pore size influence behaviour of seeded canine chondrocytes", *Biomaterials*, 18:769-776.
- Nikovits, W. and Stockdale, F.E. (2007) "Gene expression, cell determination, and differentiation", in: *Principles of Tissue Engineering*; R. Lanza, R. Langer and J. Vacanti (Eds.) Academic Press
- Norotte, C., Marga, F.S., Niklason, L.E. and Forgacs, G. (2009) "Scaffold-free vascular tissue engineering using bioprinting", *Biomaterials*, 30(30):5910-5917.
- O'Brien, F.J., Harley, B.A., Llanas, I.V. and Gibson, L.J. (2005) "The effect of pore size on cell adhesion in collagen-GAG scaffolds", *Biomaterials*, 26:433-441.
- Oota, Y., Ono, K. and Miyazima, S. (2006) "3D modeling for sagittal suture", *Physica a-Statistical Mechanics and its Applications*, 359:538-546.
- Owens, G.K. (1996) "Role of mechanical strain in regulation of differentiation of vascular smooth muscle cells", *Circ Res*, 79(5):1054-1055.
- Pardo, L., Wilson, W.C. and Boland, T. (2003) "Characterization of patterned self-assembled monolayers and protein arrays generated by the ink-jet method", *Langmuir*, 19:1462-1466.
- Park, A., Wu, B. and Griffith, L.G. (1998) "Integration of surface modification and 3D fabrication techniques to prepare patterned poly(L-lactide) substrates allowing regionally selective cell adhesion", *J Biomater Sci-Polym E*, 9:89-110.
- Park, J., Li, Y., Barthiaume, F., Toner, M., Yarmush, M., and Tilles, A. W. (2008) "Radial Flow Hepatocyte Bioreactor Using Stacked Microfabricated Grooved Substrates", *Biotechnology and Bioengineering*, 99(2):455-467.
- Pfister, A., Landers, R., Laib, A., Hübner, U., Schmelzeisen, R., Mülhaupt, R. (2004) "Biofunctional rapid prototyping for tissue-engineering applications: 3D bioplotting versus 3D printing", *Journal of Applied Polymer Science Part A: Polymer Chemistry*, 42:624-638.
- Podshivalov, L., Fischer, A. and Bar-Yoseph, P.Z. (2008) "Multi-scale finite-element analysis as a base for 3D computerized virtual biopsy system", 9th Biennial ASME Conference on Engineering Systems Design and Analysis (ESDA2008) Y. Halevi and A. Fischer (Eds.) Haifa Isreal.
- Podshivalov, L., Fischer, A. and Bar-Yoseph, P.Z. (2009) "Multiresolution geometric meshing for multiscale finite element analysis of bone micro-structures as a base for 3D computerized virtual biopsy system", ICTE 2009 International Conference on Tissue Engineering An ECCOMAS Thematic Conference, P.J. Bártolo et al (Eds.) IST Press, Lisbon, 317-323.
- Popov, V.K., Antonov, E.N., Bagratashvili, B.N., Konovalov, A.N. and Howdle, S.M. (2004) "Selective laser sintering of 3-D biodegradable scaffolds for tissue engineering", *Mat Res Soc Symp Proc.*, EXS-1, F5.4.1-F.5.4.3.
- Porter, B., Zauel, R., Stockman, H., Guldberg, R., and Fyhrie, D. (2005) "3-D computational modeling of media flow through scaffolds in a perfusion bioreactor", *Journal of Biomechanics*, 38(3):543-549.

- Portner, R., Nagel-Heyer, S., Goepfert, C., Adamietz, P. and Meenen, N.M. (2005) "Bioreactor design for tissue engineering", *Bioscience and Bioengineering*, 100:235-245.
- Prendergast, P.J. & van der Meulen, M.C.H. (2001) "Mechanics of Bone Regeneration", in: *Bone Mechanics Handbook*; S.C. Cowin (Ed.) CRC Press LLC, Boca Raton, 32.1-32.19.
- Prendergast, P.J., Huiskes, R. and Soballe, K. (1997) "Biophysical stimuli on cells during tissue differentiation at implant interfaces", *J Biomech*, 30(6):539-548.
- Qi, C. and Wang, Y. (2009) "Feature-based crystal construction in computer-aided nano-design", *Computer-Aided Design*, 41(11):792-800.
- Radisic, M., Marsano, A., Maidhof, R., Wang, Y., and Vunjak-Novakovic, G. (2008) "Cardiac tissue engineering using perfusion bioreactor systems", *Nature Protocols*, 3(4):719-738.
- Ramakrishna, S., Mayer, J., Wintermantel, E. and Leong, K.W. (2001) "Biomedical applications of polymer-composite materials: a review", *Composites Science and Technology*, 61:1189-1224.
- Reignier, J. and Huneault, M.A. (2006) "Preparation of interconnected poly(ϵ -caprolactone) porous scaffolds by a combination of polymer and salt particulate leaching", *Polymer*, 47:4703-4717.
- Reneker, D.H., Yarin, A.L., Fong, H. and Koombhongse, S. (2000) "Bending instability of electrically charged liquid jets of polymer solutions in electrospinning", *Journal of Applied Physics*, 87:4532-4547.
- Reverchon, E. and Cardea, S. (2012) "Supercritical fluids in 3-D tissue engineering", *The Journal of Supercritical Fluids*, 69:97-107.
- Riley, G.P., Curry, V., DeGroot, J., van El, B., Verzijl, N., Hazleman, B.L. and Bank, R.A. (2002) "Matrix metalloproteinase activities and their relationship with collagen remodelling in tendon pathology", *Matrix Biology*, 21(2):185-195.
- Risbud, M. (2001) "Tissue engineering: Implications in the treatment of organ and tissue defects", *Biogerontology*, 2:117-125.
- Rose, F.R. and Oreffo, R.O. (2002) "Bone Tissue Engineering: Hope vs Hype", *Biochemical and biophysical Research Communications*, 292:1-7.
- Ross, R. (1986) "The pathogenesis of atherosclerosis—an update", *N Engl J Med*, 314(8):488-500.
- Rout, P.G.J, Tarrant, S.F., Frame, J.W. and Davies, J.E. (1988) "Interaction between primary bone cell cultures and biomaterials. Part 3: a comparison of dense and macroporous hydroxyapatite", in: *Bio-ceramics and clinical applications*; A. Pizzoferratto, P.G. Ravaglioli, A.J.C. Lee (Eds.), Amsterdam: Elsevier, 591-596.
- Rouwkema, J., Rivron, N.C. and van Blitterswijk, C.A. (2008) "Vascularization in tissue engineering", *Trends Biotechnology*, 26(8):434-41.
- Rozvany, G.I.N. (2001) "Aim, scope, methods, history and unified terminology of computer-aided topology optimization in structural mechanics", *Structural and Multidisciplinary Optimization*, 21:90-108.

- Sachlos, E., Reis, N., Ainsley, C., Derby, B. and Czernuszka, J.T. (2003) "Novel collagen scaffolds with predefined internal morphology made by solid freeform fabrication", *Biomaterials* 24:1487-1497.
- Sachs, E.M., Haggerty, J.S, Cima, M.S. and Williams, P.A. (1989) "Three-dimensional printing techniques", US Pat. 5204055.
- Safinia, L., Datan, N., Höhse, M., Mantalaris, A. and Bismarck, A. (2005) "Towards a methodology for the effective surface modification of porous polymer scaffolds", *Biomaterials* 26(36):7537-7547.
- Saiz, E., Gremillard, L., Menendez, G., Miranda, P., Gryn, K and Tomsia, A.P. (2007) "Preparation of porous hydroxyapatite scaffolds", *Materials Science and Engineering C*, 27:546-550.
- Salem, A.K., Stevens, R., Pearson, R.G., Davies, M.C., Tendler, S.J.B., Roberts, C.J., Williams, P.M. and Shakesheff, K.M. (2002) "Interactions of 3T3 fibroblasts and endothelial cells with defined pore features", *Journal of Biomedical Materials Research*, 61:212-217.
- Saltzman, W.M. (1997) "Cell interactions with polymers" in *Principle of tissue engineering*, R.P. Lanza et al (Eds.), Academic Press, New York, 221.
- Santos, E., Hernández, R.M., Pedraz, J.L. and Orive, G. (2012) "Novel advances in the design of three-dimensional bio-scaffolds to control cell fate: translation from 2D to 3D", *Trends Biotechnol.*, 30(6):331-341.
- Sanz-Herrera, J.A., Garcia-Aznar, J.M. and Doblaré, M. (2009) "On scaffold designing for bone regeneration: a computational multiscale approach", *Acta Biomaterialia*, 5:219-229.
- Saunders, R., Derby, B., Gough, J. and Reis, N. (2004) "Ink-jet printing of human cells", *Mat Res Soc Symp Proc*, EXS-1, F.6.3.1-F.6.3.3.
- Schinagl, R. M., Kurtis, M. S., Ellis, K. D., Chien, S., and Sah, R. L. (1999) "Effect of Seeding Duration on the Strength of Chondrocyte Adhesion to Articular Cartilage", *Journal of Orthopaedic Research*, 17(1):121-129.
- Scriven, L.E. (1976) "Equilibrium bicontinuous structure", *Nature*, 263(5573):123-5.
- Shelton, R.M., Rasmussen, A.C. and Davies, J.E. (1988) "Protein adsorption at the interface between charged polymer substrata and migrating osteoblasts", *Biomaterials*, 9:24-29.
- Sherwood, J.K., Riley, S.L., Palazzolo, R., Brown, S.C., Monkhouse, D.C., Coates, M., Griffith, L.G., Landeen, L.K. and Ratcliffe, A. (2002) "A threedimensional osteochondral composite scaffold for articular cartilage repair", *Biomaterials*, 23:4739-4751.
- Sin, Y.M., Hohman, M.M., Brenner, M.P. and Rutledge G.C. (2001) "Experimental Characterization of Electrospinning the Electrically Forced Jet and Instabilities", *Polymer*, 42:9955-9967.
- Singhvi, R., Stephanopoulos, G. and Wang, D.I.C. (1994) "Effects of substratum morphology on cell physiology – review", *Biotechnology and Bioengineering*, 43:764-771.
- Sun, T., Norton, D., Ryan, A.J., MacNeil, S. and Haycock, J.W. (2007) "Investigation of fibroblast and keratinocyte cellscaffold interactions using a novel 3D cell culture system", *Journal of Materials Science: Materials in Medicine*, 18:321-328.

- Sun, W. and Lal, P. (2002) "Recent development on computer aided tissue engineering – a review", *Computer Methods and Programs in Biomedicine*, 67:85-103.
- Sun, W., Darling, A., Starly, B. and Gomez, C. (2004a) "Computer Aided Tissue Engineering Part II: Application to biomimetic modeling and design of tissue scaffolds", *J. Biotechnology and Applied Biochemistry*, 39(1):49-58.
- Sun, W., Darling, A., Starly, B. and Nam, J. (2004b) "Computer Aided Tissue Engineering Part I: Overview, Scope and Challenges", *J. Biotechnology and Applied Biochemistry*, 39(1):29-47.
- Sun, W., Starly, B., Nam, J. and Darling, A. (2005) "Bio-CAD modelling and its applications in computer-aided tissue engineering", *Computer-Aided Design*, 37:1097-1114.
- Sunil, V.B. and Pande, S.S. (2008) "Automatic recognition of features from freeform surface CAD models", *Computer-Aided Design*, 40:502-517.
- Szilvási-Nagy, M. and Mátyási, G. (2003) "Analysis of STL files", *Mathematical and Computer Modelling*, 38:945-960.
- Tabata, Y. (2001) "Recent progress in tissue engineering", *Drug Discov Today*, 6:483-487.
- Taboas, J.M., Maddox, R.D., Krebsbach, P.H. and Hollister, S.J. (2003) "Indirect solid free form fabrication of local and global porous biomimetic and composite 3D polymer-ceramic scaffolds", *Biomaterials*, 24:181-194.
- Taguchi, T., Sawabe, Y., Kobayashi, H., Moriyoshi, Y., Kataoka, K. and Tanaka, J. (2004) "Preparation and characterization of osteochondral scaffold", *Materials Science and Engineering: C*, 24:881-885.
- Tahara, M., Cvong, N.K. and Nakashima, Y. (2003) "Improvement in adhesion of polyethylene by glow-discharge plasma", *Surf Coat Technol*, 174-175:826-830.
- Tan, K.H., Chua, C.K., Leong, K.F., Cheah, C.M., Gui, W.S., Tan, W.S., Wiria, F.E. (2005) "Selective laser sintering of biocompatible polymers for applications in tissue engineering", *BioMedical Materials and Engineering*, 15:113-124.
- Tan, P.S. and Teoh, S.H. (2007) "Effect of stiffness of polycaprolactone (PCL) membrane on cell proliferation". *Materials Science and Engineering: C*, 27:304-308.
- Taylor, G.I. (1964) "Disintegration of water drops in an electric field", *Proceedings of the Royal Society of London A*, 280:383-397.
- Temenoff, J.S., Lu, L. and Mikos, A.G. (2000) "Bone-tissue engineering using synthetic biodegradable scaffolds", in: *Bone Engineering*; J.E. Davies (Ed.) Toronto, Em Squared Incorporated, 454-461.
- Tessmar, J.K. and Gopferich, A.M. (2007) "Matrices and scaffolds for protein delivery in tissue engineering", *Advanced Drug Delivery Reviews*, 59:274-291.
- Tormen, M., Businaro, L., Altissimo, M., Romanato, F., Cabrini, S., Perennes, F., Proitti, R., Sun, H.B., Kawata, S., Fabrizio, E.D. (2004) "3D patterning by means of nanoimprinting, X-ray and two-photon lithography", *Microelectronic Engineering*, 73/74:535-541.

- Truscello, S., Kerckhofs, G., Van Bael, S., Pyka, G., Schrooten, J. and Van Oosterwyck, H. (2012) "Prediction of permeability of regular scaffolds for skeletal tissue engineering: A combined computational and experimental study", *Acta Biomaterialia*, 8(4):1648-1658.
- Tsang, V.L. and Bhatia, S.N. (2004) "Three-dimensional tissue fabrication", *Advanced Drug Delivery Reviews*, 56:1635-1647.
- Tsubota, K., Suzuki, Y., Yamada, T., Hojo, M., Makinouchi, A. and Adachi, T. (2009) "Computer simulation of trabecular remodeling in human proximal femur using largescale voxel FE models: approach to understanding Wolff's law", *J Biomech*, 42(8):1088-1094.
- Turner, C.H. and Pavalko, F.M. (1998) "Mechanotransduction and functional response of the skeleton to physical stress: themechanisms andmechanics of bone adaptation", *J Orthop Sci*, 3(6):346-355.
- Vacanti, J.P., Morse, M.A., Saltzman, W.M., Domb, A.J., Peter-Atayde, A. and Langer, R. (1988) "Selective cell transplantation using bioabsorbable artificial polymers as matrices", *J Pediatr Surg*, 23(1):3-9.
- van der Meulen, M.C.H. and Huiskes, R. (2002) "Why mechano-biology? a survey article", *J Biomech*, 35(4):401-414.
- Vasanthan, K.S., Subramanian, A., Krishnan, U.M and Sethuraman, S. (2012) "Role of biomaterials, therapeutic molecules and cells for hepatic tissue engineering", *Biotechnology Advances*, 30(3):742-752.
- Vogel, F. (1997) "Topology Optimisation of linear-elastic Structures with ANSYS 5.4"; NAFEMS Conference on Topology Optimisation, Aalen, Germany.
- Vossenbergh, P., Higuera, G. A., van Straten, G., van Blitterswijk, C.A. and van Boxtel, A.J.B. (2009) "Darcian permeability constant as indicator for shear stresses in regular scaffold systems for tissue engineering", *Biomech Model Mechanobiol*, 8:499-507.
- Vozzi, G., Flaim, C., Ahluwalia, A. and Bhatia, S. (2003) "Fabrication of PLGA scaffolds using soft lithography and microsyringe deposition", *Biomaterials*, 24:2533-2540.
- Wang, F., Shor, L., Darling, A., Khalil, S., Güçeri, S. and Lau, A. (2004) "Precision deposition and characterization of cellular poly- ϵ -caprolactone tissue scaffolds", *Rapid Prototyping Journal*, 10:42-49.
- Wang, H., Pieper, J., Péters, F., Blitterswijk, C.A.v. and Lamme, E.N. (2005) "Synthetic scaffold morphology controls human dermal connective tissue formation", *Journal of Biomedical Materials Research Part A*, 74:523-532.
- Wang, J.H. and Thampatty, B.P. (2006) "An introductory review of cell mechanobiology", *Biomech Model Mechanobiol.*, 5(1):1-16.
- Wang, S. and Tarbell, J.M. (2000) "Effect of fluid flow on smooth muscle cells in a 3-dimensional collagen gel model", *Arterioscler Thromb Vasc Biol*, 20:2220-2225.
- Wang, Y. (2007) "Periodic surface modeling for computer aided nano design," *Computer-Aided Design*, 39(3):179-189.

- Webb, K., Hlady, V. and Tresco, P.A. (1998) "Relative importance of surface wettability and charged functional groups on NIH 3T3 fibroblast attachment, spreading, and cytoskeletal organization", *J Biomed Mater Res*, 41:422-430.
- Wei, G., Jin, Q., Giannobile, W.V. and Ma, P.X. (2007) "The enhancement of osteogenesis by nanofibrous scaffolds incorporating rhBMP-7 nanospheres", *Biomaterials*, 28:2087-2096.
- Wettergeen, M.A., Bucklen, B.S., Liebschner, M.A.K. and Sun, W. (2008) "CAD Assembly Process for Bone Replacement Scaffolds in Computer-Aided Tissue Engineering", in: *Virtual Prototyping & Bio-Manufacturing in Medical Applications*; B. Bidanda and P.J. Bártolo (Eds.) Springer, New York, 87-111.
- Wettergreen, M.A., Bucklen, B.S., Starly, B., Yuksel, E., Sun, W. and Liebschner, M.A.K. (2005a) "Creation of a unit block library of architectures for use in assembled scaffold engineering", *Computer-Aided Design*, 37(11):1141-1149.
- Wettergreen, M.A., Bucklen, B.S., Sun, W. and Liebschner, M.A.K. (2005b) "Computer-aided tissue engineering of a human vertebral body", *Annals of Biomedical Engineering*, 33(10):1333-1343.
- Whang, K., Thomas, C.H., Healy, K.E. and Nuber, G. (1995) "A novel method to fabricate bioabsorbable scaffolds", *Polymer*, 36:837-842.
- Williams, B. (1998) "Mechanical influences on vascular smooth muscle cell function", *J Hypertens*, 16(12 Pt 2):1921-1929.
- Williams, J.M., Adewunmi, A., Schek, R.M., Flanagan, C.L., Krebsbach, P.H., Feinberg, S.E., Hollister, S.J. and Das, S. (2005) "Bone tissue engineering using polycaprolactone scaffolds fabricated via selective laser sintering", *Biomaterials*, 26(23):4817-4827.
- Wohlgemuth, M., Yufa, N., Hoffman, J. and Thomas, E.L. (2001) "Triply Periodic Bicontinuous Cubic Microdomain Morphologies by Symmetries," *Macromolecules*, 34(17):6083-6089.
- Woodfield, T.B.F., Malda, J., de Wijn, J., Péters, F., Riesle, J. and van Blitterswijk, C.A. (2004) "Design of porous scaffolds for cartilage tissue engineering using a three-dimensional fiber-deposition technique", *Biomaterials* 25:4149-4161.
- Woodfield, T.B.F., Van Blitterswijk, C.A., Riesle, J., De Wijn, J., Sims, T.J. and Hollander, A.P. (2005) "Polymer scaffolds fabricated with poresize gradients as a model for studying the zonal organization within tissue engineered cartilage constructs", *Tissue Engineering*, 11:1297-1311.
- Xiong, Z., Yan, Y., Zhang, R. and Wang, X. (2005) "Organism manufacturing engineering based on rapid prototyping principles", *Rapid Prototyping Journal*, 11(3):160-166.
- Yan, Y., Wu, R. and Zhang, R (2003a) "Biomaterial forming research using RP technology, *Rapid Prototyping Journal*, 9:142-149.
- Yan, Y., Zhang, R. and Lin, F. (2003b) "Research and applications on bio-manufacturing", in: *Proceedings of the International Conference on Advanced Research in Virtual and Physical Prototyping*, P.J. Bártolo et al (Eds.) Leiria, 23-29.

- Yang, J., Bei, J. and Wang, S. (2002) "Improving cell affinity of poly(D,L-lactide) film modified by anhydrous ammonia plasma treatment", *Polym Adv Technol*, 13:220-226.
- Yang, S.F., Leong, K.F., Du, Z. and Chua, C.K. (2001) "The design of scaffolds for use in tissue engineering Part 1, Traditional factors", *Tissue Engineering*, 7:679-689.
- Yeong, W.Y., Chua, C.K., Leong, K.F. and Chandrasekaran, M. (2004). "Rapid prototyping in tissue engineering: Challenges and potential", *Trends in Biotechnology*, 22:643-652.
- Yeong, W.Y., Chua, C.K., Leong, K.F., Chandrasekaran, M. and Lee, M.W. (2005) "Development of scaffolds for tissue engineering using a 3D inkjet model maker", in: *Virtual Modelling and Rapid Manufacturing – Advanced Research in Virtual and Rapid Prototyping*, P.J. Bártolo et al (Eds.), Taylor & Francis, London, UK, 115-118.
- Yeong, W.Y., Chua, C.K., Leong, K.F., Chandrasekaran, M. and Lee, M.W. (2006) "Indirect fabrication of collagen scaffold based on inkjet printing technique", *Rapid Prototyping Journal*, 12: 229-237.
- Yildirim, E., Ayan, H., Vasilets, V., Fridman, A., Gucer, S. and Sun, W. (2008) "Effect of Dielectric Barrier Discharge Plasma on the Attachment and Proliferation of Osteoblasts Cultured over Poly (ε-Caprolactone) Scaffolds", *J. of Plasma Processes & Polymers*, 5(1):58-66.
- Zeltinger, J., Sherwood, J.K., Graham, D.A., Müller, R. and Griffith, L.G. (2001) "Effect of pore size and void fraction on cellular adhesion, proliferation, and matrix deposition", *Tissue Engineering*, 7:557-572.
- Zhao, K., Deng, Y. and Chen, G.Q. (2003) "Effects of surface morphology on the biocompatibility of polyhydroxyalkanoates", *Biochemical Engineering Journal*, 16:115-123.
- Zhou, W.Y., Lee, S.H., Wang, M., Cheung, W.L. and Ip, W.Y. (2008) "Selective laser sintering of porous tissue engineering scaffolds from poly(L-lactide)/carbonated hydroxyapatite nanocomposite microspheres", *J. Mater Sci:Mater Med*, 19:2535-2540.